Continuum Damage Mechanics Models and Their Applications to Composite Components of Aero-Engines

A thesis for the degree of Doctor of Philosophy

Tian-Hong Yu

2016

Composites Research Group, Faculty of Engineering,

The University of Nottingham, Nottingham NG7 2RD, UK

Acknowledgements

First of all, I would like to thank my supervisor, Prof. Shuguang Li, who shared valuable expertise and provided important guidance to me throughout the course of this research project, which enabled me to achieve significant progress in the last three years. His attention to detail, patience and academic professionalism not only ensured the delivery of high quality supervision to my research project, but also inspired me to tackle technical problems with persistence and confidence, from which I will benefit for the rest of my life.

I would also like to express my gratitude to my co-supervisors. My gratitude goes to Dr. Elena Sitnikova, for her helpful feedbacks on my research work and her comprehensive advice on my thesis writing, and to Dr. Richard Brooks, for his effort to help sourcing the materials for the experimental work.

The generous support from AVIC Commercial Aircraft Engine Co. Ltd. (ACAE), both financially and technically, which made this research project possible, is gratefully acknowledged. My gratitude also goes to my fellow research team members from ACAE, for their support and the quality time we spent together working for a joint research program.

Moreover, I am forever in debt to my parents for the understanding, encouragement and support they provided to me in the last few years, which allowed me to focus on my PhD study.

Abstract

Built on top of a consistent continuum damage mechanics (CDM) damage representation formulation, a novel damage evolution law based on the concept of damage driving force is proposed for modelling the evolution of matrix damage in UD composites. This damage evolution law has the advantage of allowing different damage evolution constants to be associated with different loading modes (corresponding to the fracture modes in Fracture Mechanics) when dealing with mixed-mode loading conditions, which avoids the unrealistic assumption in many existing theories that different loading modes make the same contribution to damage evolution. A new CDM model for UD composites is developed incorporating this damage evolution law.

Thanks to the laminate test cases designed and conducted in this project, it is found that the damage initiation and propagation related material constants can be determined using these tests. These damage-related material constants served as inputs to the UD composite CDM model.

Apart from the tests on laminates, detailed experimental investigation was carried out regarding damage in two types of layer-to-layer interlock 3D woven composites which are reinforced by IM7 carbon fibre (CF) and E-glass fibre (GF), respectively. The experimental data obtained and the damage processes recorded for these 3D woven composites can serve as a good reference for future interest in this area, since currently only limited studies are available in the literature regarding damage in this type of 3D woven composites.

The new UD composite CDM model is applied to predict intra-laminar damage in laminates and intra-tow damage in the 3D woven composites. Compared to the

experimental results, it is found that the model produced satisfactory predictions but lacking the capability to predict a severe stress-strain nonlinearity caused by shear.

A new pragmatic continuum damage model is developed to capture the damage effect of inter-tow cracks in the 3D woven composites caused by warp direction tensile loading. This model works in conjunction with the intra-tow damage predicted by the aforementioned UD composite CDM model.

With the successful development of these damage models, a novel damage modelling methodology for textile composites is made possible and implemented in conjunction with the UnitCells© composite characterisation tool [1] and the artificial neural network tool developed in [1]. Through the artificial neural network for data interpolation, the constitutive behaviour of textile composite incorporating the effect of damage can be interpolated for any load combination, which is then readily available for engineering applications.

Table of Contents

List of Figures

List of Tables

Abbreviations

2D	Two-dimensional
3D	Three-dimensional
AE	Acoustic emission
CF	Carbon fibre
CDM	Continuum damage mechanics
CFRP	Carbon fibre reinforced plastics
FAA	Federal Aviation Administration
GE	General Electric company
GF	E-glass fibre
GFRP	Glass fibre reinforced plastics
Micro-CT	Micro computed tomography
Prepreg	Pre-impregnated composites
QI	Quasi-isotropic
RTM	Resin transfer moulding
RVE	Representative volume element
UD	Unidirectional fibre-reinforced composites
UMAT	User-defined material subroutine
VARTM	Vacuum assisted resin transfer moulding
WWFE	World Wide Failure Exercises

Notations

σ	Direct stress component
τ	Shear stress component
ε	Direct strain component
γ	Engineering shear strain component
ν	Poisson's ratio
E	Young's modulus
G	Shear modulus
U	Complementary strain energy density function
Ψ	Helmholtz free energy density
I	Irreducible integrity bases
V	Damage vector
ω	Damage variable defined for UD composite material system
Ω	Damage variable defined for textile composites
S	Material compliance matrix
C	Material stiffness matrix
ρ	Damage driving force

1. Introduction

1.1 Background

As mentioned in [2], to improve the propulsive efficiency of aerospace turbofan engine for achieving better fuel economy, modern turbofan engines are designed with increasingly large fan sections. As shown in Fig. 1-1, for a typical fan section of a turbofan engine, the fan blades and fan case are the two major structural components.

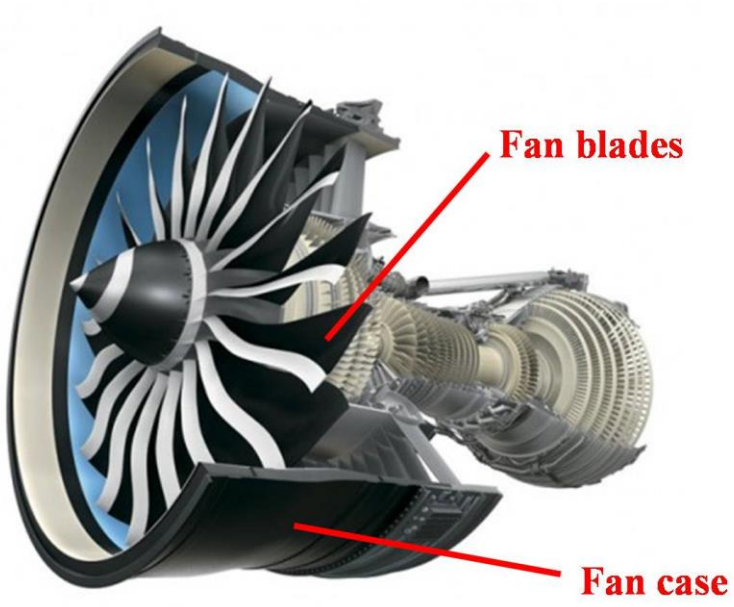

Fig. 1-1 Illustration of fan blades and fan case in a turbofan engine [3]

With the increase in size, fan sections of modern turbofan engines are becoming heavier. For example, the CF-6 engine produced by General Electric (GE) Aviation, which entered service in 1973, had a bypass ratio of 5. The fan section in that engine weighs about 820 kg and is equivalent to approximately 20% of the total engine weight. By the time of 2011, the new GEnx turbofan engine, which is developed as a modernised replacement for the CF-6 engine, featured a bypass

ratio of 10. This time, the fan section in the GEnx engine weighs about 1742 kg and accounts for roughly 30% of the total engine weight. As can be seen, the increase in size for the fan section has caused significant weight penalties. Moreover, every kilogram added to the fan section normally results in 2.25 kg of extra support structure being incorporated into the engine and aircraft wing structures [2].

To reduce the weight penalty associated with large fan section, light-weight composite materials are used in the fan sections of modern turbofan engines. According to [4] and [5], in the case of GEnx engine, the carbon fibre composite fan blades and fan case employed saved engine weight by about 160 kg per engine when compared to the metallic alternative.

Apart from weight-saving, impact resistance is another important consideration for fan blades and fan case. This is due to the aircraft engine certification requirements imposed on fan blades and fan case for the safe operation of commercial flights. For example, the Federal Aviation Administration (FAA) in the United States of America requires that fan case of a turbofan engine must be able to contain failed and released fan blades when the engine is running at full power. This dictates that the fan case must have sufficient impact resistance to prevent the penetration of high speed blade fragments through the fan case [6]. Because of this, the fan case of a turbofan engine is often referred to as the fan containment case. In addition, fan blades are also subjected to bird strike requirements. For instance, during a typical take-off scenario, if the fan blades are impacted by a bird below a certain size and weight, the damaged fan blades should not cause engine thrust reduction higher than the limits specified in related certification requirements, like those in [6].

As a result, for the design of composite fan blades and composite fan case, one should consider impact damage resistance from the start of the design process. Moreover, to predict impact damage accurately and efficiently during the design process of composite structural components, a robust and systematic composite damage modelling strategy is required.

According to [7] and [8], initially, in the engineering community, there was little interest in predicting damage in composites and only simple failure prediction methods were used for the design and sizing of laminated composites. The common practice at that time was to use fibre failure strain to predict the final failure of laminates or to adopt the "make and test" approach to measure laminate failure stress (strain) allowables directly. The former method may be acceptable for quasi-isotropic (QI) laminates since there are sufficient numbers of fibres in multiple directions, making the laminate behaviour as fibre-dominated. This method was in particular favoured by those engineers who treated carbon fibre composites as "black aluminium" where QI laminate stacking sequences were used exclusively when designing the laminates [9]. However, to exploit the full potential of laminated composites, stacking sequences other than QI should be used where appropriate. For the laminates where matrix failure modes are important, the former method is not suitable and the "make and test" approach is normally used in the industry to provide information on laminate failure [7]. However, this approach is both time-consuming and expensive as it is not a predictive method and a large number of tests on laminate samples of different stacking sequences are necessary in order to obtain corresponding failure stresses (strains) [8]. As a result, there is a growing trend in the engineering community to

move away from the “make and test” approach and rely more on the predictive methods for laminate failure analysis [7].

In response to this need of predictive laminate failure analysis methods, various failure criteria applicable to the unidirectional (UD) laminae inside laminates were developed. These criteria were later assessed in a series of World Wide Failure Exercises (WWFEs). However, it was found that instead of simple instantaneous failures, many laminates suffered gradual damage processes when subjected to loads [10]. Due to this and as a recommendation resulting from the WWFE activities, the laminate failure theories incorporating damage process modelling capabilities have been found to be superior for characterising laminate behaviour under loads [10-12]. Furthermore, another important conclusion from the WWFE activities is that failure criteria and damage modelling formulations should be physically based to reflect the true physics of failure and damage in composites [9,10,13]. It was identified that many existing laminate failure and damage theories contained deficiencies which compromised the physical justification of these theories, leading to inaccurate predictions in some cases [12,14]. These deficiencies should be rectified before the failure and damage theories can be approved for engineering applications.

Apart from laminates, textile composites are also gaining applications in the fan sections of turbofan engines. A recent example is the CFM Leap-X engine developed by Safran Aircraft Engines [15], which used 3D woven carbon fibre composites to construct the fan blades and the fan case. Due to the novelty and the more complex internal structures of 3D textile composites relative to conventional laminated composites, failure and damage analysis of 3D textile composites is not as well-developed as that for laminates. Consequently, no systematic approach

suitable for engineering applications was provided in the open literature regarding failure and damage analysis of 3D textile composites.

Based on the background information as introduced above, it can be seen that with the increasing application of composite materials in aircraft engines, especially with the use of novel textile composites, there is a genuine and urgent need in the aerospace industry for a physically rigorous, efficient and systematic composite damage modelling methodology to aid the design process of composite structures, which to the best of author's knowledge is not yet available in the engineering community. Moreover, as composites of different reinforcement configurations might be considered for aero-engine applications, such a methodology should be applicable to simple forms of composites like conventional laminates, as well as advanced textile composites like 3D textile composites.

1.2 Aims & Objectives

In response to the aforementioned demand from the aerospace industry, the aim of this research is to develop a physically based, efficient and systematic damage modelling methodology for composite structures in aero-engines, with an emphasis on the damage analysis of textile composites.

The development of this methodology is a part of the joint research effort to establish an integrated tool set for the design and analysis of composite structures in aero-engines. Due to this, the damage modelling methodology developed here serves as a necessary input to the textile composite characterisation toolbox developed in [1], where the characterisation of failure and damage in textile composites is made possible thanks to the adoption of this methodology. With the

failure and damage effect properly accounted for, the material properties predicted by the material characterisation toolbox are then used in the composite structure impact analysis models developed in [16], where impact damage in various composites structures is simulated and assessed to aid the design of these structures.

To accomplish the research aim stated above, following objectives are set:

(1) To develop a novel physically based theoretical damage model for UD composites. This model should be capable of rationally predicting the orientation, initiation and evolution of matrix damage, as well as detecting abrupt failure modes like fibre failures. Moreover, it should be applicable to general loading conditions including unloading and reloading scenarios.

(2) To implement the aforementioned UD composite theoretical damage model as practical material subroutine codes usable for damage analysis, which are catered for the prediction of damage in UD laminae within laminates, as well as for the prediction of damage in UD fibre tows inside textile composites.

(3) If applicable, to develop a pragmatic damage model to account for possible interfacial damage associated with the interfaces between the fibre tows and the matrix materials.

(4) To carry out experimental investigation regarding damage in laminates and textile composites. For the experimental work, different test cases should be designed and employed respectively for the determination of damage-related material properties and the acquisition of reference experimental data which can be used to validate the damage models developed in this research.

(5) To verify that the damage models and the material subroutines developed in this research work are mathematically rigorous and self-consistent using simple analysis cases where the correctness of the results can be judged based on common sense and analytical results.

(6) To carry out validation work for the damage models developed in this research. This can be achieved by applying the damage models for the prediction of real-life damage scenarios concerning laminates and textile composites. The predictions from the models should then be compared against the corresponding experimental data recorded so that the model performance can be evaluated and validated.

1.3 Structure of Thesis

There are eight chapters in this thesis. Apart from the current introduction chapter, the organisation for the rest of the chapters is described below.

In Chapter 2, a comprehensive and up-to-date literature review is provided for the topics relevant to this research. These topics include the background and development of aerospace composites, the investigation of failure and damage in composites of various fibre reinforcement configurations, and the theories and modelling techniques developed for predicting failure and damage in composites. Some important observations are made based on the literature review conducted, which provided valuable guidance for the present research.

Based on the appraisal of UD composite failure and damage theories as presented in the literature review, a novel theory for modelling matrix damage evolution in UD composites is developed and described in detail in Chapter 3.

In Chapter 4, the experiments conducted on the laminates and the 3D textile composites for this research project are introduced. The experimental results obtained from different test cases enabled the determination of damage-related material properties and provided reference experimental data which can be used to validate the damage model predictions.

The damage evolution law introduced in Chapter 3 is integrated with an existing UD composite failure criterion and an existing UD composite damage representation formulation to form a novel continuum damage mechanics (CDM) model applicable to UD composites. The implementation and the verification of this CDM model are presented in Chapter 5.

In Chapter 6, the validation of the novel UD composite CDM model is conducted. Through the validation work, the suitability of this CDM model to predict real-life composite damage scenarios is assessed, demonstrating the advantages and deficiencies of this model when used for practical applications.

A pragmatic damage model developed for capturing inter-tow damage effect is introduced in Chapter 7. This damage model is developed to complement the UD composite CDM model for situations when the effect of inter-tow damage like tow-matrix inter-facial debonding cannot be ignored in the process of damage analysis.

Finally, in Chapter 8, the conclusions and outcomes of this research are summarised. Based on the findings out of this project, suggestions for future research directions in this research area are also provided.

2. Literature Review

In this chapter, a comprehensive and up-to-date literature review is provided for the topics relevant to this research.

Since this research focuses on the composite materials for aerospace applications, an overview on the background and the development of aerospace composites is provided in this chapter.

Furthermore, as the aim of this research is to develop a composite material continuum damage mechanics model intended for engineering applications, experimental investigations and theoretical developments concerning failures and damage in composites are reviewed. Such review is presented in this chapter according to the order of increasing complexity of composite materials, i.e. from the simplest unidirectional (UD) composites to the more advanced 3D textile composites.

2.1 Composite Materials for Aerospace Applications

In this section, a review on the use of composite materials in the aerospace industry is presented.

First of all, to appreciate the rationale behind the increasing applications of composite materials in the aerospace industry, a general discussion on the benefits of using composites is provided, along with a brief summary for the historical developments associated with aerospace composites.

Then, the shortfalls and issues related to the most common type of aerospace composites, laminated composites, are discussed. This then leads to the review of

3D textile composites, where the reasons for its increasing popularity over laminates for certain applications are explained.

2.1.1 Benefits and History

According to [17,18], initial serious application of composites in the aerospace industry dates back to the 1960s, when high performance continues fibres and homogeneous matrix material were first combined together to form the so called advanced composite material at that time. Among the composite materials reinforced by different fibre types, the one reinforced by carbon fibres, i.e. carbon fibre reinforced plastics (CFRP), has received the widest range of applications.

In comparison to aluminium alloys, which are the most common metallic materials traditionally used in aerospace industry, CFRP has many superior properties.

First of all, specific stiffness and specific strength in the longitudinal direction of typical unidirectional (UD) CFRP are normally about 3 and 6 times higher than those offered by aluminium alloy [17]. This often allows significant weight savings to be achieved when switching from traditional metallic structures to composites structures. For almost any aerospace vehicle, weight saving is normally always beneficial as either extra payload can be accommodated or significant reduction in fuel consumption can be achieved. In the case of commercial airliners, extra payload capability may allow more passengers to be carried per flight to maximise airline profit, or alternatively, without using the additional payload capability, a resulting lighter aircraft leads to lower specific fuel consumption which reduces the direct operating cost of commercial flights. As mentioned in [17], according to the statistics in 1990, the value of weight

savings for various aerospace vehicles can be translated into corresponding life cycle fuel cost savings, which varies from a sizable $300/lb for a medium-sized helicopter to an astonishing $30,000/lb for a spacecraft. Based on this, the attractiveness of using composites for achieving lighter aerospace structures is obvious.

Other than weight saving, composites can also be tailored to suit specific structural load requirements. A well-known example is the Grumman X-29A experimental aircraft which had forward-swept wings. The forward-swept wing structures were made with composites which contained CFRP laminates with layers tailored to overcome the static divergence associated with this particular wing configuration, which cannot be practically achieved using traditional isotropic materials [18].

Composites are also known to be of better fatigue resistance than aluminium alloys. Typically, CFRP has much longer fatigue life than aluminium alloys. In composites, fatigue damage accumulation is normally in the form of slow development of multiple damage modes that are wide-spread in the material. On the contrary, in metallic materials, fatigue loading often induces a few dominant microcracks which may propagate abruptly when a critical number of fatigue cycles is reached [18]. As a result, metal fatigue is normally more abrupt and dangerous than composite fatigue.

Another advantage of using composites is that large integrated structural components can be made possible thanks to composite manufacture processes like co-curing. This may significantly reduce the numbers of parts and fasteners in a structural assembly. As illustrated in [17], the CFRP composite structure replacement for the original full metallic vertical tail plane of L-1011 airliner not

only saved 27% structural weight, but also reduced the part number and fastener number down to a third and a quarter of the original quantities respectively. This certainly reduced structural complexity and simplified the assembly process dramatically. Moreover, integrated composite structures may even improve aerodynamic performance directly. In the case of the F-22 fighter jet, some flight control surfaces were made with composites such that the control surface skins were co-cured to the supporting structures underneath. Thanks to this, no rivets were used on the skins which led to less aerodynamic drag [18].

Due to the benefits offered by composite structures as listed above, increasing applications of composite materials in the aerospace industry started around the 1960s. Initially, owing to limited experience with composites, by the time of the 1970s, attempts were only made to produce trial composite parts for replacing existing metallic structures. These early attempts include CFRP replacement structures for metallic control surfaces and sections of empennage primary structures on the Boeing 727, the Lockheed L-1011 and the McDonnell Douglas DC-10 transport aircraft [17].

Then, in the 1980s, thanks to the experience gained from earlier attempts, composite structures were designed from the start as production pieces for control surfaces, winglets and empennage structures of airliners. The Airbus A300/310 and A320 aircraft family, as well as the Boeing 757/767 and 777 aircraft, were some of the famous commercial aircraft types at that time which utilised substantial CFRP and sandwich composite materials [17].

By the time of 2009, CFRP composites had secured dominant presence in aircraft structures as not only most of the secondary structures and empennage structures were made of composites, but major primary structures like fuselage and wings

were also mainly constructed from CFRP. The latest examples are the Boeing 787 [19] and the Airbus A350 [20] airliners as both are flying with nearly complete CFRP airframes. It is truly remarkable considering that just after 50 years of development since 1960, CFRP had gained such a wide range of applications in aircraft structures to an extent that landing gear and engine pylon might be the only major aircraft structural components without extensive use of CFRP.

In terms of composite applications in aerospace turbofan engine, the trend is more conservative. The service temperature limit of polymer matrix composites effectively constrained the application of composites to "cold" sections of engines. As a result, composites are normally only employed for structures in the fan system.

Initially, around 1990, for limited types of engines, composites were only used in the nose cone which is the foremost component positioned in the fan system for guiding air stream into the engine air intake [2].

By the time of 1993, General Electric (GE) first successfully used CFRP laminates for making large fan blades for the GE90 turbofan engine. The laminates were composed of hundreds of pre-impregnated (prepreg) layers, which were moulded and cured into the blade shape required. In addition, a thin layer of titanium alloy is attached to the blade leading edge for shielding the laminates from impact and erosion damage. This marked the start of large quantity applications of composites in aero-engines [2]. Since then, composites were used in other turbofan engine components like fan containment case and bypass air duct stator vanes.

In 2006, the first composite fan containment case design emerged, which was employed on the GEnx turbofan engine. According to [21-23], this composite fan case design selected 2D tri-axial braided carbon fibre fabric as the fibre reinforcement type which was rolled into a cylinder. The cylinder was then moulded into fan case structures using resin transfer moulding (RTM) process. For each fabric layer, fibre tow orientations were set at -60º, 0º and 60º to form a quasi-isotropic material architecture. It was argued that since every fabric layer was quasi-isotropic, stiffness mismatch between layers would be minimised which should help to prevent inter-laminar damage. However, other than stiffness mismatch, weak interlaminar strength is also a major cause for delamination damage. Since the 2D tri-axial braided fabric still retained the layered configuration where the inherently weak interfaces between the layers were still present, it is envisaged that this woven architecture should still be susceptible to delamination damage.

Just seven years later, in 2013, 3D woven CFRP composites were successfully employed in the fan blade and the fan case structures of the new CFM Leap-X turbofan engine, which is expected to enter into service by 2016 [15].

2.1.2 Issues Associated with Laminates

However, the use of composite materials in the aerospace industry is not without problems and hurdles.

For laminated composites, which are the most commonly used type of composite materials, although they possess superior in-plane mechanical properties, their poor through-the-thickness properties can be a significant drawback [24,25].

Since there is no fibre reinforcement in the thickness direction, laminates have low Young's modulus and strength values in the thickness direction. For the same reason, their transverse shear modulus and strength are also low. Moreover, because of their layered architecture and low inter-laminar fracture toughness, laminates are known to be prone to delamination damage which can be easily caused by inter-laminar shear stresses arising from transverse impact. As a result, laminates usually have poor impact damage resistance.

A well-known example demonstrating the inferior impact resistance of laminates is the ill-fated development of CFRP fan blades for the Rolls-Royce RB211 turbofan engine. Developed in the 1960s, these fan blades were made of carbon fibre laminates and represented a radical new advancement in aero-engine technology at that time [26]. However, the development ceased when the blades shattered catastrophically under bird strike during the engine bird ingestion test [27]. Due to this composite fan blade design flaw and other technical issues, the RB211 engine programme suffered long delays and heavy financial penalties which led to the nationalisation of Rolls-Royce. In the end, conventional titanium alloy fan blades replaced the composite blades which then allowed the RB211 engine to enter the service.

According to [25,28], apart from the shortfalls in terms of mechanical properties as mentioned above, there are also many issues concerned with laminate manufacture.

Laminates are mostly made from prepregs which require expensive refrigeration facilities for storage. This normally causes significant increase in the production cost.

Beside this, laminate manufacture can be very labour intensive as in many cases manual hand lay-up procedure is still required if automation is not possible. A typical example is the making of a CFRP composite fan blade for the GE90 engine, where hundreds of prepreg layers were laid piece by piece by shop floor workers to form the stacking sequence desired [2]. Without a doubt, such a labour intensive process resulted in long production times as currently a single CFRP fan blade for the GE90 engine needs about 340 hours of lead time from the cutting of raw prepreg material to the delivery of a finished blade [29].

In addition, most prepreg layers used for making laminates are poor for draping. As a result, laminates normally cannot be directly moulded into complex shapes and components of complex shapes may have to be carefully machined from laminates which is time-consuming and likely to introduce defect if the process is not well-controlled.

2.1.3 3D Textile Composites

3D textile composites first emerged in the 1960s, when carbon-carbon 3D braided composite was evaluated for its application in rocket motor components [30]. However, it was not until the mid-1980s that 3D textile composites in the form of fibre reinforced polymers received serious development and 3D textile fibre reinforcements of various configurations were developed. The need of 3D composites is mainly to overcome the deficiencies associated with 2D laminates, that is, to improve through-the-thickness mechanical properties, to improve impact damage resistance and to reduce high production cost [31]. However, due to the inherent fibre undulation presenting in most 3D textile composites, they

normally have inferior in-plane mechanical properties when compared with laminates of similar fibre volume fractions. As a result, 3D textile composites may not be suitable for stiffness- and strength-critical applications where high in-plane mechanical properties are required. Nonetheless, thanks to the benefits offered by 3D textile composites, they are becoming more widely-used in the aerospace industry, especially for structural components requiring good impact resistance.

Unlike prepregs, for producing 3D textile composites, large quantities of dry fibre tows are formed into 3D textile preforms using textile processes. The preforms are then impregnated with resin according to liquid moulding processes so that the final composite component can be moulded.

In 3D textile composites, fibres are oriented or inserted in the thickness direction using textile processes such as stitching, 3D weaving, braiding and knitting [32]. With fibre reinforcement in the thickness direction, 3D textile composites have better mechanical properties in the thickness direction and are less prone to delamination when compared against laminates [24,31,32]. Thanks to the textile processes which are automated by the use of textile machinery, preforms of 3D textile composites can be produced at a fast rate with little human interference. Moreover, without much difficulty, some textile processes can be set up to produce single-piece near-net-shape 3D textile preforms of complex shapes [24,32]. Last but not least, due to the combination of automated textile processes and the use of dry textile preforms instead of prepreg materials, the production cost of 3D textile composites is usually much lower than that of laminates.

The simplest and the cheapest textile process for making 3D textile preforms is stitching, where 2D fabric layers are stitched together in the thickness direction by high-strength fibres [24,32]. This type of 3D textile composites are commonly

referred to as stitched composites. In contrast to other textile processes, stitching is considered as the most flexible process because through-the-thickness fibre reinforcements can be chosen to be applied only at where needed. Stitched composites have been used on centre fuselage skin of the Eurofighter fighter aircraft [33] and rear pressure bulkhead in the Airbus A380 airliner [34,35]. For both cases, it was reported that stitched composites achieved significant cost savings over equivalent prepreg laminate constructions.

3D weaving is the fastest and the most used textile process for producing large volumes of 3D preforms [24,25,28]. More importantly, it is capable of weaving preforms of complex shapes which makes the production of single-piece near-net-shape 3D woven composites possible. However, although a wide range of through-the-thickness weave patterns are available, in-plane fibre tow orientations are normally restricted to 0º and 90º (warp and weft directions). This means 3D woven composites normally have poor in-plane shear properties. The earliest application of 3D woven composites for commercial aviation appeared in the Beech Starship aircraft where 3D woven composite structural connectors were used to join wing panels[36]. Recently, 3D woven composites were used for constructing the fan containment case of the CFM Leap-X turbofan engine where flanges and other structural features were continuously woven together for better structural integrity [37].

3D preforms can also be made using braiding [24,32]. Braided 3D composites normally have the highest level of conformability, structural integrity and torsional stability among all types of 3D composites. The braiding process can be adjusted during operation to achieve variations in cross-sectional shape, taper, and bends for the preform that is being braided. Thanks to the wide range of braiding

angles available, fibres can be oriented from -80º to 80º in a plane with respect to the braiding axis. However, due to limitations of most braiding machines, this textile process currently can only produce slender preforms. It was reported that propeller blades for a type of naval landing craft had been made from 3D braided composites [38].

Knitting is another textile process for making 3D preforms. Knitted preforms are highly drapable which makes them most suitable for producing net-shape parts of very complex geometry [24,32]. However, due to the highly curved fibre path resulting from the knitting process, knitted 3D composites usually have low stiffness when compared with other types of 3D composites. Because of this, knitted 3D composites are mainly used for non-structural components.

Aforementioned 3D textile composites generally have better impact damage resistance than laminates.

For 3D woven composites, it was found that the impact energy required to initiate damage can be up to 60% higher than that for laminates of the same thickness [39]. Moreover, mode I type of fracture toughness values of 3D woven composites can be 6 to 20 times higher than those offered by laminates of the same thickness, resulting in improved resistance to impact-induced delamination [40,41]. In some cases, impact energy dissipation in 3D woven composites was found to be more than twice of that in laminates of comparable areal densities and fibre volume fractions under low speed impact scenarios with a fixed impact speed of 2m/s [42]. When compared with laminates, better impact damage resistance of 3D woven composites often leads to less impact-induced degradation for in-plane mechanical properties, hence, providing better residual properties after impact [43,44]. However, due to crimping of fibres, damage to fibres during

weaving processes and the existence of resin rich areas, 3D woven composites normally have lower in-plane mechanical properties than laminates of the same fibre volume fraction [43-52].

In terms of stitched composites, their improved impact resistance over laminates was reported in [53-57] for low speed impact events and in [58-60] for high speed impacts. Detailed studies on the influence of various stitch parameters to the impact resistance of stitched composites were presented in [61,62]. It was found a small volume fraction of through-the-thickness stitched fibre reinforcement is normally able to provide significant increase in mode I interlaminar fracture toughness. As a result, crack propagation in stitched composites mostly occurs in mode II type of fracture. However, similar to 3D woven composites, compared with laminates of the same fibre volume fraction, stitched composites usually have reduced in-plane mechanical properties [32,59,63-66]. This is because the needles for the stitching process often damage the in-plane fibres locally. Also, resin rich zones exist in stitched composites which are normally associated with the thickness direction threads.

According to [67,68], thanks to their tight integral textile structure, 3D braided composites were found to have the smallest damage areas under ballistic impacts when compared to all other 3D textile composites tested. Moreover, they were also reported to have the highest ballistic impact penetration resistance among all the textile composites studied in [69]. Under low speed impact, since there is no layered architecture in 3D braided composites, resin crack, tow debonding and fibre breakage were the common failure modes observed, while delamination was never discovered [70-73]. Due to curved fibre tows around the braiding axis, 3D

braided composites also have lower in-plane properties than laminates of the same fibre volume fraction [67,74].

In terms of knitted 3D composites, although the highly curved fibre tow path limited their in-plane material properties, they were reported to have the ability to absorb substantial amount of impact energy, largely due to high mode I fracture toughness [31]. As mentioned in [75], compared to the composite of uniweave reinforcements with similar fibre volume fraction, the knitted 3D composite used in that investigation was shown to absorb 64% more impact energy when tested under impacts with an incident energy of 7.3J. Chou et al. [76] conducted notched Charpy impact tests on the E-glass/epoxy composites of 3D knitted architecture and plain weave architecture. They found that for the test case they designed, the impact energy absorbed by the former was about 2.4 times of that absorbed by the latter. As suggested in [31], this ability of knitted 3D composites to absorb much greater amounts of impact energy than 2D composites implies that they are potential candidate materials for damage-prone structures or crush members.

2.2 Failure in UD Composites under Static Loadings

In this section, failure mechanisms and failure theories related to the simplest form of composites, UD composite, are reviewed.

Since most high performance fibre-reinforced composites are comprised of UD composites in the form of tows or UD laminae, a good understanding of the failure mechanisms associated with UD composite is normally beneficial for the failure and damage analysis of composites with more advanced reinforcement architectures.

As pointed out in [35] and [7], due to the brittle nature of composites, independent UD composites are normally considered to fail abruptly instead of showing a gradual damage process. As a result, failure theories for UD composite are abundant in the literature.

However, as will be discussed later, when UD composites are bonded together to form composites of more complex reinforcement architectures, gradual damage phenomenon becomes more influential.

2.2.1 Failure Mechanisms

As summarised in [77], UD composite exhibits different failure modes depending on the loading conditions and the properties of the constituent materials.

Under longitudinal tension, the constituent material inside UD composites with the lowest ultimate tensile strain should fail first. Normally, fibres have lower ultimate strains than matrix materials. As a result, longitudinal tension usually leads to fibre tensile failure in UD composites. However, this failure mechanism is normally complicated by the statistical distribution of fibre strength which varies from fibre to fibre and from point to point.

For UD composites under longitudinal compression, common failure modes observed are micro-buckling and fibre kinking. For UD composites with low fibre volume fraction, extensional mode of microbuckling is likely to occur. With increasing fibre volume fraction, shear mode microbuckling or fibre-matrix debonding become the dominant failure modes. If the UD composites is of very high fibre volume fraction and has well-aligned fibres, pure compressive failure might be encountered which is normally in the form of fibre shear failure.

When UD composite is loaded under transverse tension, high stress concentration is usually induced at fibre-matrix interface. Due to this, multiple isolated tensile cracks tend to initiate at different locations of the fibre-matrix interface throughout the material. With increasing loading, more of these cracks appear and they finally coalesce to produce a macrocrack which leads to the complete fracture of UD composites under transverse tension.

Under transverse compression, high stress concentration is again induced at fibre-matrix interface, which promotes matrix compressive failure or fibre crushing. Moreover, high interfacial shear stress may also be present which can cause matrix shear failure or debonding, resulting in a globally shear failure response.

When UD composite is loaded under in-plane shear, high shear stress concentration develops at fibre-matrix interface, which leads to matrix shear failure and debonding. Eventually, debonding cracks propagate into lengthy macrocracks parallel to the fibre direction, causing the final fracture of UD composites.

2.2.2 Failure Theories

As suggested in [78], failure theories for UD composites can be categorised into two main groups: phenomenological failure criteria and mode-dependent failure criteria.

In terms of phenomenological failure criteria, one of the earliest is the theory by Hill [79], which formed the foundation for many advanced polynomial criteria developed afterwards. In that theory, the von Mises yield criterion for isotropic ductile materials is modified for application to anisotropic ductile materials. Tsai

then converted this criterion for failure prediction in orthotropic composite materials. The resulting theory is known as the Tsai-Hill criterion [80].

Later, by resolving the coefficients associated with stress terms, Azzi and Tsai [81] used the failure theory by Hill to predict the failure of transversely isotropic UD lamina. This criterion allows for the interaction between different in-plane stress components but provides no distinction between tensile and compressive strengths. As a result, when using this criterion, strength parameters must be specified according to the stress state encountered.

To allow different tensile and compressive strengths to be addressed, Hoffman [82] modified Tsai-Hill criterion by introducing linear stress terms into the failure theory.

Tsai and Wu made the first attempt to develop an original failure theory for anisotropic composite materials, which is known as the Tsai-Wu criterion [83]. This criterion is expressed by invariants of stress tensor components, which assured objectivity. Apart from allowing interaction between stress components, this criterion is also capable of accounting for different tensile and compressive strengths.

All failure theories mentioned above are phenomenological failure criteria where each of them is expressed by a single quadratic function of stresses. Although their operation is simple and can be readily implemented for computational procedures, but they are unable to describe the mode-dependent nature of composites failure, which sometimes makes them inaccurate. For instance, in some of them, strengths for different independent failure modes are used together for creating a smooth but physically unjustifiable failure envelope. Moreover, all

of them only produce smooth continuous failure envelopes, although experience has shown that under certain circumstances the failure envelope is better described by a set of piece-wise segments for some quadrants. To allow interaction between different stress components, some of them require strength parameters of multi-axial stress state, which can be difficult to obtain experimentally.

In contrast to polynomial form failure criteria, mode-dependent failure criteria incorporate the influence and physical considerations of different failure modes into the failure criteria.

The simplest forms of mode-dependent criteria are the maximum stress and maximum strain failure criteria, in which failure is expected when any of the stress or strain components reach the strength or failure strain value defined. However, these simple criteria do not allow interaction between different stress or strain components which normally lead to inaccuracy in the failure envelope under multi-axial loading conditions. Also, the resulting failure envelopes are formed by straight lines only which is an unrealistic assumption for the shapes of failure envelopes.

A more advanced and well-received mode-dependent failure theory is the one proposed by Hashin [84]. In this theory, four failure modes are suggested as there are tensile and compressive failures associated with fibre-dominated or matrix-dominated failure modes. As a result, four failure condition expressions are proposed, with each catered for a specific failure mode. Some of these expressions are polynomial quadratic functions of stress invariants which reproduced features from the expression of Tsai-Wu criterion. Thanks to this, for some failure modes, necessary stress interaction is allowed. However, some linear stress terms

originally presented in Tsai-Wu criterion is dismissed in the theory by Hashin without much justification.

Later, Puck developed a sophisticated physically based failure criterion (Puck criterion) [85]. In this criterion, similar to the failure theory by Hashin, fibre dominated failure and matrix dominated failure are distinguished. For the former, separate tensile and compressive failure modes are defined. For the latter, the concept of the fracture plane is employed such that a plane parallel to the fibre direction is determined to be the plane of inter-fibre matrix cracks. This treatment for matrix crack prediction is inspired by the Mohr-Coulomb failure criterion [86], which is originally proposed for brittle isotropic materials. In the Puck criterion, for matrix failure under tension, the corresponding failure condition expression is modified from that defined in the Hashin failure criterion. On the other hand, for matrix failure under compression, the corresponding formulation is based on the Mohr-Coulomb failure criterion which accounts for the effect of friction on compression-induced shear failure. Compared to the failure theory by Hashin, the Puck criterion inherited all the capabilities offered by the former, while providing the added capability of predicting matrix cracking orientation. Moreover, the physical consideration for compression-induced shear failure in brittle materials is also included in the Puck criterion, which is an advantage over the failure theory by Hashin.

As discussed above, phenomenological failure criteria do not integrate physical considerations and failure modes of composites. Although they can be used to predict failure to some extent, the way they accomplish this is via the use of non-physical formulations in a seemingly “curve-fitting” fashion. In light of this, it is

recommended to use mode-dependent failure criteria as they are superior in reflecting the real physics of UD composite failure.

In addition, comprehensive benchmarking and assessment for various UD composite failure criteria can be found in the outcomes from the World Wide Failure Exercises (WWFEs) [9-14,87].

The formulations of the failure criteria reviewed above are listed in Table 2-1 below.

Table 2-1 Summary of UD composite failure criteria

Tsai-Hill [80]
$F(\sigma_{11}-\sigma_{22})^2+G(\sigma_{22}-\sigma_{33})^2+H(\sigma_{33}-\sigma_{11})^2+2L\sigma_{23}^2+2M\sigma_{13}^2+2N\sigma_{12}^2=1$ where F, G, H, L, M, N are material properties.
Azzi-Tsai [81]
$\sigma_{11}^2-\sigma_{11}\sigma_{22}+\frac{X^2}{Y^2}\sigma_{22}^2+\frac{X^2}{T^2}\sigma_{12}^2=X^2$ in which X is the strength in the fibre direction, Y is the strength in the transverse direction, T is the in-plane shear strength
Hoffman [82]
$C_1(\sigma_{11}-\sigma_{22})^2+C_2(\sigma_{22}-\sigma_{33})^2+C_3(\sigma_{33}-\sigma_{11})^2+C_4\sigma_{11}+C_5\sigma_{22}+C_6\sigma_{33}+$ $C_7\sigma_{23}^2+C_8\sigma_{13}^2+C_9\sigma_{12}^2=1$ where $C_i\ (i=1-9)$ are nine independent material parameters
Tsai-Wu [81]
$F_{11}\sigma_{11}^2+F_{22}\sigma_{22}^2+F_{33}\sigma_{33}^2+F_{44}\sigma_{23}^2+F_{55}\sigma_{13}^2+F_{66}\sigma_{12}^2+2F_{12}\sigma_{11}\sigma_{22}+$ $2F_{13}\sigma_{11}\sigma_{33}+2F_{23}\sigma_{22}\sigma_{33}+F_1\sigma_{11}+F_2\sigma_{22}+F_3\sigma_{33}=1$ where F_i are material parameters as follows $F_{11}=\frac{1}{S_{11T}S_{11C}},\ F_{22}=F_{33}=\frac{1}{S_{22T}S_{22C}},\ F_{44}=\frac{1}{S_{23}^2},\ F_{55}=F_{66}=\frac{1}{S_{12}^2}$ $F_{12}=F_{13}=-0.5\sqrt{F_{11}F_{22}},\ F_{23}=-0.5\sqrt{F_{33}F_{22}}$ $F_1=\frac{1}{S_{11T}}-\frac{1}{S_{11C}},\ F_2=F_3=\frac{1}{S_{22T}}-\frac{1}{S_{22C}}$
Hashin[84]
Fibre tensile mode:

$$f_1 = (\frac{\sigma_{11}}{S_{11T}})^2 + \frac{1}{S_{12}^2}(\sigma_{12}{}^2 + \sigma_{13}{}^2) = 1$$

Fibre compressive mode:

$$f_2 = \frac{|\sigma_{11}|}{S_{11C}} = 1$$

Matrix tensile mode:

$$f_3 = \frac{1}{S_{22T}^2}(\sigma_{22} + \sigma_{33})^2 + \frac{1}{S_{23}^2}(\sigma_{23}^2 - \sigma_{22}\sigma_{33}) + \frac{1}{S_{12}^2}(\sigma_{12}^2 + \sigma_{13}^2) = 1$$

Matrix compressive mode:

$$f_4 = \frac{1}{S_{22C}}[(\frac{S_{22C}}{2S_{23}})^2 - 1] + \frac{1}{4S_{23}^2}(\sigma_{22} + \sigma_{33})^2 + \frac{1}{S_{23}^2}(\sigma_{23}^2 - \sigma_{22}\sigma_{33}) + \frac{1}{S_{12}^2}(\sigma_{12}^2 + \sigma_{13}^2) = 1$$

Puck [88]

Fibre tensile mode:

$$\frac{1}{\varepsilon_{11T}}(\varepsilon_{11} + \frac{v_{f12}}{E_{f1}} m_{\sigma f}\sigma_{22}) = 1$$

Fibre compressive mode:

$$\frac{1}{\varepsilon_{11C}}\left|\varepsilon_{11} + \frac{v_{f12}}{E_{f1}} m_{\sigma f}\sigma_{22}\right| = 1 - (10\gamma_{12})$$

Inter-fibre matrix failure tensile mode:

$$\sqrt{\left(\frac{\tau_{nl}}{R_{\perp\parallel}}\right)^2 + \left(\frac{1}{R_{\perp}^T} - \frac{p_{\perp\theta}^T}{R_{\perp\theta}}\right)^2 \sigma_n{}^2 + \left(\frac{\tau_{nt}}{R_{\perp\perp}}\right)^2} + \frac{p_{\perp\theta}^T}{R_{\perp\theta}}\sigma_n = 1$$

Inter-fibre matrix failure compressive mode:

$$\sqrt{\left(\frac{\tau_{nl}}{R_{\perp\parallel}}\right)^2+\left(\frac{p^C_{\perp\theta}}{R_{\perp\theta}}\right)^2\sigma_n{}^2+\left(\frac{\tau_{nt}}{R_{\perp\perp}}\right)^2}+\frac{p^C_{\perp\theta}}{R_{\perp\theta}}\sigma_n=1$$

where

$$R_{\perp\perp}=\frac{R^C_{\perp}}{2\left(1+p^C_{\perp\perp}\right)}$$

$$\frac{p^{T,C}_{\perp\theta}}{R_{\perp\theta}}=\frac{p^{T,C}_{\perp\perp}}{R_{\perp\perp}}\cos^2\theta+\frac{p^{T,C}_{\perp\parallel}}{R_{\perp\parallel}}\sin^2\theta$$

$$\sin^2\theta=\frac{\tau_{nl}{}^2}{\tau_{nl}{}^2+\tau_{nt}{}^2},\ \cos^2\theta=\frac{\tau_{nt}{}^2}{\tau_{nl}{}^2+\tau_{nt}{}^2}$$

ε_{11} and γ_{12} are the longitudinal uniaxial strain and longitudinal shear strain, ε_{11T} and ε_{11C} are the longitudinal tensile and compressive failure strains of the UD composite, v_{f12} is the longitudinal Poisson's ratio of pure fibre, E_{f1} is the longitudinal Young's modulus of pure fibre, $m_{\sigma f}$ is the stress magnification factor for fibre bundles, σ_n, τ_{nl} and τ_{nt} are the normal, longitudinal shear and transverse shear stresses on the fracture plane, θ is the orientation of the fracture plane anticlockwise from the second material principal plane, $p^T_{\perp\parallel}$, $p^C_{\perp\parallel}$, $p^T_{\perp\perp}$ and $p^C_{\perp\perp}$ are the slopes of the failure envelope related to the tensile, compressive normal stresses, longitudinal shear stress and transverse shear stress on the fracture plane, $R^T_{\perp}$, $R^C_{\perp}$, $R_{\perp\parallel}$ and $R_{\perp\perp}$ are the strength values for triggering inter-tow matrix failure in terms of tensile normal, compressive normal, longitudinal shear and transverse shear stresses on the fracture plane.

In Table 2-1, S_{11T} and S_{11C} are the longitudinal direction tensile and compressive strengths, S_{22T} and S_{22C} are transverse direction tensile and compressive strengths, S_{12} and S_{23} are longitudinal and transverse shear strengths.

2.3 Damage in Laminates under Static Loading

As pointed out in [7,11,35], when laminates formed by UD laminae are subjected to loads, not all laminae fail instantly as often there are different gradual damage development processes associated with laminates depending on their stacking sequences. As a result, only predicting the failure of a UD lamina does not provide the full picture of damage process in laminates. In the composite research industry, more attention is now being shifted to the study of damage process [89]. In this section, a review of both experimental investigation and theoretical development concerning damage in laminates are presented.

2.3.1 Damage Mechanisms

Major damage modes observed in laminates under static loading are intra-laminar cracking, inter-laminar cracking, fibre fracture and micro-buckling [7,89].

In general, intra-laminar cracks are the first damage to occur which signifies damage initiation in laminates. When laminates are loaded under uniaxial tension, depending on their stacking sequences, these cracks were reported to initiate in the laminate axial strain range of 0.4-1% [89]. The effect of off-axis ply orientation on intra-laminar crack initiation was studied in [90-92]. It was found with the decrease of off-axis ply angle, increase in laminate axial strain was observed for the initiation of intra-laminar cracks. Once initiated, due to the nature

of brittle failure, intra-laminar cracks normally propagate in an unstable manner through the thickness of the plies containing them, until they are arrested by neighbouring plies of different orientations. In the width direction, cracks tend to run right to the edges of the laminates or to stop at places where the overall stress distribution no longer promotes the cracking process [90,93,94].

Unlike in ductile materials where propagation of cracks is the main damage evolution process, further loading in laminates leads to multiplication of intra-laminar cracks [89]. During the crack multiplication stage, when crack density is sufficiently high, interaction between cracks promotes a "shielding effect" which effectively reduces the stress between adjacent cracks. This then results in reduced crack multiplication rate and leads to the crack saturation phenomenon [93,95-97].

Once propagated across the ply thickness, intra-laminar cracks may then develop into delamination and trigger longitudinal splitting. Continued loading of laminates beyond this point causes more severe debonding, delamination and local failures like fibre fracture, until final catastrophic failure is reached [89]. However, the dominant mode of damage is reported to be different for laminates with different stacking sequences [91,98,99].

For cross-ply laminates under uniaxial tension, extensive experimental investigations have been conducted to characterise their damage processes. As mentioned in [93,94,100-104], damage initiation in cross-ply laminates is usually in the form of intra-laminar cracks originating from ply edges of 90º plies. These cracks then propagate instantly in the thickness and width directions of 90º plies. It was found that the thickness ratio between the 0º and 90º plies can affect the constraint effect provided by the 0º plies, which in turn influences damage initiation and stress-strain behaviour of cross-ply laminate. As reported in

[105,106], if the number of the 0º plies is more than 10 times of that for the 90º plies in cross-ply laminates, complete suppression of intra-laminar cracks in the 90º plies is possible. Different damage behaviours were also noticed for cross-ply laminates with $[90/0]_S$ and $[0/90]_S$ stacking sequences, where the former showed earlier damage initiation and faster crack density growth due to its outer 90º plies being less constrained from the 0º plies [107,108].

A detailed study of intra-laminar cracks in quasi-isotropic (QI) laminates is provided in [90]. In contrast to cross-ply laminates, although intra-laminar cracks appeared in both the 90º and the ±45º plies in QI laminates, cracks in the ±45º plies initiated much later than those in the 90º plies. Moreover, cracks in the ±45º plies did not propagate to full ply width and full ply thickness. In terms of crack multiplication, the crack density growth rate in the ±45º plies is much lower than that in the 90º plies. Compared to cross-ply laminates, less stiffness reduction was observed and higher crack density was reached for the QI laminates.

Although angle-ply laminates are not common in practical applications, a comprehensive study of intra-laminar cracks in this kind of laminate can be found in [91], where the effect of notch on angle-ply laminate damage behaviour is also addressed.

2.3.2 Damage Modelling

According to [89], damage modelling approaches for laminates can be categorised into two types: micro-damage mechanics approach and continuum damage mechanics approach.

2.3.2.1 Micro-damage Mechanics Approach

In this kind of approach, cracks and voids inside laminates are treated as microstructures, for which local stress distribution and displacement field around them are worked out using micromechanics methods. Lamina level in-situ strengths are required in this approach to predict the emergence of new intra-laminar cracks, which then enables the prediction of crack density growth with respect to the loads applied.

One of the earliest analytical methods developed in this area is the one published by Aveston et al. [109], which is known as the "ACK" model and formed the foundation of shear lag analysis. Shear lag analysis is essentially a one-dimensional analysis which captures the interfacial shear stress of the stress transfer phenomenon between cracked lamina and undamaged lamina. Cox [110] initially used shear lag analysis to predict the stress transfer between fibre and matrix. Later, Aveston and Kelly [111] presented a shear lag model for predicting the strain to initiate matrix cracking in the UD composites. Further extensions to the shear lag model by Cox [110] were developed by Garrett, Bailey and Parvizi [93,94] and Manders et al. [112] to analyse transverse cracks in cross-ply laminates. Smith et al. [113-115] developed shear lag models for the analysis of intra-laminar cracks inside cross-ply laminates and QI laminates under bending. Using shear lag analysis in conjunction with fracture mechanics and simple bending theory, they managed to predict the flexure stiffness, the neutral axis positions and the residual curvature of the laminates as a function of the transverse crack density and the lamina in-situ strength.

However, due to the one-dimensional nature of shear lag analysis, it cannot provide accurate stress analysis. For example, it is unable to distinguish between

[90/0]s and [0/90]s laminates as it cannot account for the different stress boundary conditions associated with the 90º plies in these stacking sequences [108]. Moreover, for damage analysis of cross-ply laminates, shear lag models give the non-physical prediction of having nonzero interfacial shear stress at locations of transverse cracks [89].

In light of the deficiency of 1D shear lag analysis, variational analysis methods were developed which extended the analysis to two-dimensional stress analysis. The first application of this method to the analysis of cracked laminates was reported by Hashin [116]. In this kind of method, principle of minimum complementary energy is applied to a cracked laminate volume. When used for cross-ply laminate analysis, this method can correctly predict zero interfacial shear stress at the locations of transverse cracks [105]. Later, Varna and Berglund [117-119] modified the variational method by Hashin [116] by determining the axial stress variations across the thickness of plies, instead of assuming constant stress values for these. In addition, Kuriakose and Talreja [120] successfully used the variational method to predict damage in cross-ply laminates under bending. The variational approaches based on Hashin's work [116] were applicable only to symmetric laminates of three layers in principle due to the lack of sufficient boundary conditions. This restriction had not been recognised until the emergence of [121] where the difficulty was overcome by the supplement of natural boundary conditions.

Although capable of providing analytical solutions, the micro-damage mechanics approach mentioned above may not always be readily applicable to complex damage scenarios where multiple damage mechanisms, complex interaction

between cracks and complex constraint effect from neighbouring plies of various orientations are present [89].

For highly complex damage situations, finite element method, which can be regarded as a numerical experiment approach, can be used to analyse cracks inside laminates. Examples of this method are reported in [122-124].

In addition, another computational method for cracked laminate analysis, known as the finite strip method, was developed by Li et al. [125]. By using this method, analysis for laminates of arbitrary layup is possible. However, the restriction in this method is that all cracked plies have to be of the same orientation.

2.3.2.2 Continuum Damage Mechanics Approach

At around the same time as the development of the micro-damage mechanics approach, continuum damage mechanics (CDM) approach was also adopted for the analysis of damage in laminates.

The concept of CDM was first introduced by Kachanov [126] for characterising creep damage in metallic materials, where damage was represented by a scalar internal state variable. After this, Lemaitre and Chaboche [127] applied the work of Kachanov for the analysis of materials with distributed cavities and cracks. Further advance was made by Krajcinovic [128] who not only associated CDM theory with concepts from fracture mechanics and plasticity, but also addressed thermodynamic implications for CDM theory. In terms of the application of CDM to composites, one of the earliest attempt was made by Talreja [129], who later developed the theory further for predicting damage evolution in cross-ply laminates [130] and damage evolution in laminates under fatigue loadings [131].

Other well-known CDM theories for laminate analysis are the ones proposed by Matzenmiller et al. [132] and Ladeveze et al. [133-136].

The fundamental assumption in CDM theory is treating the damaged material as a statically homogeneous continuum so that a macro-scale material constitutive relationship involving elasticity and damage can be used to describe the overall material behaviour. As a result, the concept central to CDM is the homogenisation of damage for a representative volume element (RVE) inside the damaged material. For this concept to be legitimate, the size of RVE has to be sufficiently large so that the effective material properties of damaged material do not depend on the locations of microcracks [89,137,138].

Unlike cracking damage in monolithic metallic materials, where a single dominant crack often contributes to overall material degradation and failure, cracking damage in composites is normally dissipated within the affected materials such that a large number of almost evenly distributed microcracks are usually observed [89]. Due to such a widespread and seemingly uniform distribution of microcracks within the material volume, damaged composites can therefore be regarded as an effective homogeneous continuum which is especially suitable for the application of CDM.

Furthermore, due to the multitude of microcracks in damaged composites, the use of fracture mechanics and micro-damage mechanics types of analysis, which is to account for every individual crack and the interactions between the cracks, is not always practical for predicting the overall material behaviour of damaged composites. In particular, for engineering applications, analysis of these kinds for product design will be unacceptably time-consuming and prohibitively expensive in terms of computational power required. As an alternative, CDM presented a

suitable approach for developing constitutive models of damaged composites. When using the CDM approach, the overall damage effect due to numerous cracks is represented by a homogeneous damage field, which introduces irreversible changes into the constitutive behaviour of damaged composites, thereby removing the need of studying every individual crack.

A large number of damage models based on CDM theory (CDM models) were developed by various researchers for modelling the damage of UD laminae in laminates. These damage models are normally comprised of three major components as listed in Table 2-2.

Table 2-2 Components in the CDM models for UD lamina

Components	Functions
Damage initiation criteria for monotonic loading and reloading scenarios	To predict the starting point of initial damage process and continued damage process.
Damage representation formulation	To introduce damage variables into the constitutive relationship of damaged composites
Damage evolution law	To govern the growth of damage variables

As can be seen in Table 2-2, the damage initiation criterion forms a part of the CDM models because for identifying the starting point of damage process, the onset of damage needs to be predicted. Many CDM models adapted failure theories of UD composites as damage initiation criteria. For example, the CDM model proposed by Zinoviev et al. [139] used the maximum stress failure criterion, Matzenmiller et al. [132] selected the failure theory by Hashin [84] for their CDM

model and the maximum strain failure criterion was chosen as the damage initiation criterion in the CDM model developed by Bogetti et al. [140]. In this report, discussions on various failure theories of UD composites have already been provided in Section 2.2.2.

In addition to the damage initiation criterion, damage representation is another major component in CDM models because this is where material internal state variables (damage variables) representing damage effect are introduced into the material constitutive relationship. With the definition of damage representation, the specific terms in the stiffness/compliance matrix of damaged composites, which are affected by the damage effect, can be clearly identified and related.

Last but not least, with the inclusion of damage variables in the material constitutive relationship, a damage evolution law is required in the CDM model for governing the growth of damage variables.

In the following subsections, a review on various damage representation formulations and damage evolution laws used in different CDM models is presented.

2.3.2.2.1 Damage Representation

There appeared to be no unified form of damage representation formulation as researchers proposed different constitutive relationships incorporating damage. In fact, this issue was addressed in [137] with the argument that there were so many inconsistent forms of suggested constitutive relationships involving damage, such that this situation should be reviewed and improved by adding more "physics"

into the derivation of these constitutive relationships, implying that some of them may not even be considered as physically rigorous.

One of the major differences between various damage representation formulations is the way of accounting for the relationship between the degradation of transverse Young's modulus, E_2, and in-plane shear modulus, G_{12}. A simple example of such a damage scenario is matrix cracking parallel to the fibre direction. This should result in degradation to both the transverse tensile modulus (E_2) and the longitudinal shear modulus (G_{12}). The experimental evidence for such coupled damage effect was obtained by Knops and Bögle [141], who conducted tests on tubular glass fibre laminate specimens. It was shown for that particular test case the transverse tensile modulus suffered higher extent of degradation than the in-plane shear modulus.

However, some of the well-known CDM models for UD lamina, as summarised in Table 2-3, employed unrealistic artificial restrictions for the representation of this coupled damage effect [142]. In some cases, complete independence between the degradation of E_2 and G_{12} is assumed, while in others, exactly the same percentage of degradation to E_2 and G_{12} with respect to their undamaged values is assumed. Both assumptions are physically unjustifiable. This issue was also identified during the recent WWFE-III activities [12]. Moreover, for general 3D stress problems, with the presence of matrix crack parallel to the fibre direction, there will also be a coupled damage effect between E_2 and G_{23} in addition to that between E_2 and G_{12}. However, since most of the existing damage representation formulations were developed only for plane stress problems suitable for application to laminates, the summary provided in Table 2-3 is limited to the representation of coupled damage effect between E_2 and G_{12} only.

Table 2-3 Classification of CDM models for UD lamina with regard to the representation of coupled damage effect between E2 and G12

Representation of coupled damage effect between E_2 and G_{12}	**CDM models**
Assumed complete independence between the degradations of E_2 and G_{12}.	A structural-phenomenological model for multi-layered composites under plane-stress state by Zinoviev et al. from WWFE-I [139]
	Enhanced mesomodel for laminated composites by Ladeveze and Daghia from WWFE-III [143]
	Generalized Daniel's model for fibre-reinforced polymer under a complex loading by Sapozhnikov and Cheremnykh from WWFE-III [144]
Assumed E_2 and G_{12} to have exactly the same percentage of degradation with respect to their undamaged values (i.e. a 30% degradation of E_2 would result in a 30% degradation of G_{12} and vice versa).	Physically based phenomenological models for failure analysis of FRP laminates by Puck and Schurmann from WWEF-I [85]
	A stress-based Grant-Sanders method for predicting failure of composite laminates by Edge from WWFE-I [145]
	Implementation of the damage theory by Matzenmiller et al. [132] as MAT 162 composite material damage model in LS-DYNA [146]
	A structural modelling framework for prediction of damage development and failure of composite laminates by Vaziri et al. from WWFE-III [147]

Interaction between degradations of E_2 and G_{12} is accounted for, with no artificial restriction imposed on how much the interaction should be.	Finite element implementation of Puck's failure theory for fibre-reinforced composites under three-dimensional stress by Deuschle and Kröplin from WWFE-II [148]
	Damage mechanics model of composite materials based on thermodynamics with internal variables by Talreja [129]
	Constitutive model for anisotropic damage in fibre composites by Matzenmiller et al. [132]
	Continuum damage mechanics framework for UD composites containing matrix cracking by Li et al. [149]

Comparing various methods of damage representation in Table 2-3, it is interesting to note that in the original theory, Matzenmiller et al. [132] suggested using experimental data to account for coupled damage effect. However, when this theory was implemented into LS-DYNA finite element analysis package as MAT 162 material model, the unrealistic assumption of identical degradations for E_2 and G_{12} was adopted [146]. Other than this, modification to Puck's damage theory can also be noted as the original version in WWFE-I [85] was modified for WWFE-II [148] in order to better characterise the coupled damage effect.

Among these CDM models in Table 2-3, the one developed by Li et al. [149] stands out as it used an analytical method for quantifying some of the coupled damage effects for the case of having an array of dispersed matrix cracks parallel to the fibre direction.

In detail, their work is based on the derivation of constitutive relationship for damaged UD composites provided by Talreja [129], which used Helmholtz free energy expression as the state function for damaged UD composites. The energy expression in there incorporated strain terms and a vector damage variable in the form of irreducible integrity bases so that the objectivity principle can be satisfied. During the derivation process, there are many damage related unknown material constants in the constitutive relationship. In contrast to the work by Talreja [129], where these unknown constants were all interpolated from the experimental data, Li et al. [149] developed an analytical method for solving as many as possible of these unknowns by virtue of the fact that many properties of the damaged UD composites would be unaffected under certain damage conditions.

As shown in [149], this analytical method was applied to the case of having an array of closed cracks parallel to the fibre direction with the normal to the crack plane coincident to the material principal axis-2 (Fig.2-1). Using this method, although the material constant characterising coupled damage effect between E_2 and G_{12} still needs to be determined experimentally, the constant quantifying coupled damage effect between E_2 and G_{23} can be determined analytically. The significance of this is not only in the sense that analytical expressions for quantifying coupled damage effect can indeed be found, but also in the reduction of dependence on experimental work and therefore associated empiricism.

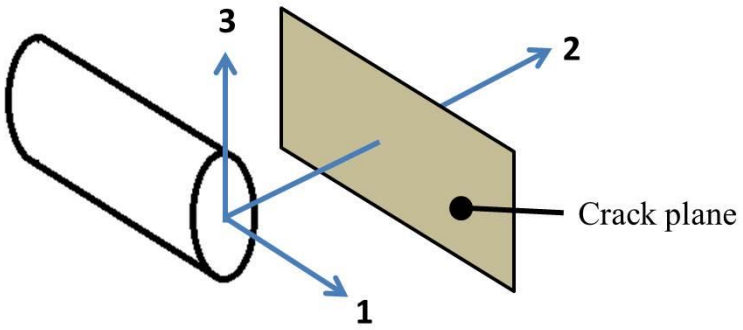

Fig.2-1 Illustration of crack plane parallel to fibre direction with its normal coincident to material principal axis-2

Based on above review for damage representation formulations, it is envisaged that the damage representation formulation proposed by Li et al. [149], while being physically sound, should also be regarded as the most capable one, provided that the damage scenario encountered is suitable for its application.

2.3.2.2.2 Damage Evolution

Similar to the lack of a unified methodology for damage representation definition, different types of damage evolution laws were also suggested by researchers. These damage evolution laws can be classified into three types in general, as shown in Table 2-4.

Table 2-4 Classification of CDM models for UD lamina with regard to damage evolution laws

Damage evolution law types	CDM models
Independent curve-fitting functions derived using direct interpolation of experimental stress-strain curves under specific loading cases, which are not applicable to other loading cases.	A structural-phenomenological model for multi-layered composites under plane-stress state by Zinoviev et al. from WWFE-I [139]
	A stress-based Grant-Sanders method for predicting failure of composite laminates by Edge from WWFE-I [145]
	Generalized Daniel's model for fibre-reinforced polymer under a complex loading by Sapozhnikov and Cheremnykh from WWFE-III [144]
Damage evolution laws applicable to general loading cases, but with the assumption that direct stresses (strains) and shear stresses (strains) always have the same contribution to damage evolution. (i.e. a 30% increase in direct or shear stress would result in the same amount of damage growth)	Physically based phenomenological models for failure analysis of FRP laminates by Puck and Schurmann from WWEF-I [85]
	A structural modelling framework for prediction of damage development and failure of composite laminates by Vaziri et al. from WWFE-III [147]
	Implementation of the damage theory by Matzenmiller et al. [132] as MAT 162 composite material damage model in LS-DYNA [146]
Damage evolution laws applicable to general loading cases, permitting direct stresses (strains) and shear	Enhanced mesomodel for laminated composites by Ladeveze and Daghia from WWFE-III [143]

stresses (strains) to have different contributions on damage evolution.	Damage mechanics model of composite materials based on thermodynamics with internal variables by Talreja [129]

Damage evolution laws in the first group are based entirely on direct interpolation of experimental stress-strain curves, where empirical functions are devised to modify the linear elastic stress-strain responses into nonlinear ones for including the damage effect. However, this type of damage evolution laws are normally only applicable to limited loading cases, because the damage evolution processes are essentially prescribed by independent functions, fitting to the experimental stress-strain curves obtained under specific loading cases involving damage. As a result, with every function corresponding to a specific loading case, these adhoc curve-fitting functions can only reproduce the experimental stress-strain curves if exactly the same loading cases are encountered.

Moreover, strictly speaking, these functions might not even be considered as formal damage evolution laws since the use of them is effectively no different than using already available experimental stress-strain curves, meaning that they are unable to make any theoretical prediction, but merely duplicating existing experimental results for the sake of modelling.

On the other hand, there are also damage evolution laws developed that are suitable for all possible loading cases. For these, all stress or strain components contributing to damage growth are accounted for by integrating them into expressions like stress exposure functions as suggested by Puck and Schurmann [85], equivalent strain expressions as suggested by Vaziri et al. [147] or damage driving force expressions derived by Ladeveze and Daghia [143] and Talreja

[130]. However, although these damage evolution laws are applicable to all the loading cases associated with damage growth, some of them employed the unrealistic assumption that direct stresses (strains) and shear stresses (strains) should always have the same contribution to damage growth.

In particular, the MAT162 damage model in LS-DYNA [146] employs a damage evolution law based on the definition of damage surface, where all stress components affecting damage growth are included, which makes the model applicable to any loading case. However, the damage evolution law formulated therein only allocated a single parameter for governing the rate of damage growth. Consequently, as long as the final stress is at a certain value above the threshold stress value for damage initiation, the same amount of damage growth will always be predicted, regardless whether a direct stress or a shear stress induced the damage growth. In reality, damage may not always evolve this way. The experimental result for UD composites provided in WWFE-I [150,151] suggested that the damage growth rates (modulus degradation rates) due to direct stresses and shear stresses can be very different. Based on this, it can be concluded that from the damage evolution laws as summarised in Table 2-4, only those proposed by Ladeveze and Daghia [143] and Talreja [129] can be regarded as physically rigorous.

In terms of derivation of damage evolution laws, two major approaches were identified, one following the concept of a damage surface which is similar to the concept of a yield surface in plasticity, the other one is based on the derivation of a damage driving force which is a concept similar to energy release rate in fracture mechanics [89,152].

For the former method, damage surface expressions are often derived from damage initiation criteria so that as soon as damage is initiated, the damage surface will be updated continuously during the subsequent damage evolution process [85,146]. Then, an incremental damage evolution law based on a damage surface can be devised in a similar way to that in the incremental theory of plasticity. Li et al. [153] developed a CDM model for charactering transverse matrix cracks in laminates, which employed the concept of damage surface for formulating a damage evolution law.

On the other hand, unlike the damage surface concept, damage driving force expressions are normally derived from energy functions of damaged materials. In the CDM model proposed by Ladeveze et al. [143], strain energy density function of damaged UD composite was used to derive the damage driving force. Alternatively, specific Helmholtz free energy function was chosen by Talreja [129].

Regardless of the form of energy function employed, due to the internal dissipation inequality condition imposed by the second law of thermodynamics, which states that energy dissipation caused by any change of internal state must always be non-negative, partial derivatives of energy with respect to damage variables have to be obtained for demonstrating the compliance to this inequality condition. These partial derivatives are defined as damage driving forces [130], also known as thermodynamic forces conjugate to internal damage variables, as stated in [138]. In order to satisfy the internal dissipation inequality condition, the product of damage driving force and rate of change of damage must be of non-negative value.

2.4 Damage in 3D Textile Composites under Static Loading

There is a growing trend of using 3D textile composites to replace conventional laminated composites in structural components where through-the-thickness loadings are substantial or better impact resistance is required. With its increasing popularity, there has been a steady stream of investigations regarding the damage behaviour of 3D textile composites. In this section, damage mechanisms and methods of damage modelling for 3D textile composites are reviewed.

2.4.1 Damage Mechanisms

There are a large number of experimental investigations reported in the literature for characterising damage in various types of 3D textile composites. Among them, most are focused on the damage in 3D orthogonal woven composite.

Tan et al. [154] conducted static tensile tests in the warp and weft directions of a 3D orthogonal woven carbon fibre composite material. Although the resulting stress-strain curves were linear, debonding of the z-fibre tows, tow pull-out and tow breakage were discovered in the tested specimens.

Kuo et al. [155] studied the compressive response of orthogonal 3-axis woven carbon fibre composites. They observed progressive compressive damage and kink bands associated with stuffer rods and stuffer tows. Later, Kuo et al. [156] investigated the effect of varying surface tow patterns on the compressive response of 3-axis orthogonal composites.

Leong et al. [157] reported extensive longitudinal tow splitting in a 3D orthogonal woven carbon fibre composite during tensile testing. They deduced that such a

damage mode should be caused by the extensive longitudinal matrix cracking as a result of the Poisson's ratio mismatch between the matrix and longitudinal tows.

A detailed experimental methodology for characterising damage in 3D textile composites was suggested by Lomov et al. [158]. They recommended the use of acoustic emission for identifying strain levels of interest, the use of full-field strain measurement for locating strain concentrations, and the use of computerised axial tomography scan and optical microscopy for identifying local damage modes. Bogdanovich et al. [159] and Lomov et al. [160] applied this experimental methodology for identifying damage events during tensile loading of 3D orthogonal woven carbon composites. The damage events discovered were cracking of boundary tows, intra-tow transverse cracks and tow/matrix debonding.

Apart from 3D orthogonal woven composites, studies regarding the damage in 3D interlock woven composites are also available in the literature.

Normal-layered interlock and offset-layered interlock glass fibre composites were tested in tension by Callus et al. [52]. It was found that crimped tow straightening may have contributed to substantial nonlinearity in the stress-strain responses obtained. John et al.[161] also reported damage in these two kinds of 3D woven composites under tensile loading. They concluded that intra-tow cracking and debonding of warp tows were the major damage modes observed.

Damage in a 3D angle interlock carbon fibre woven composite was studied by Cox et al. [162]. They conducted tensile, compressive and bending tests for the material. It was found kink band formation and debonding were the major damage modes caused by compressive loading while tow rupture and tow pull-out were the major damage modes observed under tensile loading. A combination of these

damage modes were discovered when the material was subjected to bending. Later, Cox et al. [163,164] identified warp tow straightening as the primary damage mechanism for causing softening in the tensile stress-strain responses of layer-to-layer and through-the-thickness interlock 3D woven carbon fibre composites.

Tensile, compressive and in-plane shear tests were carried out by Warren et al. [165] for ply-to-ply angle interlock 3D woven composites reinforced by IM7 carbon fibre tows. Based on the test result, it was concluded that crimped warp tows contributed to the reduced strengths and the non-linear stress-strain behaviours in the warp direction when compared with those in the weft direction. For in-plane shear, the non-linear stress-strain response observed was similar to that of plain woven laminates with the same fibre volume fraction.

Based on the experimental result available in the literature, it is found for most 3D textile composites, damage initiates in the form of intra-tow transverse cracks. With further loading, multiplication of intra-tow cracks occurs until crack saturation state is reached. This is then followed by the formation and propagation of inter-tow cracks which are normally found around crimping tows. Depending on the textile reinforcement architecture, tow straightening may occur after the formation of inter-tow cracks. Final failure modes of 3D textile composites are usually tow rupture under tensile loading and extensive brooming or kink band type of tow failure under compression.

Moreover, it has been observed that the textile reinforcement architecture and the type of loading affect many aspects of the damage process in 3D textile composites. These aspects include the point of damage initiation, non-linearity induced by damage, crack density, damage modes and so on.

2.4.2 Damage Modelling

In contrast to damage modelling for laminates where most models are only two-dimensional, for 3D textile composites, three-dimensional models capturing detailed geometry of textile reinforcement may become a necessity. The reason for this is that the damage process in 3D textile composites is highly influenced by the internal architectures of these materials [166].

However, a few simplified two-dimensional damage analysis methods for 3D textile composites were developed. Most of these can be classified as the equivalent laminate method, where the 3D textile architectures were approximated as laminates comprised of UD laminae. For example, Pickett et al.[167] and Fouinneteau et al. [168] used a laminate representation for analysing damage in carbon fibre and glass fibre braided composites, where the continuum damage model by Ladeveze [169] was incorporated for damage prediction. The same approach was used by Greve et al. [170] for predicting damage in carbon fibre non-crimp fabric composites. Despite the simplicity of two dimensional analysis methods, they are unable to capture the effect of tow crimp, which is known to cause damage like inter-tow cracks, fibre rupture and tow micro-buckling [166].

In contrast to two-dimensional damage analysis methods, three-dimensional finite element analysis models, capturing tow shape and tow path explicitly, can provide the maximum of geometrical details for the textile reinforcements inside the 3D textile composites. Thanks to this, these finite element models are normally capable of predicting local damage associated with textile geometry [171]. In these models, due to the periodicity of 3D textile reinforcement, the representation

of 3D textile composites is normally in the form of a unit cell. The unit cell is further discretised into element volumes of tows and matrix material so that tow shape and tow path are explicitly modelled. Different material constitutive models are assigned to tow elements and matrix elements as the former is normally treated as a transversely-isotropic material and the latter as an isotropic material [171].

Among the finite element analysis models developed for damage prediction in 3D textile composites, there appeared to be two major approaches adopted for introducing damage into the models: the continuum damage mechanics (CDM) approach and the cohesive element approach [172].

In the CDM approach, damage variables are introduced into the constitutive relationships of tow and matrix materials. Since tows are normally regarded as UD composites, well-established UD composite failure criteria as reviewed in Section 2.2.2 and the CDM models for UD composite as mentioned in Section 2.3.2.2 can be used for tow damage modelling. However, for simplicity, many researchers used element discount method such that once damage initiation is detected, damage variables would jump to the maximum value and result in a sudden complete loss of stiffness. Based on finite element modelling, these researchers used CDM approach combined with element discount method to predict the damage in woven [173,174], braided [175], and non-crimp fabric composites [176]. On the other hand, CDM approach combined with gradual damage evolution laws were applied by others for the damage analysis of 3D braided composites [177] and 3D woven composites [178].

As an alternative to the CDM approach, the cohesive element approach models cracks as discontinuities, where damageable surfaces represented by cohesive

elements are introduced into the finite element model. However, it requires the definition of crack orientation and location prior to the analysis which is not always possible. McLendon and Whitcomb [179] used this approach to predict tow-matrix interfacial damage inside textile composites, where they found that the choice of stiffness degradation law affects greatly the accuracy of the prediction since stress redistribution is sensitive to the stiffness degradation law formulated.

2.5 Summary

Based on the literature review presented above, some conclusions are drawn as follows:

Composite materials are receiving increasing applications in the aerospace industry thanks to their high specific mechanical properties for weight-saving, their ability to be tailored for the most critical loading conditions and their superior fatigue resistance over traditional metallic materials. As a result, composites are gradually becoming the primary type of material used in airframe structures.

Moreover, thanks to the textile processes which are capable of producing integrated near-net-shape performs of complex geometry, as well as improved mechanical properties in the thickness direction, 3D textile composites are more suitable than conventional laminated composites for constructing structural components of complex shapes and requiring good impact resistance.

In terms of failure of UD composites, different failure modes were discovered depending on the loading conditions and the properties of the constituent materials. Consequently, phenomenological failure criteria for UD composites

which do not include the physical consideration of failure modes are not recommended. Instead, whenever possible, mode-dependent UD composite failure criteria should be used as they are superior in modelling the real physics of UD composite failure. As a result, for the current research objective of developing a novel theoretical damage model for UD composites, mode-dependent UD composite failure criteria are to be incorporated into the damage model, as addressed in Chapter 3 and Chapter 5.

With regard to laminates, different damage processes were observed for laminates of different stacking sequences, which imply that in addition to failure criteria, damage process modelling is indeed required in order to capture the full picture of laminate damage phenomenon. Based on this, the novel UD composite damage model developed in this project is applied for predicting intralaminar damage in laminates, which is shown in Chapter 6. The predicted results are then compared against the experimental results, so that the model performance can be assessed.

The micro-damage mechanics approach for damage modelling, which relies on analytical methods or numerical methods to predict the damage effect caused by every single crack, may not be suitable for engineering applications. This is because at present, this approach is time-consuming and prohibitively computational expensive if it is applied to engineering problems where a multitude of cracks would need to be studied one by one. On the other hand, the continuum damage mechanics approach, which homogenises the damage effect of all individual cracks into an overall combined damage effect, thereby removing the need of studying every individual crack, presents as an efficient and viable damage modelling approach for engineering applications. Consequently, as illustrated in Chapter 3, for this research project, the continuum damage

mechanics approach is adopted for developing the new damage model of UD composites.

Among the existing continuum damage mechanics models, different formulations of damage representation were suggested and some imposed unrealistic assumptions regarding the coupled damage effect phenomenon. It is deemed that the damage representation formulation proposed by Li et al. [149] is physically sound and is the most capable one as in their theory an analytical method was developed to quantify part of the coupled damage effect. As a result, this damage representation formulation is incorporated into the UD composite CDM model being developed in this project.

Based on the review of UD composite continuum damage mechanics models, it is envisaged that a physically rigorous damage evolution law with general applicability should be applicable to general loading cases while permitting direct stresses and shear stresses to have different contributions to the damage evolution process. Consequently, the UD composite CDM model being developed in this project should possess these attributes.

Similar to laminates, damage processes were also observed in 3D textile composites. While the damage processes in laminates are dependent on the laminate stacking sequences, the damage processes in 3D textile composites are influenced by the textile reinforcement configuration. This means that for satisfactory modelling of damage processes in 3D textile composites, accurate modelling of textile reinforcement geometry becomes a necessity. As a result, 3D finite element analysis is found to be the ideal approach for damage modelling of 3D textile composites since detailed reinforcement geometry can be constructed in finite element models for damage analysis. Based on this, as shown in Chapter 6,

the UD composite CDM model developed in this project is used to predict intra-tow damage in 3D textile composites, where finite element models capturing textile reinforcement configurations are used for carrying out the analyses.

Thanks to the literature review presented above, some valuable recommadations regarding the development of UD composite damage models are found. Based on these recommandations, a novel theoretical formulation characterising damage evolution in UD composites is developed and introduced in the next chapter.

3. A Novel Formulation for Damage Evolution of UD Composites based on the Concept of Damage Driving Force

3.1 Introduction

As discussed in the previous chapter, among the damage representation formulations that imposed no unrealistic restriction on coupled damage effect, the proposal from Li, et al. [180] (hereafter referred to as Li's damage representation) is deemed to be the most capable one for characterising an array of planar matrix cracks parallel to fibre direction. However, to make use of Li's damage representation in the context of CDM framework, a suitable damage evolution law is still required so that a complete CDM model for UD composites can be established. As a result, in this chapter, a novel damage evolution law is proposed to pair up with Li's damage representation.

Moreover, as Li's damage representation was derived from the Helmholtz free energy expression, the decision was made to develop the new damage evolution law based on damage driving force concept so that the same Helmholtz free energy expression can be utilised which may promote a more seamless transition from the theoretical work of damage representation to that of damage evolution.

3.2 Derivation of Damage Driving Force

The derivation starts from the original Helmholtz free energy expression presented in [180] for UD composites with the inclusion of a damage vector

$V = \{v_1 \quad v_2 \quad v_3\}^T$. Before rushing straight into the derivation of damage driving force, for the terms formed by irreducible invariant integrity bases in the Helmholtz free energy expression, second order terms containing only damage vector components are now added into the original energy expression since these were neglected previously in [180] but will affect the current derivation of damage driving force. Due to this, the original expression for Helmholtz free energy Ψ is now modified as:

$$\Psi = \frac{1}{2}\left(\begin{array}{l} A_1 I_1^2 + A_2 I_1 I_2 + A_3 I_1^2 I_5^2 + A_4 I_1 I_5 I_6 + A_5 I_1^2 I_8 + A_6 I_1 I_9 + A_7 I_1 I_2 I_5^2 + A_8 I_1 I_2 I_8 \\ \quad + B_1 I_2^2 + B_2 I_2^2 I_5^2 + B_3 I_2 I_5 I_6 + B_4 I_2^2 I_8 + B_5 I_2 I_9 \\ \quad + C_1 I_3 + C_2 I_3 I_5^2 + C_3 I_3 I_8 \\ \quad + D_1 I_4 + D_2 I_4 I_5^2 + D_3 I_4 I_8 \\ \quad + E_1 I_5 I_7 \\ \quad + F_1 I_6^2 \\ \quad + G_1 I_5^2 + G_2 I_8 \end{array}\right) + O_2(\varepsilon, V) \tag{3-1}$$

with the irreducible integrity bases defined as:

$$\begin{aligned} I_1 &= \varepsilon_1 \\ I_2 &= \varepsilon_2 + \varepsilon_3 \\ I_3 &= 2\varepsilon_2^2 + \varepsilon_4^2 + 2\varepsilon_3^2 \\ I_4 &= \varepsilon_5^2 + \varepsilon_6^2 \\ I_5 &= v_1 \\ I_6 &= v_2\varepsilon_6 + v_3\varepsilon_5 \\ I_7 &= 2v_2\varepsilon_2\varepsilon_6 + v_2\varepsilon_4\varepsilon_5 + v_3\varepsilon_4\varepsilon_6 + 2v_3\varepsilon_3\varepsilon_5 \\ I_8 &= v_2^2 + v_3^2 \\ I_9 &= v_2^2\varepsilon_2 + v_2v_3\varepsilon_4 + v_3^2\varepsilon_3 \end{aligned}$$

where $\varepsilon_4 = \gamma_{23}$, $\varepsilon_5 = \gamma_{13}$ and $\varepsilon_6 = \gamma_{12}$.

Apart from this modification, all other assumptions stated originally in [180] with regard to this Helmholtz free energy expression are still in effect here. With the Helmholtz free energy expression established, the damage driving force

components are therefore formulated as shown in (3-2) which will drive the growth of damage, where v_i are components of the damage vector $V = \{v_1 \quad v_2 \quad v_3\}^T$ as originally defined in [180].

$$R_i = -\frac{\partial \Psi}{\partial v_i} (i\text{=1-3}) \qquad (3\text{-}2)$$

A point to note is that since internal energy is being released from the material during a cracking process, a negative sign is added here denoting that energy is being released out of the system. Then, the damage driving force components R_i can be rearranged into a matrix form with respect to the damage vector components v_i as shown below:

$$\begin{Bmatrix} R_1 \\ R_2 \\ R_3 \end{Bmatrix} = \begin{bmatrix} W_{11} & W_{12} & W_{13} \\ W_{21} & W_{22} & W_{23} \\ W_{31} & W_{32} & W_{33} \end{bmatrix} \begin{Bmatrix} v_1 \\ v_2 \\ v_3 \end{Bmatrix} \qquad (3\text{-}3)$$

where

$$W_{11} = A_3\varepsilon_1^2 + C_2(2\varepsilon_2^2 + \varepsilon_4^2 + 2\varepsilon_3^2) + A_7\varepsilon_1(\varepsilon_2 + \varepsilon_3) + B_2(\varepsilon_2 + \varepsilon_3)^2 + G_1 + D_2(\varepsilon_5^2 + \varepsilon_6^2)$$

$$W_{12} = W_{21} = \frac{1}{2}A_4\varepsilon_1\varepsilon_6 + \frac{1}{2}E_1(2\varepsilon_2\varepsilon_6 + \varepsilon_4\varepsilon_5) + \frac{1}{2}B_3(\varepsilon_2 + \varepsilon_3)\varepsilon_6$$

$$W_{13} = W_{31} = \frac{1}{2}A_4\varepsilon_1\varepsilon_5 + \frac{1}{2}B_3(\varepsilon_2 + \varepsilon_3)\varepsilon_5 + \frac{1}{2}E_1(\varepsilon_4\varepsilon_6 + 2\varepsilon_3\varepsilon_5)$$

$$W_{22} = A_6\varepsilon_1\varepsilon_2 + A_8\varepsilon_1(\varepsilon_2 + \varepsilon_3) + A_5{\varepsilon_1}^2 + B_4(\varepsilon_2 + \varepsilon_3)^2 + B_5\varepsilon_2(\varepsilon_2 + \varepsilon_3) + F_1{\varepsilon_6}^2 + C_3(2{\varepsilon_2}^2 + {\varepsilon_4}^2 + 2{\varepsilon_3}^2) + D_3({\varepsilon_5}^2 + {\varepsilon_6}^2) + G_2$$

$$W_{23} = W_{32} = \frac{1}{2}A_6\varepsilon_1\varepsilon_4 + \frac{1}{2}B_5(\varepsilon_2 + \varepsilon_3)\varepsilon_4 + F_1\varepsilon_5\varepsilon_6$$

$$W_{33} = A_5\varepsilon_1^2 + B_4(\varepsilon_2+\varepsilon_3)^2 + A_8\varepsilon_1(\varepsilon_2+\varepsilon_3) + C_3(2\varepsilon_2{}^2 + \varepsilon_4{}^2 + 2\varepsilon_3{}^2) + D_3(\varepsilon_5{}^2 + \varepsilon_6{}^2) + A_6\varepsilon_1\varepsilon_3 + B_5\varepsilon_3(\varepsilon_2+\varepsilon_3) + F_1\varepsilon_5{}^2 + G_2$$

As shown above, all elements in the matrix $[W]$ are functions of strains, undamaged UD composite elastic properties and damage representation related material constants obtained from [180], except for W_{11}, W_{22} and W_{33} elements where new unknown constant terms containing solely G_1 and G_2 from (3-1) are present.

However, looking at the full expression of W_{22} in (3-3) as an example, consider that if no strain loading is applied, G_2 would be the only remaining term in W_{22}, implying the existence of a damage driving force R_i and damage v_i even before any loading is applied to the material.

The same argument also applies to the constant term of G_1 in W_{11}. Obviously, such a scenario is due to the initial condition where initial damage exists in the material. For simplicity, by setting G_1 and G_2 to zero, the effect of initial damage is neglected for later development of the theory.

Since the matrix damage is assumed to be an array of planar cracks with a common orientation parallel to fibre direction, by assigning a rectangular material coordinate system (Fig. 3-1) to UD composites and choosing the 2-axis to be perpendicular to the crack surfaces, v_1 and v_3 should then become zero while v_2 remains as the only non-zero component in the damage vector to reflect such a form of cracking damage, i.e. $V = \{0 \quad v_2 \quad 0\}^T$. As a result, only W_{12}, W_{22} and W_{32} matrix elements in (3-3) need to be considered for v_2.

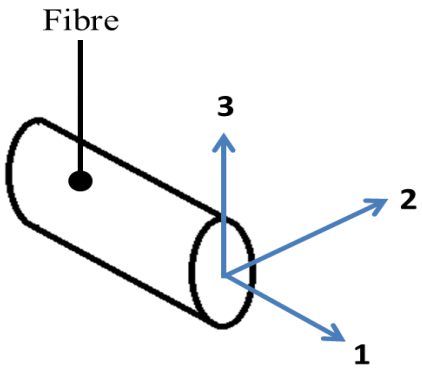

Fig. 3-1 Rectangular material coordinate system assigned to UD composites

Instead of pursuing further with W_{12}, W_{22} and W_{32} terms expressed in the strain space, these terms are rearranged and expressed by stresses so that damage driving force can be presented in the stress space. For this, partial derivatives of W_{12}, W_{22} and W_{32} are taken twice with respect to strains as shown in (3-4) so that these terms can be rearranged into (3-5).

$$X_{pq} = \frac{\partial^2 W_{12}}{\partial \varepsilon_p \partial \varepsilon_q}$$

$$Y_{pq} = \frac{\partial^2 W_{22}}{\partial \varepsilon_p \partial \varepsilon_q} \qquad (3\text{-}4)$$

$$Z_{pq} = \frac{\partial^2 W_{32}}{\partial \varepsilon_p \partial \varepsilon_q}$$

(p =1-6, q =1-6)

$$W_{12} = [\varepsilon]^T [X][\varepsilon]$$

$$W_{22} = [\varepsilon]^T [Y][\varepsilon] \qquad (3\text{-}5)$$

$$W_{32} = [\varepsilon]^T [Z][\varepsilon]$$

After this, by making use of the compliance matrix $[S]$ of the damaged UD composites (3-6), (3-5) can be manipulated into (3-7) which is now expressed by stress loadings.

$$[S]=\begin{bmatrix} \frac{1}{E_1^0} & -\frac{\nu_{12}^0}{E_1^0} & -\frac{\nu_{12}^0}{E_1^0} & 0 & 0 & 0 \\ & \frac{1}{E_2^0(1-\omega)} & -\frac{\nu_{23}^0}{E_2^0} & 0 & 0 & 0 \\ & & \frac{1}{E_2^0} & 0 & 0 & 0 \\ & & & \frac{1}{G_{23}} & 0 & 0 \\ & \textit{Symm} & & & \frac{1}{G_{12}^0} & 0 \\ & & & & & \frac{1}{G_{12}} \end{bmatrix} \tag{3-6}$$

By doing so, the presentation of damage driving force for uniaxial stress states will be much tidier as otherwise strain terms due to Poisson's effect would appear.

$$\begin{aligned} W_{12} &= [\sigma]^T[S]^T[X][S][\sigma] \\ W_{22} &= [\sigma]^T[S]^T[Y][S][\sigma] \\ W_{32} &= [\sigma]^T[S]^T[Z][S][\sigma] \end{aligned} \tag{3-7}$$

By denoting $[M]=[S]^T[X][S]$, $[P]=[S]^T[Y][S]$ and $[Q]=[S]^T[Z][S]$, (3-8) can be obtained.

$$\begin{aligned} W_{12} &= [\sigma]^T[M][\sigma] \\ W_{22} &= [\sigma]^T[P][\sigma] \\ W_{32} &= [\sigma]^T[Q][\sigma] \end{aligned} \tag{3-8}$$

where

$$M = \begin{bmatrix} 0 & 0 & 0 & 0 & 0 & M_{16} \\ & 0 & 0 & 0 & 0 & M_{26} \\ & & 0 & 0 & 0 & M_{36} \\ & & & 0 & M_{45} & 0 \\ & \textit{Symm.} & & & 0 & 0 \\ & & & & & 0 \end{bmatrix},$$

$$P = \begin{bmatrix} 0 & 0 & 0 & 0 & 0 & 0 \\ & P_{22} & 0 & 0 & 0 & 0 \\ & & 0 & 0 & 0 & 0 \\ & & & P_{44} & 0 & 0 \\ & \textit{Symm.} & & & 0 & 0 \\ & & & & & P_{66} \end{bmatrix},$$

and $$Q = \begin{bmatrix} 0 & 0 & 0 & 0 & 0 & 0 \\ & 0 & 0 & Q_{24} & 0 & 0 \\ & & 0 & Q_{34} & 0 & 0 \\ & & & 0 & 0 & 0 \\ & \textit{Symm.} & & & 0 & Q_{56} \\ & & & & & 0 \end{bmatrix}.$$

The above derivation then yields the following expressions for W_{12}, W_{22} and W_{32}:

$$\begin{aligned} W_{12} &= 2M_{16}\sigma_1\sigma_6 + 2M_{26}\sigma_2\sigma_6 + 2M_{36}\sigma_3\sigma_6 + 2M_{45}\sigma_4\sigma_5 \\ W_{22} &= P_{22}\sigma_2^2 + P_{44}\sigma_4^2 + P_{66}\sigma_6^2 \\ W_{32} &= 2Q_{24}\sigma_2\sigma_4 + 2Q_{34}\sigma_3\sigma_4 + 2Q_{56}\sigma_5\sigma_6 \end{aligned} \qquad (3\text{-}9)$$

A closer look at (3-9) reveals that W_{12} and W_{32} contain stresses like σ_1, σ_3 and σ_5 (τ_{13}), which do not directly cause matrix cracks with crack surface perpendicular to axis-2 ($V = \{0 \quad v_2 \quad 0\}^T$). As can be seen, these stresses are

arranged in W_{12} and W_{32} expressions in multiplication with other stress components, forming terms characterising the interactions between these stresses. For simplicity, such interactions are not addressed here and W_{12} and W_{32} expressions are neglected for the derivation of damage driving force. In this case, only R_2 and W_{12} are considered which simplified the damage driving force expression to (3-10).

$$R_2 = W_{22} v_2 \qquad (3\text{-}10)$$

Now, in the case of W_{22} (3-9), the only three non-zero terms dictate the damage driving force R_2 to be made up by three components corresponding to the contributions from transverse tensile stress σ_2 , transverse shear stress σ_4 (τ_{23}) and longitudinal shear stress σ_6 (τ_{12}) respectively.

This expression of W_{22} is rational and of great importance. The reason for this is that, first of all, it is a theoretical formulation matching the real physical phenomenon. This can be explained by looking at Fig.2-1 which shows that, physically, only these three stresses are expected to cause the kind of planar cracks parallel to fibre direction for making the damage vector as $V = \{0 \quad v_2 \quad 0\}^T$.

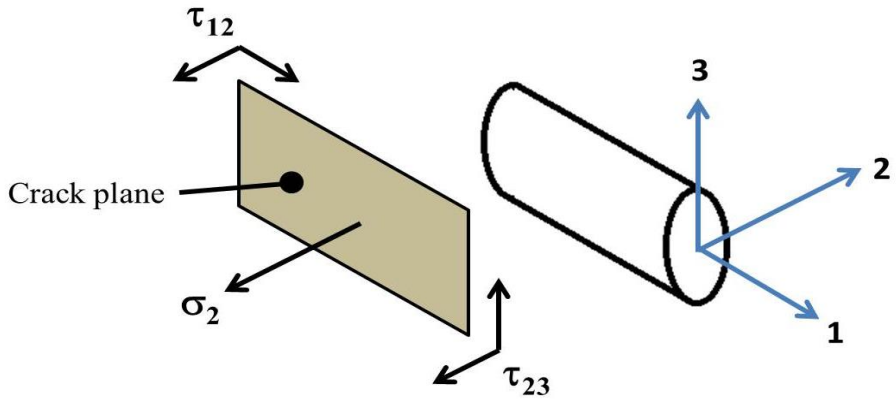

Fig. 3-2 Stresses for causing planar cracks parallel to fibre direction

Moreover, one may also recall that this very physical phenomenon actually formed the basis of Li's damage representation work in [180]. Bearing this in mind, along with the fact that the derivation here for damage driving force is also based on the material constants obtained from Li's damage representation, it is therefore, not surprising, that these three stresses are once again worked out to be the contributors for damage, but this time, in the form of damage driving force for driving the damage evolution process.

Actually, rather than surprising, this result may be seen as an assurance that the new damage driving force expression developed here is indeed consistent with Li's damage representation, demonstrating a smooth theoretical work transition from damage representation to damage evolution as mentioned at the beginning of this chapter.

In addition, this result is also in agreement with Puck's failure criterion [88] since in there, transverse tensile, transverse shear and longitudinal shear stresses are also identified to be the three stress components on an action plane responsible for generating planar matrix cracks parallel to fibre direction in UD composites. Then, it is envisaged that Puck's criterion is suitable to be employed as a damage initiation criterion in conjunction with the damage driving force derived here.

Recall in [180], the relationship between damage vector component v_2 and damage variable ω was introduced as (3-11).

$$\omega = \lambda v_2^{\,2} \text{ with } \omega = \frac{E_2^0 - E_2}{E_2^0} \tag{3-11}$$

Since the damage variable ω is a direct measure of modulus degradation, damage driving force expression (3-10) is now redefined with respect to ω as shown in (3-12).

$$\begin{aligned} \rho &= -\frac{\partial \psi}{\partial \omega} = -\frac{\partial \psi}{\partial v_2}\frac{\partial v_2}{\partial \omega} = -\frac{W_{22}}{2\lambda} \\ &= P_I \sigma_2^2 + P_{III}\sigma_4^2 + P_{II}\sigma_6^2 \end{aligned} \tag{3-12}$$

where

$$P_I = P_I^0 + P_I^D \omega = \frac{1}{E_2^0} + \frac{2\left(1 - \nu_{12}^0 \nu_{21}^0\right)}{\left(1 - \nu_{23}^0 - 2\nu_{12}^0 \nu_{21}^0\right)\left(1 + \nu_{23}^0\right) E_2^0}\omega$$

$$P_{II} = P_{II}^0 + P_{II}^D \omega = \frac{k}{G_{12}^0} + \frac{2k^2}{G_{12}^0}\omega$$

$$P_{III} = P_{III}^0 + P_{III}^D \omega = \frac{1}{E_2^0} + \frac{1}{\left(1 + \nu_{23}^0\right) E_2^0}\omega$$

and k is the coupled damage effect factor between transverse tensile damage and longitudinal shear damage as defined in [180].

The new subscripts introduced in (3-12) for P terms not only serve as a reminder that the new expression has now accounted for the coefficient $-\frac{1}{2\lambda}$ in order to bring in ω, but also indicate the adoption of a naming rule for different fracture modes caused by different modes of loading similar to that defined in classical

fracture mechanics, i.e. mode I for transverse tensile (σ_2) fracture and mode II & III for sliding and tearing types of shear (σ_6 & σ_4) induced fracture. However, in a slight contrast to classical fracture mechanics, the fracture mode naming concept adopted here is not targeted to specific cracks, but rather, intended for smeared damage effect in the form of modulus degradation.

Following the idea of fracture mode classification, ρ can then be regarded as the total damage driving force consisting of three damage driving force subcomponents corresponding to the three fracture modes (loading modes) as shown below.

$$\rho = \rho_I + \rho_{II} + \rho_{III} \quad \text{with} \quad \begin{aligned} \rho_I &= P_I \sigma_2^2 \\ \rho_{II} &= P_{II} \tau_{12}^2 \\ \rho_{III} &= P_{III} \tau_{23}^2 \end{aligned} \qquad (3\text{-}13)$$

Also from (3-12), it can be seen that the damage driving force ρ is actually a function of undamaged UD composites elastic constants, damage variable and stresses, resulting in the unit of stress as the physical dimension for ρ . In this case, under monotonic increasing stress loading, according to (3-12), damage driving force ρ value would have to increase. During such a loading process from an initial stress-free state, damage evolution would be triggered when a certain damage initiation criterion is satisfied.

3.3 Critical Damage Driving Force

For the time being, leave the issue of selecting appropriate damage initiation criterion to be addressed elsewhere, but focus instead on the damage driving force formula (3-13). At the point of damage initiation, one should not fall into the trap of treating the total damage driving force ρ as a material property by regarding it as the critical total damage driving force. This is similar to the observation in fracture mechanics where critical total energy release rate is not a material property since it is not unique and varies with the modes of fracture, i.e. loading conditions. Instead, critical energy release rates associated with specific fracture modes like G_{IC}, G_{IIC} and G_{IIIC} are defined as true material properties in fracture mechanics [181].

The same argument also applies here for damage driving force, as only critical damage driving forces for each loading modes denoted by ρ_{IC}, ρ_{IIC} and ρ_{IIIC} can be considered as true material properties. Each of these critical damage driving forces has to be obtained under a single mode of loading right up to the point of damage initiation. Therefore, ρ_{IC}, ρ_{IIC} and ρ_{IIIC} are defined as in (3-14).

$$\begin{aligned} \rho_{IC} &= P_I{}^0 \sigma_{2C}^2 \\ \rho_{IIC} &= P_{II}{}^0 \tau_{12C}^2 \\ \rho_{IIIC} &= P_{III}{}^0 \tau_{23C}^2 \end{aligned} \qquad (3\text{-}14)$$

where σ_{2C}, τ_{12C} and τ_{23C} are uniaxial or pure shear stress threshold values for triggering damage initiation and are expected to be material properties.

Since initial damage is not considered here, one should be aware that the value of damage variable ω is zero at the point of damage initiation as damage is just about to grow in a virgin material. Therefore, ω does not appear at all in (3-14).

Based on above discussion, the total damage driving force ρ is merely to account for mixed-mode loading scenarios, but ρ_{IC}, ρ_{IIC} and ρ_{IIIC} are real material properties as long as the same type of UD composites is being dealt with.

3.4 Unloading and Reloading Scenarios

On the other hand, if the material is unloaded after loading, according to (3-12), the total damage driving force ρ value would decrease to reflect the reduction in stressing. However, one should acknowledge that damage cannot be healed during the unloading process, at least not for conventional composites. Therefore, once the reduction in total damage driving force value signifies the start of the unloading process, the damage evolution process has to be paused and the current level of damage should remain unchanged during the unloading process, resulting in the unloading criterion shown in (3-15).

$$\text{If } \Delta\rho < 0,\ \Delta\omega = 0 \qquad (3\text{-}15)$$

With the issue of unloading introduced, there is also the issue of reloading when the previously unloaded material is loaded again. For such a scenario, since the damage evolution process would have been stopped due to previous unloading action, a reloading criterion is therefore needed to define an envelope beyond which damage evolution process is expected to resume during reloading stage. Furthermore, this scenario may also be encountered under a mixed-mode loading

condition which complicates this matter even further. Because damage driving forces are the quantities causing damage evolution, it is envisaged that such a reloading criterion should be based on damage driving forces. Then, inspired by common forms of mixed-mode fracture criteria from fracture mechanics [181], the reloading criterion is formulated as (3-16), where the ratio EQ represents the combined equivalent effect from all damage driving forces so that mixed-mode loading condition can be accounted for.

$$EQ = \frac{\rho_I}{\rho_{IC}} + \frac{\rho_{II}}{\rho_{IIC}} + \frac{\rho_{III}}{\rho_{IIIC}} \qquad (3\text{-}16)$$

In order to make use of this criterion, provided that the material is already damaged, the EQ value at the end of loading process just before unloading should be recorded which registers the current highest level of combined equivalent effect from all damage driving forces. After this, during subsequent reloading stage, if damage driving forces increase such that they cause a new EQ value higher than the previously recorded highest EQ value, damage evolution process should then resume. Otherwise, the current damage state still remains unchanged.

3.5 Damage Evolution Law and Incremental Material Constitutive Relationship

With the successful derivation of damage driving force, the quantities driving the evolution of damage are clearly identified and these would determine whether the damage will grow. However, as mentioned in the earlier review for damage evolution laws (Section 2.3.2.2.2), to determine how much the damage will grow, an additional relationship governing the magnitude of damage growth is still

needed. In this case, a relationship between the damage driving force and the value of damage growth.

For this, a proposed way forward is described as follows. Since damage growth is driven by damage driving force, it is then conceivable that

$$\omega = fn\left(\rho_I, \rho_{II}, \rho_{III}\right) \qquad (3\text{-}17)$$

Imagine the critical state for damage initiation is met with values of damage driving force components reaching ρ_{I0}, ρ_{II0} and ρ_{III0}. One can expand the function in (3-17) into a Taylor's series in the neighbourhood of the critical state at a given damage level of ω_0, with higher than first order terms neglected, (3-18) is obtained.

$$\begin{aligned}\omega = \omega_0 &+ \mu_I\left(\rho_I - \rho_{I0}\right) + \mu_{II}\left(\rho_{II} - \rho_{II0}\right) \\ &+ \mu_{III}\left(\rho_{III} - \rho_{III0}\right) + \cdots\end{aligned} \qquad (3\text{-}18)$$

or

$$\Delta\omega = \mu_I \Delta\rho_I + \mu_{II}\Delta\rho_{II} + \mu_{III}\Delta\rho_{III}$$

where μ_I, μ_{II} and μ_{III} are damage evolution constants which are material properties specific to the material system concerned and they will have to be determined empirically through experiments.

Moreover, thanks to the natural partition of total damage driving force into three components as previously derived in Section 3.2, different damage evolution constants μ_I, μ_{II} and μ_{III} are allocated for three different loading modes in (3-18), which avoids the unrealistic assumption that different loading modes

should always have the same contribution to damage growth as mentioned earlier in Section 2.3.2.2.2. However, the new assumption herein (3-18) is the proposed linear relationship between different loading modes when accounting for damage evolution under mixed-mode loading condition.

Also can be seen from (3-18), it is obvious that damage only evolves as a result of increasing damage driving force values. On the other hand, decreasing damage driving force values signify unloading process which was already discussed in Section 3.4.

As mentioned previously in Section 2.3.2.2.2, the internal dissipation inequality condition (Clausius - Duhem Inequality**)** resulting from the second law of thermodynamics requires the product of damage driving force and rate of damage growth to be of non-negative value, which can be expressed as (3-19).

$$\rho\dot{\omega} \geq 0 \qquad (3\text{-}19)$$

Due to this, the damage evolution constants μ_I , μ_{II} and μ_{III} are also restricted by this condition such that the incremental damage value $\Delta\omega$ predicted by (3-18) should satisfy (3-19).

Now, substituting (3-13) into (3-18), we have

$$\begin{aligned}\Delta\omega = {} & \mu_I \left\{ \left[P_I^0 + P_I^D \left(\omega_0 + \Delta\omega \right) \right] \left(\sigma_2 + \Delta\sigma_2 \right)^2 - \left(P_I^0 + P_I^D \omega_0 \right) \sigma_2^2 \right\} \\ & + \mu_{II} \left\{ \left[P_{II}^0 + P_{II}^D \left(\omega_0 + \Delta\omega \right) \right] \left(\tau_{12} + \Delta\tau_{12} \right)^2 - \left(P_{II}^0 + P_{II}^D \omega_0 \right) \tau_{12}^2 \right\} \\ & + \mu_{III} \left\{ \left[P_{III}^0 + P_{III}^D \left(\omega_0 + \Delta\omega \right) \right] \left(\tau_{23} + \Delta\tau_{23} \right)^2 - \left(P_{III}^0 + P_{III}^D \omega_0 \right) \tau_{23}^2 \right\}\end{aligned} \qquad (3\text{-}20)$$

However, one may notice here that the incremental stress terms $\Delta\sigma_2$, $\Delta\tau_{12}$ and $\Delta\tau_{23}$ in above expression are also dependent on incremental damage $\Delta\omega$. They

can be expressed as shown in (3-21) with stiffness matrix components $\mathbf{C}^0$ and $\mathbf{C}^D$, where $\mathbf{C}^0$ is the original stiffness matrix of undamaged UD composite material and $\mathbf{C}^D$ contains terms representing changes to the stiffness matrix due to damage effect.

$$\begin{aligned}
\Delta\sigma_2 &= \sum_{i=1}^{6}\left[c_{2i}^0 - c_{2i}^D\left(\omega_0+\Delta\omega\right)\right]\left(\varepsilon_i+\Delta\varepsilon_i\right) \\
&\quad - \sum_{i=1}^{6}\left(c_{2i}^0 - c_{2i}^D\omega_0\right)\varepsilon_i \\
\Delta\tau_{23} &= \sum_{i=1}^{6}\left[c_{4i}^0 - c_{4i}^D\left(\omega_0+\Delta\omega\right)\right]\left(\varepsilon_i+\Delta\varepsilon_i\right) \\
&\quad - \sum_{i=1}^{6}\left(c_{4i}^0 - c_{4i}^D\omega_0\right)\varepsilon_i \\
\Delta\tau_{12} &= \sum_{i=1}^{6}\left[c_{6i}^0 - c_{6i}^D\left(\omega_0+\Delta\omega\right)\right]\left(\varepsilon_i+\Delta\varepsilon_i\right) \\
&\quad - \sum_{i=1}^{6}\left(c_{6i}^0 - c_{6i}^D\omega_0\right)\varepsilon_i
\end{aligned} \tag{3-21}$$

Based on this, it is obvious that (3-20) is a nonlinear algebraic equation of the damage increment $\Delta\omega$. To solve for $\Delta\omega$, Newton's iterative method is employed to find the value of $\Delta\omega$ satisfying both (3-20) and (3-21). To facilitate this, rearrange (3-20) into (3-22):

$$\begin{aligned}
f\left(\Delta\omega\right) = \Delta\omega &- \mu_I\left\{\left[P_I^0 + P_I^D\left(\omega_0+\Delta\omega\right)\right]\left(\sigma_2+\Delta\sigma_2\right)^2 - \left(P_I^0 + P_I^D\omega_0\right)\sigma_2^2\right\} \\
&- \mu_{II}\left\{\left[P_{II}^0 + P_{II}^D\left(\omega_0+\Delta\omega\right)\right]\left(\tau_{12}+\Delta\tau_{12}\right)^2 - \left(P_{II}^0 + P_{II}^D\omega_0\right)\tau_{12}^2\right\} \\
&- \mu_{III}\left\{\left[P_{III}^0 + P_{III}^D\left(\omega_0+\Delta\omega\right)\right]\left(\tau_{23}+\Delta\tau_{23}\right)^2 - \left(P_{III}^0 + P_{III}^D\omega_0\right)\tau_{23}^2\right\}
\end{aligned} \tag{3-22}$$

The satisfaction of (3-22) about $\Delta\omega$ is to find an appropriate $\Delta\omega$ value which makes $f\left(\Delta\omega\right)=0$. Then, Newton's iteration formula as below can be used to find the root for such a homogeneous equation.

$$\text{For } \Delta\omega_k=\Delta\omega_{k-1}+\delta_k \text{ with } \Delta\omega_0=0,$$

$$\delta_k=-\frac{f\left(\Delta\omega_{k-1}\right)}{f'\left(\Delta\omega_{k-1}\right)} \tag{3-23}$$

where

$$\begin{aligned} f'\left(\Delta\omega\right)=1&-\mu_I\left(\sigma_2+\Delta\sigma_2\right)\left\{P_I^D\left(\sigma_2+\Delta\sigma_2\right)+2\left[P_I^0+P_I^D\left(\omega_0+\Delta\omega\right)\right]\frac{\partial\Delta\sigma_2}{\partial\Delta\omega}\right\}\\ &-\mu_{II}\left(\tau_{12}+\Delta\tau_{12}\right)\left\{P_{II}^D\left(\tau_{12}+\Delta\tau_{12}\right)+2\left[P_{II}^0+P_{II}^D\left(\omega_0+\Delta\omega\right)\right]\frac{\partial\Delta\tau_{12}}{\partial\Delta\omega}\right\}\\ &-\mu_{III}\left(\tau_{23}+\Delta\tau_{23}\right)\left\{P_{III}^D\left(\tau_{23}+\Delta\tau_{23}\right)+2\left[P_{III}^0+P_{III}^D\left(\omega_0+\Delta\omega\right)\right]\frac{\partial\Delta\tau_{23}}{\partial\Delta\omega}\right\}\end{aligned}$$

and

$$\frac{\partial\Delta\sigma_2}{\partial\Delta\omega}=-\sum_{i=1}^{6}c_{2i}^D\left(\varepsilon_i+\Delta\varepsilon_i\right)$$

$$\frac{\partial\Delta\tau_{23}}{\partial\Delta\omega}=-\sum_{i=1}^{6}c_{4i}^D\left(\varepsilon_i+\Delta\varepsilon_i\right)$$

$$\frac{\partial\Delta\tau_{12}}{\partial\Delta\omega}=-\sum_{i=1}^{6}c_{6i}^D\left(\varepsilon_i+\Delta\varepsilon_i\right)$$

with subscript k indicating number of iteration.

When the above defined iterations converge, $\Delta\omega_k$ converges to $\Delta\omega$. This value should then be used to update the damage state.

Based on this, at a given deformation state $\left(\boldsymbol{\varepsilon}+\Delta\boldsymbol{\varepsilon}\right)$, the tangential stiffness matrix of damaged material incorporating evolving damage variable can be derived as follows.

Starting from incremental stress-strain relationship:

$$\begin{aligned}\Delta\boldsymbol{\sigma} &= \left(\mathbf{C}^0 - \mathbf{C}^D\left(\omega_0 + \Delta\omega\right)\right)\left(\boldsymbol{\varepsilon} + \Delta\boldsymbol{\varepsilon}\right) - \left(\mathbf{C}^0 - \mathbf{C}^D\omega_0\right)\boldsymbol{\varepsilon} \\ &= \left(\mathbf{C}^0 - \mathbf{C}^D\omega_0\right)\Delta\boldsymbol{\varepsilon} - \mathbf{C}^D\left(\boldsymbol{\varepsilon} + \Delta\boldsymbol{\varepsilon}\right)\Delta\omega\end{aligned} \tag{3-24}$$

The tangential stiffness $[\mathbf{C}_t]$ can then be expressed as

$$\begin{aligned}\mathbf{C}_t &= \frac{\partial\Delta\boldsymbol{\sigma}}{\partial\Delta\boldsymbol{\varepsilon}} = \left(\mathbf{C}^0 - \mathbf{C}^D\omega_0\right) - \mathbf{C}^D\left(\boldsymbol{\varepsilon} + \Delta\boldsymbol{\varepsilon}\right)\frac{\partial\Delta\omega}{\partial\Delta\boldsymbol{\varepsilon}} \\ &= \left(\mathbf{C}^0 - \mathbf{C}^D\omega_0\right) - \mathbf{C}^D\left(\boldsymbol{\varepsilon} + \Delta\boldsymbol{\varepsilon}\right)\frac{\partial\Delta\omega}{\partial\Delta\boldsymbol{\sigma}}\frac{\partial\Delta\boldsymbol{\sigma}}{\partial\Delta\boldsymbol{\varepsilon}} \\ &= \left(\mathbf{C}^0 - \mathbf{C}^D\omega_0\right) - \mathbf{C}^D\left(\boldsymbol{\varepsilon} + \Delta\boldsymbol{\varepsilon}\right)\frac{\partial\Delta\omega}{\partial\Delta\boldsymbol{\sigma}}\mathbf{C}_t\end{aligned} \tag{3-25}$$

and rearranged into

$$\mathbf{C}_t = \left(I + \mathbf{C}^D\left(\boldsymbol{\varepsilon} + \Delta\boldsymbol{\varepsilon}\right)\frac{\partial\Delta\omega}{\partial\Delta\boldsymbol{\sigma}}\right)^{-1}\left(\mathbf{C}^0 - \mathbf{C}^D\omega_0\right) \tag{3-26}$$

where $[I]$ is identity matrix and $\dfrac{\partial\Delta\omega}{\partial\Delta\boldsymbol{\sigma}}$ can be found using (3-20).

The tangential stiffness matrix as above must be defined when an implicit FEA solver is used, such as ABAQUS™/Standard. Moreover, when a user defined material subroutine is utilised for the analysis, such a tangential stiffness matrix normally needs to be included in the subroutine.

3.6 Summary

In this chapter, a new damage evolution law based on the concept of damage driving force is proposed. It is to be applied in conjunction with Li's damage representation formulation for predicting the evolution of matrix damage in UD

composites in the form of planar cracks with a common orientation parallel to the fibre direction.

The damage evolution law proposed is capable of dealing with mixed-mode loading condition such that different modes of loading are allowed to have different contributions on damage evolution. In addition, it is also applicable to unloading and reloading scenarios thanks to the unloading and reloading criteria introduced here based on damage driving force.

In order to apply this damage evolution law, damage-related material properties are needed as necessary input parameters. For the determination of these parameters, experimental investigation of damage processes in composites is conducted and introduced in the next chapter.

Moreover, this damage evolution law is combined with Li's damage representation formulation, a damage initiation criterion, a damage evolution law and an instantaneous failure criterion to form a complete damage model for UD composites. This new UD composite CDM model is introduced in detail in Chapter 5.

4. Experimental Investigation of Damage in Composites by Quasi-static Tests

4.1 Introduction

With all the appropriate mathematical derivations presented in the previous chapter, a new damage evolution law for defining the progressive matrix damage in UD composites has been developed. In order to apply it for the prediction of damage in real UD composites, a number of damage-related material properties should be specified as input parameters for the damage evolution law. The experimental work necessary for determining the values of these parameters are presented in this chapter. A series of quasi-static tensile tests and in-plane shear tests were carried out on laminates of various stacking sequences which provided information regarding damage initiation and damage evolution.

Since the damage evolution law developed for UD composites is also considered to be appropriate for defining damage in UD tows of 3D woven composites, the same types of experiments were conducted on layer-to-layer interlock 3D woven composites. The data obtained from these tests was intended for validating the damage prediction produced by the damage evolution law when it is used for modelling damage inside the tows. In addition to that, to gain an in-depth understanding of damage development in the 3D woven composites, a series of tests for damage inspection have been devised, where samples subjected to different extent of damage were examined using microscopy.

Since only a limited number of studies on damage in layer-to-layer interlock 3D woven composites can be found in the open literature, the experimental

investigation presented here also provides an important insight into the complexity of damage development process in these materials.

4.2 Experimental Method

All tensile and shear tests were conducted according to ASTM D3039 testing standard [182] and ASTM D3518 testing standard [183] respectively.

4.2.1 Material Types and Specimens

Two types of composite materials were used, one being carbon fibre (CF) laminates of various ply stacking sequences, the other being layer-to-layer interlock 3D woven composites with E-glass fibre (GF) or carbon fibre reinforcement. Panels of the laminated and the 3D woven composite materials were produced following different manufacturing procedures, which are outlined in Sections 4.3.1 and 4.4.1 respectively, where the material data is also given.

All specimens were cut from the panels using a diamond-tipped wheel saw. The final geometries of all specimens were in accordance with the requirements listed in ASTM D3039 [182] testing standard. Aluminium alloy end tabs were attached to all specimens using Araldite® Standard epoxy adhesive. The bonding process was carried out according to the instructions set by the adhesive supplier [184]. Dimensions of specimens and end tabs are summarised in Section 4.3.1 for the laminates and in Section 4.4.1 for the 3D woven composites.

4.2.2 Loading Device and Test Environment

The tests were conducted using an electromechanical Instron® 5985 universal testing machine, with a 250 kN load cell. A constant testing speed of 2 mm/min (cross-head displacement rate) was applied. Load and extension data acquisition rate of 1 kHz was set in all the tests. The specimens were gripped with a pressure of 15 MPa by a set of Instron® 2716-003 manual wedge action grips capable of withstanding 100 kN. Instron® 2703-011 or 2703-012 jaw faces were used depending on the thicknesses of specimens. An ambient temperature of 18 $^{\circ}$C and a relative humidity of 43% were maintained in the laboratory throughout the duration of tests. All specimens were kept in such an atmospheric condition for at least 24 hours prior to the tests.

4.2.3 Strain Measurement

An Imetrum™ contactless video strain gauge system with a standard camera and a telecentric lens was used for strain measurement. Black speckle patterns on top of white coat paint were applied to the specimens, so that the video gauge camera would capture the local displacement on the surface of the specimens. Details of the video gauge set up are summarised in Table 4-1.

Table 4-1 Video strain gauge parameter summary

Controlling system	Imetrum Video Gauge™ software
Camera resolution	1.3 Megapixel
Gauge length (mm)	27
Working distance (mm)	180
Strain resolution (με)	5

4.2.4 Acoustic Emission

In some of the tests, real time acoustic emission (AE) data collection was performed, along with the stress and strain measurements. A PCI-2 based AE bench top system was used in conjunction with a 0/2/4 preamplifier and a R50D sensor, which were all supplied by Physical Acoustics Corporation™. As shown in Fig. 4-1, the sensor was attached to one of the grips of the Instron® testing machine with a couplant gel applied to the interface between them to improve signal transmission.

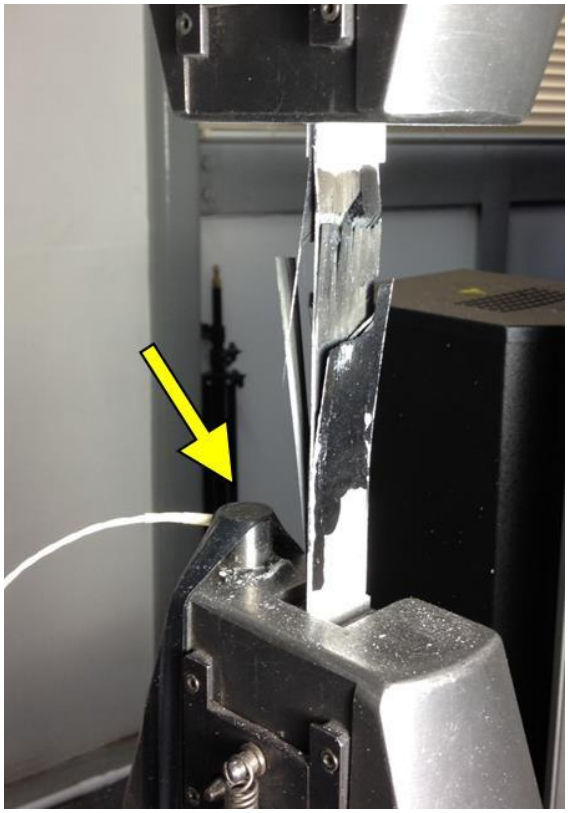

Fig. 4-1 Attachment of the AE sensor

The AE system was set up for composite material testing according to the recommendations listed in [185]. The main setting parameters for the AE equipment are summarised in Table 4-2.

Table 4-2 Acoustic emission equipment parameter summary

Amplification (dB)	20
Data processing software	AEwin™
Hit definition time (μs)	150
Hit lock-out time (μs)	300
Peak definition time (μs)	35
Sample rate (MHz)	5
Range (KHz)	100 – 700
Threshold (dB)	50

When cracking damage events occur in composites, elastic strain energy is suddenly released, resulting in propagation of elastic waves within the material. The mechanical energy of elastic waves is then detected by the AE sensor and converted into electrical signals before they are amplified and processed by the AE equipment.

The AE data collected serves as a record of sound signals emitted due to material cracking events. As mentioned in [158,186], it is especially useful when cumulative AE energy data is plotted against strain data, so that different levels of cumulative AE energy registered can be associated with different strain levels applied to a specimen in an uniaxial tensile test. Moreover, since cumulative AE energy is the sum of instant energy from every AE event over time, it shows the trend of AE event development during a test, which might reflect different stages of damage development in a specimen. Based on this, AE data plots are presented as "AE energy vs. tensile strain" plots in this chapter.

4.3 Quasi-static Test on Laminates of IM7 Carbon Fibre

4.3.1 Specimen Manufacture and Dimensions

Laminate panels were produced using IM7 carbon fibre UD pre-impregnated (prepreg) composite material supplied by Hexcel® [187]. Panels of different stacking sequences were manufactured.

From the supplier provided raw prepreg material roll, layers of raw prepreg material were cut into square-shaped panels with a side length of 300 mm. A hand lay-up procedure was then followed to stack up the prepreg layers manually on a flat aluminium tool plate. Care was taken to ensure good alignment of the fibre orientation for each layer according to the stacking sequence desired. After this, the laid up prepreg panels were debulked, vacuum bagged and cured using an autoclave according to the curing cycle recommended by the material supplier [188].

The stacking sequences and dimensions of the laminate specimens are summarised in Table 4-3. As can be seen, specimens with different stacking sequences were intended for the determination of different damage initiation stresses and different damage evolution constants for the matrix cracking damage in UD laminae inside the laminates.

Table 4-3 Laminate specimen summary*

Stacking sequences	Overall length (mm)	Width (mm)	Thickness (mm)	Material properties to be determined
$[0]_8$	250 (1.87)	15.5 (0.184)	1.03 (0.0124)	Longitudinal strength

$[90]_{12}$	251 (1.32)	25.3 (0.158)	1.49 (0.0273)	$R_{\perp}^{T}$
$[+45°/-45°]_{3S}$	250 (1.22)	25.2 (0.241)	1.98 (0.0233)	$R_{\perp\parallel}$, μ_{II}
$[0°/90°_7]_S$	251 (1.41)	25.6 (0.272)	1.98 (0.0214)	μ_I
$[0°/45°/-45°/90°]_S$	249 (1.71)	25.3 (0.162)	1.01 (0.0112)	Mixed-mode case for validation

∗ Values in "( )" are standard deviation values

Ten tensile specimens were produced for each stacking sequence category. Two untested specimens from each stacking sequence category were subjected to microscopic inspection for manufacturing defect checking. No defect in the form of cracks and voids was found for any of the specimens checked. The dimensions of the aluminium alloy end tabs attached to the specimens are presented in Table 4-4.

Table 4-4 Aluminium alloy end tab information for laminate specimens*

Tabs attached to	Length (mm)	Width (mm)	Thickness (mm)	Tab bevel angle (°)
$[0]_8$laminates	60.2 (0.684)	15.2 (0.104)	1.52 (0.0102)	90
$[90]_{12}$ laminates	25.1 (0.131)	25.3 (0.137)	1.51 (0.011)	90
All other specimens	40.2 (0.324)	25.3 (0.151)	1.51 (0.0105)	90

∗ Values in "( )" are standard deviation values

4.3.2 Material Properties of the UD Lamina

Since the laminates were composed of plies of Hexcel® IM7 carbon fibre UD prepreg, cured prepreg material data are presented in Table 4-5 for reference. The data were extracted from the test report [187] provided by the manufacturer for the specific batch of prepreg material supplied. Additional details for the neat matrix and pure fibre materials of the prepreg can be found in [188] and [189].

Table 4-5 Cured IM7/8552 CF UD prepreg material property summary [187]

Carbon fibre type	HexTow® IM7
Fibre tow size	12K
Epoxy matrix type	HexPly® 8552
Resin content by weight (%)	33.2 ± 0.65
Fibre areal weight (g/m^2)	135 ± 2.53
Total fibre volume fraction (%)	59.6 ± 0.6
Ply thickness (mm)	0.124 ± 0.003
Fibre direction ultimate tensile strength (MPa)	2895 ± 118
Fibre direction Young's modulus (GPa)	189 ± 3.27

4.3.3 Result and Discussion

4.3.3.1 Fibre Direction Uniaxial Tensile Test of UD Laminates

Typical experimental stress-strain curve demonstrating the material response under tension in fibre direction is shown in Fig. 4-2. The material properties determined based on the experimental data are summarised in Table 4-6. It should

be noted that the measured values of Young's modulus and strength in the fibre direction are comparable to those provided by the material manufacturer (Table 4-5).

Table 4-6 IM7/8552 CF UD laminate fibre direction test result

Property	Mean value	Std. dev.	COV %	Number of tests
Young's modulus (GPa)*	186	9.84	5.3	7
ν_{12}*	0.312	0.0499	16	7
Ultimate strength (MPa)	2550	142	5.6	7
Ultimate strain %	1.51	0.102	6.8	7
Stress at initial nonlinearity (MPa)	2170	113	5.2	7

* Values were obtained in the strain range of 1000-3000 microstrain

As can be seen in Fig. 4-2, the nonlinearity occurred after strain in the fibre direction exceeded 1%. The likely cause for this is gradual fibre breakage and fibre splitting damage, which were observed at this level of strain.

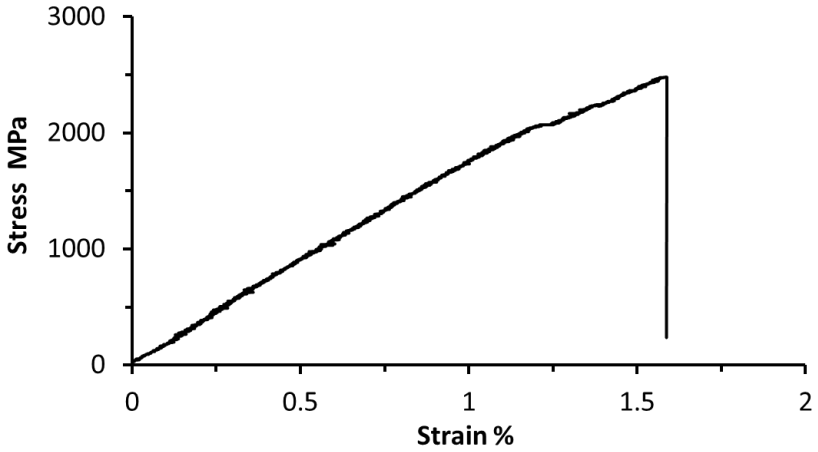

Fig. 4-2 Typical fibre direction tensile test stress-strain curve of IM7/8552 CF UD laminate

The final failure for all the specimens was a combination of severe fibre splitting and sudden fibre breakage in an explosive manner, when the specimens burst into very small pieces at the end. The specimens were so fragmented after final failure such that all that remained were a few broken fibre bundles that were still attached to the specimen end tabs. Such a severe specimen fragmentation phenomenon during a quasi-static test might be caused by the instantaneous stress waves induced by the sudden fibre breakage upon final failure.

4.3.3.2 Transverse Direction Uniaxial Tensile Test of UD Laminates

As was expected, in the transverse direction of UD laminates, the Young's modulus and strength values measured (Table 4-7) were significantly lower than those in the fibre direction (Table 4-6). Furthermore, the typical transverse direction stress-strain curve (Fig. 4-3) appears to be linear until the final failure of the specimen, indicating that under this type of loading, if any cracking damage occurred, it did not become severe enough to affect the stiffness of the material.

Table 4-7 IM7/8552 CF UD laminate transverse direction test result

Property	Mean value	Std. dev.	COV %	Number of tests
Young's modulus(GPa)∗	10.9	0.371	3.4	7
Ultimate strength (MPa)	49.2	5.76	12	7
Ultimate strain %	0.447	0.0411	9.2	7

∗Values were obtained in the strain range of 1000-3000 microstrain

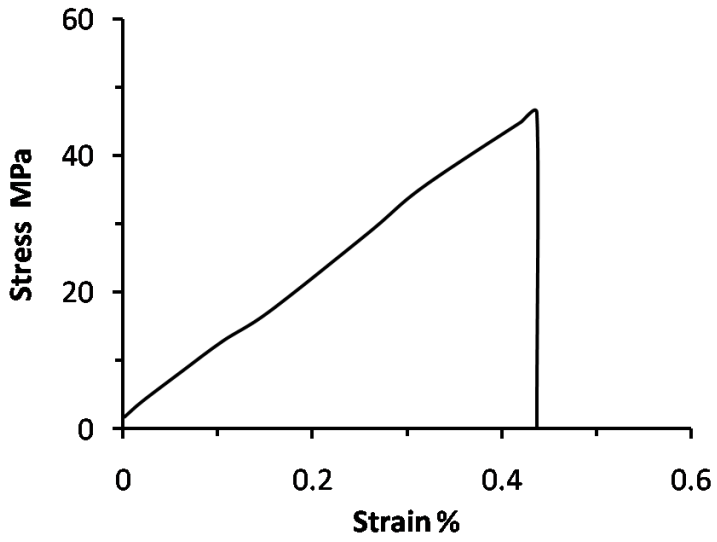

Fig. 4-3 Typical transverse direction tensile test stress-strain curve of IM7/8552 CF UD laminate

All specimens in this test case failed by clear cut fracture aligned in the fibre direction as shown in Fig. 4-4. It is obvious that such failure was caused by the tensile load applied perpendicular to the fibre direction. No other damage or failure mode was detected from visual inspections of the tested specimens.

Fig. 4-4 Typical final failure of IM7/8552 CF UD laminate in transverse direction tensile test

The implementation of the damage evolution law developed in this research requires the definition of the conditions that trigger the initiation of damage, which involves the definition of the material property $R_{\perp}^{T}$. $R_{\perp}^{T}$ is essentially a damage initiation threshold strength for mode I type of damage which should be caused by transverse tensile stress. Since no effects of damage were detected prior to the ultimate failure under the transverse tensile loading, it can be concluded that the strength value determined in this loading case should serve as the damage initiation stress $R_{\perp}^{T}$.

4.3.3.3 In-plane Shear Test of ±45° Laminates

In-plane shear tests were carried out on laminates of $[+45°/-45°]_{3S}$ stacking sequence by loading them in 0° direction. The tests were conducted according to ASTM D3518 testing standard [183] for obtaining effective in-plane shear properties of UD laminates.

Due to limitations of the video strain gauge, strain measurement was stopped automatically at approximately 3% of engineering shear strain, as the painted speckle pattern on the specimens distorted excessively and became no longer recognisable by the video gauge. As a result, tests were stopped once strain measurement ceased. Due to this, no specimen in this test case was tested to reach final failure. Consequently, ultimate shear strength is not specified in Table 4-8. Also, neither visible damage nor obvious deformation was observed from the specimens tested.

A typical stress-strain curve captured in in-plane shear tests is shown in Fig. 4-5. The stress-strain relationship is very nonlinear, which is characteristic of typical

shear response of UD laminates [190]. A possible explanation for this nonlinearity is the combined effect of shear cracking damage and plastic deformation of the matrix material.

Table 4-8 IM7/8552 CF UD laminate in-plane shear test result

Property	Mean value	Std. dev.	COV %	Number of tests
Shear modulus(GPa)∗	5.19	0.203	3.9	7
0.2% offset shear strength (MPa)	55.9	4.39	7.9	7

∗Values were obtained in engineering shear strain range of 2000-6000 microstrain

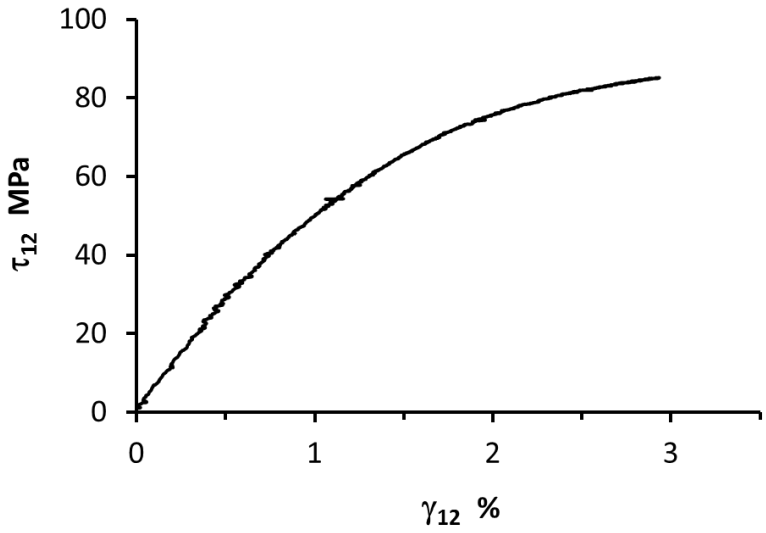

Fig. 4-5 Typical in-plane shear stress-strain curve of IM7/8552 CF UD laminate

From this test case, the in-plane shear stress-strain plot obtained not only indicated the point of damage initiation as nonlinearity started when the 0.2% offset shear strength was reached, but also displayed the damage evolution process since the slope of the stress-strain curve reduced gradually with increasing shear strain.

Consequently, the 0.2% offset shear strength can be regarded as the damage initiation threshold stress value $R_{\perp\parallel}$ under in-plane shear loading, while the nonlinear part of the stress-strain curve beyond the 0.2% offset shear strength can be used for determining the in-plane shear damage evolution constant μ_{II}. In this way, both of the $R_{\perp\parallel}$ and μ_{II} damage-related material constants can be determined from UD composite in-plane shear stress-strain plot like the one in Fig. 4-5.

4.3.3.4 Uniaxial Tensile Test of Cross-Ply Laminates

Tensile tests were carried out on cross-ply laminates with the stacking sequence as $[0°/90°_7]_S$. In these experiments, damage mainly occurred in the form of transverse matrix cracking in the 90° plies, which was caused by the tensile loading transverse to the fibre direction and corresponds to mode I type of damage.

Table 4-9 IM7/8552 CF Cross-ply laminate test result

Property	Mean value	Std. dev.	COV %	Number of tests
Young's modulus(GPa)*	31.1	0.653	2.1	7
Strength (Mpa)	326	17.7	5.4	7
Ultimate strain %	1.37	0.0354	2.6	7
Stress at initial nonlinearity (MPa)	132	19.7	15	7

∗Values obtained in the strain range of 500-2500 microstrain

As can be seen from the typical stress-strain curve shown in Fig. 4-6(a), the effect of damage is obvious, as it caused significant changes in the slope of the curve.

On the other hand, in AE energy plot (Fig. 4-6(b)), two strain levels of significance were identified and marked by letters "A" and "B". Strain level "A" is considered significant because it marked the beginning of detected AE events, while strain level “B” stands out because a sudden steep increase in cumulative AE energy was recorded at this strain level.

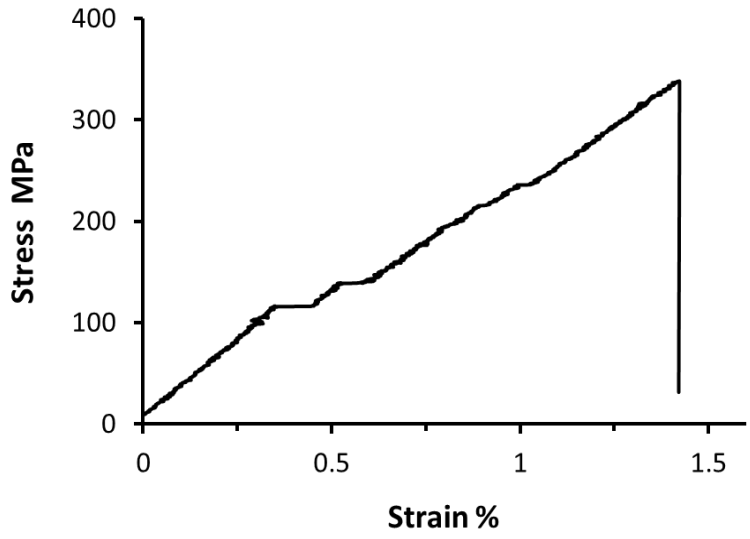

(a)

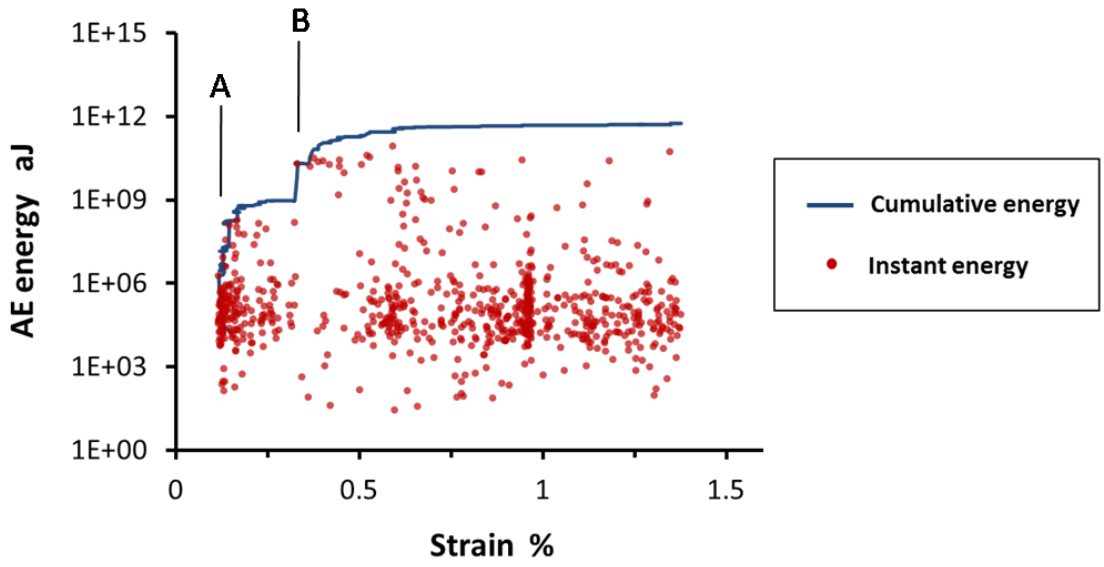

(b)

Fig. 4-6 Typical IM7/8552 CF cross-ply laminate test result: a) stress-strain curve, b) AE energy plot

Comparing Fig. 4-6(a) and Fig. 4-6(b), it can be seen that the initial rapid change in the slope of stress-strain curve occurred at strain level "B", when a steep increase in cumulative acoustic energy was also detected. The likely cause for that is the coalescence of matrix cracks in 90° UD plies, which was the first damage event severe enough to be reflected in the stress-strain curve. This damage could also have caused AE events of higher than 1×10^{9}aJ instant energy, which resulted in the steep rise of cumulative acoustic energy at the same time.

However, as shown in Fig. 4-6(b), there are also numerous AE events recorded between strain level “A” and strain level “B”. These AE events might be caused by matrix cracking and delamination damage which occurred before strain level “B”. Despite their presence being picked up by the acoustic emission, these damage events were not severe enough to be reflected on the stress-strain curve.

In terms of the stress-strain response recorded (Fig. 4-6(a)), it is worth noting that there are several stress plateaus after strain level “B” was reached. It is believed that these plateaux are related to the residual curing stresses within laminates, which were caused by the mismatch of thermal expansion coefficients between adjacent plies of different orientations. Specifically, the 90° plies in a cross-ply laminate would be held in place by 0° plies due to laminate deformation compatibility condition, therefore they would resist tension from 0° plies, because the 90° plies tend to contract more during the cooling down period of the curing process.

When the transverse matrix cracks initiated in the 90° plies, the transverse stiffness in these plies reduces rapidly. Because of this, the residual stresses left

behind from the curing process would be released in response to this change. The release of residual stresses is accompanied by an increase in the tensile deformation of the laminate, which does not correspond to any increase in loading, but results from the emergence of transverse matrix cracks in the 90° plies. Apparently, the higher the concentration of 90° plies there is in the laminate, the more pronounced these stress plateaux would be.

In this test case, since the 90° UD plies were loaded under transverse tension, the damage in these plies resembles the mode I type of damage. If no damage occurs in the 0° UD plies until the final failure of the specimen, variation of the slope of the stress-strain curve in Fig. 4-6(a) should be due to the development of mode I damage in the 90° UD plies. In this sense, the mode I damage evolution constant μ_I can therefore be determined from the cross-ply laminate stress-strain curve like the one in Fig. 4-6(a).

However, considering that the stress plateaux in the laminate stress-strain plot (Fig. 4-6(a)) are envisaged to be caused by the release of residual curing stresses rather than the stiffness degradation due to damage in the 90° UD plies, only the part of laminate stress-strain curve beyond the major stress plateaux should be used for μ_I constant determination.

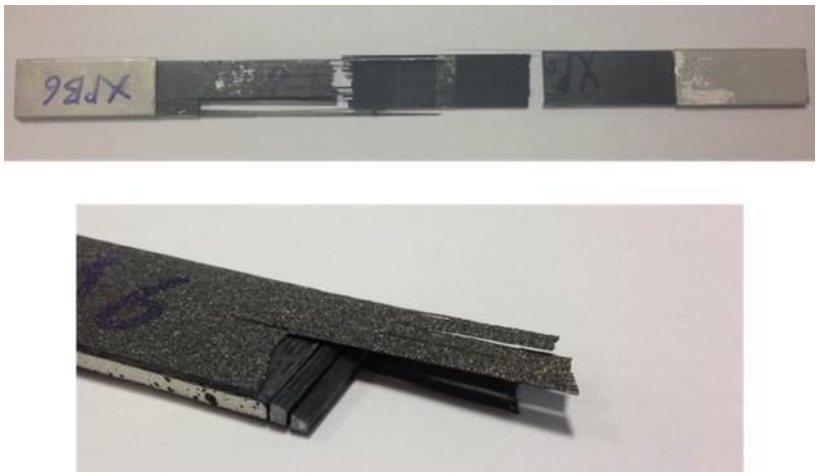

Fig. 4-7 Typical IM7/8552 CF cross-ply laminate failure modes

As shown in Fig. 4-7, multiple failure modes can be observed from the failed cross-ply laminate specimens. There were large delamination cracks between 90° and 0° plies, fracture of 90° plies in the form of through-the-thickness transverse cracks which are considered to be mode I type and fibre fracture in the outermost 0° plies which is expected to be the catastrophic failure responsible for final disintegration of the specimens.

4.3.3.5 Uniaxial Tensile Test of Quasi-isotropic Laminates

Quasi-isotropic (QI) laminates of stacking sequence $[0°/45°/-45°/90°]_S$ were also subjected to tensile testing to create a scenario where both mode I and mode II loadings were present in the laminate specimens. In detail, the plies with ±45° orientations are expected to experience a combination of mode I and mode II loadings, since they would be loaded under both transverse tensile and in-plane shear stresses in the laminate. The 90° plies, on the other hand, are expected to

show mode I type of damage only as they would be mainly loaded under transverse tension.

The experimental result obtained from this test case for QI laminates can be used for the future validation of the damage model incorporating the new damage evolution law as the damage predicted for the QI laminates can be assessed against the real experimental data collected here.

Table 4-10 IM7/8552 CF QI laminate test result

Property	Mean value	Std. dev.	COV %	Number of tests
Young's modulus(GPa)*	68.1	1.23	1.8	7
Strength (MPa)	805	35.3	4.4	7
Ultimate strain %	1.19	0.0286	2.4	7

* Values were obtained in the strain range of 1000-3000 microstrain

The stress-strain curve obtained for the QI laminates under tension is shown in Fig. 4-8(a). The stress-strain dependence appears to be linear, suggesting that QI laminate did not show clear sign of any damage before final failure. However, the large number of instant energy points and a rising cumulative AE energy curve in the AE plot as shown in Fig. 4-8(b) indicate that actually a lot of damage events happened inside the QI laminates during the loading process.

Based on this, it is suspected that, although matrix cracking occurred in plies of ±45° and 90° orientations, the QI laminate stress-strain curve remained linear due to the high Young's modulus value in the fibre direction offered by the 0° plies, which effectively undermined the influence of matrix cracking at the laminate level of stress-strain response.

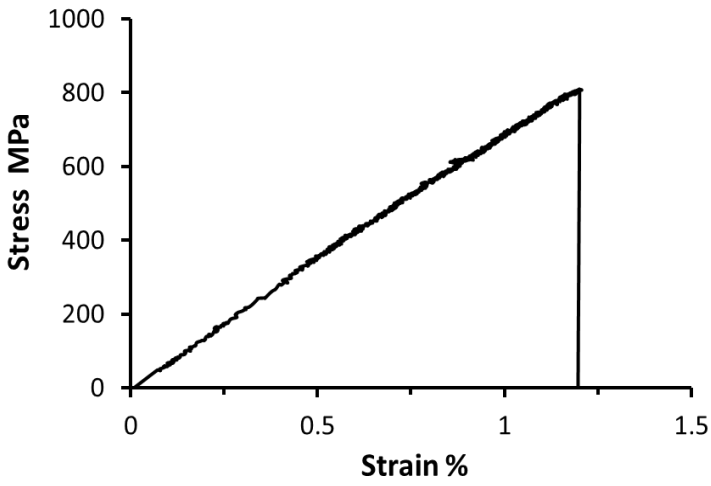

(a)

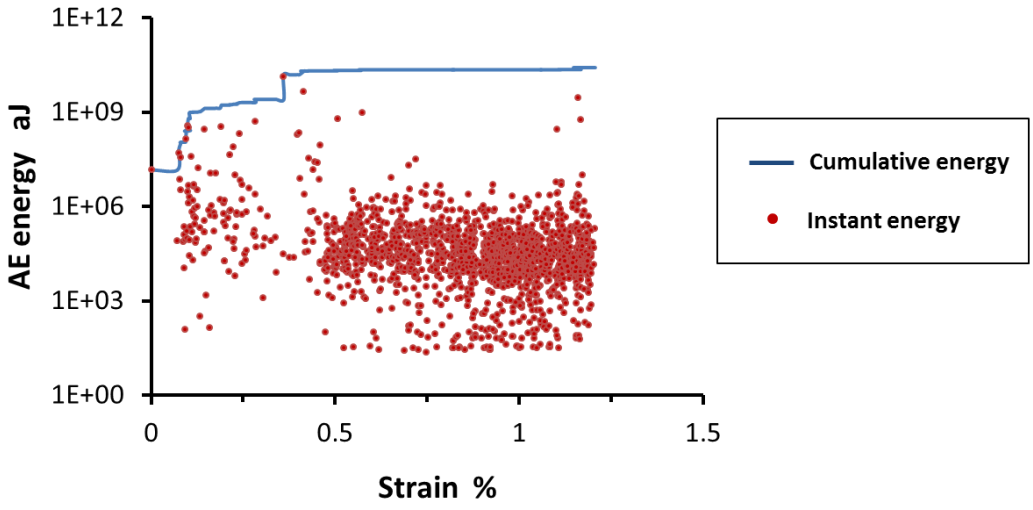

(b)

Fig. 4-8 Typical IM7/8552 CF QI laminate test result: a) Stress-strain curve, b) AE energy plot

As captured in Fig. 4-9, failure modes observed from tested QI laminates are similar to those found previously in the cross-ply laminate test case, but with the addition of ±45° ply fracture.

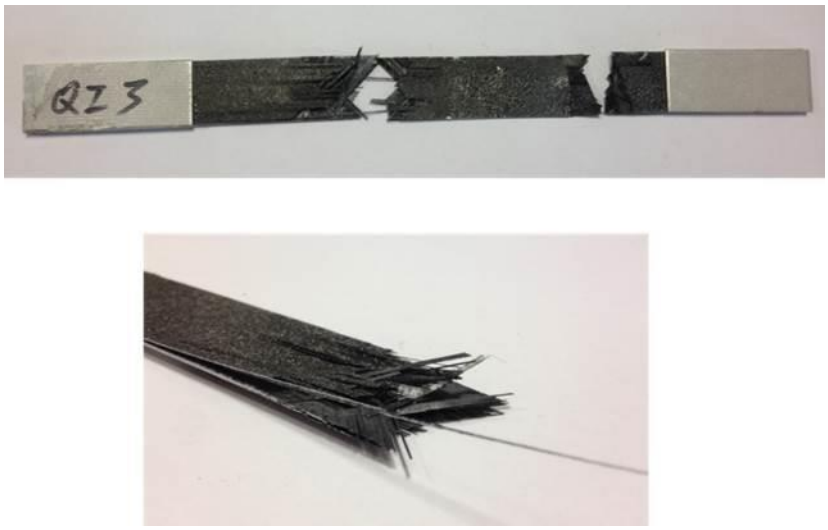

Fig. 4-9 Typical IM7/8552 CF QI laminate failure modes

4.4 Quasi-static Test on 3D Woven Composites

4.4.1 Specimen Manufacture and Dimensions

Layer-to-layer interlock 3D woven composites with E-glass fibre or carbon fibre reinforcement were provided by Sinoma® [191,192]. Both types of 3D woven composites were moulded into square-shaped composite panels with a side length of 300 mm using vacuum assisted resin transfer moulding (VARTM) process. Closed-mould tools of mild steel were used for the RTM process. Corner injection method was employed to fill the mould cavity with Gurit Prime™ 20LV infusion epoxy resin. The epoxy resin was mixed with Prime™ slow hardener prior to the injection. The mixing, resin injection and curing processes were all carried out according to the guidance published by the resin supplier [193]. Further details for the manufacturing process can be found in [194].

In addition to in-plane shear tests, uniaxial tensile tests in the warp and weft directions were also conducted for the 3D woven composites. Sixteen specimens were made for each test direction. Dimensions of the specimens and the

aluminium alloy end tabs attached to them are presented in Table 4-11 and Table 4-12 respectively.

Table 4-11 3D woven composites specimen summary*

Material type	Test direction	Overall length (mm)	Width (mm)	Thickness (mm)
CF 3D woven composite	Warp direction	250 (1.54)	25.1 (0.134)	4.29 (0.0431)
	Weft direction	251 (1.26)	25.3 (0.165)	4.31 (0.0332)
	In-plane shear	251 (1.33)	25.4 (0.113)	4.28 (0.0291)
GF 3D woven composite	Warp direction	250 (1.31)	25.5 (0.174)	4.11 (0.0309)
	Weft direction	249 (1.24)	25.4 (0.112)	4.13 (0.0402)
	In-plane shear	250 (1.81)	25.1 (0.164)	4.09 (0.0311)

* Values in "( )" are standard deviation values

Table 4-12 3D woven composites specimen end tab dimension*

Length (mm)	Width (mm)	Thickness (mm)	Tab bevel angle (º)
40.2 (0.324)	25.3 (0.151)	1.51 (0.0105)	90

* Values in "( )" are standard deviation values

4.4.2 3D Woven Composite Reinforced by IM7 Carbon Fibre

4.4.2.1 Material Properties and Structure of the Weave

The woven reinforcements in this type of 3D composite were produced with IM7 carbon fibres, which were the same type of fibre material as was used for the UD reinforcement in the laminates mentioned in Section 4.3. General information of

the 3D woven composite is summarised in Table 4-13. Material properties for the IM7 carbon fibre tows and cured Gurit Prime™ 20LV infusion epoxy resin are listed in Table 4-14 and Table 4-15 respectively.

Table 4-13 General information of IM7 CF 3D woven composite [191]

Weave pattern	Layer-to-layer interlock (Fig. 4-10 - Fig. 4-12)
Reinforcement type	HexTow® IM7 12K carbon fibre
Matrix material type	Gurit Prime™ 20LV epoxy resin
Weft to warp ratio (By weight per cm)	0.625
Number of weft tow layers	7
Dry fabric areal density (kg/m^2)	4.05 ± 0.04
Total fibre volume fraction (%)	$55.5\% \pm 0.8\%$

Table 4-14 IM7 12K carbon fibre tow material properties [189]

Tensile modulus (GPa)	276
Tensile strength (MPa)	5655
Ultimate tensile failure strain	1.9%

Table 4-15 Cured Gurit Prime™ 20LV epoxy resin material properties [193]

Young's modulus (GPa)	3.5
Poisson's ratio	0.35
Tensile strength (MPa)	73

As specified in Table 4-13, the total fibre volume fraction in the 3D woven CF composite was 55.5%. It was lower than that in laminates, for which the total fibre volume fraction was 59.6% (Table 4-5). This is expected as it is well known that 3D woven composites made by using RTM process are normally unable to

achieve fibre volume fractions as high as those of high performance laminates due to limitations of RTM process.

To study the internal structure of the composite, a sample of cured IM7 CF 3D woven composite was subjected to a micro computed tomography (micro-CT) scan. The micro-CT images are presented in Fig. 4-10, Fig. 4-11 and Fig. 4-12, showing views of the internal structure in the weft, warp and through-the-thickness directions accordingly. For the ease of reference, a rectangular coordinate system was assigned to the 3D woven composite with *X*-, *Y*- and *Z*-axes correspond to the warp, weft and through-thickness directions, respectively.

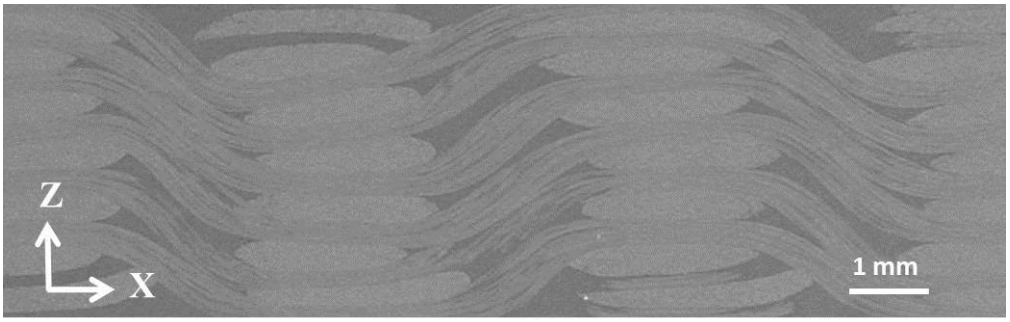

(a)

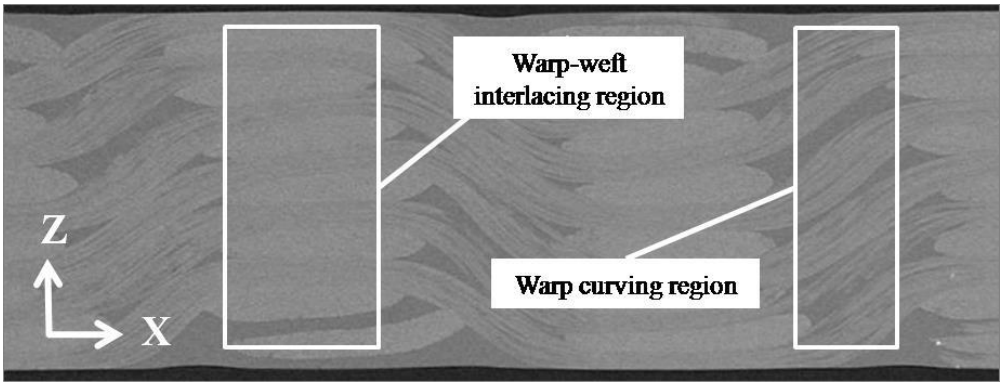

(b)

Fig. 4-10 *XZ*-plane CT scan images of cured IM7 CF 3D woven composite: a) original image, b) image with annotation of distinctive regions

As can be seen in Fig. 4-10, where view of the internal structure in the weft direction is shown, the adjacent layers of the weft tows are interlocked by the warp tows, hence there are no explicit interfaces between the layers of the weft tows. This is one of the most important differences between layer-to-layer interlock 3D woven composites and conventional laminates. In absence of explicit interfaces, inter-ply delamination, which is common in laminated composites, does not occur in 3D woven composites with layer-to-layer angle interlock reinforcement.

For the ease of description, the regions where warp tows were curved and where warp and weft tows crossed each other will be referred to as "warp curving region" and "warp-weft interlacing region", respectively, as shown in Fig. 4-10(b).

In the warp curving region, the warp tows, interlacing the straight weft tows, provided reinforcement in through-the-thickness direction. Therefore, it is expected that such architecture would provide substantially better transverse shear properties than conventional laminates.

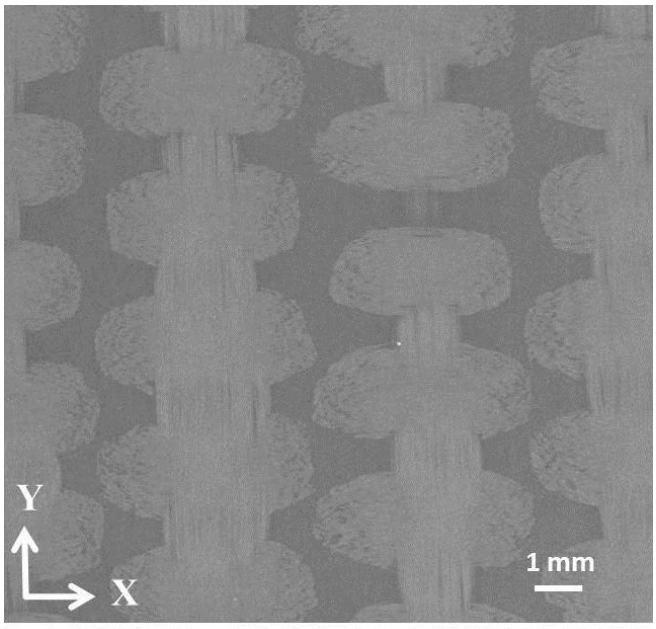

Fig. 4-11 *XY*-plane CT scan image of cured IM7 CF 3D woven composite

The tow packing in warp-weft interlacing regions is shown in Fig. 4-12. Here the warp tows were more densely packed due to the presence of straight weft tows, so much so that the boundaries between warp tows became indistinguishable in some layers between the weft tows.

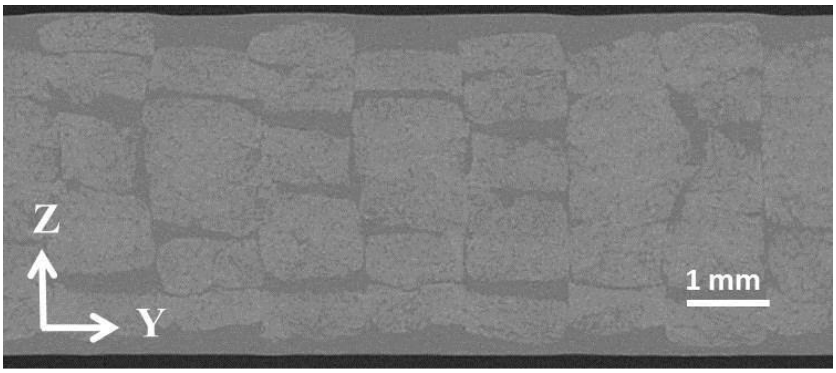

(a)

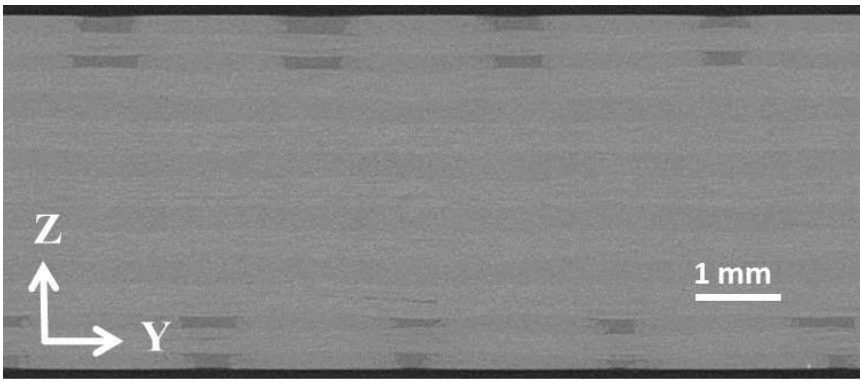

(b)

Fig. 4-12 *YZ*-plane CT scan images of cured IM7 CF 3D woven composite: a) at warp curving region, b) at warp-weft interlacing region

Based on the CT images obtained, geometric properties of the woven reinforcement were measured and summarised in Table 4-16. These geometrical data was later used for generating unit cell models for conducting analysis of the 3D woven composite.

Table 4-16 Weave pattern geometries of cured IM7 CF 3D woven composite

Warp tow weaving angle	31.6 ± 3º
Warp tow width	1.28±0.09 mm
Warp tow thickness	0.37±0.04 mm
Weft tow space	4.52±0.14 mm
Weft tow width	2.26±0.16 mm
Weft tow thickness	0.37±0.03 mm

4.4.2.2 Results and Discussion

4.4.2.2.1 Warp Direction Uniaxial Tensile Test

Although both used the same carbon fibre material type, the values of Young's modulus and strength for the 3D woven composite in the warp direction (Table 4-17) were only about half of those obtained from the QI laminates (Table 4-10). Moreover, the failure strain in the warp direction of the 3D woven composite was about 1% higher than that of the QI laminates. This indicates that when the 3D woven composite was under warp direction quasi-static tension, its response was more compliant than that of the QI laminates.

Table 4-17 Measured properties of IM7 CF 3D woven composite in warp direction

Property	Mean value	Std. dev.	COV %	Number of tests
Young's modulus (GPa)*	37.8	1.25	3.3	7
Strength (MPa)	421	25.3	6	7
Ultimate strain %	2.29	0.569	24.8	7
Stress at initial nonlinearity (MPa)	91.2	8.94	9.8	7

* Values were obtained in the strain range of 500-2500 microstrain

Comparing the stress-strain curves in Fig. 4-13 and Fig. 4-8, it can be seen that the former shows a very early onset of nonlinearity while the latter is mostly linear up to final failure. The differences in material response are probably due to the combined effect of lower fibre volume fraction and curved warp tow path (Fig. 4-10) in the 3D woven composites as opposed to the straight fibres and higher fibre volume fraction in the laminates.

A reasonably good correlation can be found between the stress-strain plot and the AE data in Fig. 4-13. The sudden increase in cumulative energy to around 1×10^9 aJ (indicated by the arrow in AE data plot) occurred at the same strain level (around 0.25%) where the stress-strain curve deviated away from the initial linear part. In addition, occurrence of AE events became much more frequent beyond this particular strain level, as density of red points representing instant energy from individual AE events increased rapidly after 0.25% warp direction strain in Fig. 4-13(b). Based on these observations, it is envisaged that 0.25% warp direction strain was a critical strain level, beyond which a change in damage development phase had occurred and resulted in the effective bilinear shape of the stress-strain curve.

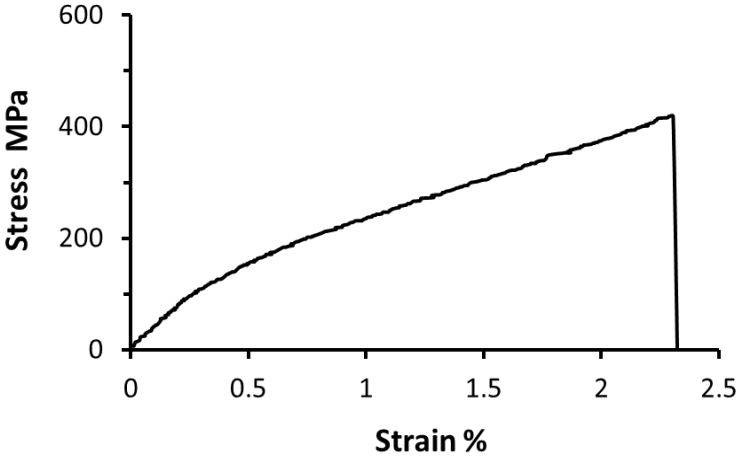

(a)

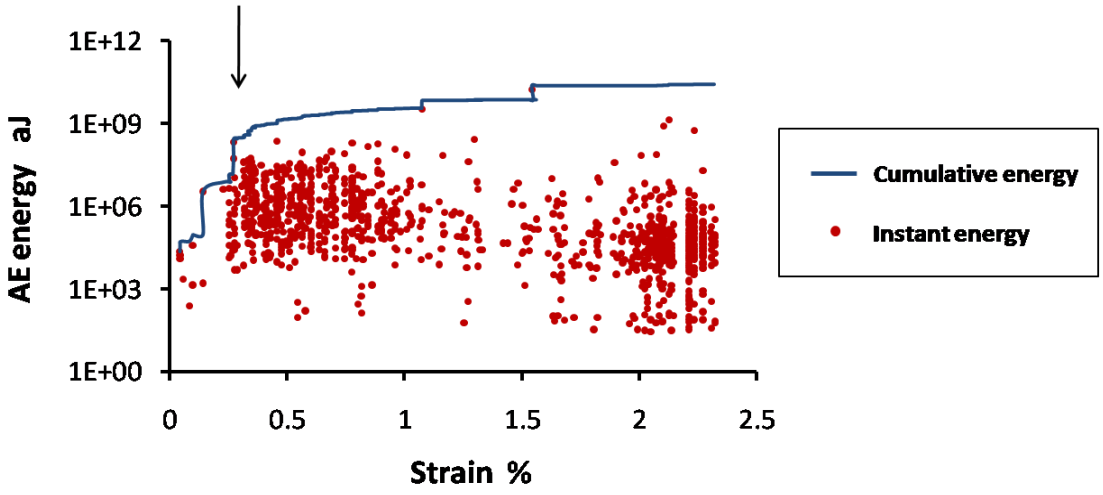

(b)

Fig. 4-13 Typical experimental output for IM7 3D woven composite tested under the warp tension: a) stress-strain curve, b) AE data plot

To identify the cause for this bilinearity of stress-strain response in the warp direction, a number of additional tensile tests were conducted, where a certain degree of damage was introduced to the specimens by loading them in the warp direction until 0.2%, 0.35% or 1% strains were reached. These specimens, along with those tested to final failure, were cut into smaller samples, which were then

polished for microscopic examination using optical microscope. By doing so, internal structures of the material before and after reaching the critical strain level were visually examined, and the damage development in the material was monitored.

The microscopic examination of damaged specimens has proven to be very helpful in showing the evolution of damage. As can be seen in Fig. 4-14, at 0.2% warp direction strain, no visible cracking damage occurred in either the warp curving region or the warp-weft interlacing region, which is consistent with the record of very limited AE events before 0.25% warp direction strain.

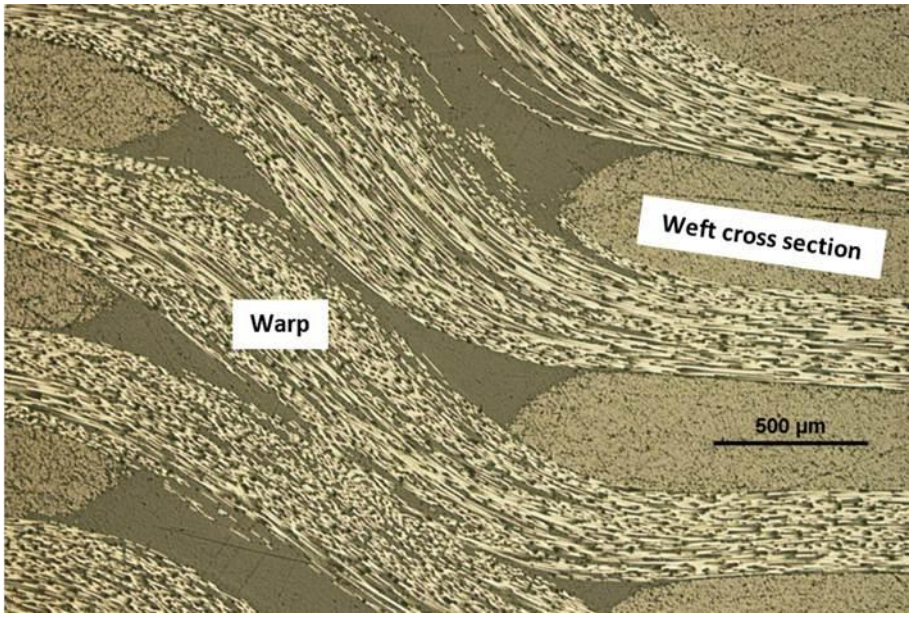

(a)

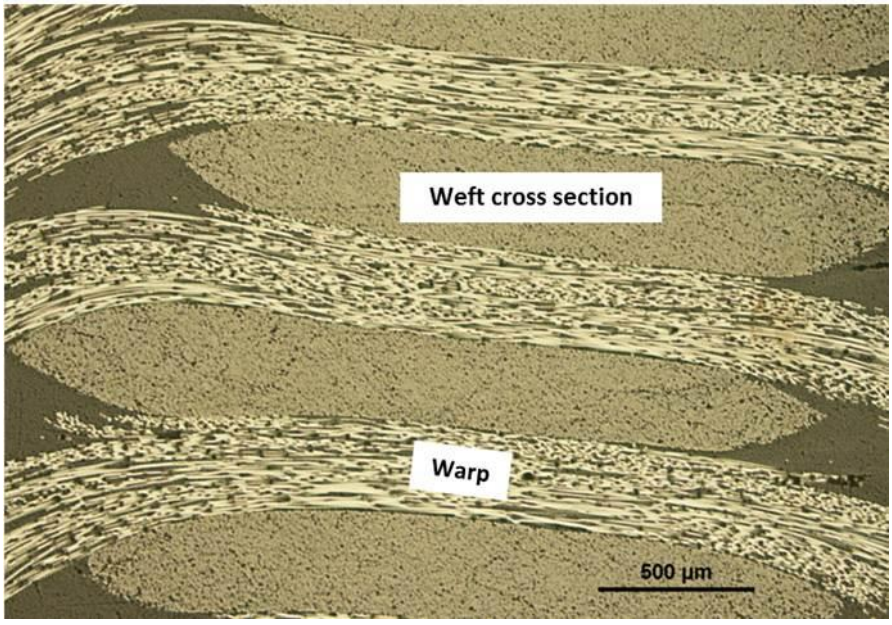

(b)

Fig. 4-14 Typical microscopic images of IM7 CF 3D woven composite loaded to 0.2% warp direction strain: a) at warp curving region, b) at warp-weft interlacing region

However, at 0.35% warp direction strain, inter-tow cracks between warp tows appeared in many of the warp curving regions (Fig. 4-15). No other form of damage was found at this stage. Based on this, considering the sudden increase of AE event occurrence after 0.25% warp direction strain, it was concluded that the initiation and propagation of these inter-tow cracks caused the increase of AE event activity.

Therefore, it was deduced that at around 0.25% warp direction strain, the damage development process progressed from a phase where no obvious cracking was found to a new phase where cracks between warp tows started to occur. This was also reflected by the deviation of stress-strain curve from its initial linear part (Fig. 4-13(a)) and the sharp increase of AE activity (Fig. 4-13(b)).

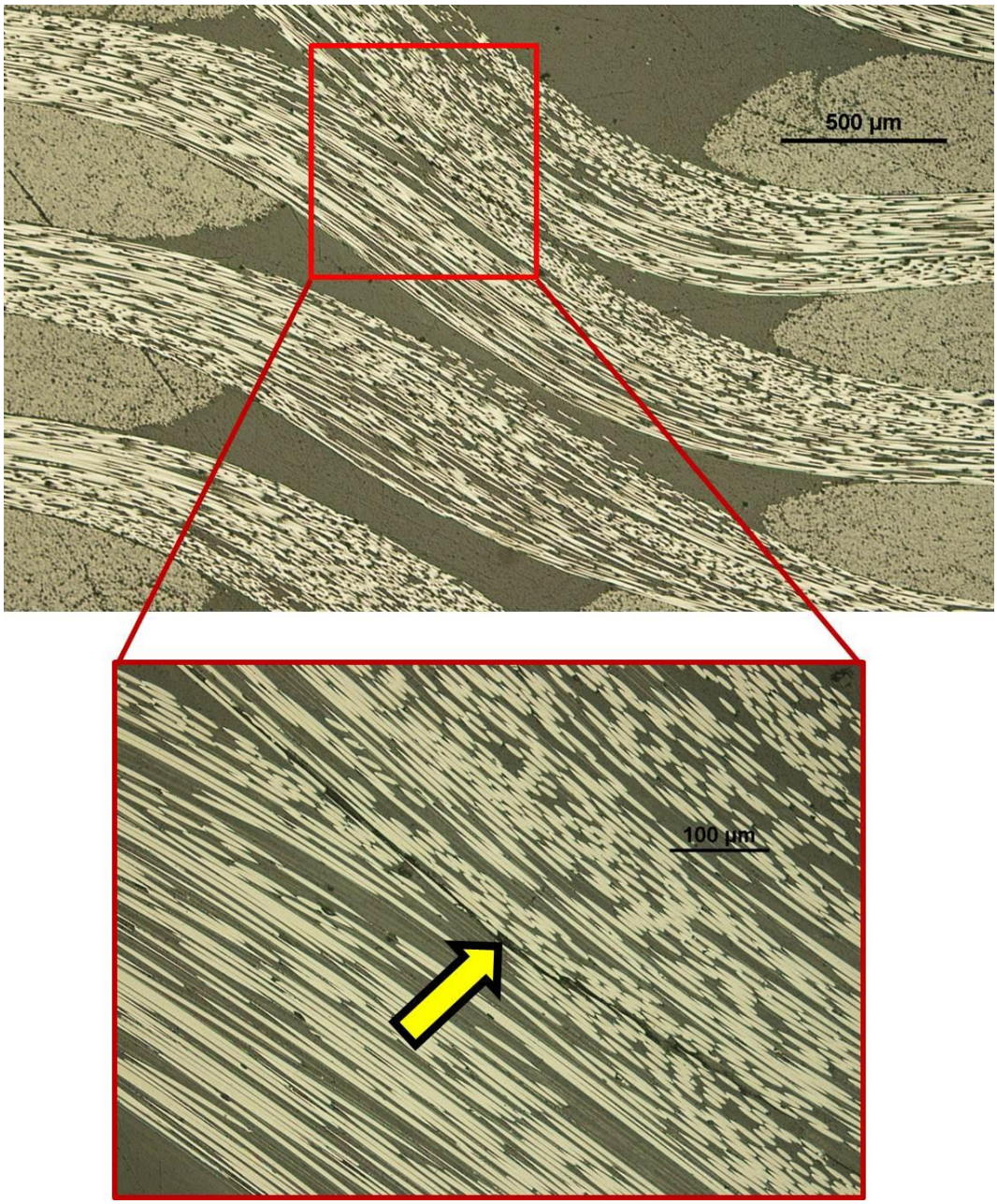

Fig. 4-15 Typical microscopic images of inter-tow cracks in IM7 CF 3D woven composite loaded to 0.35% strain in the warp direction

At 1% warp direction strain, cracking between the warp tows was detected in every warp curving region. Moreover, as shown in Fig. 4-16, not only there were more cracks per warp curving region, but also the cracks appeared to be much wider and longer than those discovered at 0.35% warp direction strain. However, still no other form of damage was found at this strain level.

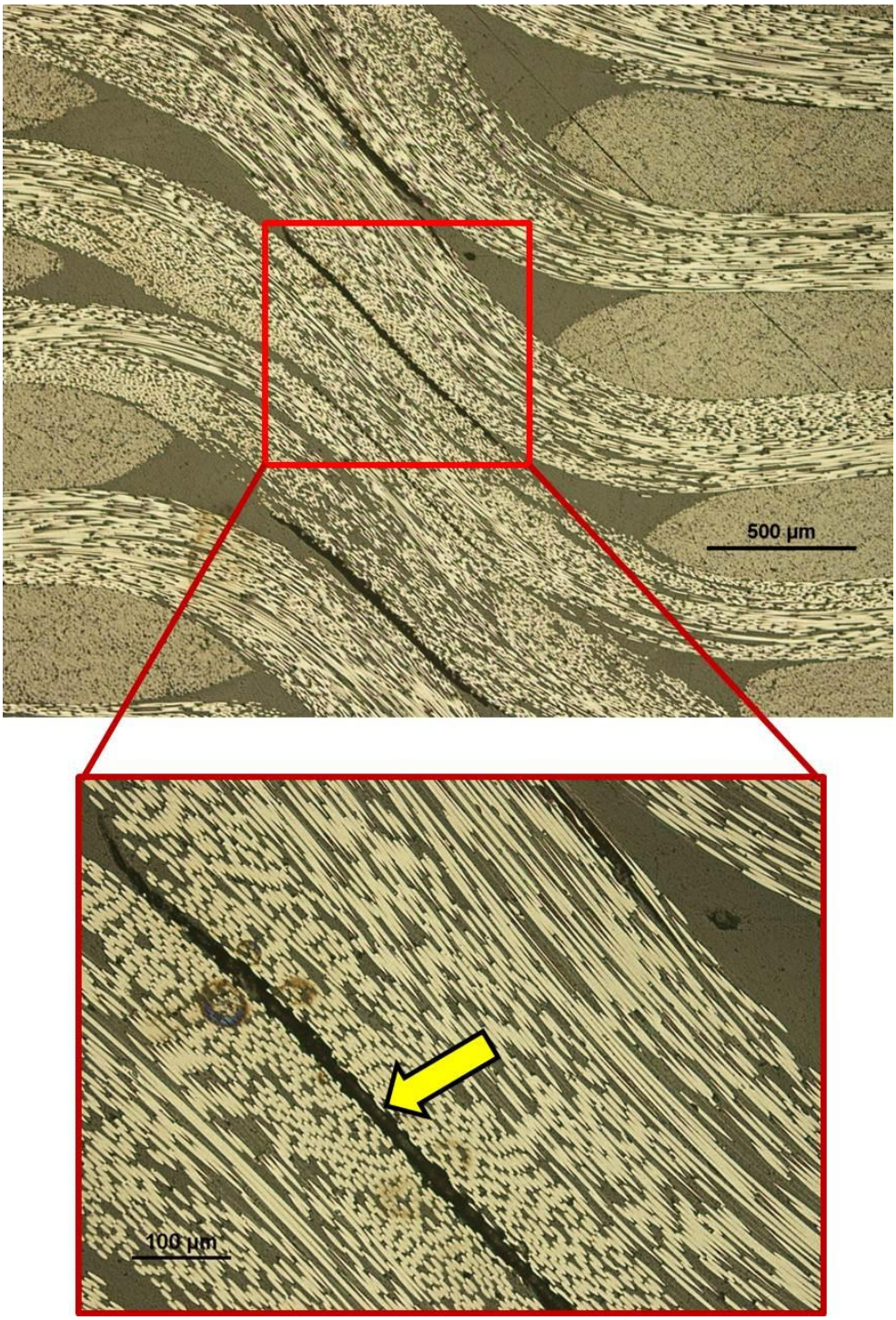

Fig. 4-16 Typical microscopic image of inter-tow cracks in IM7 CF 3D woven composite loaded to 1% warp direction strain

The microscopic images of specimens tested to final failure are shown in Fig. 4-17. As can be seen, some of inter-tow cracks propagated from warp curving

region into warp-weft interlacing region along the boundaries between warp and weft tows, effectively forming new cracks between the warp and the weft tows. In addition to that, warp tow breakage was observed and cracks associated with it were mostly connected to the inter-tow cracks.

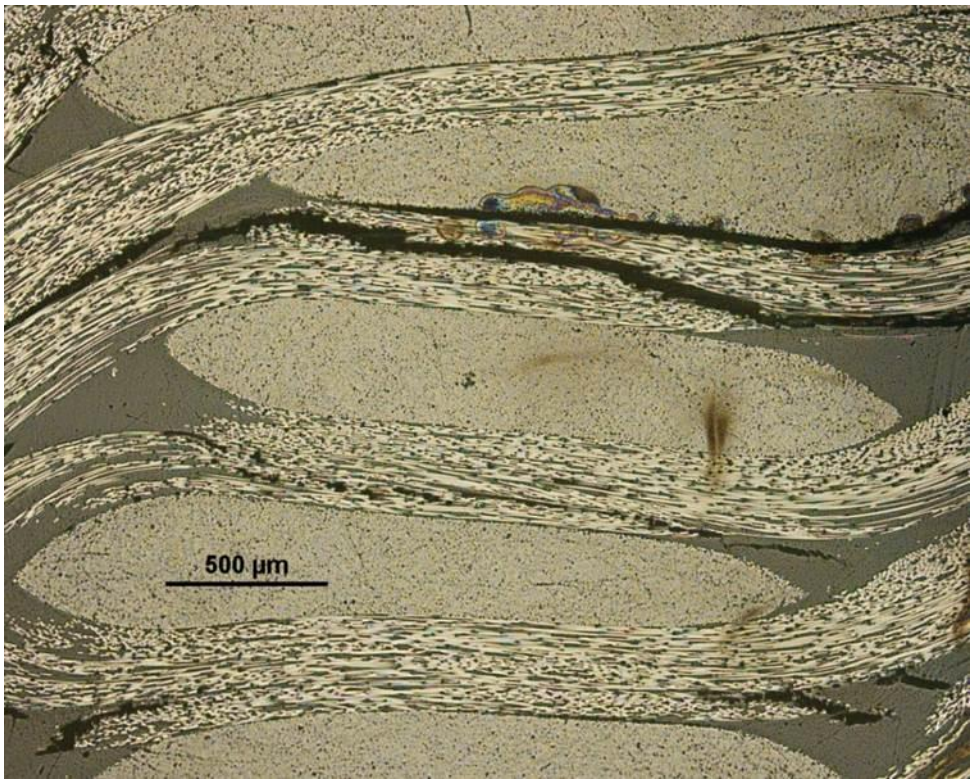

Fig. 4-17 Typical microscopic image of cracks in IM7 CF 3D woven composite loaded to warp direction ultimate strain

Furthermore, warp tow breakage was the failure mechanism led to the final fracture of the specimens as shown in Fig. 4-18.

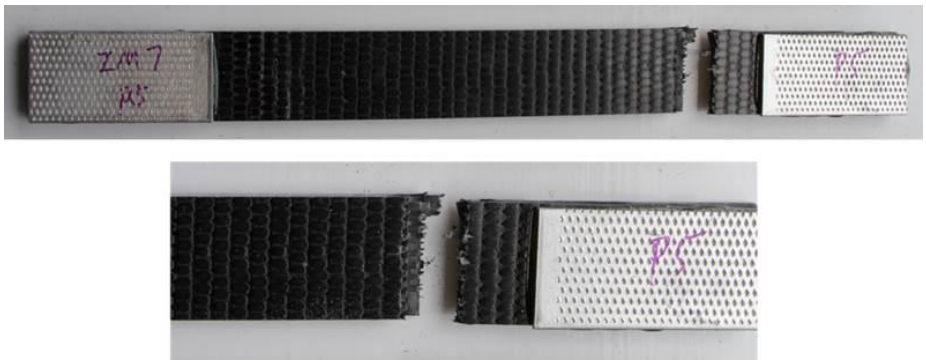

Fig. 4-18 Typical final failure of IM7 CF 3D woven composite tested in warp direction

It can be concluded that under uniaxial tensile loading in the warp direction, the damage development in IM7 CF 3D woven composite started around 0.25% warp direction strain with the formation of inter-tow cracks between warp tows, which are believed to have caused the sharp increase in AE activity and triggered the nonlinearity in the stress-strain curve. More inter-tow cracks appeared and they became wider in the specimens as 1% warp direction strain was reached. Upon final failure, some inter-tow cracks extended into boundaries between the warp and the weft tows. At the same time, warp tow breakage also occurred and led to final fracture of the specimens. Surprisingly, although normally perceived as a common form of damage, intra-tow cracking transverse to the loading direction was not discovered within the weft tows.

4.4.2.2.2 Weft Direction Uniaxial Tensile Test

Unlike the properties in warp direction, the Young's modulus value (62.7 GPa) and strength value (832 MPa) in the weft direction for the IM7 CF 3D woven composite (Table 4-18) were comparable to the Young's modulus value (68.1

GPa) and strength value (805 MPa) of the QI laminates mentioned earlier (Table 4-10).

Table 4-18 IM7 CF 3D woven composite weft direction test result

Property	Mean value	Std. dev.	COV %	Number of tests
Young's modulus (GPa)*	62.7	2.57	4.1	7
Strength (MPa)	832	46.3	5.6	7
Ultimate strain %	1.49	0.373	25	7
Stress at initial nonlinearity (MPa)	463	33.8	7.3	7

* Values were obtained in the strain range of 1000-3000 microstrain

Moreover, the typical stress-strain curve obtained under weft loading (Fig. 4-19(a)) is nearly linear up to the final failure which occurred at a strain of 1.49%. This value of ultimate strain was approximately 1.5 times lower than that in the warp direction. In fact, the stress-strain behaviour observed is qualitatively similar to that of UD composites under tension in longitudinal direction, in terms of high stiffness, low strain to failure and linear elastic response. The explanation to this is as follows. Since the weft tows were straight, combined with the high stiffness and strength values of IM7 carbon fibres, it is believed that under weft direction tension, the linear elastic response from the weft tows should provide the most substantial contribution to the stress-strain response of the entire composite, provided that the fibre volume fraction in the weft direction is sufficiently high.

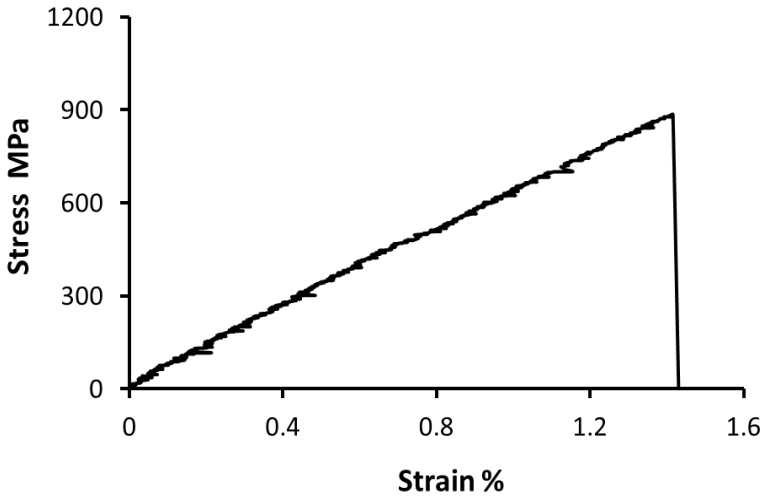

(a)

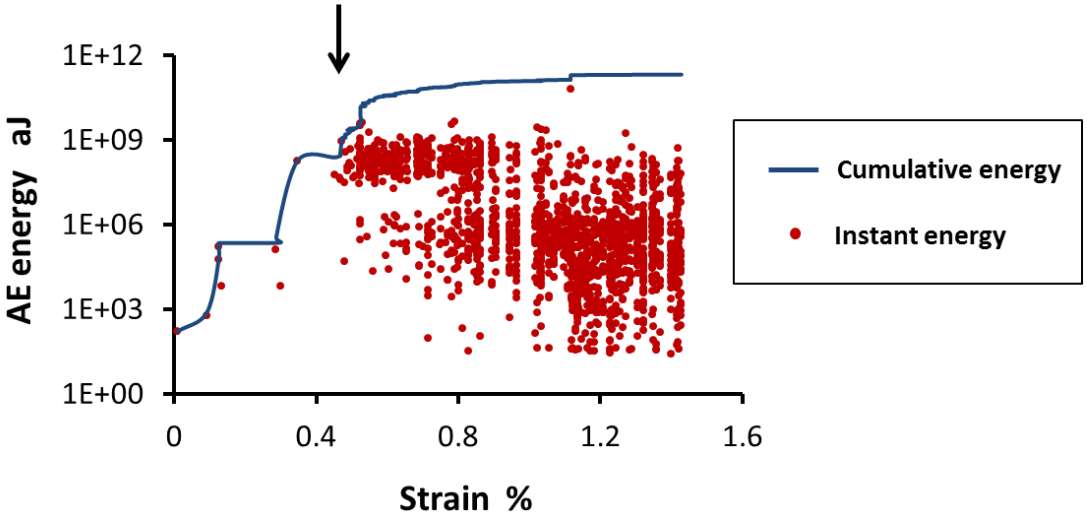

(b)

Fig. 4-19 Typical IM7 CF 3D woven composite weft direction test result: a) Stress-strain curve, b) AE data plot

AE data collected during the test are shown in Fig. 4-19(b). Similar to the previous warp direction testing case, a sudden increase of AE activity was detected, but it took place at a later stage, at approximately 0.5% weft direction strain (indicated by an arrow), which is double the strain value in the warp direction testing case. Another observation to make is that although the AE data plot indicates that damage should occur when the material was loaded beyond

0.5% weft direction strain, this was not reflected in the stress-strain curves, which remained generally linear up to failure.

To investigate damage initiation and evolution under tensile loading in weft direction, microscopic inspection procedure used for the previous warp direction test case was repeated here. The microscopic images of the specimen that was loaded to 0.4% strain is shown in Fig. 4-20. At this strain level, no crack was observed in the specimen, which is consistent with the AE data in Fig. 4-19(b), where only a few AE events were registered below 0.5% weft direction strain.

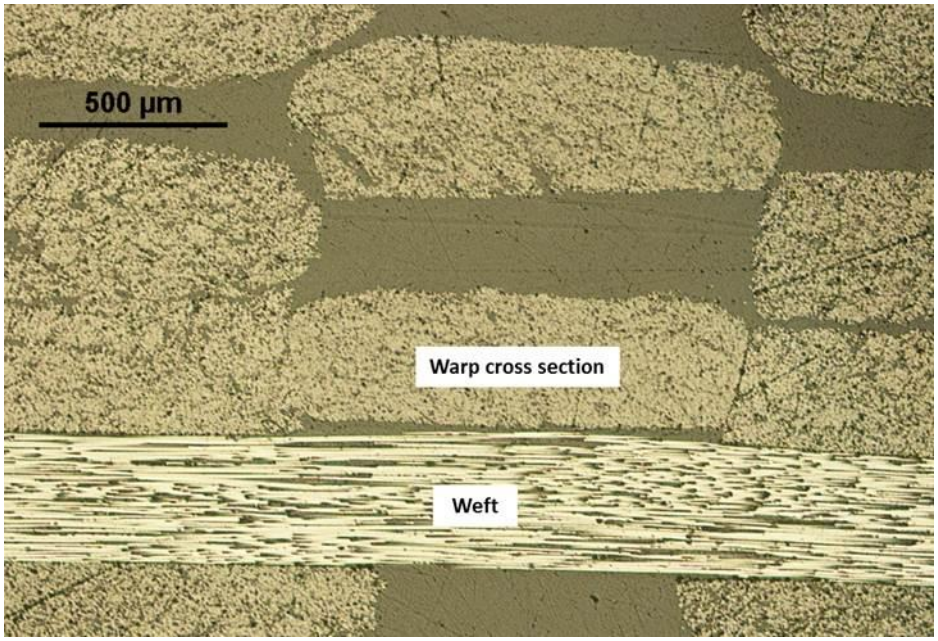

(a)

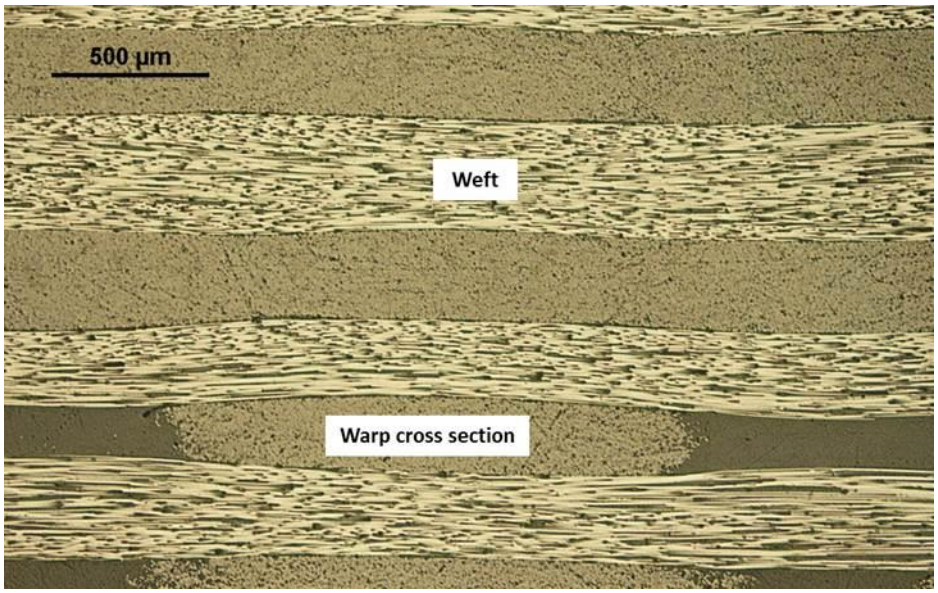

(b)

Fig. 4-20 Typical microscopic images of IM7 CF 3D woven composite loaded to 0.4% weft direction strain: a) warp curving region, b) warp-weft interlacing region

On the other hand, at around 0.7% weft direction strain, cracks transverse to weft direction were discovered in both warp curving and warp-weft interlacing

regions, as shown in Fig. 4-21. These cracks managed to bypass the weft tows to form very long cracks extending across the entire thickness of the specimen. Since no other type of damage was observed, formation of these cracks is believed to be the main cause for increased AE activity beyond 0.5% weft direction strain.

However, it is difficult to tell whether these were inter-tow or intra-tow cracks because a single lengthy crack could appear on warp tow boundary as well as cutting through warp tow cross sections like the one captured in Fig. 4-21(a). To make matters worse, the boundaries of warp tows can be barely seen in the warp-weft interlacing regions since the warp tows were so densely packed together (Fig. 4-21(b)). Nonetheless, at this stage, all the cracks were oriented transverse to the weft direction (loading direction), meaning that they were probably caused by transverse tension due to the applied weft direction loading.

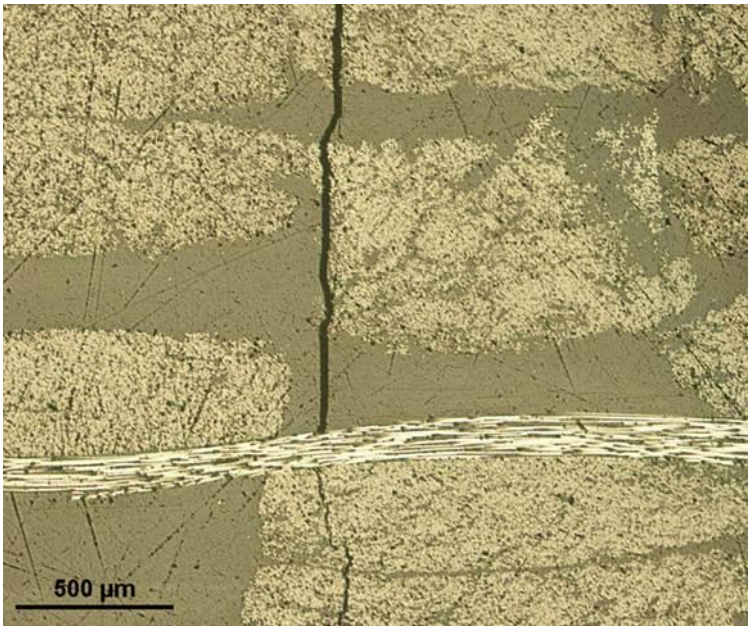

(a)

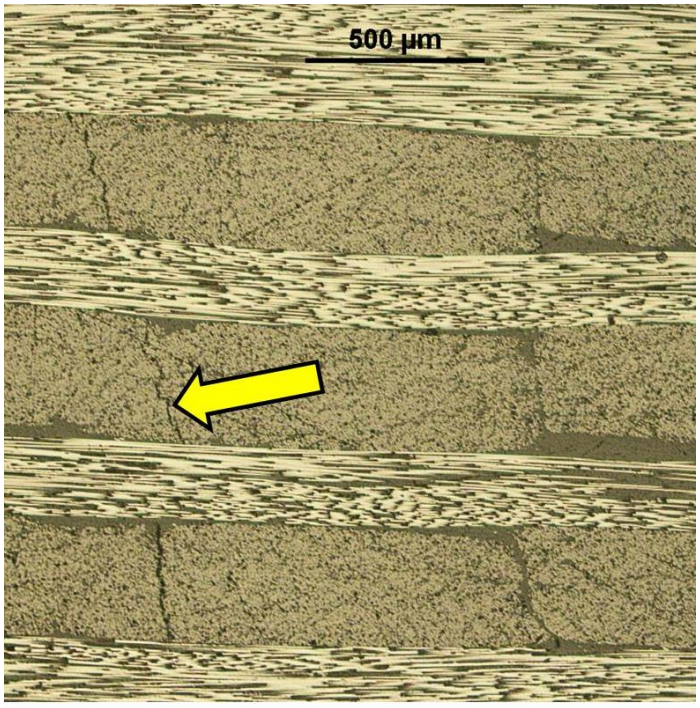

(b)

Fig. 4-21 Typical microscopic images of transverse cracks in IM7 CF 3D woven composite loaded to 0.7% weft direction strain: a) warp curving region, b) warp-weft interlacing region

At ultimate strain, more through-the-thickness transverse cracks appeared and a significant increase in crack density can be seen (Fig. 4-22). In addition to that, new inter-tow cracks parallel to the weft tows were formed as some of the through-the-thickness cracks branched and propagated into boundaries between warp and weft tows (Fig. 4-22(b)).

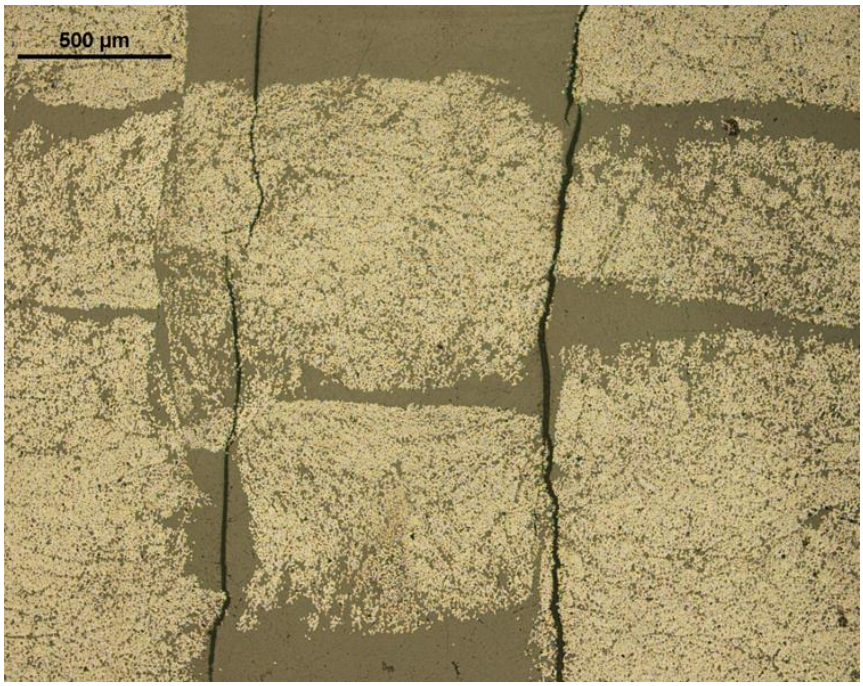

(a)

(b)

Fig. 4-22 Typical microscopic images of cracks in IM7 CF 3D woven composite loaded to weft direction ultimate strain: a) warp curving region, b) warp-weft interlacing region

Summarising the observations made, it can be concluded that for the specimens tested in the weft direction, damage initiated at 0.5% strain in the form of through-the-thickness transverse cracks. Further loading caused an increase in number of these cracks, some of which propagated into boundaries between warp and weft tows. In terms of final failure, typical final fracture of the specimens is shown in Fig. 4-23, where weft tow breakage can be clearly seen.

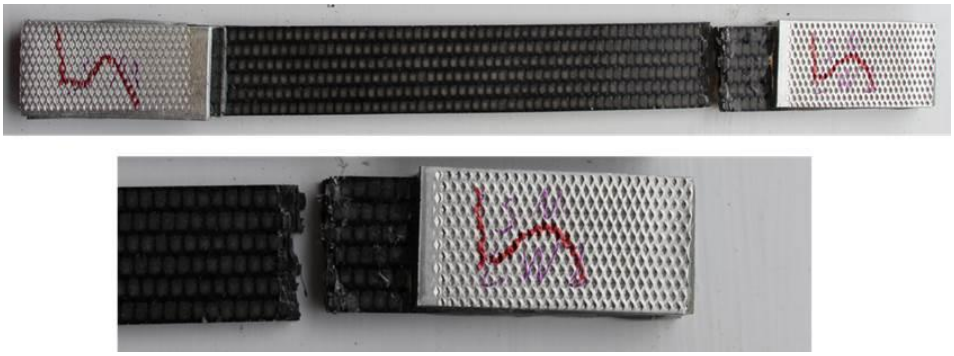

Fig. 4-23 Typical final failure of IM7 CF 3D woven composite tested in weft direction

The experimental investigation presented here has confirmed that damage did indeed occur in the specimens tested in the weft direction, even though the recorded stress-strain response remained linear until final failure. The possible explanation for this is as follows. Although the damage occurred in the form of transverse cracks spanning across the specimen thickness, but these cracks bypassed the weft tows which remained intact until the final failure. Because of the high longitudinal stiffness and strength of weft tows, their contribution was high enough to dominate the weft direction stress-strain response of the entire 3D woven composites, such that the damage effect from the transverse cracks became negligible.

In contrast, although warp tows remained intact up to the final failure for the specimens loaded in the warp direction (Section 4.4.2.2.1), because of crimps in the warp tows, those specimens were more compliant, hence the contribution of damage was more significant as the stress-strain response became nonlinear due to the inter-tow cracks between the warp tows.

4.4.2.2.3 ASTM D3518 In-plane Shear Test

Similar to the aforementioned case for laminates, with the specimens made to have warp and weft tows at a 45º offset from the loading direction in the XY plane, in-plane shear testing for 3D woven composites was conducted.

For the same reason stated in Section 4.3.3.3 concerning the limitations of the video strain gauge, no specimens were tested to final failure. The properties measured in the tests were shear modulus and 0.2% offset shear strength as specified in Table 4-19. Their values were lower than those of IM7 CF UD laminates (Table 4-8). Since both kinds of composites were based on the same type of fibre reinforcement material, it is envisaged that the lower shear modulus and strength in the woven composites might be due to its lower total fibre volume fraction and differences in the epoxy resin systems used.

Table 4-19 IM7 CF 3D woven composite in-plane shear test result

Property	Mean value	Std. dev.	COV %	Number of tests
Shear modulus (GPa)*	3.92	0.173	4.4	7
0.2% offset shear strength (MPa)	42.6	1.62	3.8	7

* Values were obtained in engineering shear strain range of 2000-6000 microstrain

The general trend of in-plane shear stress-strain curve for the IM7 CF 3D woven composite (Fig. 4-24) was very similar to that of UD laminates (Fig. 4-5).

Moreover, both of them had reached their 0.2% offset shear strengths at an engineering shear strain just beyond 1%.

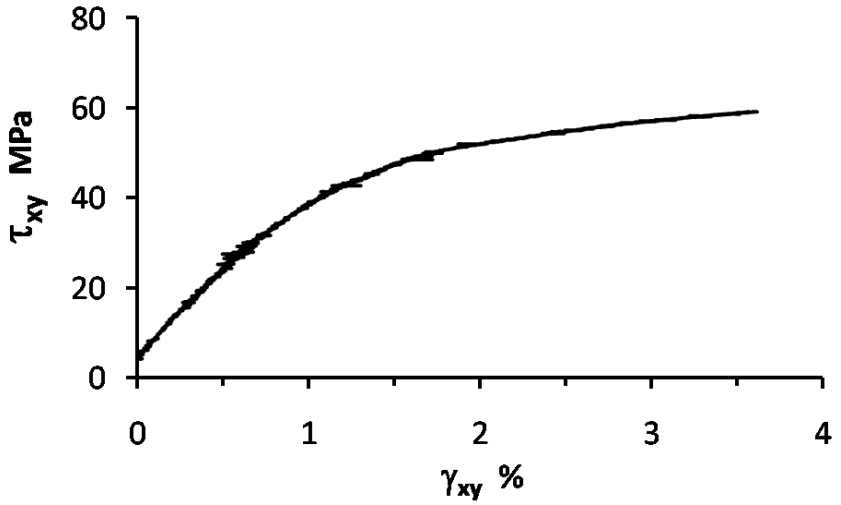

Fig. 4-24 Typical in-plane shear test stress-strain curve of IM7 CF 3D woven composite

As shown in Fig. 4-25, unlike shear specimens of laminated composites, 3D woven CF composite suffered very obvious local deformations for the fibre tows. It was also observed during tests that while the tows deformed locally, the matrix material surrounding the tows fractured and very small fragments of it detached from the specimens. This offers an explanation for the visible cross-sectional shrinkage in the middle of the specimens, namely, the tows tend to deform and align in the loading direction when the matrix material between them is eroded.

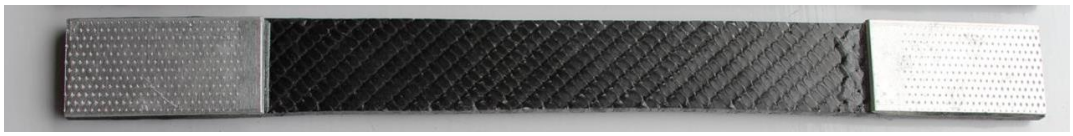

Fig. 4-25 Typical deformation of IM7 CF 3D woven composite under in-plane shear

4.4.3 3D Woven Composite Reinforced by E-glass Fibre

4.4.3.1 Material Properties and Structure of the Weave

Another type of 3D woven composite tested were layer-to-layer angle interlock composite with glass fibre woven reinforcement. This composite had the same type of weave pattern and matrix material as the IM7 CF 3D woven composite, but with slightly higher weft-to-warp ratio and higher warp weaving angle, as specified in Table 4-20. The material properties of the E-glass fibre tows used are summarised in Table 4-21.

The purpose of testing on this type of 3D woven composite was to investigate to what extent different materials of reinforcement can affect the mechanical properties and the damage development process in the 3D woven composites.

Table 4-20 General information of GF 3D woven composite [192]

Weave pattern	Layer-to-layer interlock (Fig. 4-26 - Fig. 4-28)
Reinforcement type	E-glass (75 tex)
Matrix material type	Gurit Prime™ 20LV epoxy resin
Weft to warp ratio (By weight per cm)	0.651
Number of weft tow layers	6
Dry fabric areal weight (kg/m^2)	5.68 ± 0.09
Total fibre volume fraction (%)	$50.2\% \pm 0.8\%$

Table 4-21 Sinoma® E-glass fibre tow (75 tex) material properties [195]

Tensile modulus (GPa)	73
Tensile strength (MPa)	3140
Ultimate tensile failure strain	4.8%

To ensure that the thickness and total fibre volume fraction in the GF 3D woven composite are similar to those in the IM7 CF 3D woven composite, the former had six layers of weft tows, which is one layer less than the latter. The cured GF 3D woven composite were also subjected to CT scan and the images are presented in Fig. 4-26, Fig. 4-27 and Fig. 4-28.

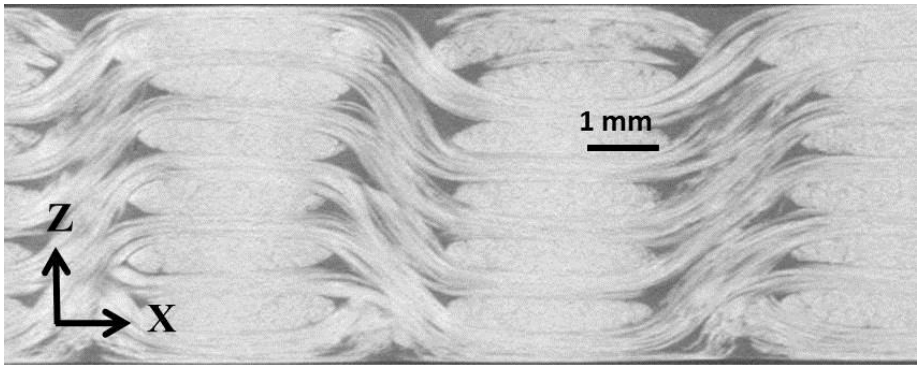

Fig. 4-26 *XZ*-plane CT scan image of cured GF 3D woven composite

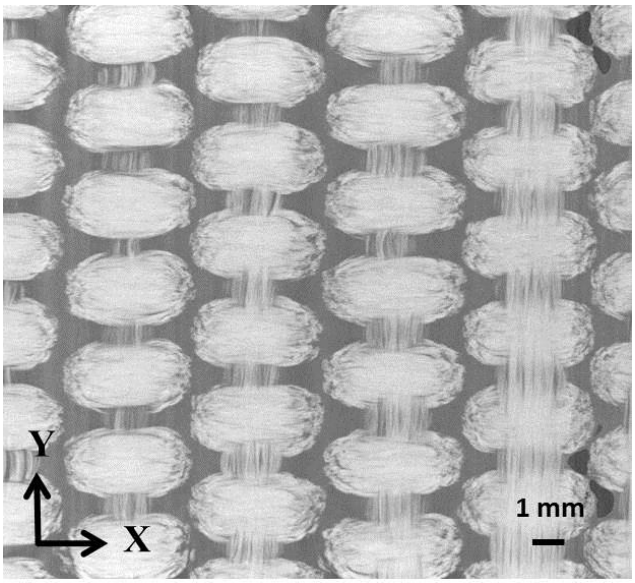

Fig. 4-27 *XY*-plane CT scan image of cured GF 3D woven composite

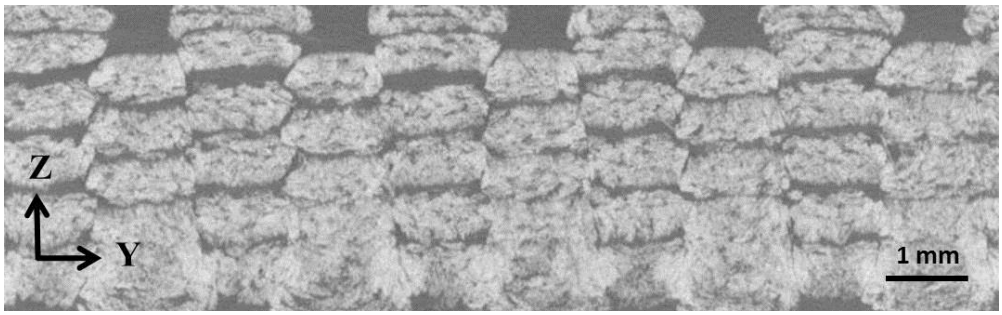

(a)

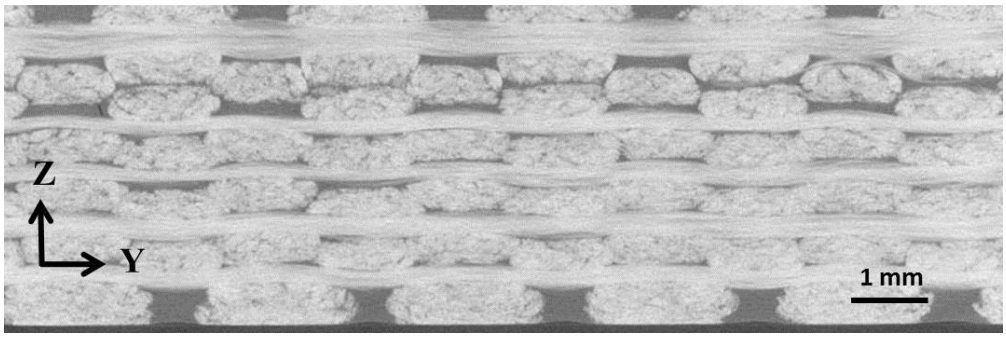

(b)

Fig. 4-28 *YZ*-plane CT scan images of cured GF 3D woven composite: a) warp curving region, b) warp-weft interlacing region

Table 4-22 Weave pattern geometries of cured GF 3D woven composite

Warp tow weaving angle	4.35±0.3º
Warp tow width	1.31±0.1 mm
Warp tow thickness	0.37±0.15 mm
Weft tow space	4.35±0.3 mm
Weft tow width	2.48±0.2 mm
Weft tow thickness	0.42±0.06 mm

4.4.3.2 Results and Discussion

4.4.3.2.1 Warp Direction Uniaxial Tensile Test

The first type of experiments conducted was a tensile test, where the warp tows in the specimens were aligned in the loading directions. The properties measured are summarised in Table 4-23. Comparing them with properties of IM7 CF 3D woven composite in Table 4-17, it can be seen that the Young's modulus and the strength of GF 3D woven composite in the warp direction are substantially lower. Since both types of composites had the same epoxy resin system, similar total fibre volume fractions and the same weave pattern, it is believed that the lower properties of GF composite were mainly caused by the inherent lower Young's modulus and strength values of its E-glass fibre reinforcements (Table 4-21).

Table 4-23 GF 3D woven composite warp direction test result

Property	Mean value	Std. dev.	COV %	Number of tests
Young's modulus (GPa)*	21.8	0.762	3.5	7
Strength (MPa)	213	13.6	6.4	7
Ultimate strain %	2.05	0.311	15	7
Stress at initial nonlinearity (MPa)	81.3	4.15	5.1	7

* Values were obtained in the strain range of 500-2500 microstrain

Typical stress-strain curve recorded during the experiment is shown in Fig. 4-29(a). Comparing it with the stress-strain response of IM7 CF 3D woven composite (Fig. 4-13(a)), it can be seen that, qualitatively, the responses of the two composites are similar.

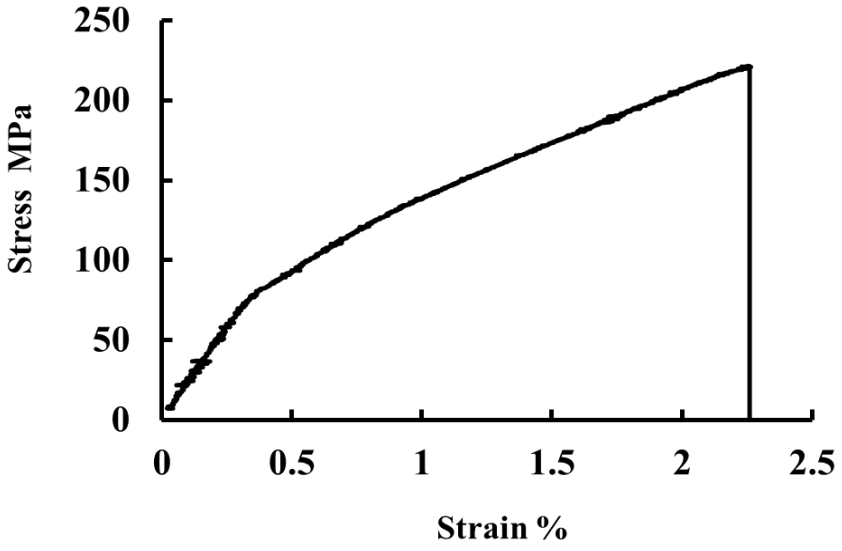

(a)

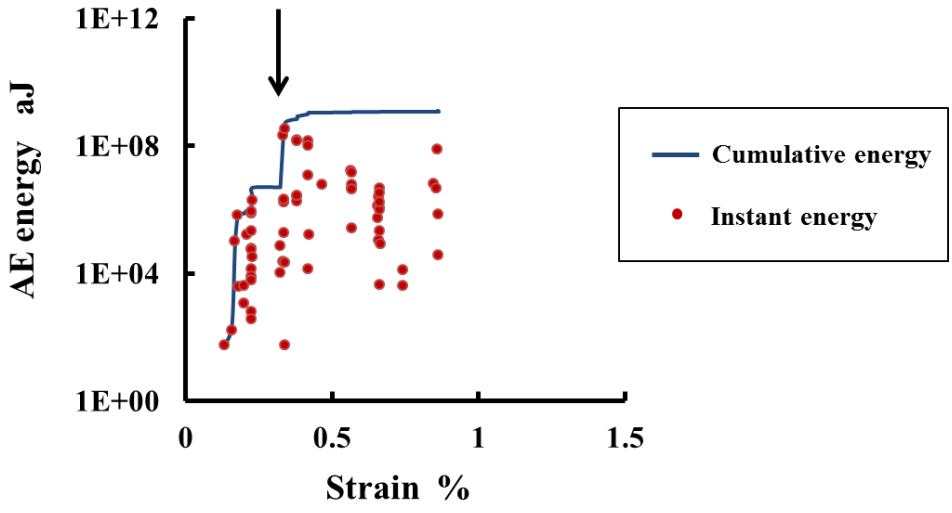

(b)

Fig. 4-29 Typical GF 3D woven composite warp direction test result: a) Stress-strain curve, b) AE data plot

The AE data collected in the same experiment are shown in Fig. 4-29(b). A step increase in cumulative energy was observed at 0.35% warp direction strain (indicated by an arrow), which corresponds to the onset of nonlinearity in the stress-strain curve. Similar correlation was also observed for the IM7 CF 3D woven composite tested under warp direction tension as shown previously in Fig. 4-13. However, comparing the AE plots of the two composites, it is noticeable

that while a substantial amount of AE events were registered for the GF composite before the onset of stress-strain nonlinearity, only limited AE activity was registered for the IM7 CF composite before such a point. To identify the cause for this phenomenon, samples of specimens subjected to different extent of damage were examined under the microscope, following the same procedure as mentioned previously in Section 4.4.2.2.1.

The internal structure of the specimen that was loaded to 0.25% warp direction strain is shown in Fig. 4-30. As can be seen, numerous intra-tow cracks formed in the weft tows. At this strain level, the strain-stress response was still linear, but substantial amount of AE events were captured. Since no other type of damage was observed at this stage, the intra-tow cracks were considered to be responsible for causing the substantial AE events before the onset of nonlinearity at 0.35% warp direction strain as shown in Fig. 4-29.

In contrast, as mentioned in Section 4.4.2.2.1, no damage was found before the onset of stress-strain nonlinearity for the IM7 CF 3D woven composite tested in warp direction. This suggests a marked difference in terms of damage development for the GF and CF 3D woven composites tested. Moreover, cracking of the weft tows in the GF composite did not seem to affect the stress-strain response, which remained linear until 0.35% warp direction strain. This indicates that the stiffness reduction due to intra-tow cracks was rather insignificant as it was not reflected on the stress-strain curve.

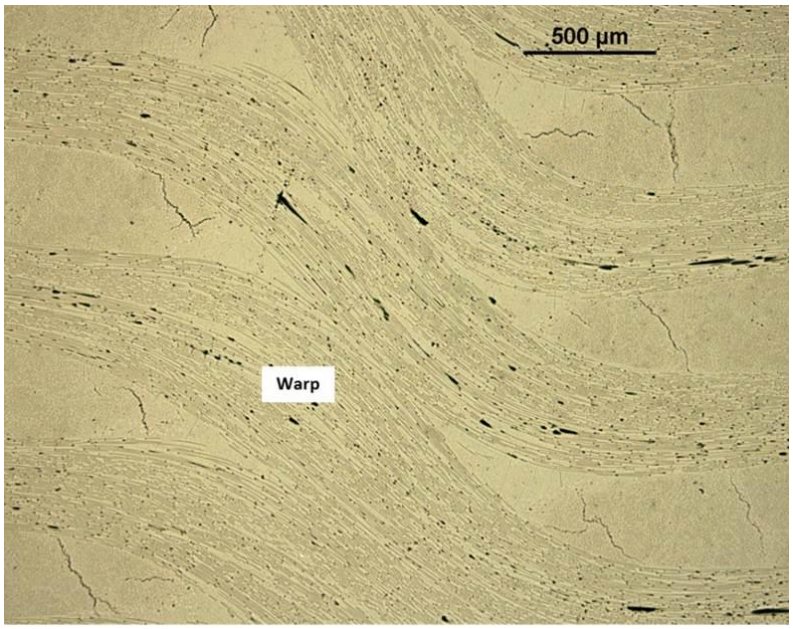

(a)

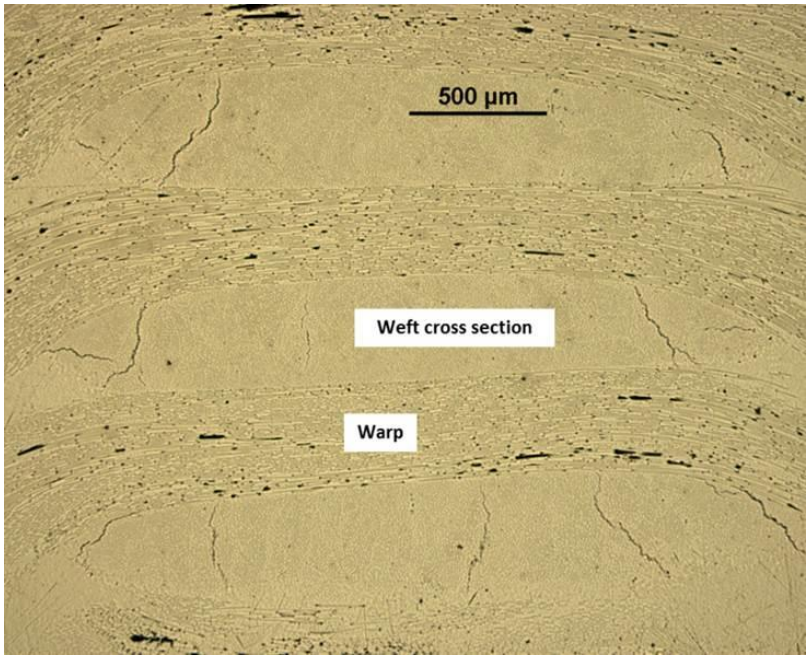

(b)

Fig. 4-30 Typical microscopic images of intra-tow cracks in GF 3D woven composite loaded to 0.25% warp direction strain: a) warp curving region, b) warp-weft interlacing region

The internal structure of the specimens loaded to 0.47% strain, which is beyond the nonlinearity onset strain, is shown in Fig. 4-31. As can be seen, at this strain

level, in addition to the intra-tow cracks, inter-tow cracks between warp tows had developed. Some of them even connected to the existing intra-tow cracks as shown in Fig. 4-31(b). These inter-tow cracks were very similar to those discovered in the samples of IM7 CF 3D woven composite tested under warp direction tension.

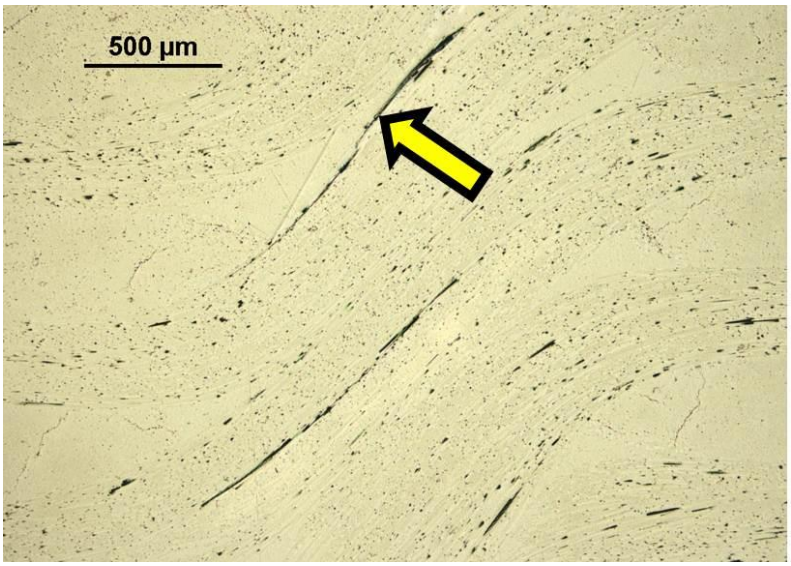

(a)

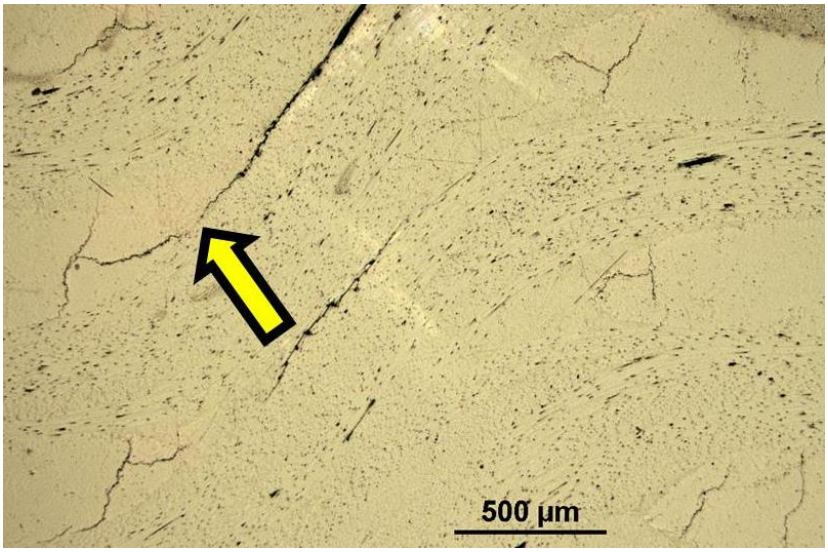

(b)

Fig. 4-31 Typical microscopic images of cracks in GF 3D woven composite loaded to 0.47% warp direction strain

Furthermore, when the GF 3D woven composite specimens were loaded to the warp direction ultimate failure (Fig. 4-32), these inter-tow cracks became longer and wider, which is again similar to what was observed in the damaged IM7 CF 3D woven composite specimens. As shown in Fig. 4-33, the final failure of the GF 3D woven composite was due to fracture of the warp tows.

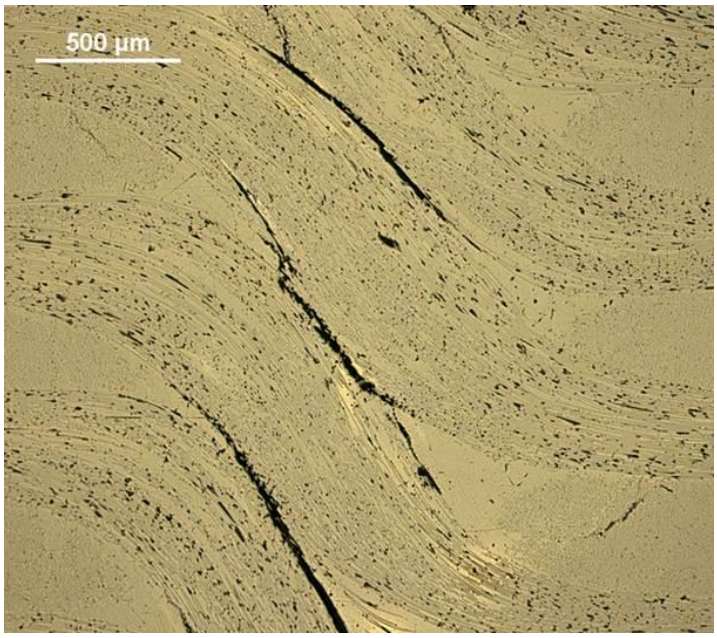

(a)

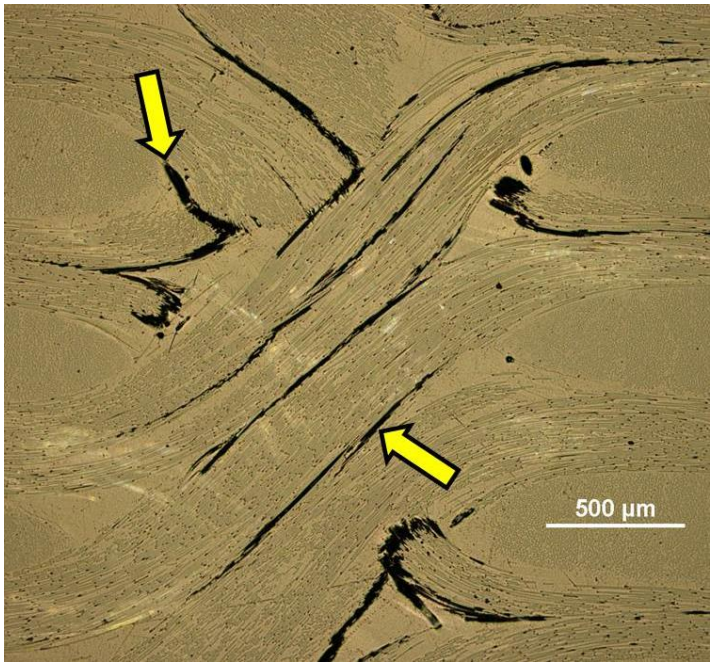

(b)

Fig. 4-32 Typical microscopic images of cracks in GF 3D woven composite loaded to warp direction ultimate strain

Fig. 4-33 Typical final failure of GF 3D woven composite tested in warp direction

It is worth noting that, after the emergence of inter-tow cracks, there seemed to be no visible increase in crack density for the intra-tow cracks. This suggests that the effect of inter-tow cracks in GF 3D woven composite is no different from that in the IM7 CF 3D woven composite. Specifically, it is believed that the inter-tow cracks, rather than the intra-tow cracks, triggered the stress-strain nonlinearity in Fig. 4-29(a) and contributed to the step increase of AE activity in Fig. 4-29(b).

It can be concluded that the damage development process in GF 3D woven composite under warp direction tensile stress was very similar to that in IM7 CF 3D woven composite. The only new form of damage observed was the intra-tow cracks in the weft tows.

4.4.3.2.2 Weft Direction Uniaxial Tensile Test

The weft direction properties of GF 3D woven composite are listed in Table 4-24. Similar to the warp direction tension case, the weft direction Young's modulus and strength (Table 4-24) are substantially lower than those of the IM7 CF 3D

woven composite (Table 4-18). The explanation for this was already given in the previous section.

Table 4-24 GF 3D woven composite weft direction test result

Property	Mean value	Std. dev.	COV %	Number of tests
Young's modulus (GPa)*	25.7	1.45	5.6	7
Strength (MPa)	337	32.6	9.7	7
Ultimate strain %	1.85	0.299	16	7
Stress at initial nonlinearity (MPa)	94.4	8.72	9.2	7

* Values were obtained in the strain range of 500-2500 microstrain

It is worth noting that for the GF 3D woven composite the Young's modulus in the weft direction is only 18% higher than that in the warp direction, although a marked improvement (58%) can be seen in terms of strength. For the low Young's modulus value, this again is likely to be due to the effect from the inherently low stiffness of E-glass fibre. Because of the low stiffness of glass fibres, even when the straight weft tows were aligned in the loading direction, the improvement to the specimen level weft direction Young's modulus was still not apparent.

Alternatively, one may arrive at the argument that the stress-strain response in 3D woven composites with fibre constituent of low stiffness is less sensitive to the variation of warp weaving angle. Such argument can be further supported by comparing the Young's modulus value of E-glass fibre tow to that of IM7 carbon fibre tow. The longitudinal Young's modulus of IM7 carbon fibre tow, 276 GPa (Table 4-14), is almost four times of that of E-glass fibre tow, 73 GPa (Table 4-21). Consequently, as seen here, having E-glass fibres rather than IM7 carbon

fibres aligned in the loading direction would have much less influence on the weft direction Young's modulus.

In contrast to its carbon fibre counterpart, GF 3D woven composite demonstrated a bilinear curve trend for its weft direction stress-strain response (Fig. 4-34(a)), with the onset of stress-strain nonlinearity correlating well with the sudden increase of cumulative AE energy (Fig. 4-34 (b)).

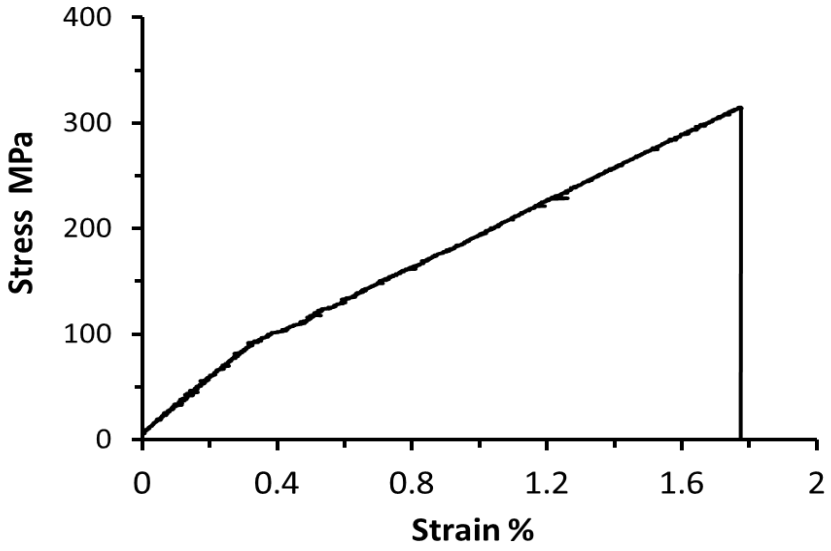

(a)

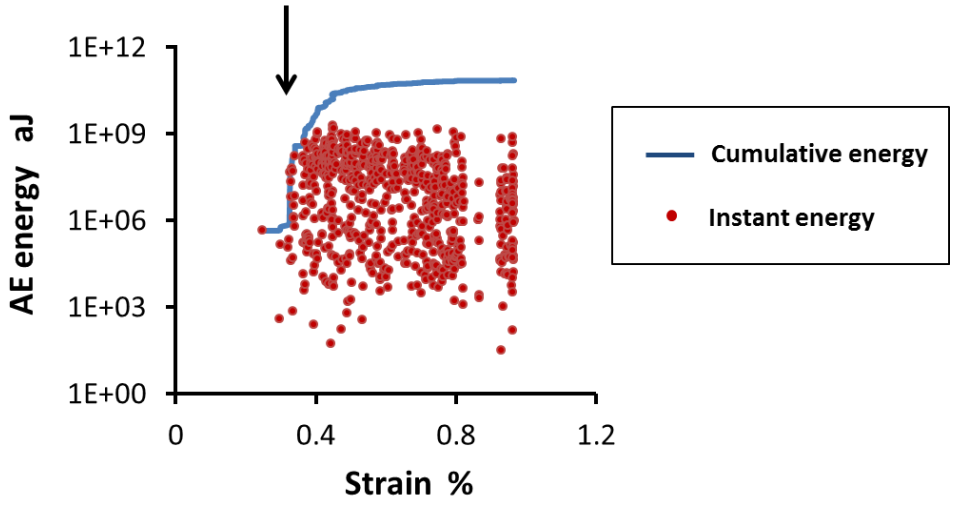

(b)

Fig. 4-34 Typical GF 3D woven composite weft direction test result: a) Stress-strain curve, b) AE data plot

In terms of microscopic inspection, the internal damage in the GF 3D woven composite specimens loaded to 0.23%, 0.43% and ultimate failure strains can be seen in Fig. 4-35, Fig. 4-36 and Fig. 4-37. Comparing to the internal damage observed in IM7 CF 3D woven composite tested in the weft direction (Fig. 4-20 - Fig. 4-22), it becomes apparent that both types of composites had a very similar damage development process when loaded in the weft direction. The only difference observed was the higher crack density at the ultimate strain level in the GF composite.

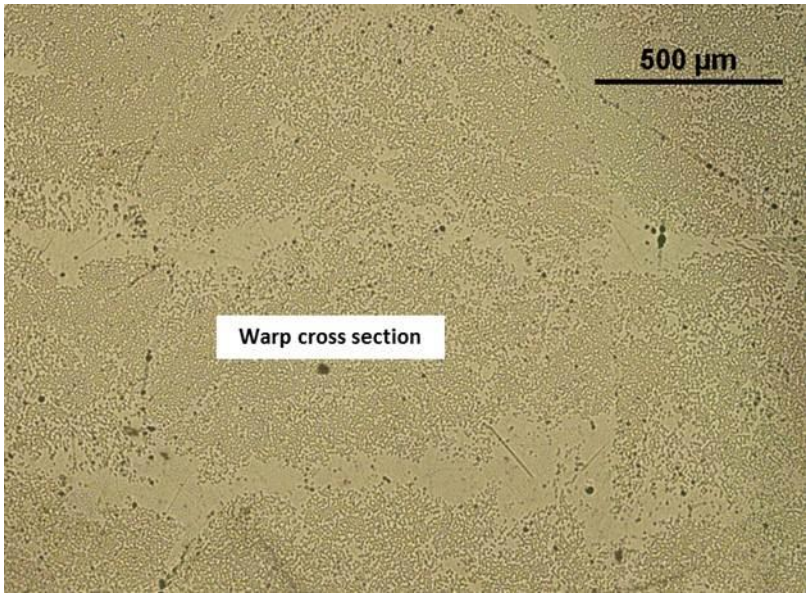

(a)

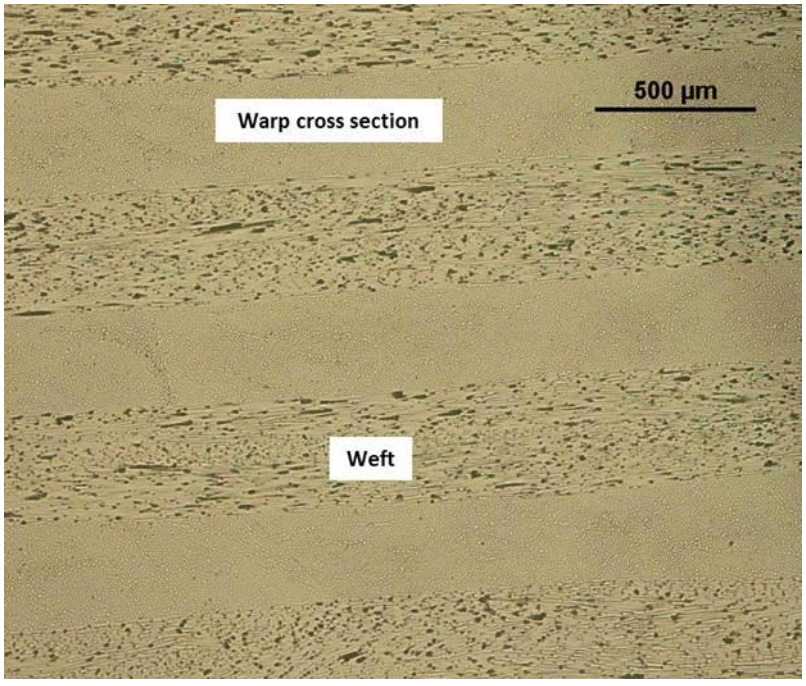

(b)

Fig. 4-35 Typical microscopic images of GF 3D woven composite loaded to 0.23% weft direction strain: a) warp curving region, b) warp-weft interlacing region

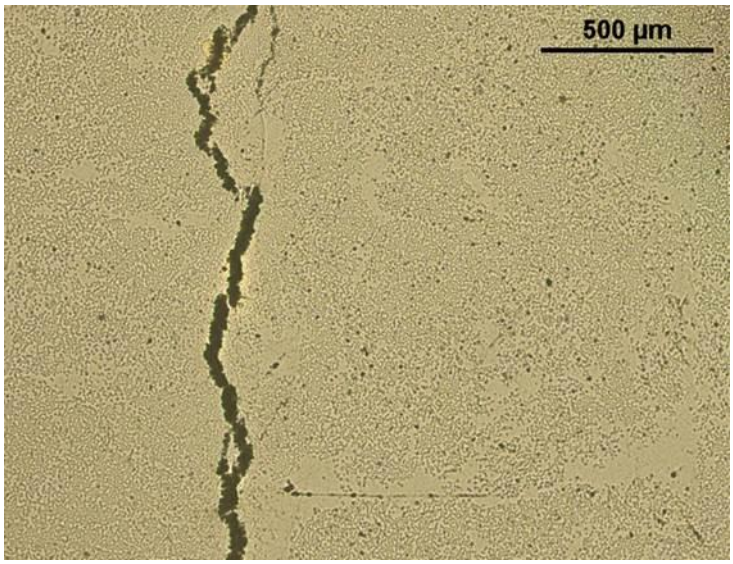

(a)

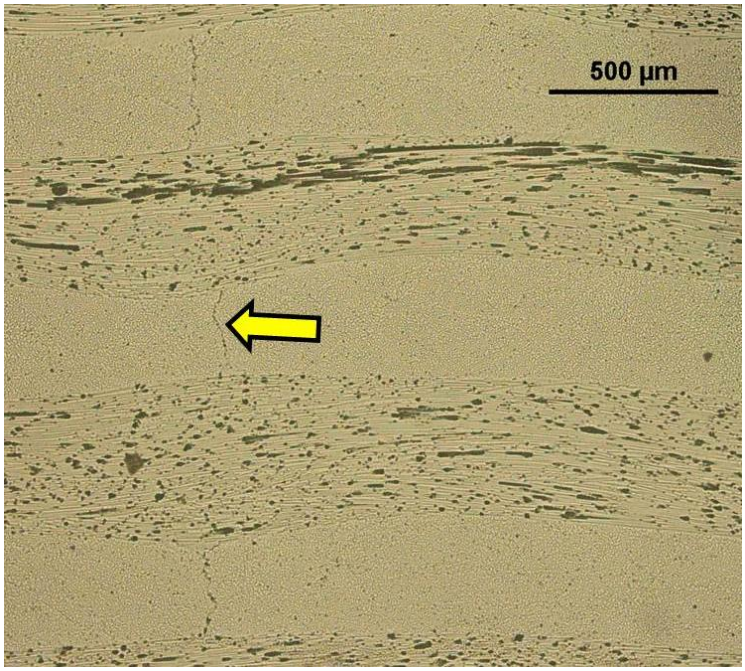

(b)

Fig. 4-36 Typical microscopic images of transverse cracks in GF 3D woven composite loaded to 0.43% weft direction strain: a) warp curving region, b) warp-weft interlacing region

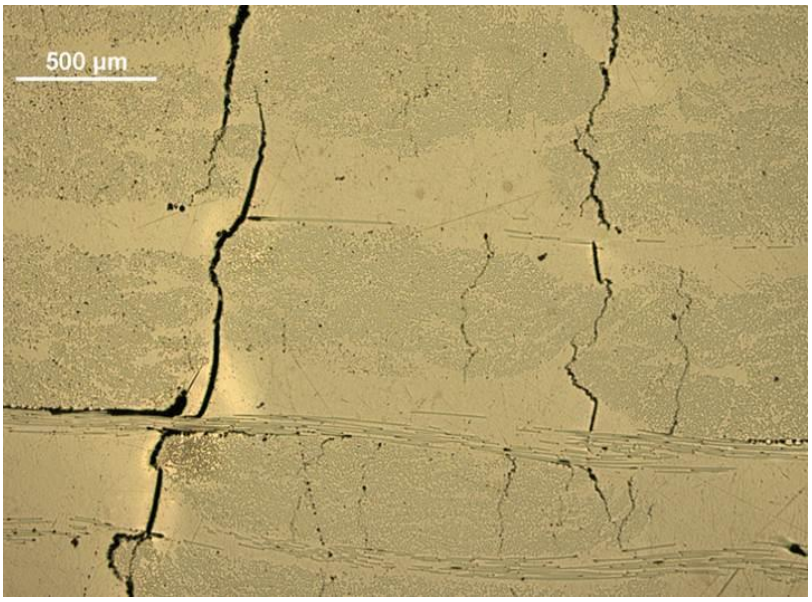

(a)

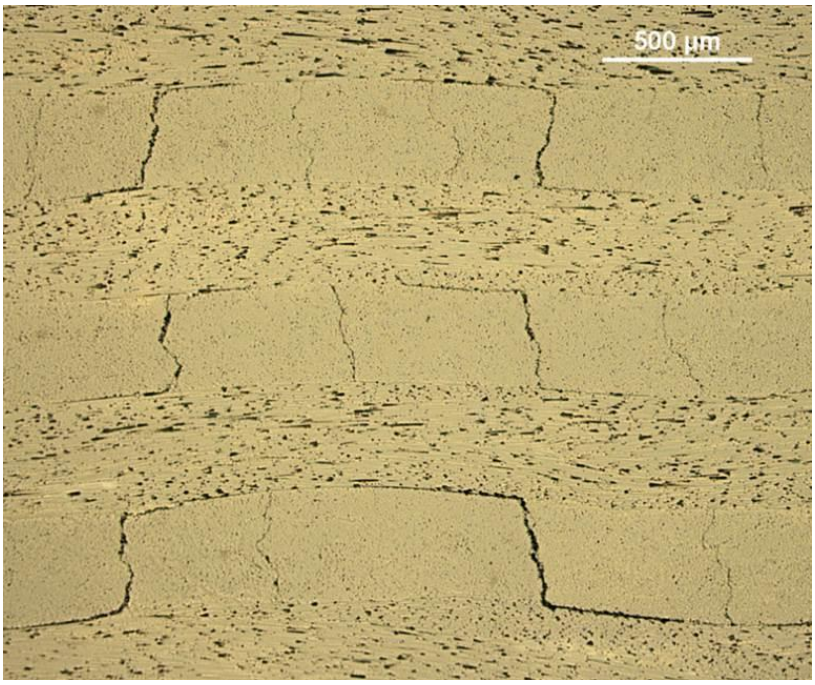

(b)

Fig. 4-37 Typical microscopic images of cracks in GF 3D woven composite loaded to weft direction ultimate strain: a) warp curving region, b) warp-weft interlacing region

With the damage process identified, it is clear that the stress-strain nonlinearity was caused by the through-the-thickness cracks. However, recall the argument

presented in Section 4.4.2.2.2 stating that for the IM7 CF 3D woven composite the linear stress-strain response under weft loading was due to the high stiffness of the weft tows in the loading direction, which dominated the stress-strain response of the entire specimen even with the presence of through-the-thickness cracks. Apparently, for GF 3D woven composite loaded in the weft direction, the stiffness of the weft tows was not high enough to prevent the stiffness reduction caused by the development of through-the-thickness cracks.

Photographs of the specimens failed under weft direction tension are shown in Fig. 4-38, where weft tow fracture and areas of whitening due to extensive matrix cracks can be seen.

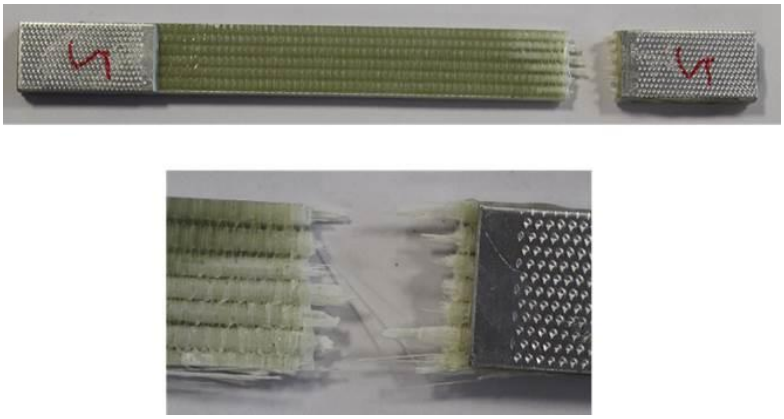

Fig. 4-38 Typical final failure of GF 3D woven composite tested in weft direction

4.4.3.2.3 ASTM D3518 In-plane Shear Test

Typical result and stress-strain curve obtained from the in-plane shear test of GF 3D woven composite are shown in Table 4-25 and Fig. 4-39. The measured in-plane shear properties of GF 3D woven composite, namely, the in-plane shear modulus and 0.2% offset shear strength, are very close to those of the IM7 CF 3D

woven composite. Also, the in-plane shear stress-strain responses of these two types of composites are very similar, both qualitatively and quantitatively.

Table 4-25 GF 3D woven composite in-plane shear test result

Property	Mean value	Std. dev.	COV %	Number of tests
Shear modulus (GPa)*	4.03	0.157	3.9	7
0.2% Offset shear strength (MPa)	38.8	1.63	4.2	7

* Values were obtained in engineering shear strain range of 3500-7500 microstrain

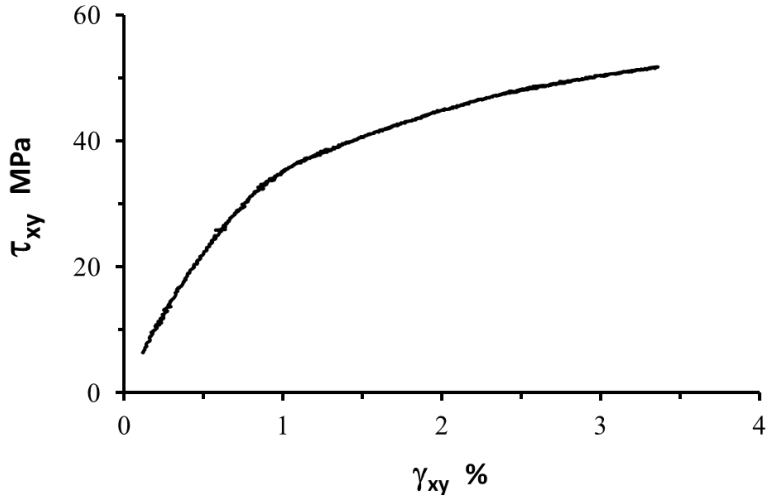

Fig. 4-39 Typical in-plane shear test stress-strain curve of GF 3D woven composite

4.5 Summary

In this chapter, the experiments conducted for investigating damage inside laminates and 3D woven composites are described in detail.

Based on the experimental result from laminate test cases, it is determined that damage-related material properties $R_{\perp}^{T}$, μ_I , $R_{\perp\parallel}$ and μ_{II} can be determined

using test cases of transverse tensile testing on UD laminates, tensile testing on cross-ply laminates and in-plane shear testing on UD laminates.

As shown in the next chapter, with the experimental result available for the determination of damage-related material properties, a new UD composite CDM model containing the novel damage evolution law is proposed and implemented for carrying out damage analyses. The method and detailed processes of using the experimental result to determine the damage-related material properties are also illustrated in the next chapter.

In terms of the 3D woven composites loaded in the warp direction, both IM7 CF and GF 3D woven composite demonstrated nonlinear stress-strain responses in the form of almost bilinear stress-strain curves, which are shown to be caused by the inter-tow cracks discovered in the warp-curving regions. Moreover, transverse intra-tow cracks were also found inside the weft tows of the GF 3D woven composite, but no such damage was discovered in the IM7 CF 3D woven composite.

On the other hand, for the 3D woven composites loaded in the weft direction, through-the-thickness transverse cracks bypassing weft tows were found in both the IM7 CF and GF 3D woven composites. However, while these cracks made the weft direction stress-strain response of GF 3D woven composite to be nonlinear, but that of IM7 CF 3D woven composite remained to be linear as high fibre direction Young's modulus value of IM7 carbon fibre weft tows is believed to have dominated the specimen level stress-strain response.

As the damage effect of the inter-tow cracks is not accounted for by the UD composite CDM model used for intra-tow damage modelling, a separate damage

model catered for characterising the damage effect of inter-tow cracks is introduced in Chapter 7.

5. Implementation and Verification of Proposed Damage Evolution Formulation

5.1 Introduction

Although the damage evolution law developed in Chapter 3 can be paired up with Li's damage representation to characterise damage process, in order to implement them in the form of a new CDM model for UD composites, a suitable damage initiation criterion is required to predict the start of the damage process. In this chapter, the issue of incorporating appropriate damage initiation criterion is addressed.

Furthermore, other than the damage evolution law which is targeted for characterising a damage process, failure criteria predicting instant failures of UD composites are also introduced in this chapter and added into the new CDM model proposed in this chapter.

This CDM model is then implemented for both 2D plane stress state and 3D stress state situations where the former case could be of laminates consisting of UD plies while the latter case could be UD fibre tows inside textile composites.

As a necessary sanity check for derived theoretical formulation and algorithm, the implemented CDM model is subjected to verification using numerical examples. These numerical examples are illustrated in this chapter.

In addition, as a part of the implementation process for the CDM model, the determination of damage-related material properties, which serve as input parameters to the CDM model, is also described in detail in this chapter.

5.2 Incorporation of Damage Initiation Criteria and Instant Failure Criteria

As mentioned in Chapter 3, Puck's failure criteria for UD composites are suitable to be used in conjunction with the newly developed damage evolution law because both identified transverse tensile, transverse shear and in-plane shear stresses on an action plane as contributors for causing matrix cracking parallel to the fibre direction. Moreover, Puck's failure criterion has been found to be one of the most promising failure criteria from World Wide Failure Exercise (WWFE) [10] for predicting the failure of UD composites. As a result, Puck's failure criterion [88] is chosen to be the damage initiation criterion employed for the current CDM model.

Adapted as a damage initiation criterion, Puck's criterion predicts both the onset of the matrix damage as well as the orientation θ of emerging planar matrix cracks. As shown in Fig. 5-1, the orientation θ is measured from the second axis of material coordinate system to the fracture plane normal (marked with "***n***") with anticlockwise direction defined as the positive direction.

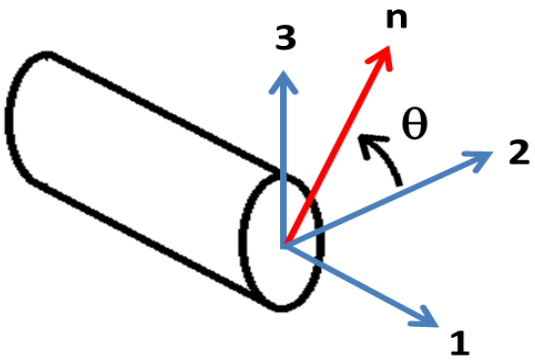

Fig. 5-1 UD composite matrix cracking damage orientation definition

It is necessary and advantageous to have the crack orientation predicted because for UD composites under 3D stress state like in the case of fibre tows inside textile composites, tows may be subjected to different load combinations at different locations which may result in the same tow having different matrix crack orientations at different locations, not to mention it is even more common for different tows to have different matrix crack orientations. With the incorporation of Puck's criterion for taking care of damage orientation determination, differences in matrix cracking orientation can be duly reflected.

In addition, by referring to Fig. 5-1, the damage vector $V = \{v_1 \quad v_2 \quad v_3\}^T$ can be rotated about the fibre direction according to the predicted matrix crack orientation (θ) so that the damage vector component v_2 can always be aligned in the direction normal to the crack plane. In this way, the damage vector would always be $V = \{0 \quad v_2 \quad 0\}^T$, which is the type of damage already dealt with in Chapter 3 and in Li's damage representation work, i.e. a single array of microcracks within each representative volume of the material. Therefore, all the damage-related theoretical formulations derived there are available for use without the need of further modification. The obtained effective material properties are expressed in the local material coordinate system which can be at different orientations than that defined by the damage vector. However, if one needs to obtain these properties in another coordinate system, e.g. that for a meso-scale unit cell representing the 3D textile composite [1], a standard coordinate transformation can be employed using the fibre orientation and the matrix cracking orientation (θ) predicted.

In contrast to matrix cracking which is a gradual damage process, failures of instant nature, i.e. fibre direction failures, are also addressed in Puck's criterion. For these instant failure modes, Puck's criterion used the stress within fibre which is calculated according to (5-1) under a multi-axial stress state:

$$\sigma_{1f} = E_{1f}\varepsilon_1 + \nu_{12f} m_{\sigma f}(\sigma_2 + \sigma_3) \qquad (5\text{-}1)$$

where E_{1f} is Young's modulus of pure fibre in its longitudinal direction,

ν_{12f} is the major Poisson's ratio of pure fibre,

$m_{\sigma f}$ is stress magnification factor due to transverse stresses on pure fibre.

If the fibre stress σ_{1f} obtained from (5-1) exceeds tensile or compressive strengths of the fibre, instant fibre direction failure is expected. This part of Puck's criterion to predict instant fibre direction failures of UD composites is also incorporated in the CDM model proposed here.

However, one should be aware that the fibre failure predicted here is a local material failure, not an ultimate structural failure. To allow this local failure to be traced during the analysis of laminates or textile composites, tow properties associated with fibres like E_1, G_{12} and G_{13} at the material point concerned should be reduced to a trivial value, so that a complete loss of load-carrying capability for these directions can be simulated when fibre failure occurs.

5.3 Implementation as a New CDM Model for UD Composites

With all components of a CDM model, namely damage representation, damage initiation criterion, damage evolution law and instant failure criterion clearly

defined as shown in above paragraphs, a new CDM model is established and implemented as a MATLAB code for laminate analysis, also as a user-defined material subroutine (UMAT) running in ABAQUS™/Standard for full 3D analysis.

For understanding the operation of this implemented CDM model, a flow chart is given in Fig. 5-2. As can be seen, the model first checks if there is any fibre failure occurred based on failure indicator determined from previous strain increment calculation. If there is, for example, fibre tensile failure detected, then associated Young's modulus and shear modulus values will be reduced to a trivial value (5% of their virgin values) to simulate the abrupt and catastrophic nature of fibre direction failure, while maintaining the positive definitiveness of the materials stiffness matrix as a numerical requirement from ABAQUS™/Standard.

Next, if matrix damage has not been initiated, Puck's criterion will be used to determine if matrix damage should initiate and its corresponding fracture plane orientation. If matrix damage has not been initiated and it is not predicted to initiate, the model will skip the matrix damage calculation process and update stresses directly. On the other hand, if matrix damage has been initiated, the damage orientation determined previously will be unchanged.

With the matrix damage predicted to occur, stresses on the fracture plane will be calculated. The effect of compressive normal stress on the crack plane will be ignored for damage evolution calculation since obviously such a stress does not contribute to cracking damage propagation on the fracture plane.

With the stresses on the fracture plane identified, the model then checks if this is a case of reloading. If it is, damage evolution will not be activated until the reloading criteria are met for damage evolution process to resume.

If damage is to evolve, the damage evolution law is applied to calculate a damage increment value $\Delta\omega$ based on Newton's iterative method. During this iterative process, stresses and damage increment value $\Delta\omega$ are updated in every iteration according to theoretical formulations presented in Chapter 3, as required by ABAQUS™/Standard in order to implement it through its user defined material subroutine UMAT, until a converged $\Delta\omega$ value is reached. If the converged damage increment value $\Delta\omega$ is negative, it signifies unloading and the damage increment $\Delta\omega$ is set to zero for retaining the previous total value of the damage variable ω since damage cannot be "healed" during unloading.

In the end, the damage variable ω will be updated based on the calculation of damage increment $\Delta\omega$, which then enables the material stiffness matrix and stresses to be updated accordingly.

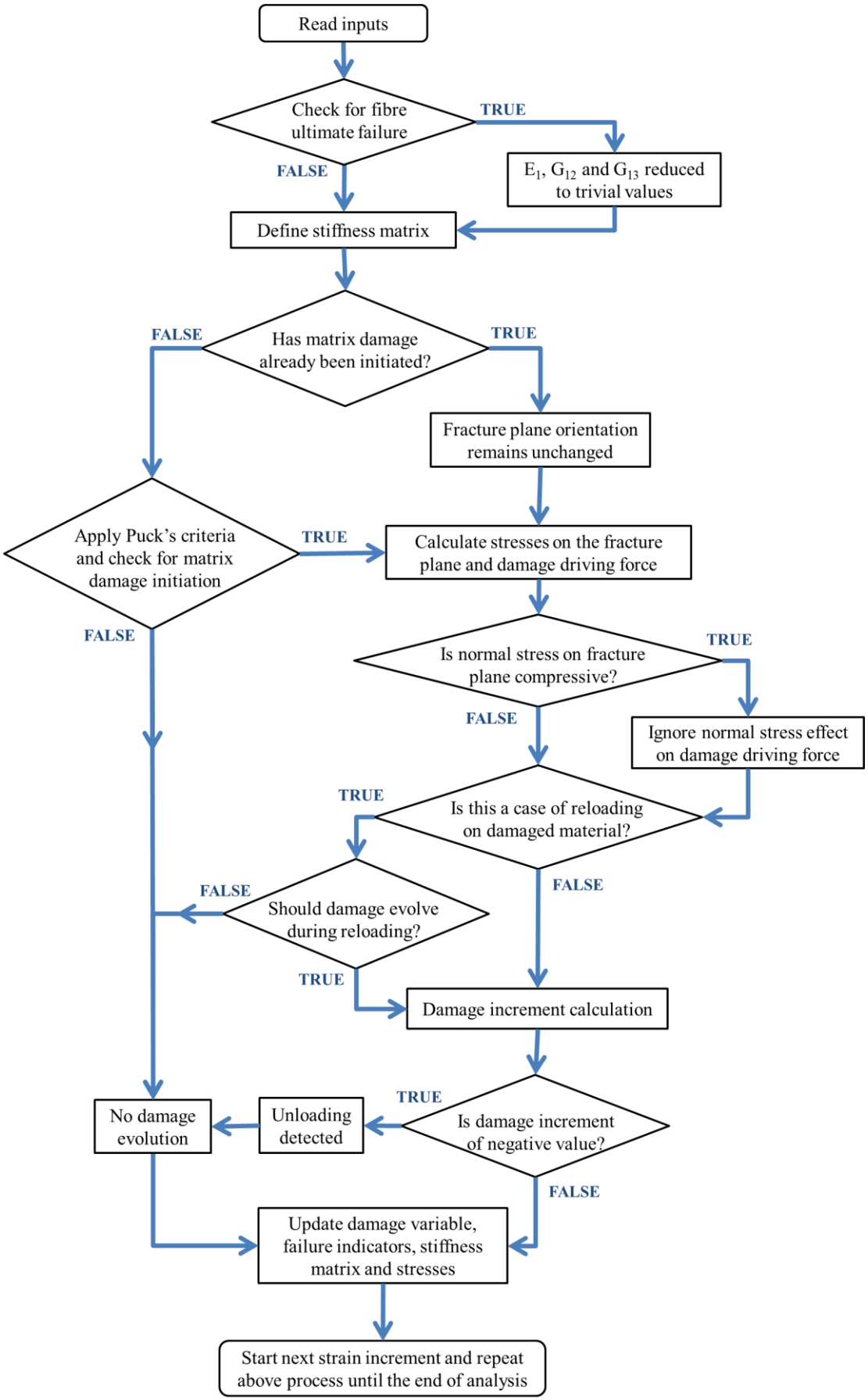

Fig. 5-2 CDM model operation flowchart

5.4 Verification Cases

To verify the implemented CDM model, verification examples are used. These examples are designed by assuming the damage evolution characteristics of an imaginary UD composite material. These verification cases are so introduced such that, for the assumed damage processes, damage driving force and stress values at different damage levels can be obtained analytically by using the theoretical formulations in Chapter 3. It is essential that the results obtained by the analytical method can be reproduced by the implemented numerical model using UMAT of ABAQUS™/Standard before contemplating any practical applications.

5.4.1 Set-up of the Verification Examples

The material properties assumed for the numerical verification examples are summarised in Table 5-1.

Table 5-1 UD composite material properties assumed for the verification examples

Symbol	Explanation	Value
E_1	Young's modulus in fibre direction	100 (GPa)
$E_2\ (=E_3)$	Young's modulus in transverse direction	10 (GPa)
G_{12}	In-plane shear modulus	5 (GPa)
G_{23}	Transverse shear modulus	3.45 (GPa)
ν_{12}	Major Poisson's ratio	0.1
k	Coupled damage effect factor between transverse tensile damage and in-plane shear damage as defined	0.25

	in [180]	
σ_{f-T}	Pure fibre ultimate tensile strength	2000 (MPa)
σ_{f-C}	Pure fibre ultimate compressive strength	-1000 (MPa)
E_{1f}	Pure fibre longitudinal direction Young's modulus	200 (GPa)
υ_{12f}	Pure fibre major Poisson's ratio	0.333
$m_{\sigma f}$	Stress magnification factor for fibre bundles as defined in Puck's criterion [88]	1.1
$p^{T}_{\perp\perp}$	Slope of the failure envelope relating to transverse tensile and transverse shear action stresses as defined in Puck's criterion [88]	0.3
$p^{C}_{\perp\perp}$	Slope of the failure envelope relating to transverse compressive and transverse shear action stresses as defined in Puck's criterion [88]	0.26
$p^{T}_{\perp\parallel}$	Slope of the failure envelope relating to transverse tensile and in-plane shear action stresses as defined in Puck's criterion [88]	0.35
$p^{C}_{\perp\parallel}$	Slope of the failure envelope relating to transverse compressive and in-plane shear action stresses as defined in Puck's criterion [88]	0.3
$R^{T}_{\perp}$	Transverse tensile stress threshold value for triggering matrix damage initiation	50 (MPa)
$R^{C}_{\perp}$	Transverse compressive stress threshold value for triggering matrix damage initiation	150 (MPa)
$R_{\perp\parallel}$	In-plane shear stress threshold value for triggering matrix damage initiation	70 (MPa)

As can be seen from Table 5-1, since UD composites are normally regarded as transversely-isotropic materials, the transverse Young's moduli E_2 and E_3 are therefore identical. Also, the transverse compressive stress threshold for matrix damage initiation $R_{\perp}^{C}$ is set to be more than twice the value of $R_{\perp}^{T}$ since this is typical of brittle composite material as mentioned in [88].

For clear illustration of the verification cases, the assumed damage evolution processes corresponding to each single mode loading case are designed to be as illustrated in Table 5-2, where the values of damage driving force are calculated according to the theoretical formulations presented in Chapter 3.

Table 5-2 Damage evolution processes assumed for each single mode loading case

Loading modes	Quantities	Values	
		At damage initiation with ω = 0%	At damaged state with ω = 40%
Uniaxial transverse direction stress $\sigma_{n\theta}$	$\sigma_{n\theta}$ (MPa)	50	80
	ρ_I (MPa)	0.25	1.28
Pure In-plane shear stress $\tau_{nl\theta}$	$\tau_{nl\theta}$ (MPa)	70	100
	ρ_{II} (MPa)	0.245	0.6
Pure transverse shear stress $\tau_{nt\theta}$	$\tau_{nt\theta}$ (MPa)	75	140
	ρ_{III} (MPa)	0.563	2.5

Based on the damage processes in Table 5-2, where variations of stresses, damage levels and damage driving force values are clearly shown, the corresponding

damage evolution constants μ_I , μ_{II} and μ_{III} for each single mode of loading are evaluated using (5-2), which is introduced in Chapter 3.

$$\Delta\omega = \mu_I \Delta\rho_I + \mu_{II} \Delta\rho_{II} + \mu_{III} \Delta\rho_{III} \qquad (5\text{-}2)$$

These damage evolution constants are then used as material property inputs (Table 5-3) for the numerical simulation work where the CDM model UMAT code will calculate damage evolution processes based on them. In doing so, the damage evolution scenarios presented in Table 5-2 should be reproduced by the simulation work if the theoretical formulations, e.g. the derivation of the tangential stiffness matrix in Chapter 3, are indeed mathematically sound and correctly coded as material subroutines. This then fulfils the purpose of this verification work.

Table 5-3 Damage evolution constants for the verification examples

Symbol	Explanation	Value
μ_I	Damage evolution constant under mode I type of loading.	0.387 $(MPa)^{-1}$
μ_{II}	Damage evolution constant under mode II type of loading.	1.13 $(MPa)^{-1}$
μ_{III}	Damage evolution constant under mode III type of loading.	0.206 $(MPa)^{-1}$

The numerical simulation models are constructed using ABAQUS™/Standard. For simplicity, a single C3D8 solid element (Fig. 5-3) is used and subjected to different loading conditions which covered not only the damage processes in

Table 5-2, but also unloading and reloading scenarios. Result and discussion of these numerical examples are presented in the next section.

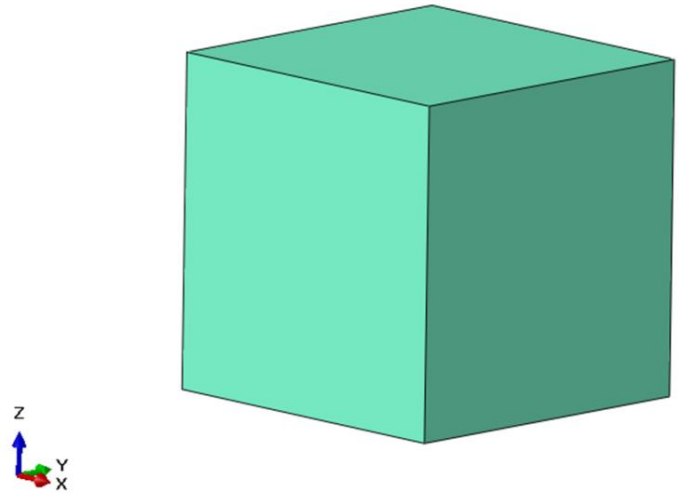

Fig. 5-3 Single solid element (C3D8) used for the simulation work in ABAQUS™/Standard

5.4.2 Results from the Numerical Examples

5.4.2.1 The Case of Transverse Direction Uniaxial Tension

In this example, the imaginary UD composite is loaded under uniaxial tension in axis-3 direction of the material coordinate (refer to Fig. 5-1). The load is repeatedly applied to simulate an unloading-reloading scenario.

First, looking at the stress-strain plot in Fig. 5-4, it can be seen that nonlinearity appeared when σ_3 reached 50 MPa. This is expected since 50 MPa is the value of $R_{\perp}^{T}$ set in Table 5-1. As a result, the stress-strain nonlinearity is due to initiation and evolution of matrix damage predicted by the CDM model.

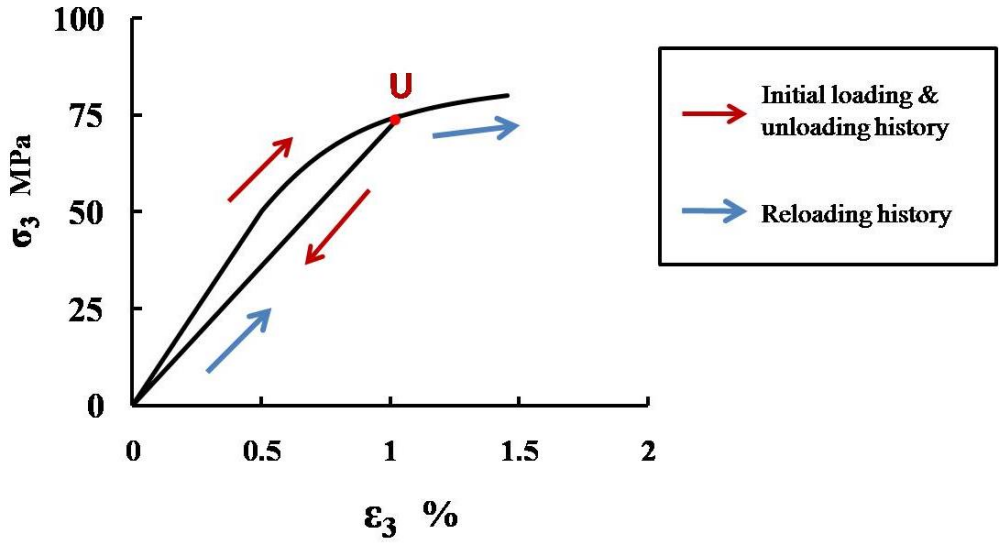

Fig. 5-4 Stress-strain plot for the case of uniaxial transverse tension and reloading

Moreover, one may see the unloading and reloading history in Fig. 5-4 (indicated by arrows), where the state returned to the point of zero stress and strain during unloading, before it followed the same path as unloading back for reloading and went up to the point where the previous loading process was stopped (marked as U in Fig. 5-4). It is obvious that only after reaching this "U" point during reloading, the damage evolution process then resumed. This can be seen from the continuous and smooth nonlinear curve shape in the vicinity of this "U" point in Fig. 5-4. This also means that the secant modulus value for E_3 did not change during the unloading and reloading processes, causing the unloading and reloading curve paths to be identical before damage evolution was reactivated. Such an unloading-reloading behaviour is made possible thanks to the unloading and reloading criteria introduced in Chapter 3.

Since only uniaxial σ_3 stress is applied in this example, according to Puck's criterion, the fracture plane would be the action plane of σ_3 where only a normal

stress $\sigma_{n\theta}$ would exist with all other shear stresses at zero value. This is correctly predicted by the CDM model with a calculated fracture plane orientation at ±90º from axis-2 of the material coordinate system (refer to Fig. 5-1 for the definition of damage orientation). Considering that σ_3 acting on the plane perpendicular to the axis-3 is indeed at ±90º from the plane perpendicular to the axis-2, this facture plane orientation prediction is therefore correct.

The cause for stress-strain nonlinearity beyond 50 MPa is also reflected in Fig. 5-5 as damage variable ω started to grow from zero once $\sigma_{n\theta}$ reached 50 MPa. In terms of predicted damage evolution behaviour, Fig. 5-5 shows that the damage variable grew to 40% when $\sigma_{n\theta}$ reached 80MPa, which is consistent with the assumed damage evolution process in Table 5-2. In addition, the nonlinear trend in Fig. 5-5 is due to the fact that damage driving force is defined as a nonlinear function of stresses as illustrated in Chapter 3.

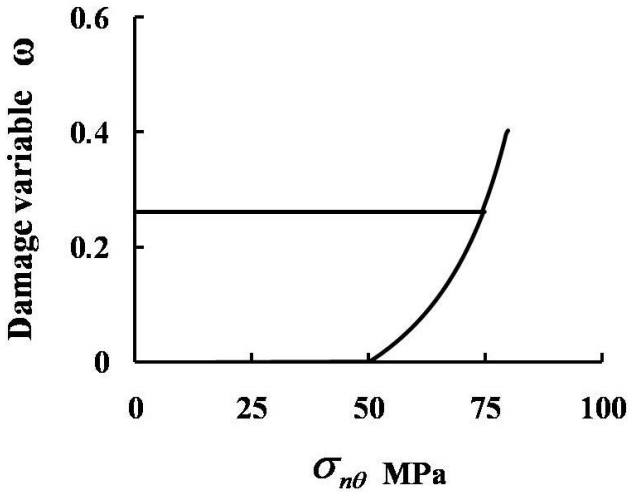

Fig. 5-5 Damage-stress plot for the case of uniaxial transverse tension and reloading

On the other hand, Fig. 5-6 confirms that the predicted damage driving force values matched with the damage driving force values in Table 5-2. The linear trend in Fig. 5-6 is a reflection of the linear damage evolution law defined in Chapter 3.

However, one may notice that in both Fig. 5-5 and Fig. 5-6, a horizontal line appeared. This is due to unloading and reloading processes since the damage variable value remained constant during these processes while stress value and damage driving force value continued to vary.

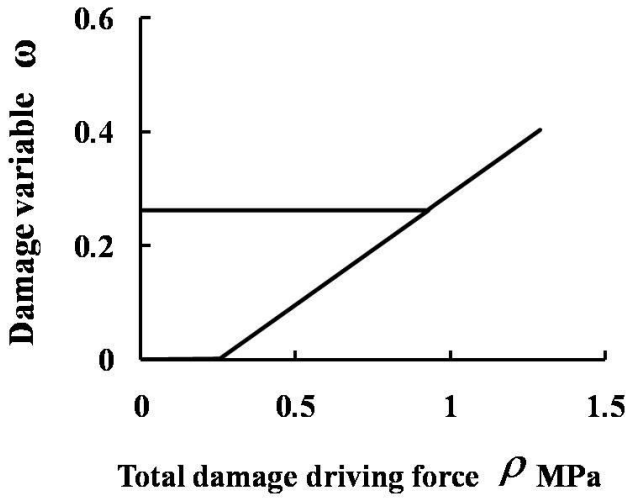

Fig. 5-6 Damage variable - damage driving force plot for the case of uniaxial transverse tension and reloading

Based on above result, it can be concluded that the UMAT code did indeed reproduce the damage process in Table 5-2 for the case of transverse direction uniaxial tension loading.

5.4.2.2 The Case of Transverse Direction Uniaxial Compression

For this case, transverse direction uniaxial compressive stress σ_2 is applied. The UMAT code predicted a stress-strain response as shown in Fig. 5-7, where the stress-strain nonlinearity after reaching -150 MPa is correctly accounted for since $R_{\perp}^{C}$ is set at 150 MPa in Table 5-1.

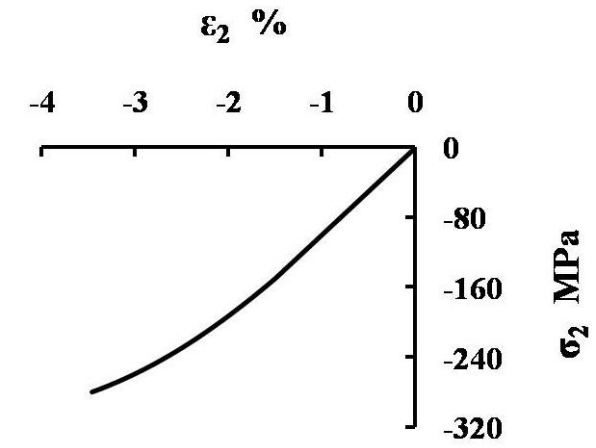

Fig. 5-7 Stress-strain plot for the case of uniaxial transverse compression

Fig. 5-8 further confirms that the stress-strain nonlinearity in Fig. 5-7 is indeed caused by the damage predicted.

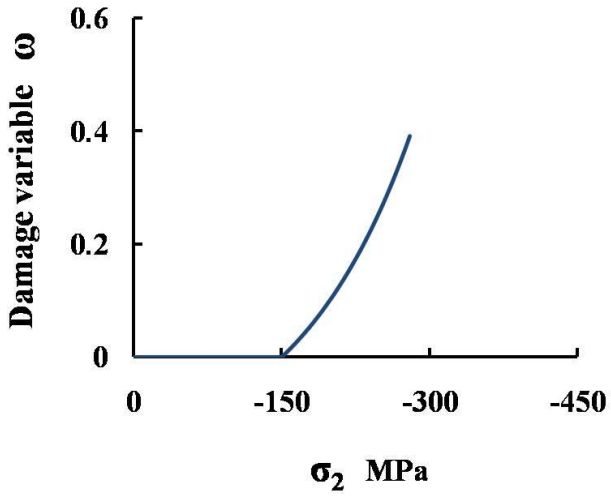

Fig. 5-8 Damage-stress plot for the case of uniaxial transverse compression

Recall that Puck's criterion stated that the damage due to transverse compression for brittle UD composites should be in the form of transverse shear cracking at a fracture plane orientation slightly greater than 45° from the direction of the uniaxial transverse compressive stress. This is because on the stress action plane of that orientation, transverse shear stress will eventually cause the fracture when compressive normal stress on that action plane becomes too low to resist the shear fracture.

Such form of damage is successfully predicted by the UMAT code for this example with a resulting crack orientation at ±50.4° from axis-2. The predicted stresses on the fracture plane are shown in Fig. 5-9 where both transverse shear and normal compressive stresses are present.

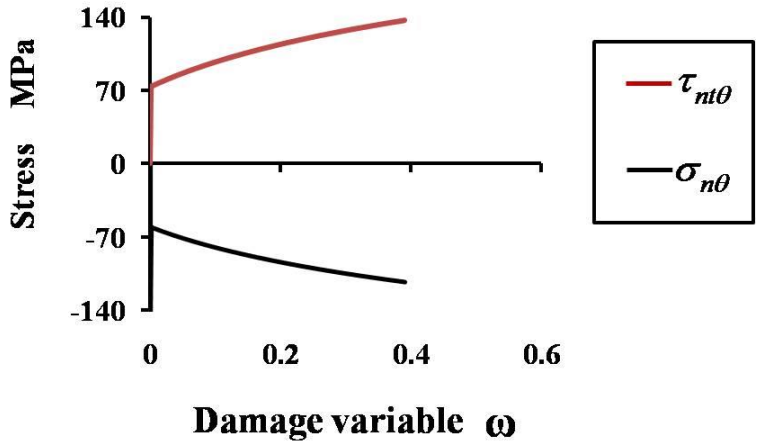

Fig. 5-9 Stresses on the fracture plane for the case of uniaxial transverse compression

From Fig. 5-9, one may see that the prediction of transverse shear stress $\tau_{nt\theta}$ and damage variable ω is in agreement with the assumed damage evolution process for pure transverse shear loading mode in Table 5-2.

Moreover, only the transverse shear stress $\tau_{nt\theta}$ contributed to the damage driving force value in Fig. 5-10. Although a compressive direct stress is found on the fracture plane, it will not contribute to damage evolution.

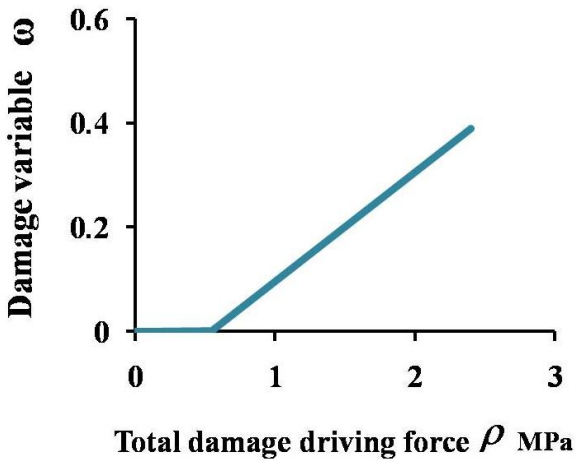

Fig. 5-10 Damage variable – damage driving force plot for the case of uniaxial transverse compression

Again, the prediction of damage driving force in Fig. 5-10 is consistent with the values listed in Table 5-2 for transverse shear loading mode.

5.4.2.3 The Case of Pure Transverse Shear

Pure transverse shear stress τ_{23} is applied in this case before unloading. As can be seen from the predicted nonlinear stress-strain curve in Fig. 5-11, damage occurred during the loading process.

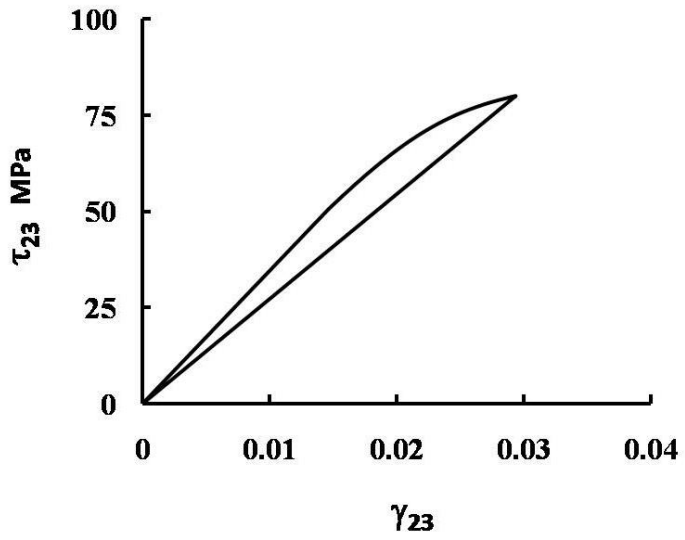

Fig. 5-11 Stress-strain plot for the case of pure transverse shear

However, such damage is not a case of transverse shear cracking. A closer look at the simulation result revealed that the matrix damage in this case is actually caused by normal tensile stress $\sigma_{n\theta}$, with the predicted fracture plane orientation at 45° to axis-2. This is essentially a case of tensile fracture in principal stress direction under the application of pure transverse shear stress. This result is in agreement with Puck's criterion and such damage behaviour was reported to be characteristic of brittle UD composites which normally have transverse tensile strength lower than transverse shear strength [88].

Since the matrix damage here is once again due to normal tensile stress $\sigma_{n\theta}$, plots in Fig. 5-12 and Fig. 5-13 for the current case are therefore similar to those in Fig. 5-5 and Fig. 5-6 for the earlier transverse tension case.

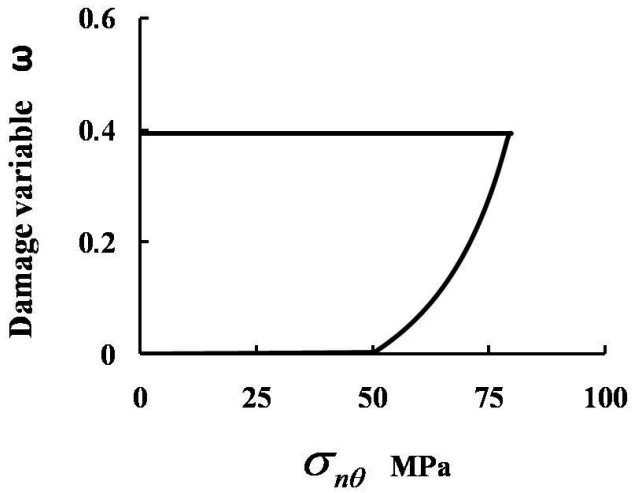

Fig. 5-12 Damage-stress plot for the case of pure transverse shear

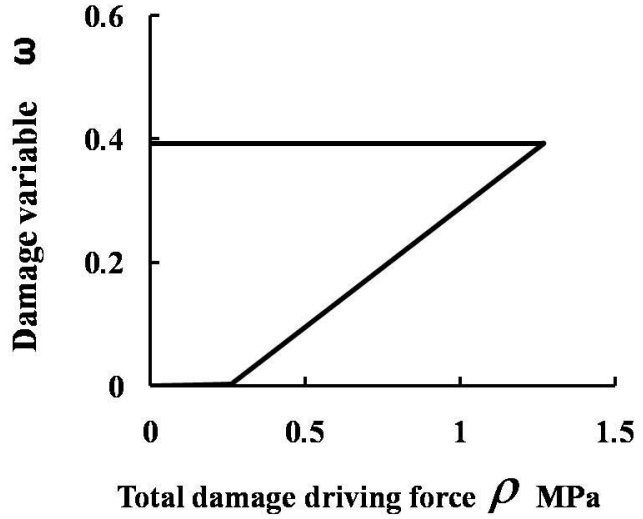

Fig. 5-13 Damage variable -damage driving force plot for the case of pure transverse shear

As illustrated in Fig. 5-14, another interesting point to note is that there are non-trivial increasing direct strain values predicted for ε_2 and ε_3 during the damage evolution process.

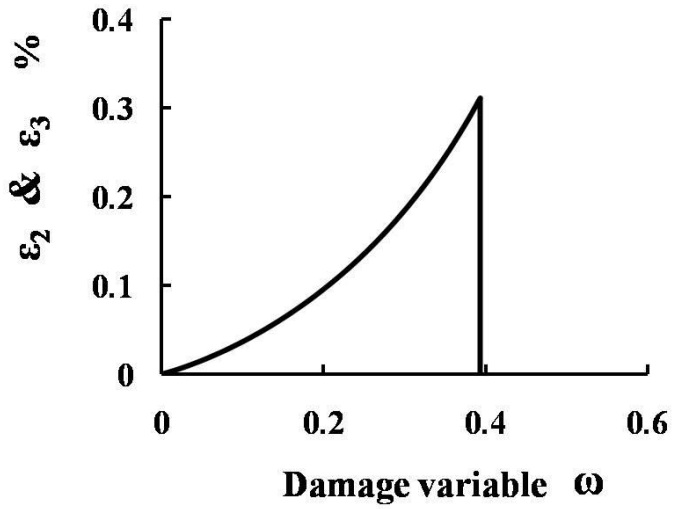

Fig. 5-14 Strain-damage plot for the case of pure transverse shear

Although this may appear at first to be strange since a pure shear stress τ_{23} somehow caused direct strains ε_2 and ε_3 to increase, but considering that the crack orientation predicted here is at 45° from axis-2 which effectively transformed the original transversely-isotopic material into an anisotropic material. In this sense, the application of a pure shear stress would cause non-zero direct strains and such a shear-extension coupling effect would become more severe if the matrix cracking damage at 45° to axis-2 were to grow further.

5.4.2.4 The Case of Pure In-plane Shear

In this example, pure in-plane shear stress τ_{13} is applied before unloading. From Fig. 5-15 and Fig. 5-16, it can be seen that damage initiation is modelled correctly as stress-strain nonlinearity due to damage appeared when τ_{13} reached 70 MPa, which corresponds to the $R_{\perp\parallel}$ value in Table 5-1.

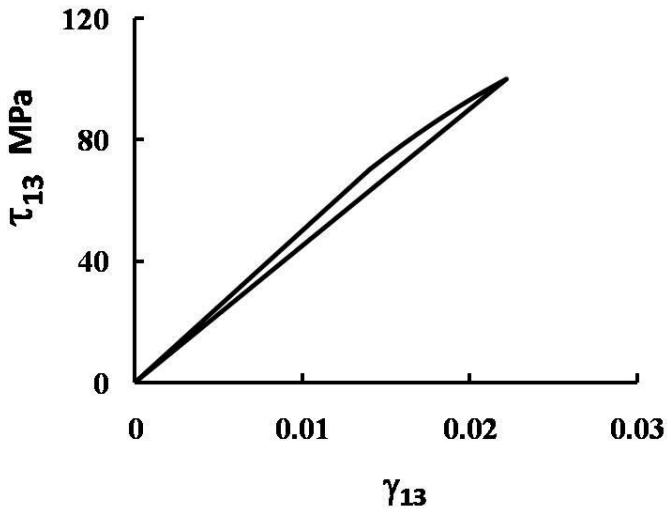

Fig. 5-15 Stress-strain plot for the case of pure in-plane shear

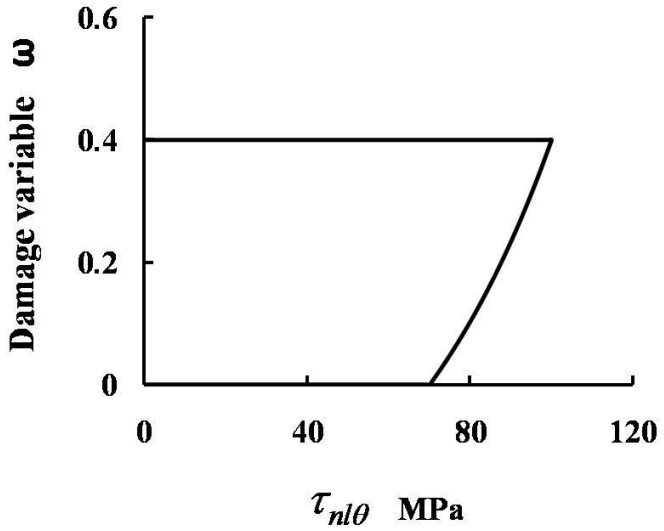

Fig. 5-16 Damage-stress plot for the case of pure in-plane shear

In terms of fracture plane orientation, the UMAT code predicted it to be of ±90° from axis-2 which is correct as the fracture plane caused by τ_{13} should have its normal in the direction of axis-3 which is indeed a 90° shift from axis-2.

As shown in Fig. 5-16 and Fig. 5-17, the predicted values of damage variable, damage driving force and in-plane shear stress are all consistent with the values listed in Table 5-1 for the case of pure in-plane shear stress $\tau_{nl\theta}$.

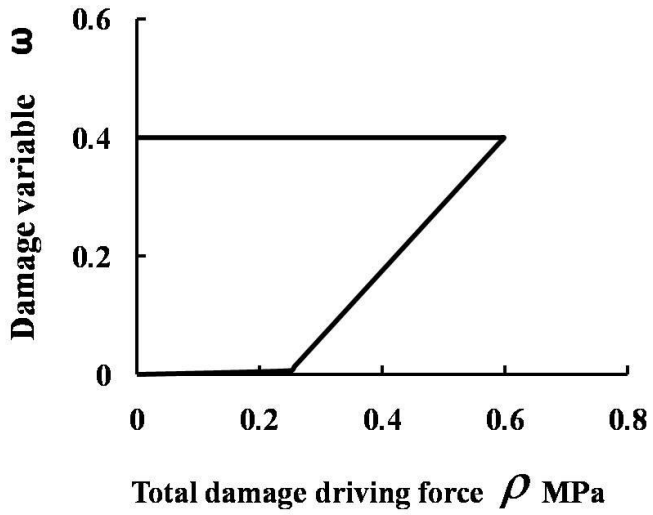

Fig. 5-17 Damage - damage driving force plot for the case of pure in-plane shear

5.4.2.5 The Case of Fibre Direction Failures

In this example, fibre direction instant failure scenario is verified. Uniaxial tensile and uniaxial compressive stress loadings are applied separately in the fibre direction (axis-1).

As can be seen from Fig. 5-18, for the tensile case, instant failure is predicted to occur when σ_1 hit 1000 MPa.

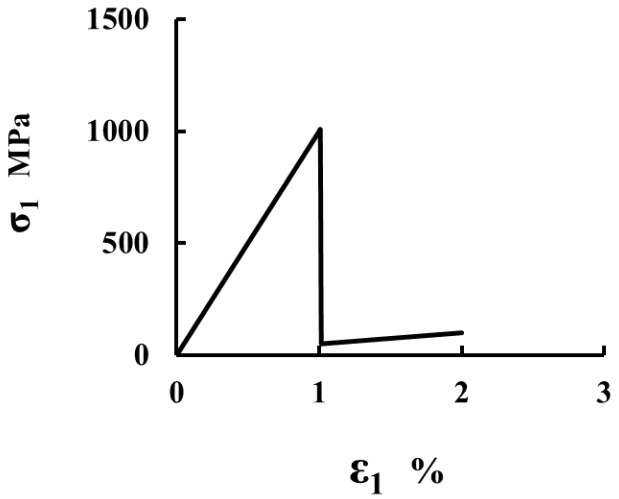

Fig. 5-18 Stress-strain plot for the case of fibre direction tension

This result is correct and can be explained as follows. First, by referring to the formula (5-3) extracted from Puck's criterion for pure fibre longitudinal stress calculation, fibres in a UD composite are expected to share the same longitudinal strain ε_1 as in the composite in the same direction.

$$\sigma_{1f} = E_{1f}\varepsilon_1 + \upsilon_{12f} m_{\sigma f}(\sigma_2 + \sigma_3) \qquad (5\text{-}3)$$

Considering that in Table 5-1 the longitudinal Young's modulus value of pure fibre E_{1f} is twice of that of the UD composites (E_1), it is therefore expected that the pure fibre ultimate tensile strength σ_{f-T} of 2000 MPa would be reached when σ_1 in UD composites reached around 1000 MPa. This should then trigger fibre direction instant tensile failure which is properly modelled in this example.

For the compressive case, instant failure is also predicted to occur (Fig. 5-19), but at a lower stress level since ultimate fibre compressive strength σ_{f-C} is 1000

MPa. For both cases, upon instant failure, the prescribed sudden reduction of E_1 to 5% of its virgin value is evident in Fig. 5-18 and Fig. 5-19.

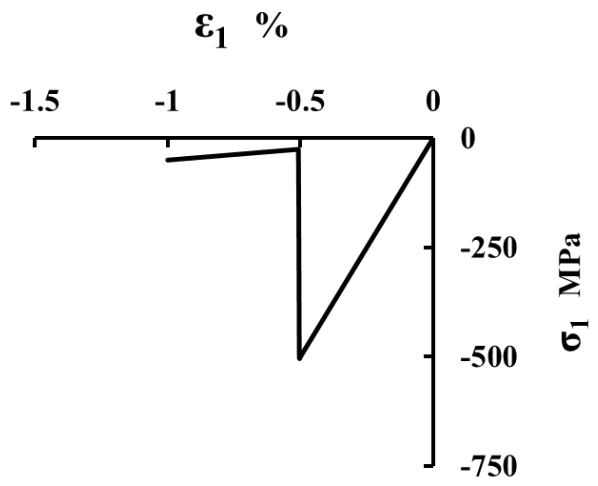

Fig. 5-19 Stress-strain plot for the case of fibre direction compression

5.5 Test Cases for Damage-related Material Property Determination

Three laminate test cases are employed to determine damage-related material properties. The corresponding experiments are described previously in Chapter 4 and are summarised as follows:

- Transverse direction uniaxial tensile test on UD laminates, which is for measuring the transverse tensile stress value $R_{\perp}^{T}$ that triggers the initiation of mode I type matrix damage.
- Uniaxial tensile test on cross-ply laminates, which is for measuring the damage evolution constant μ_I for mode I type matrix damage.

- In-plane shear test on UD laminates, which is for measuring the in-plane shear stress $R_{\perp\parallel}$ that triggers the initiation of mode II type matrix damage, as well as for determining the damage evolution constant μ_{II}.

It is worth noting that, based on the analysis of the experimental data in Section 4.3.3.2 of Chapter 4, the mode I damage initiation stress, $R_{\perp}^{T}$, was found to be the same as the transverse tensile strength of the UD composite. This is the case for most of the UD composites as they are brittle and fail abruptly under transverse tension, instead of suffering gradual stiffness degradation. Because of this, it may not be necessary to conduct the transverse tensile tests to obtain $R_{\perp}^{T}$, as long as the UD composite transverse tensile strength values are available.

The procedure for the determination of damage evolution constants μ_I and μ_{II} are summarised as follows:

1. From the experimental stress-strain plots of uniaxial tensile test on cross-ply laminates and in-plane shear test on UD laminates, ply level stress values for the plies subjected to mode I or mode II types of damage can be extracted. As a result, ply level stress-strain relationships can be obtained which enables ply level damage variables ω to be calculated using $\omega = \frac{E_2^0 - E_2}{E_2^0}$ and $\omega = \frac{G_{12}^0 - G_{12}}{kG_{12}^0}$.
2. Using these ply level stress values, damage variables and the UD ply material elastic properties, the damage driving force values ρ_I and ρ_{II} can be calculated according to $\rho = P_I\sigma_2^2 + P_{III}\sigma_{13}^2 + P_{II}\sigma_{12}^2$, which is introduced in Chapter 3.

3. Using the damage driving force values and the damage variable values, $\omega - \rho_I$ and $\omega - \rho_{II}$ data curves can be obtained. The gradients in these curves are expected to be damage evolution constants as defined in the damage evolution law: $\Delta\omega = \mu_I \Delta\rho_I + \mu_{II} \Delta\rho_{II} + \mu_{III} \Delta\rho_{III}$.

In addition to the IM7 carbon fibre laminate test cases described in Chapter 4, the determination of damage-related material properties and the subsequent laminate analysis are also carried out using the experimental data of E-glass/MY750 laminates supplied in WWFE-I [150,151].

The value of doing so is not only to demonstrate that the CDM model can be employed for different material systems, but also for the benefit of additional validation test cases being available in WWFE-I [150,151]. Specifically, biaxial loading with different loading ratios can offer more diverse damage scenarios to which the CDM model can be exposed through the validation work. Needless to say, the more real-life damage scenarios the CDM model is validated for and assessed against, the higher the confidence level which can be accredited to this model for practical engineering applications.

5.5.1 IM7 Carbon Fibre Laminates

For the IM7 carbon fibre UD lamina, the values of strength parameters $R_{\perp}^{T}$ (49.2 MPa) and $R_{\perp\parallel}$ (55.9 MPa) were measured directly from the transverse tensile test and the in-plane shear test on UD laminates, respectively, which were described in Section 4.3.3.3 of Chapter 4.

To determine the value of damage evolution constant μ_I for mode I type matrix damage, the experimental stress-strain curve from the cross-ply laminate test case, as reported in Section 4.3.3.4 of Chapter 4, is used. This experimental stress-strain curve is reproduced here in Fig. 5-20 and designated as the "original experimental result".

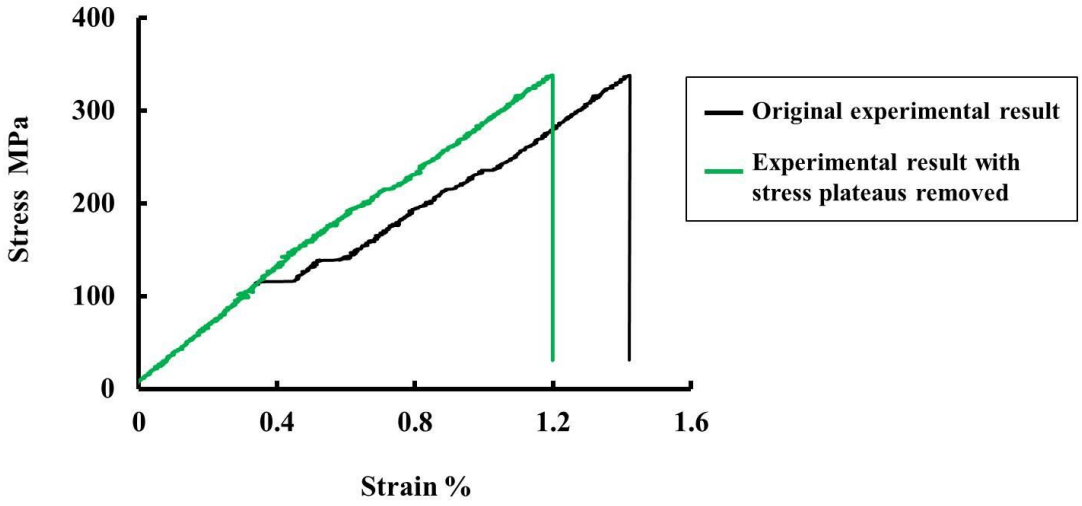

Fig. 5-20 Original and edited experimental stress-strain curves for IM7/8552 cross-ply laminate

As was explained in Section 4.3.3.4, the stress plateaux on the original experimental stress-strain curve in Fig. 5-20 occurred because of the release of residual curing stresses, rather than the stiffness degradation due to matrix cracking in the 90° UD plies. In order to better visualise the stiffness degradation solely due to matrix cracking, the original stress-strain curve is post-processed with stress plateaux removed by shifting parts of the curve on the right of the plateaus to the left. The resulting edited stress-strain curve is plotted in Fig. 5-20 alongside the original curve.

Since the current CDM model formulation does not include conditions for capturing the effect of residual stress numerically, the edited stress-strain curve,

which filtered out the effect from residual stress, should be used for the determination of the damage evolution constant μ_I .

The ideal method to determine the value of μ_I is to plot the damage variable value ω against the damage driving force value ρ_I for the damaged 90° plies inside the cross-ply laminate. Then, according to the damage evolution law formulation defined in Chapter 3, which is restated here in (5-4), the μ_I value can be determined as the gradient of the $\omega - \rho_I$ curve.

$$\Delta\omega = \mu_I \Delta\rho_I + \mu_{II} \Delta\rho_{II} + \mu_{III} \Delta\rho_{III} \qquad (5\text{-}4)$$

However, to do so, one needs to obtain the ply level stress-strain response for the 90° plies. This can be achieved by employing some assumptions and using the edited laminate level experimental stress-strain curve in Fig. 5-20.

First of all, due to balance of force, the relationship between laminate level stress and ply level stresses can be expressed as (5-5).

$$\sigma_L DT = \sigma_{90} DT_{90} + \sigma_0 DT_0 \qquad (5\text{-}5)$$

where σ_L is the laminate level stress in the loading direction, σ_{90} is the transverse stress in the 90° plies, σ_0 is the longitudinal stress in the 0° plies, D is the width of the laminate and T , T_{90} , T_0 are total thicknesses of the laminate, the 90° plies, the 0° plies respectively.

Then, assuming there is no fibre damage in the 0° plies until the final failure of the cross-ply laminate and that the stresses in the 90° plies are uniformly

distributed, transverse tensile stress in the 90° plies can be calculated according to (5-6).

$$\sigma_{90} = \frac{\sigma_L T - \sigma_0 T_0}{T_{90}} = \frac{\sigma_L T - E_1 \varepsilon_L T_0}{T_{90}} \quad (5\text{-}6)$$

where E_1 is the longitudinal Young's modulus value of the 0° plies, ε_L is the laminate level strain in the loading direction.

Thanks to this, using the data points in the edited laminate level stress-strain curve in Fig. 5-20, transverse stress in the 90° plies (σ_{90}) can be obtained and plotted against the strain data as shown in Fig. 5-21.

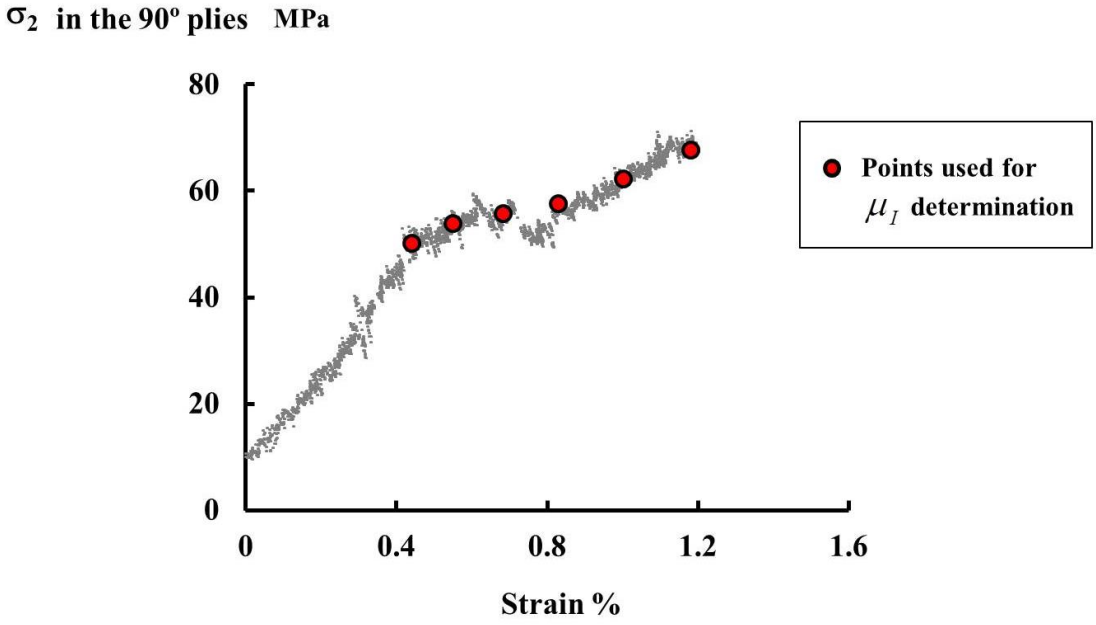

Fig. 5-21 Derived ply level stress-strain response for the 90° plies in the IM7/8552 cross-ply laminate

With the knowledge of stress-strain response in the 90° plies, the corresponding damage driving force can be calculated using properties of the UD lamina as summarised in Table 5-4. Six distributed data points which located beyond the mode I damage initiation stress $R_{\perp}^{T}$ (49.2 MPa) in the above stress-strain curve are selected for damage driving force calculation, since that part of the stress-strain curve should have included the damage effect from mode I type matrix damage. In addition, the corresponding damage variable values ω for these six data points can also be obtained as $\omega = \frac{E_2^0 - E_2}{E_2^0}$.

Table 5-4 Properties of IM7/8552 UD lamina for damage driving force calculation

Symbol	Explanation	Value
E_1	Young's modulus in fibre direction	186 (GPa)
E_2	Young's modulus in transverse direction	10.9 (GPa)
G_{12}	In-plane shear modulus	5.19 (GPa)
ν_{12}	Major Poisson's ratio	0.312
ν_{23}	Transverse Poisson's ratio	0.45
k	Coupled damage effect factor between transverse tensile damage and longitudinal shear damage as defined in [180]	0.21

In Table 5-4, apart from the material elastic properties which are obtained through experiments as reported previously in Chapter 4, the k value is determined by a

numerical experiment documented in [142,180]. In there, different extents of damage ω were represented by matrix cracks of different lengths which were introduced into the unit cell models of homogenised UD composites. The relative degradation of the effective in-plane shear modulus G_{12} and that of the effective transverse modulus E_2 at each state of damage was determined, and the value of k was calculated as the ratio of the two [180], as expressed in (5-7).

$$k = \frac{1 - \frac{G_{12}}{G_{12}^0}}{\omega} \tag{5-7}$$

The same numerical experiment method is used to determine the values of k in the UD composites of different material systems that are involved in the present research.

Then, based on the properties from Table 5-4, as well as the definition of damage driving force introduced in Chapter 3 (reproduced here in (5-8)). Damage driving force values for the six data sample points selected in Fig. 5-21 are calculated and plotted in Fig. 5-22 with corresponding damage variables.

$$\rho = P_I \sigma_2^2 + P_{III} \sigma_{13}^2 + P_{II} \sigma_{12}^2 \tag{5-8}$$

where

$$P_I = P_I^0 + P_I^D \omega = \frac{1}{E_2^0} + \frac{2\left(1 - \nu_{12}^0 \nu_{21}^0\right)}{\left(1 - \nu_{23}^0 - 2\nu_{12}^0 \nu_{21}^0\right)\left(1 + \nu_{23}^0\right) E_2^0} \omega$$

$$P_{II} = P_{II}^0 + P_{II}^D \omega = \frac{k}{G_{12}^0} + \frac{2k^2}{G_{12}^0} \omega$$

$$P_{III} = P_{III}^0 + P_{III}^D \omega = \frac{1}{E_2^0} + \frac{1}{\left(1 + \nu_{23}^0\right) E_2^0} \omega$$

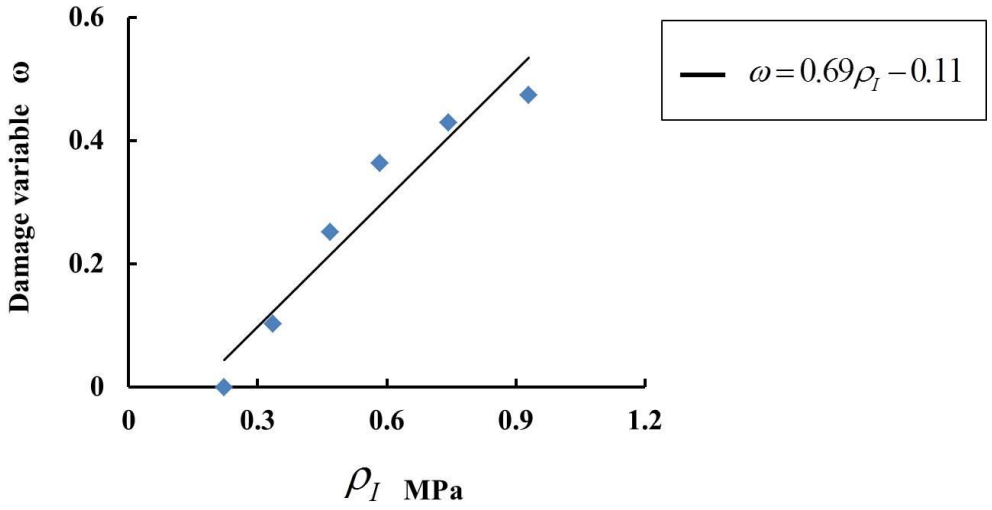

Fig. 5-22 Relationship between damage and damage driving force for the 90° plies in the IM7/8552 cross-ply laminate

The $\omega - \rho_I$ data points in Fig. 5-22 can be approximated by the best-fit line expressed as "$\omega = 0.69\rho_I - 0.11$", from which the gradient of 0.69 is the value of the damage evolution constant μ_I determined.

For the determination of the damage evolution constant μ_{II} for mode II type of matrix damage, in-plane shear test result reported in Section 4.3.3.3 is used. The same approach described above is followed to obtain the $\omega - \rho_{II}$ data points and a value of 6.4 is determined to be the value of μ_{II} for IM7 carbon fibre UD lamina.

With the damage evolution constants determined (listed in Table 5-5), the CDM model is ready to predict intra-lamina damage in laminates.

Table 5-5 Damage evolution constants determined for IM7/8552 UD lamina

Symbol	Value
μ_I	0.69 $(MPa)^{-1}$
μ_{II}	6.4 $(MPa)^{-1}$

To verify that the damage evolution constants determined above will enable the CDM model to reproduce the cross-ply test case and the in-plane shear test case reported in Chapter 4, laminate analyses are carried out using the MATLAB code to simulate these test cases. Material properties used for the laminate analyses in addition to these in Table 5-4 and Table 5-5 are listed in Table 5-6.

Table 5-6 Additional IM7/8552 UD lamina material properties used for laminate analysis

Symbol	Explanation	Value
$p_{\perp\parallel}^{T}$	Slope of the failure envelope relating to transverse tensile and longitudinal shear action stresses as defined in Puck's criterion [88].	0.35
$p_{\perp\parallel}^{C}$	Slope of the failure envelope relating to transverse compressive and longitudinal shear action stresses as defined in Puck's criterion [88].	0.3
$R_{\perp}^{T}$	Transverse tensile stress threshold value for matrix damage initiation.	49.2 (MPa)
$R_{\perp}^{C}$	Transverse compressive stress threshold value for matrix damage initiation [196]	286 (MPa)
$R_{\perp\parallel}$	Longitudinal shear stress threshold value for matrix damage initiation.	55.9 (MPa)

For the cross-ply laminate test case, the stress-strain prediction generated by the MATLAB code is presented in Fig. 5-23 along with the experimental result. As can be seen, the model prediction successfully reproduced the experimental stress-strain response.

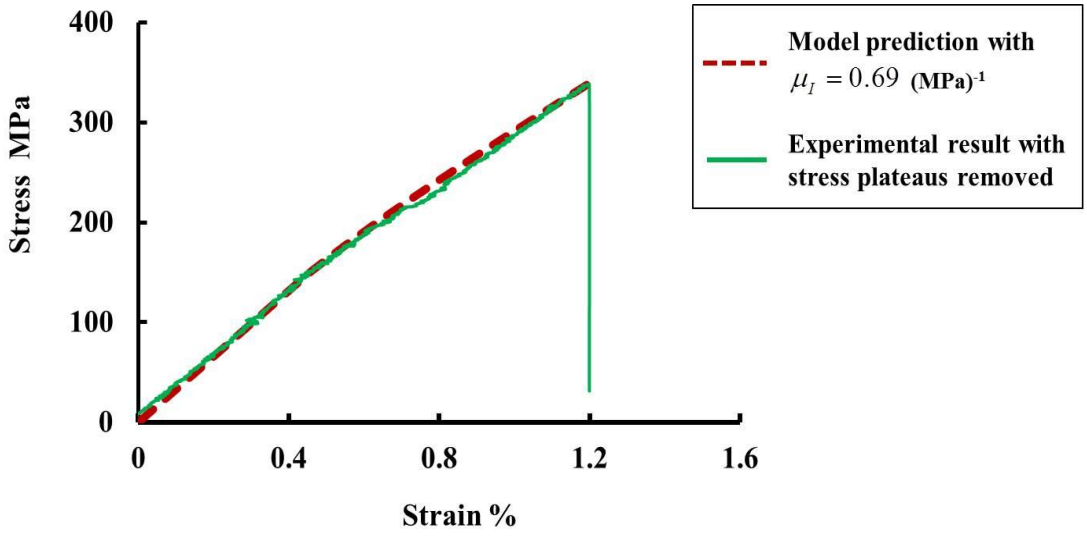

Fig. 5-23 Stress-strain prediction for IM7/8552 cross-ply laminate with the experimental result

For the purpose of demonstrating the performance of the CDM model, two more analyses are carried out for this cross-ply test case, but with made-up values of μ_I at 0.1 (MPa)$^{-1}$ and 6 (MPa)$^{-1}$ respectively to show the sensitivity of the model to these material properties.

Stress-strain curves and damage predictions generated by the MATLAB code, using aforementioned three different values of μ_I, are plotted in Fig. 5-24(a). As can be seen, μ_I has significant influence on the damage evolution behaviour with higher values of μ_I resulting in faster growth of damage.

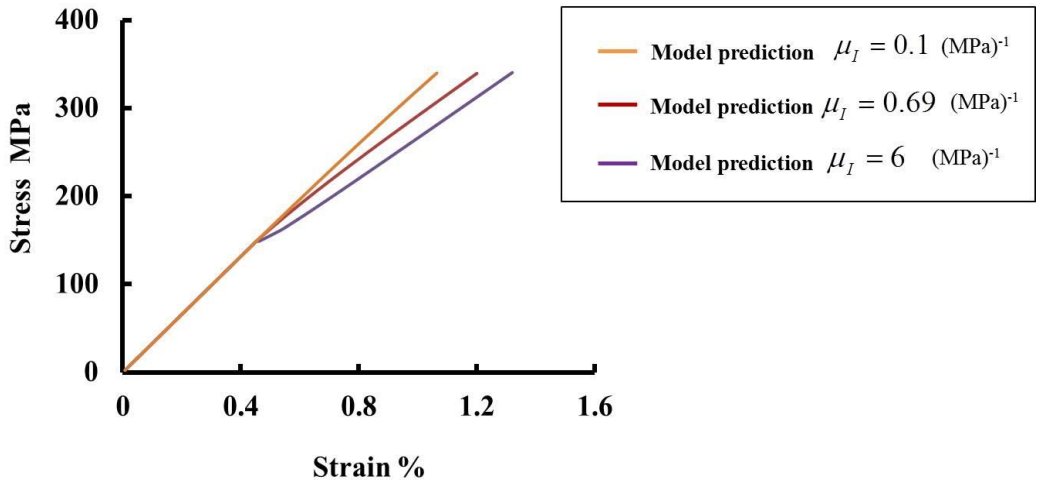

(a)

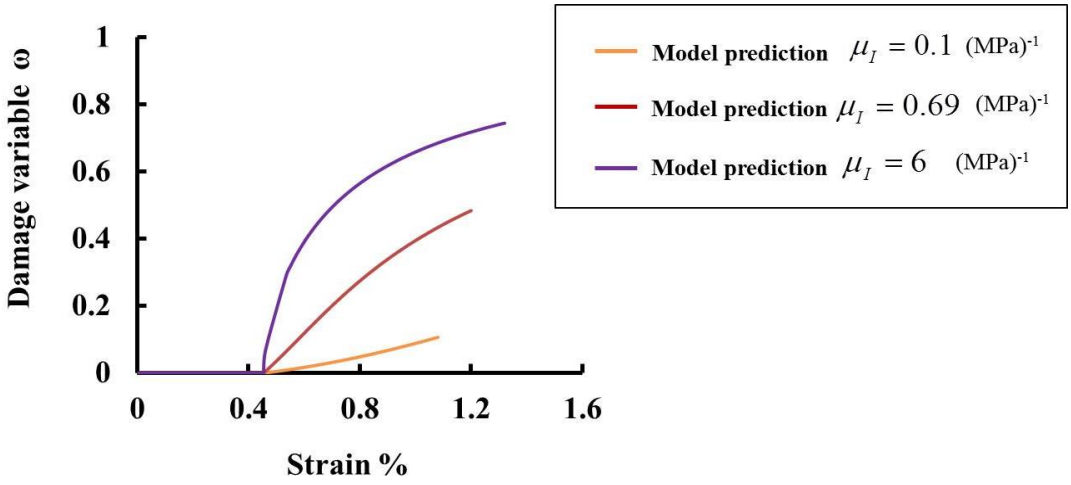

(b)

Fig. 5-24 Different predictions for IM7/8552 cross-ply laminate: a) Laminate level stress-strain curve, b) Damage variable in the 90º plies

Moreover, the ply level stress-strain curves predicted for the 90° plies are shown in Fig. 5-25. In all three cases, damage initiation was triggered when transverse stress in these plies reached the value of $R_{\perp}^{T}$ (49.2 MPa), which is the damage initiation threshold for mode I type of matrix damage. Another point to note is that the stress-strain curve prediction with μ_I = 6 (MPa)$^{-1}$ shows a strain softening behaviour after damage initiation, as the damage growth in that case

was too severe. Such a behaviour could lead to numerical instability problems, especially if an implicit algorithm is used for the analysis, such as that in ABAQUS™/Standard.

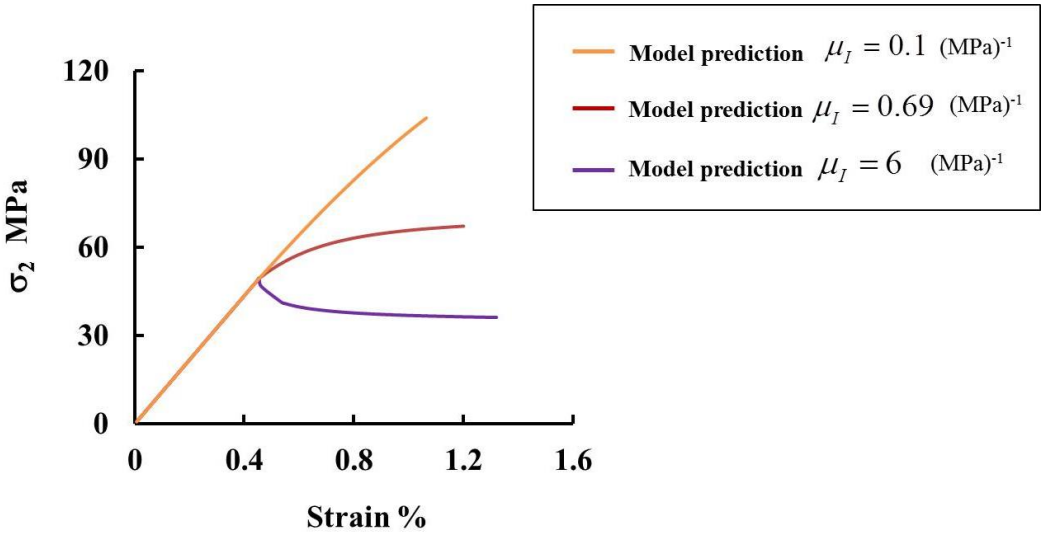

Fig. 5-25 Predictions of transverse stress in the 90º plies in IM7/8552 cross-ply laminate

Also, the range of characteristics as shown in Fig. 5-25 illustrates that the CDM model developed has the capability to simulate different stress-strain behaviours by choosing an appropriate value for μ_I, regardless of whether it is a material hardening or a material softening behaviour.

For the in-plane shear test case, the predicted stress-strain response and damage variable value are presented in Fig. 5-26. As can be seen, the model prediction reproduced the experimental stress-strain behaviour.

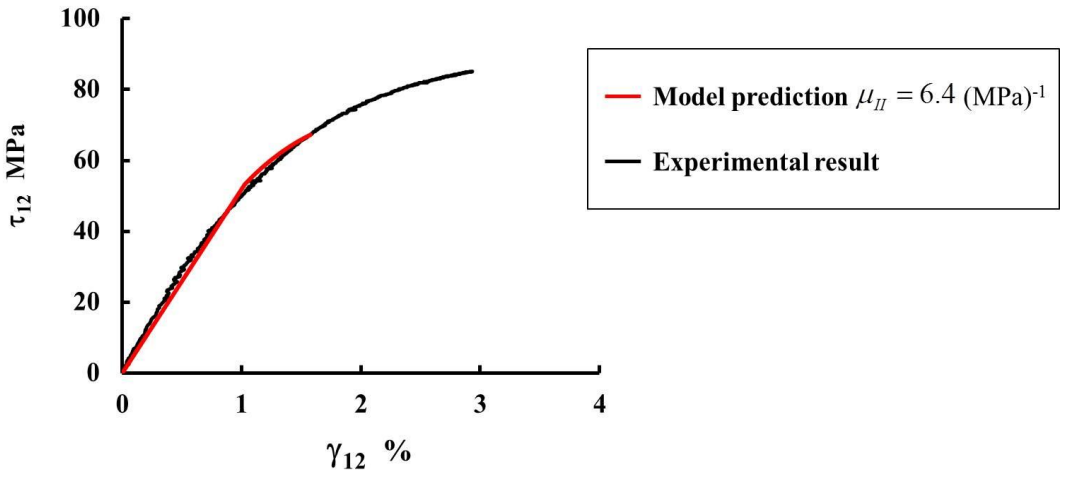

(a)

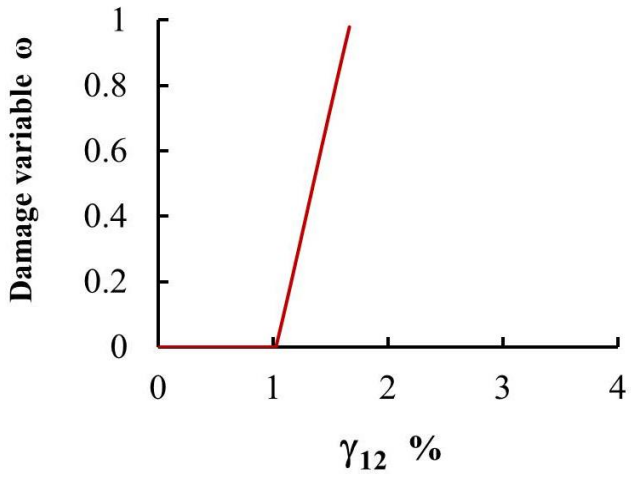

(b)

Fig. 5-26 Prediction for in-plane shear of IM7/8552 ±45° laminate: a) Stress-strain response, b) Damage variable

However, it is important to note that the experimental result of nonlinear shear behaviour included a shear nonlinearity effect in addition to pure damage effect. Therefore, strictly speaking, using only a damage model to predict the shear behaviour should not be considered as comprehensive. Here, for simplicity, all shear nonlinearity effects are represented by the damage model as an approximation.

In terms of damage prediction as shown in Fig. 5-26(b), one may notice that the predicted damage variable ω had reached 100%, which is the reason why the modelling process suffered an early termination even before 2% engineering shear strain was reached. This again demonstrates the drawback of using only a damage model to simulate the entire nonlinear shear behaviour, as in order to account for the shear nonlinearity effect, a much quicker damage evolution process has to be introduced into the CDM model, resulting in reaching 100% of damage variable at an early stage as it is in this case.

Since the ASTM D3518 shear testing method [183] used for carrying out the in-plane shear experiment does not lead to pure shear stress state in the material principal directions of the UD plies, direct stresses should arise in these directions as a result. This is successfully predicted by the CDM model and illustrated in Fig. 5-27. Moreover, ply stress in the transverse direction never reached $R_{\perp}^{T}$, therefore mode I damage never occurred in this in-plane shear test case.

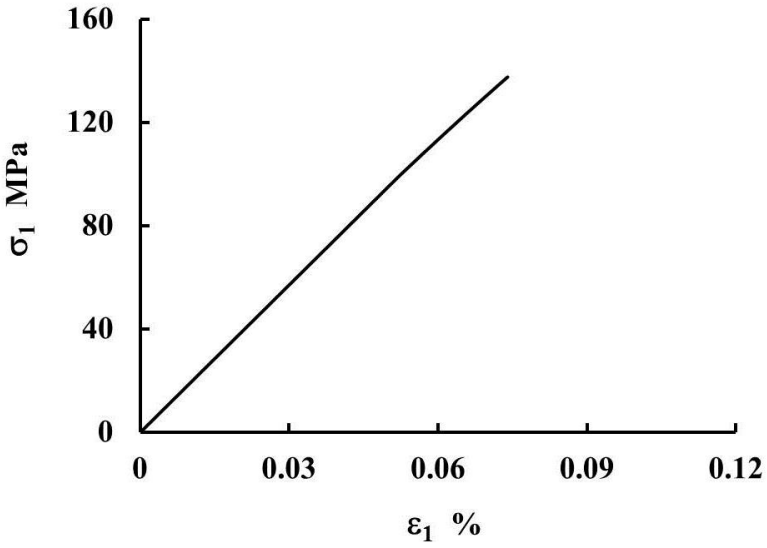

(a)

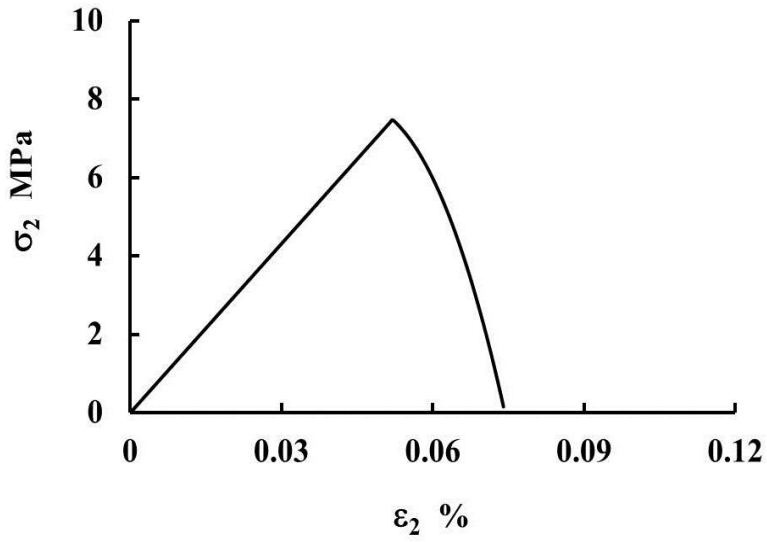

(b)

Fig. 5-27 Ply level stress prediction for in-plane shear of IM7/8552 ±45°laminate: a) Fibre direction, b) Transverse direction

However, one should still be aware that the damage caused by in-plane shear also has its effect on the stress-strain behaviour in the transverse direction according to formulation of the CDM model. This effect is visualised in Fig. 5-27(b), where, following the initiation of mode II damage, the ply-level stress in the transverse direction is shown to reduce while strain continued to increase. In the end, zero

stress value is reached in the transverse direction corresponding to the damage variable ω reaching 100%.

As shown above, with both values of μ_I and μ_{II} being demonstrated to enable the CDM model to reproduce the experimental result of the cross-ply test case and the in-plane shear test case, they are confirmed to be valid damage evolution constants for the IM7 carbon fibre UD lamina.

5.5.2 E-glass Fibre Laminates

In order to validate the CDM model against the experimental data obtained for the E-glass fibre laminates, as supplied in WWFE-I [150], the damage-related material property determination procedure is also carried out for these laminates. The laminates are based on various stacking sequences of UD laminae, in which Silenka 1200tex E-glass fibre and MY750 epoxy are the constituent materials.

The corresponding UD lamina material elastic properties and strength properties as provided in [150] are used as input parameters for the CDM model, which are summarised in Table 5-7. Thanks to the experimental data reported in [150,151] for the $[0^o/90^o]_S$ cross-ply test case and the in-plane shear test case for the E-glass fibre laminates, the damage evolution constants μ_I and μ_{II} for the E-glass fibre UD lamina are determined using the same approach as described previously in Section 5.5.1 for the IM7 carbon fibre UD lamina. These damage evolution constants are also listed in Table 5-7.

Table 5-7 E-glass/MY750UD lamina material properties used for laminate analysis

Symbol	Explanation	Value
E_1	Young's modulus in fibre direction	45.6 (GPa)
E_2	Young's modulus in transverse direction	16.2 (GPa)
G_{12}	In-plane shear modulus	5.83 (GPa)
ν_{12}	Major Poisson's ratio	0.278
ν_{23}	Transverse Poisson's ratio	0.4
k	Coupled damage effect factor between transverse tensile damage and longitudinal shear damage as defined in [180]	0.25
$p^T_{\perp\parallel}$	Slope of the failure envelope relating to transverse tensile and longitudinal shear action stresses as defined in Puck's criterion [88].	0.3
$p^C_{\perp\parallel}$	Slope of the failure envelope relating to transverse compressive and longitudinal shear action stresses as defined in Puck's criterion [88].	0.25
$R^T_{\perp}$	Transverse tensile stress threshold value for matrix damage initiation.	40 (MPa)
$R^C_{\perp}$	Transverse compressive stress threshold value for matrix damage initiation	145 (MPa)
$R_{\perp\parallel}$	Longitudinal shear stress threshold value for matrix damage initiation.	35 (MPa)
μ_I	Damage evolution constant under mode I type of loading.	0.98 $(MPa)^{-1}$
μ_{II}	Damage evolution constant under mode II type of loading.	8.6 $(MPa)^{-1}$

Similar to the procedure presented in Section 5.5.1, for assessing the validity of the damage evolution constants determined, laminate analyses are carried out using the MATLAB code to reproduce the cross-ply laminate and the in-plane shear test cases reported in [150,151] for the E-glass fibre laminate.

The experimental and the predicted stress-strain curves corresponding to the cross-ply test case are shown in Fig. 5-28. As can be seen, there is a good agreement between the two.

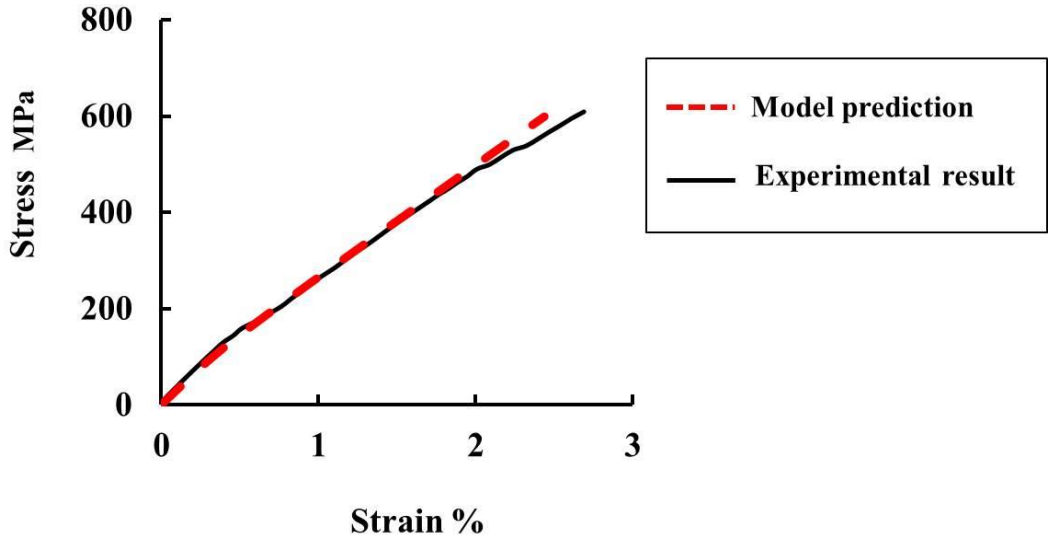

Fig. 5-28 Stress-strain prediction for the E-glass/MY750 cross-ply laminate with the experimental result

The damage variable predictions are plotted in Fig. 5-29(a). It is worth noting that in addition to the 90° plies, the matrix damage is also predicted to occur in the 0° plies at a late stage. This prediction is different from that obtained for the IM7 carbon fibre cross-ply laminate in Section 5.5.1, where damage was predicted to develop only in the 90° plies.

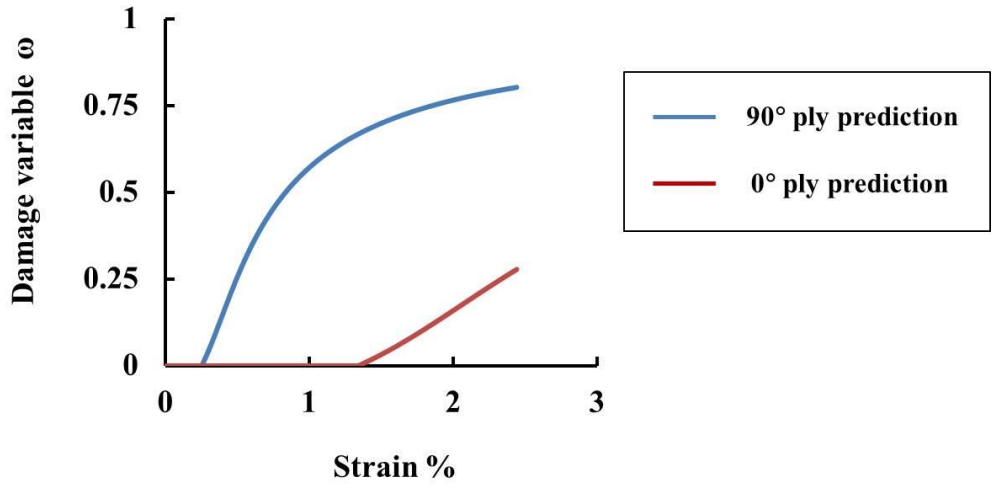

(a)

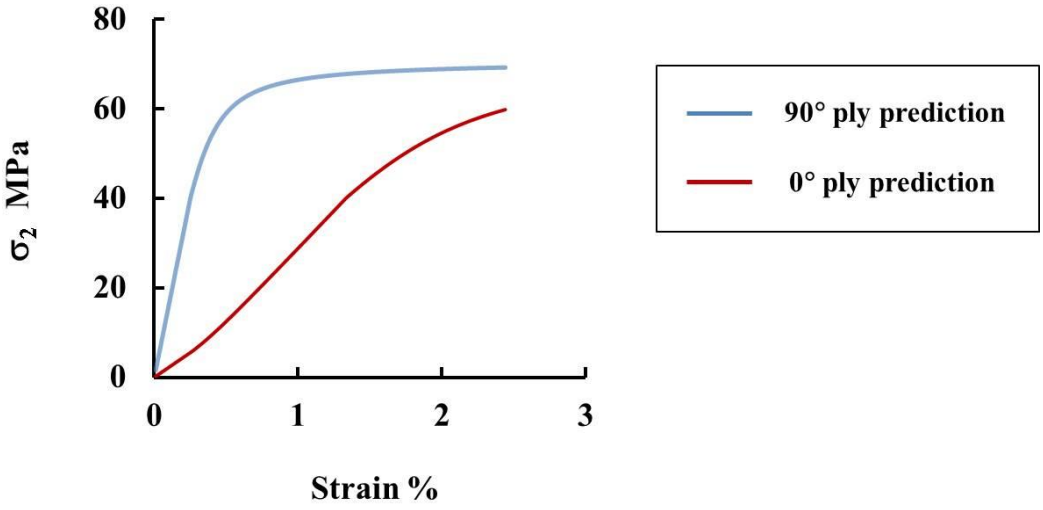

(b)

Fig. 5-29 Prediction for E-glass/MY750 cross-ply laminate: a) Damage variable, b) Ply stress

In Fig. 5-29(b), transverse stresses σ_2 in the 0° and 90° plies are plotted. Comparing Fig. 5-29(a) and Fig. 5-29 (b), one may see the cause for the predicted damage development in the 0° plies, as transverse stress in the 0° plies is predicted to reach $R_\perp^T$ (40 MPa) to trigger mode I type matrix damage.

Then, considering the stacking sequence of $[0^o/90^o]_S$ for the cross-ply laminate, it is obvious that for this test case, the transverse tensile stress in the 0° plies should be due to the combined influence from the Poisson's ratio and the constraint provided by the fibres in the 90° plies. Specifically, as the laminate was gradually loaded, the 0° plies tend to shrink in the transverse direction due to Poisson's effect. However, stiff fibres in the adjacent 90° plies would impede this natural transverse shrinkage of the 0° plies, resulting in transverse tensile stress in the 0° plies as the cross-ply laminate is loaded further, until $R_\perp^T$ is reached to trigger mode I damage in these plies.

This prediction of matrix damage in the 0° plies is validated by checking with the experimental result reported in [151] for this particular test case, where longitudinal fibre splitting damage was discovered when the actual cross-ply laminate specimen was loaded in tension just beyond 1.25% strain.

On the other hand, for the IM7 carbon fibre cross-ply laminate, damage in 0° plies was neither captured experimentally, nor predicted in the analysis in Section 5.5.1. There are two main reasons for this. First of all, the $R_\perp^T$ value of IM7 carbon fibre UD lamina (49.2 MPa) is higher than that in E-glass fibre UD lamina (40 MPa), hence the mode I matrix damage in the IM7 carbon fibre laminates is triggered at higher values of transverse tensile stress. Secondly, the IM7 carbon fibre cross-ply laminate experienced a much lower displacement (final strain) in the loading direction (Fig. 5-24(a)), which should have led to a reduced transverse shrinkage tendency for the 0° plies due to the Poisson's ratio, resulting in lower transverse tensile stress in those plies.

Apart from the cross-ply laminate analysis case, for the laminate analysis case reproducing the in-plane shear test conducted on the E-glass fibre UD laminate as reported in [150], the model prediction and the experimental result for stress-strain behaviour are presented in Fig. 5-30(a), where a good match between the two can be seen. The damage variable prediction is shown in Fig. 5-30(b). However, similar to the predicted shear response of IM7 carbon fibre UD laminates in Section 5.5.1, the damage variable ω reached 100% at an early stage. This limitation of the current CDM model for predicting shear response has already been discussed in Section 5.5.1.

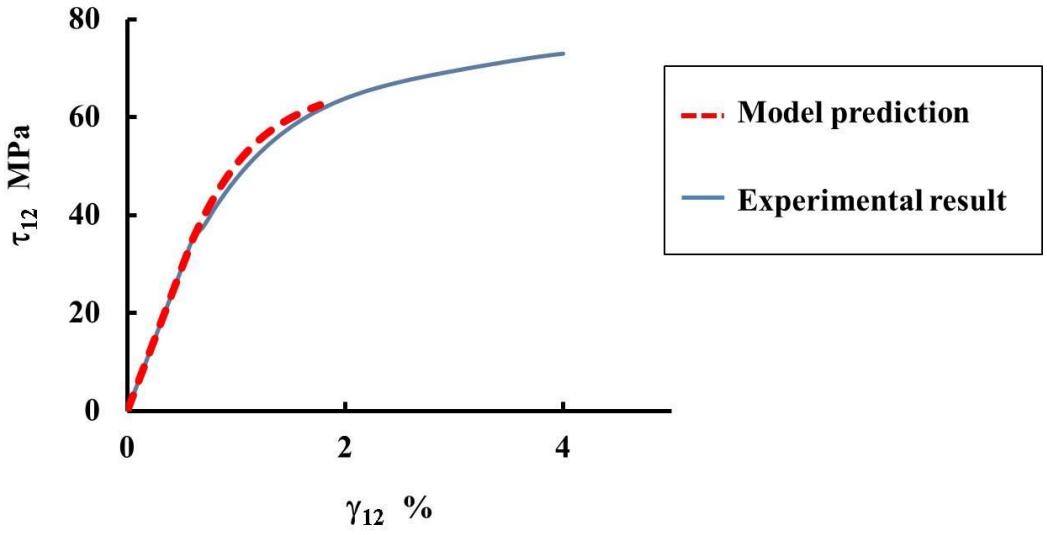

(a)

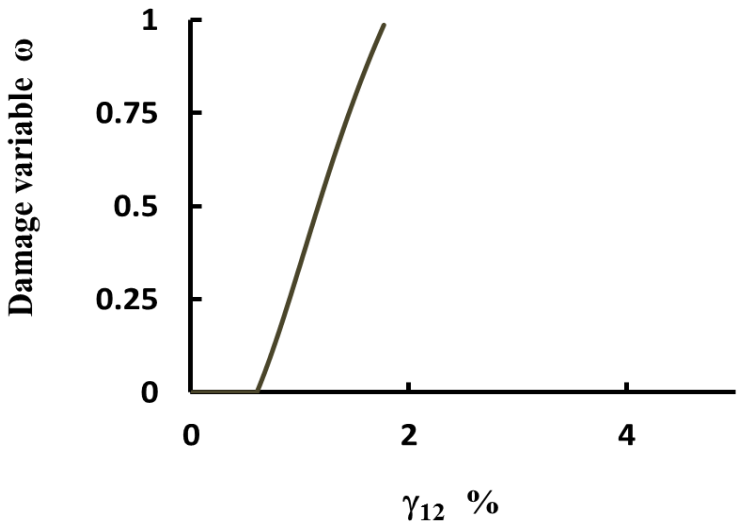

(b)

Fig. 5-30 Predictions for in-plane shear of the E-glass/MY750UD laminate: a) Stress-strain curve, b) Damage variable

5.6 Summary

With the incorporation of Puck's failure criterion for damage initiation prediction, Li's damage representation formulation and the novel damage evolution law

based on damage driving force, a new CDM model is developed and implemented for UD composites. The CDM model is implemented both in the form of a MATLAB code for laminate analysis and in the form of an ABAQUS™/Standard UMAT code for full 3D analysis.

As some sanity checks, verification work is carried out using this new CDM model for running numerical simulation examples in ABAQUS™/Standard. The verification cases demonstrated that the CDM model is correctly coded as material subroutines and the theoretical formulations are numerically verified to be mathematically sound.

Moreover, the procedure and method for the determination of damage-related material properties are presented in this chapter. The damage-related material properties of the IM7/8552 carbon fibre laminate and the E-glass/MY750 laminate material systems are determined and verified to be of correct values.

With the knowledge of these properties, the current CDM model is fully geared for the prediction of intralaminar damage in laminates and intra-tow damage in textile composites. Consequently, as shown in the next chapter, the CDM model is used to predict real-life material damage scenarios, where the validity of the predicted result is assessed against corresponding experimental result.

6. Validation of the Proposed UD Composite Damage Model

The UD composite CDM model developed in the current project has been verified in Chapter 5, where it is shown that the results produced by the model are consistent with the assumed damage evolution processes and the failure criterion of Puck. This confirmed that the CDM model has been correctly implemented as a computer code, and also verified numerically that the theoretical formulations derived in Chapter 3 are mathematically sound. However, beyond verification, to validate the CDM model, its ability to predict damage should be assessed against real-life material damage scenarios, rather than the assumed ones.

With the successful determination of damage-related material constants as shown previously in Chapter 5, in this chapter, validation of the UD composite CDM model is addressed, where the model is used to predict damage in laminates, as well as in 3D woven composites, under the same loading conditions as in the experiments described in Chapter 4. To achieve this, the UD composite CDM model is employed to define the constitutive responses of the UD laminae inside the laminates and that of the UD tows within the 3D woven composites. Predictions from the CDM model are then compared against the experimental data so that the model performance can be evaluated and validated. The experimental data from both the laminate test cases and the 3D woven composite test cases as described in Chapter 4 are used as the reference for the current validation work.

6.1 Application to Laminates

The implementation of the UD composite CDM model as a MATLAB code has been discussed in Chapter 5. The code was developed for laminate analysis, where the CDM model was used to predict the initiation and evolution of intra-laminar matrix cracking damage within the individual UD lamina inside laminates. The assumption of plane stress is adopted for laminate analysis, hence, the damage-related properties $p_{\perp\perp}^{T}$, $p_{\perp\perp}^{C}$ and μ_{III}, which are associated with the transverse shear stresses, are not involved in the material definition. All other damage-related material constants for the IM7/8552 and the E-glass/MY750 laminate material systems are determined as shown in the previous chapter, which are readily available to be used in the CDM model.

Based on the real-life laminate test cases, both reported in Chapter 4 and those available in the literature, analyses for CDM model validation are designed and implemented. These validation cases are presented in the following subsections.

6.1.1 IM7 Carbon Fibre Laminates

6.1.1.1 Uniaxial Tensile Test on IM7/8552 QI Laminates

The first validation case considered is the tensile testing of IM7/8552 QI laminate, which was described in Section 4.3.3.5. Based on the same material properties as presented earlier in Table 5-4 and Table 5-5 in Section 5.5.1 for the IM7 carbon fibre UD lamina, the analysis was conducted using the MATLAB code of the CDM model.

In Fig. 6-1, the predicted stress-strain curve is plotted along with the experimental one, showing a very close agreement between the two.

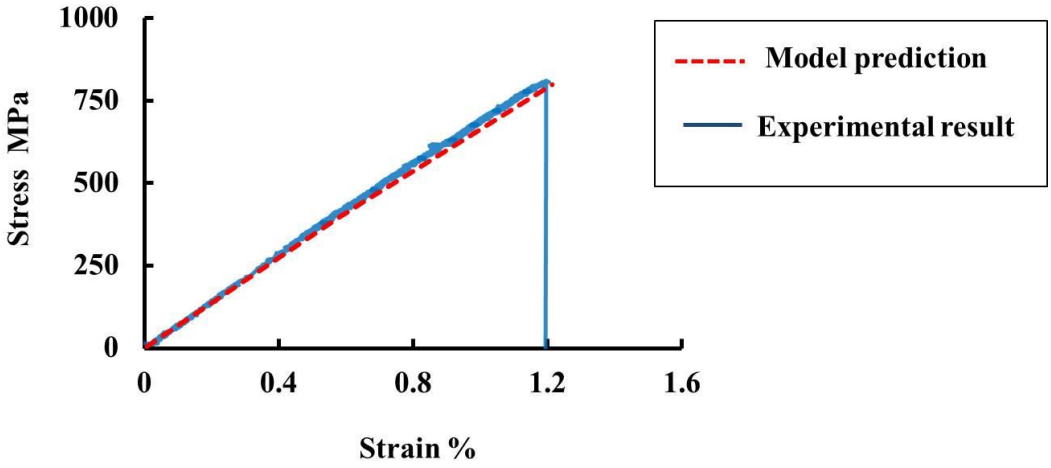

Fig. 6-1 Predicted stress-strain behaviour for the IM7/8552 QI laminate

Recall the acoustic emission data captured in the same experiment as presented in Fig. 4-8(b), which indicated that while the stress-strain curve appeared to be linear, the matrix damage had actually occurred in the QI laminates tested. This experimental observation was successfully reproduced by the CDM model. Specifically, the damage prediction plot in Fig. 6-2 demonstrates that matrix damage was indeed predicted to occur for both the 90° and ±45° plies, while in the 0° plies matrix damage did not occur since the presence of the ±45° plies introduced more transverse shrinkage and hence reduced the transverse tension in the 0° plies.

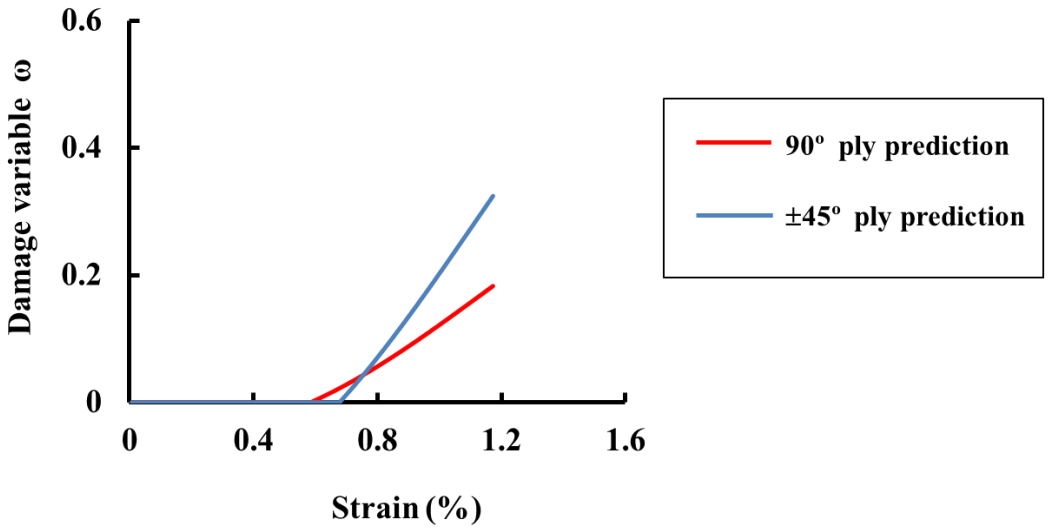

Fig. 6-2 Damage prediction for the ±45° and 90° plies in the IM7/8552 QI laminate

In order to understand why the predicted matrix damage in the ±45° plies initiated at a higher strain value than that in the 90° plies, as shown in Fig. 6-2, stresses in those plies are examined. The transverse tensile stress-strain curve in the 90° plies is shown in Fig. 6-3(a). As can be seen, the transverse stress reached the value of $R_{\perp}^{T}$ (49.2 MPa) at around 0.6% laminate strain, which led to mode I damage growth. In contrast to that, in the ±45° plies, the damage initiation point was reached after 0.6% laminate strain and the transverse tensile stress was significantly lower than that in the 90° plies. The damage initiation was in fact due to a combination of the in-plane shear stress and the transverse tensile stress, which are shown in Fig. 6-3(b). Therefore, unlike the 90° plies, the ±45° plies have experienced a mixed-mode damage scenario, with damage onset being triggered at a higher level of strain.

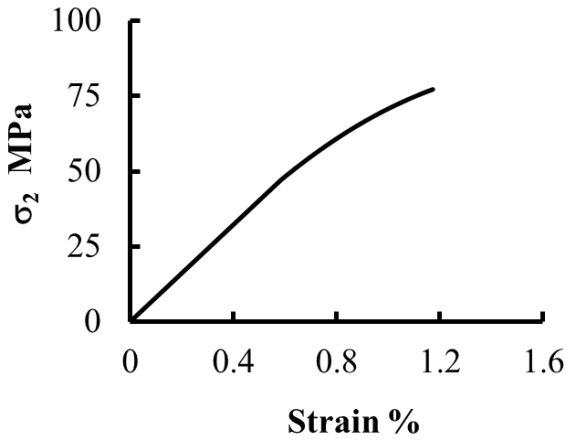

(a)

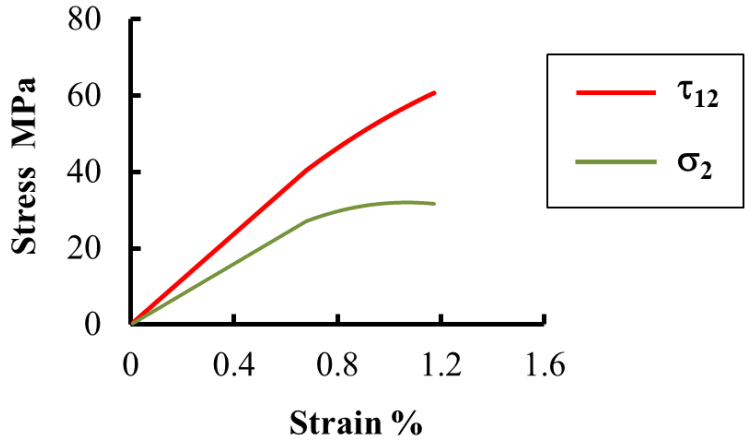

(b)

Fig. 6-3 Ply stress prediction for IM7/8552 QI laminate: a) 90˚ ply, b) ±45˚ ply

6.1.1.2 Validation Using IM7/8552 Cross-ply Laminate Test Data Reported in the Literatures

This validation case is devised based on the IM7/8552 cross-ply laminate test case reported in [197]. In there, the cross-ply laminates with $[0°/90°_4]_S$ stacking sequence were tested under uniaxial tension. Since the same laminate material system as the previous case was used, the same material elastic and damage property input data is used for the CDM model as was employed for the previous

validation case involving the IM7/8552 laminates. The only change in the input data for the CDM model is the laminate stacking sequence information as it is changed to $[0°/90°_4]_S$.

As shown in Fig. 6-4, the model reproduced the experimental result from [197] with a good degree of accuracy. This confirms that for the same material system, the same damage-related material properties as input to the CDM model should be used for the analysis, regardless of the laminate stacking sequence encountered, because these parameters are indeed inherent material properties of the UD lamina.

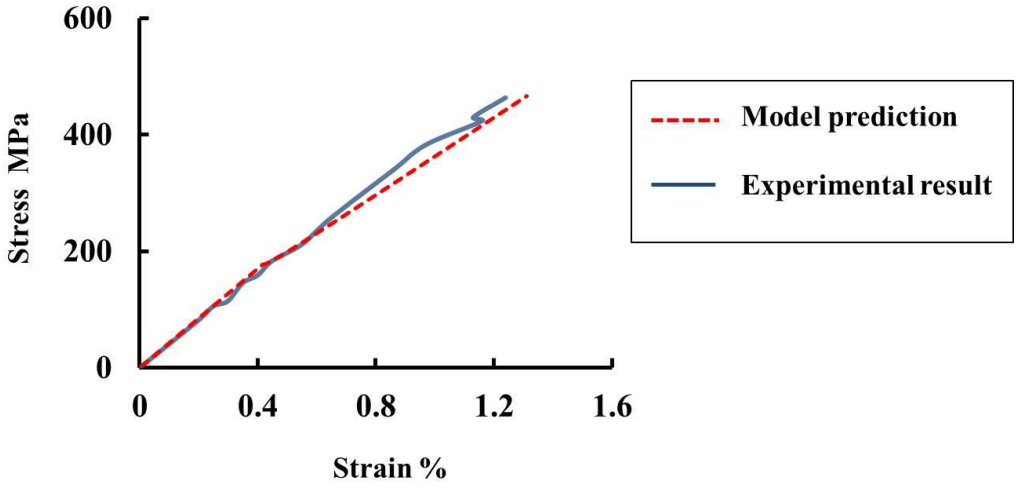

Fig. 6-4 Prediction for IM7/8552 cross-ply laminate test case reported in [197]

6.1.2 E-glass Fibre Laminates

Based on the material properties listed in Table 5-7 for the E-glass/MY750 UD lamina, the CDM model is also configured to predict the E-glass/MY750 laminate test cases documented in [151]. Comparisons between the model prediction and the experimental result are presented below.

6.1.2.1 Biaxial Tensile Test for [±45º] E-glass/MY750 Laminate at a 1:1 Stress Ratio

In this test case, a biaxial tensile stress loading with a 1:1 load ratio was applied to the [±45º] angle-ply E-glass/MY750 laminate as detailed in [151].

Since the biaxial stress loading in this case was applied symmetrically along two principal axes of this specially orthotropic laminate, in theory, the material stress-strain responses in these two loading directions should be exactly the same. However, the slight differences between the two experimental stress-strain curves in Fig. 6-5(a) are likely to be caused by experimental error. In particular, precisely the same loading rate for both loading directions to satisfy the 1:1 load ratio requirement may have not been achieved during the experiment.

On the other hand, in Fig. 6-5(a), the predicted stress-strain curves in both loading directions appeared to be identical. This is in agreement with the theoretical prediction, however, as one could imagine, this behaviour should be very difficult to demonstrate experimentally. Nonetheless, in terms of the general trend for the stress-strain behaviour, the predicted curves are in good agreement with the experimental ones.

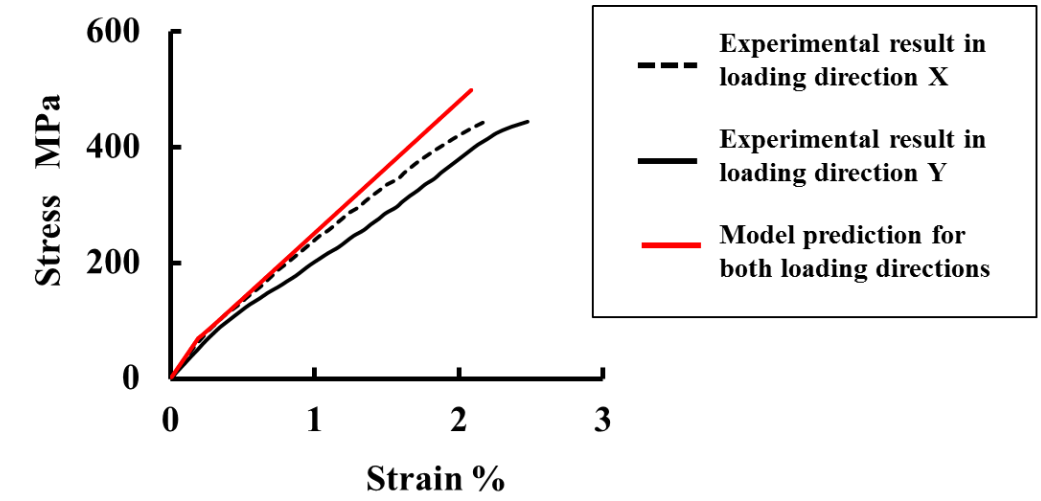

(a)

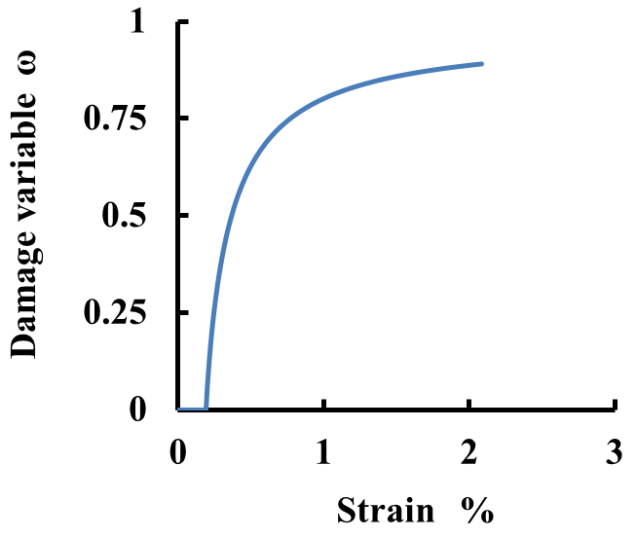

(b)

Fig. 6-5 Prediction for E-glass/MY750 [±45°] laminate: a) Stress-strain response, b) Damage variable

In terms of the damage predictions, as shown in Fig. 6-5(b), substantial matrix damage was predicted for each ply within the laminate. After checking with the ply stress prediction, it is clear that the damage was caused by ply-level transverse tensile stress as shown in Fig. 6-6(b). Furthermore, the prediction of ply-level in-plane shear stress turned out to be zero for the entire loading process, which is valid because under this particular biaxial loading scenario, in-plane shear

deformations and shear stresses are not expected to occur in this specially orthotropic laminate.

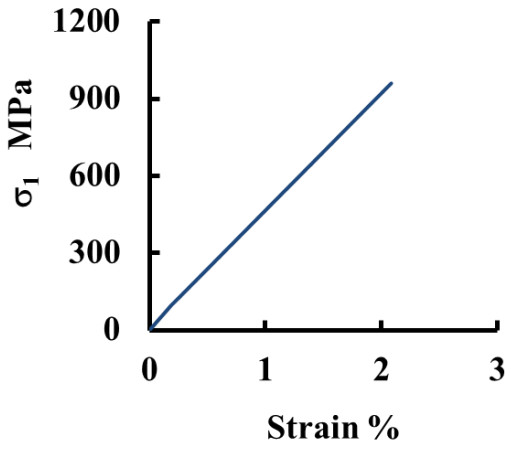

(a)

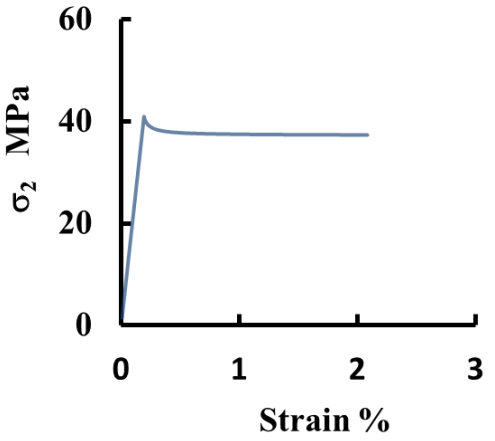

(b)

Fig. 6-6 Ply stress prediction for E-glass/MY750 [±45º] laminate: a) Fibre direction, b) Transverse direction

6.1.2.2 Biaxial Tensile Test for [±55º] E-glass/MY750 Laminate at 1:2 Stress Ratio

Another validation case devised based on the test data in WWFE-I [151] is an angle-ply E-glass/MY750 laminate with a stacking sequence of [±55º] subjected

to a biaxial tensile loading, for which the stress ratio of $\sigma_X : \sigma_Y$ was maintained at 1:2. As shown in Fig. 6-7, the stress-strain curves predicted by the CDM model are similar to the experimental ones, but with notable deviations at higher strain values.

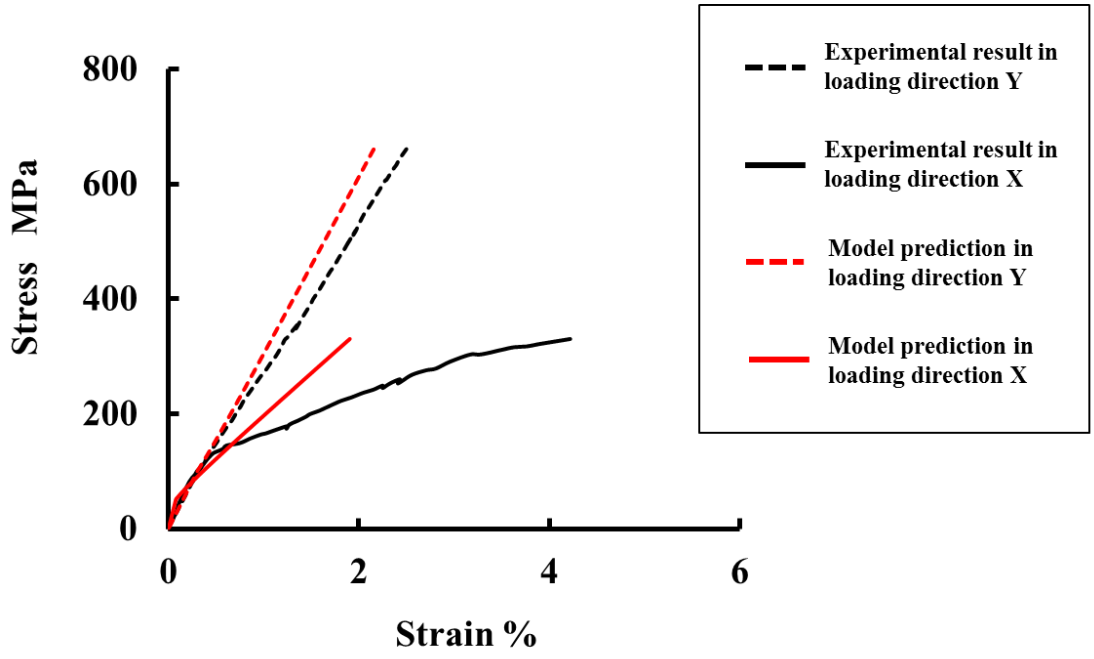

Fig. 6-7 Stress-strain plots of biaxial tensile test on E-glass/MY750 [±55º] laminate

To understand the cause for such discrepancies, especially that between the *X*-direction stress-strain curves, the damage prediction plot shown in Fig. 6-8 was analysed. It can be seen that, even with the damage variable value approaching 100% in Fig. 6-8, the CDM model still did not reproduce the severe *X*-direction stress-strain nonlinearity demonstrated by the experimental result in Fig. 6-7.

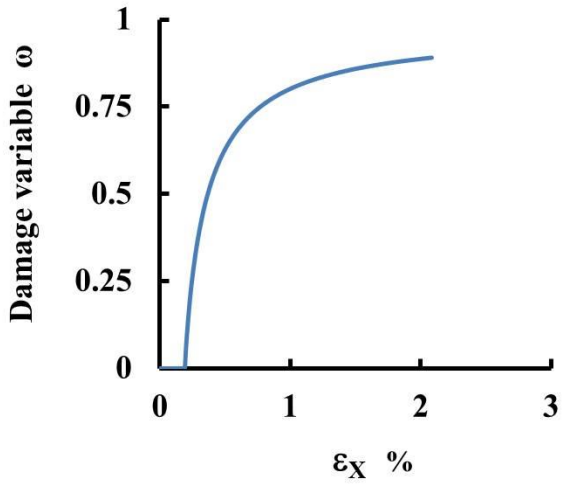

Fig. 6-8 Damage variable VS strain in the *X*-direction for biaxial tensile test on E-glass/MY750 [±55º] laminate

Since the laminate was not orthotropic, it should have exhibited some in-plane shear deformation. This is confirmed by outputting the transverse direction and in-plane shear direction ply stress curves as shown in Fig. 6-9. As can be seen, both the in-plane shear and the transverse tensile stresses contributed to damage growth in every ply of the laminate. Consequently, the matrix damage predicted should be of mixed-mode type.

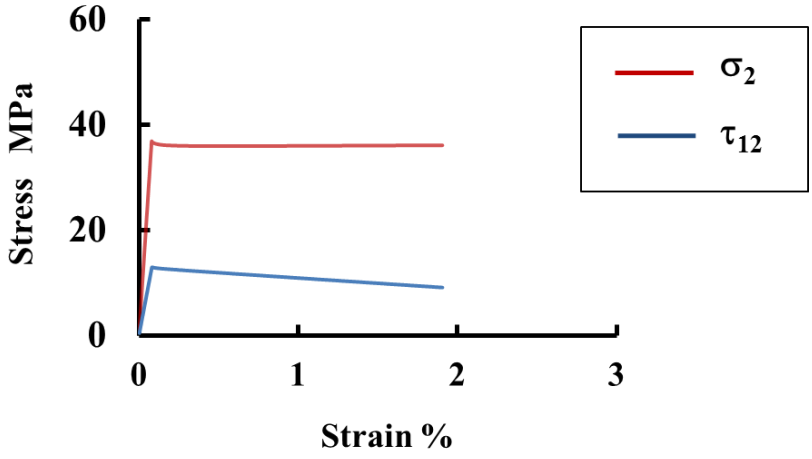

Fig. 6-9 Ply stress prediction for biaxial tensile test on E-glass/MY750 [±55º] laminate

Based on this, it is envisaged that the limited ability of the CDM model in simulating shear nonlinearity, as well as the material local failures that might have occurred in the specimen during the experiment, have all contributed to the discrepancies between the predictions and the experimental results for this non-symmetric biaxial loading case. However, the general trend of the stress-strain curves was captured by the CDM model reasonably well.

6.1.2.3 Uniaxial Tensile Test on E-glass/MY750 [±55º] Laminate

In Fig. 6-10, both the predicted and the experimental stress values in *X*-direction (the loading direction) are plotted against the strains in *X*- and *Y*-directions. As can be seen, the CDM model produced a good approximation of the experimental data, but only at small strain values.

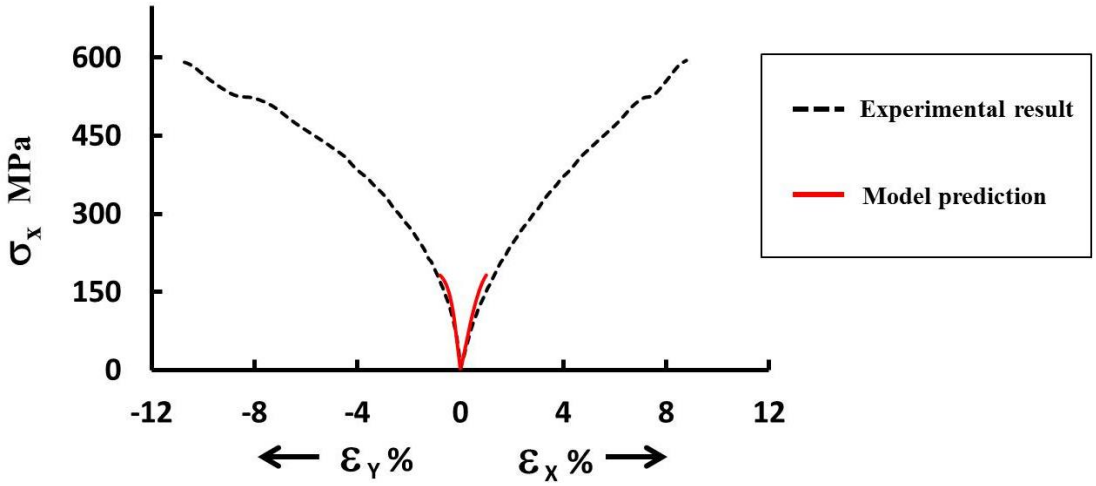

Fig. 6-10 Ply Stress-strain plots for uniaxial tensile test on E-glass/MY750 [±55º] laminate

Again, the same reasoning applies here for this phenomenon as was given previously in Section 6.1.2.2 when discussing the issue of shear modelling.

Namely, since the CDM model did not incorporate an extended definition for the shear nonlinearity, the damage variable reached 100% due to shear.

This is confirmed by plotting the damage variable ω against the strain in the loading direction as shown in Fig. 6-11, where the damage variable reached its maximum value of unity when the strain was still relatively small.

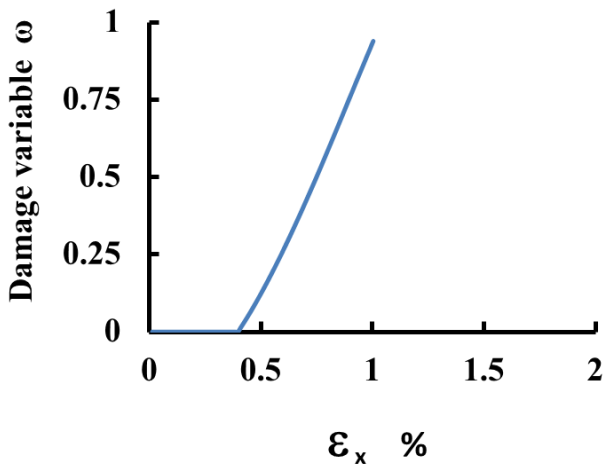

Fig. 6-11 Damage prediction for uniaxial tensile test on E-glass/MY750 [±55°] laminate

Also, as shown in Fig. 6-12, this damage was apparently caused by the ply-level in-plane shear stress predicted, as it went beyond the damage initiation stress $R_{\perp\parallel}$ (35 MPa) for mode II type damage.

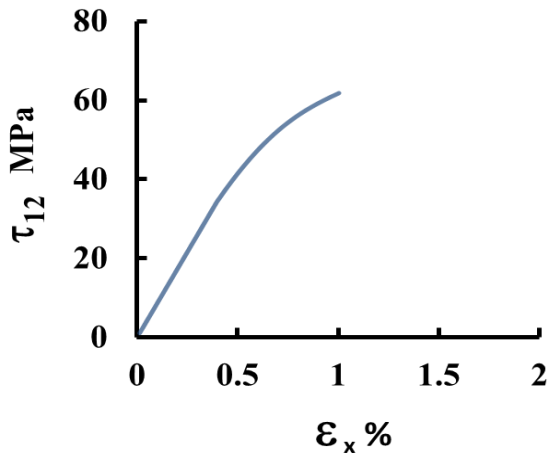

Fig. 6-12 Ply stress prediction for uniaxial tensile test on E-glass/MY750 [±55º] laminate

6.1.3 Summary of Model Validation using Laminate Test Cases

The CDM model validation against the experimental data obtained from various laminate tests has confirmed that the model can be applied to laminate analysis with some promising outcomes.

As long as the damage model is calibrated based on the experimental data obtained from uniaxial tensile tests on cross-ply laminates and in-plane shear tests on UD laminates, it is ready for independent prediction of damage and stress-strain response for laminates of various stacking sequences under different loading conditions.

The only shortfall exposed for the model is the lack of capability to predict a severe stress-strain nonlinearity caused by shear. Whenever there was a strong presence of shear, model prediction deviated away from the experimental data.

It can therefore be concluded that the current CDM model is capable of delivering accurate predictions of damage in laminates for loading cases where the shear deformation involved is small.

6.2 Application to the 3D Woven Composites

After being validated by the laminate test data, the UD composite CDM model is also applied to predict the intra-tow damage in the 3D woven composites used for this research project. The corresponding analyses are conducted in ABAQUS™/Standard, where the 3D woven composites are represented by unit cell models. The damage model is implemented in the unit cell models as a user-defined material subroutine, UMAT, to define the constitutive behaviour of the tows within the 3D woven composites. In this chapter, these unit cell analysis cases for intra-tow damage prediction are presented.

6.2.1 Unit Cell Analysis of Undamaged 3D Woven Composites

Before attempting the prediction of intra-tow damage using the unit cell analysis, credible and validated unit cell models which can accurately predict undamaged material properties for the 3D woven composites investigated in this research project should be established. Only then, can these validated 3D woven composite unit cell models be used to incorporate the UD composite CDM model in the form of UMAT for intra-tow damage prediction.

To determine undamaged material properties for both the IM7 carbon fibre and the E-glass fibre reinforced 3D woven composites mentioned in Chapter 4, unit cell models of two length-scale levels are developed.

The first level of unit cell analysis is categorised as microscopic level analysis to predict the effective properties of the tows which are modelled as UD composites. The next level of analysis is meso-scale where effective properties of the 3D

woven composites are predicted with the tows considered as UD composites suspended in the matrix in a configuration as defined by the weave pattern of the 3D woven composites.

Both levels of unit cell analyses are carried out using ABAQUS™/Standard with periodic boundary conditions as formulated in [198] applied to the models so that uniaxial direct stress and pure shear stress loadings can be properly assigned. To obtain the effective properties, load perturbations are applied in terms of uniaxial direct stresses and pure shear stresses. The resulting stress and strain values are then used for effective material property calculation. An automated material characterisation toolbox named as UnitCells© is used for implementing the unit cell analysis cases. Details of the toolbox and the procedure involved for carrying out analysis can be found in [1].

As shown in Fig. 6-13, as the first step, the geometrical models for the 3D woven composite unit cells are constructed according to the actual fabric parameters (Table 4-13, Table 4-16, Table 4-20, Table 4-22) and weave pattern CT images (Fig. 4-10 - Fig. 4-12 and Fig. 4-26 - Fig. 4-28) presented in Chapter 4.

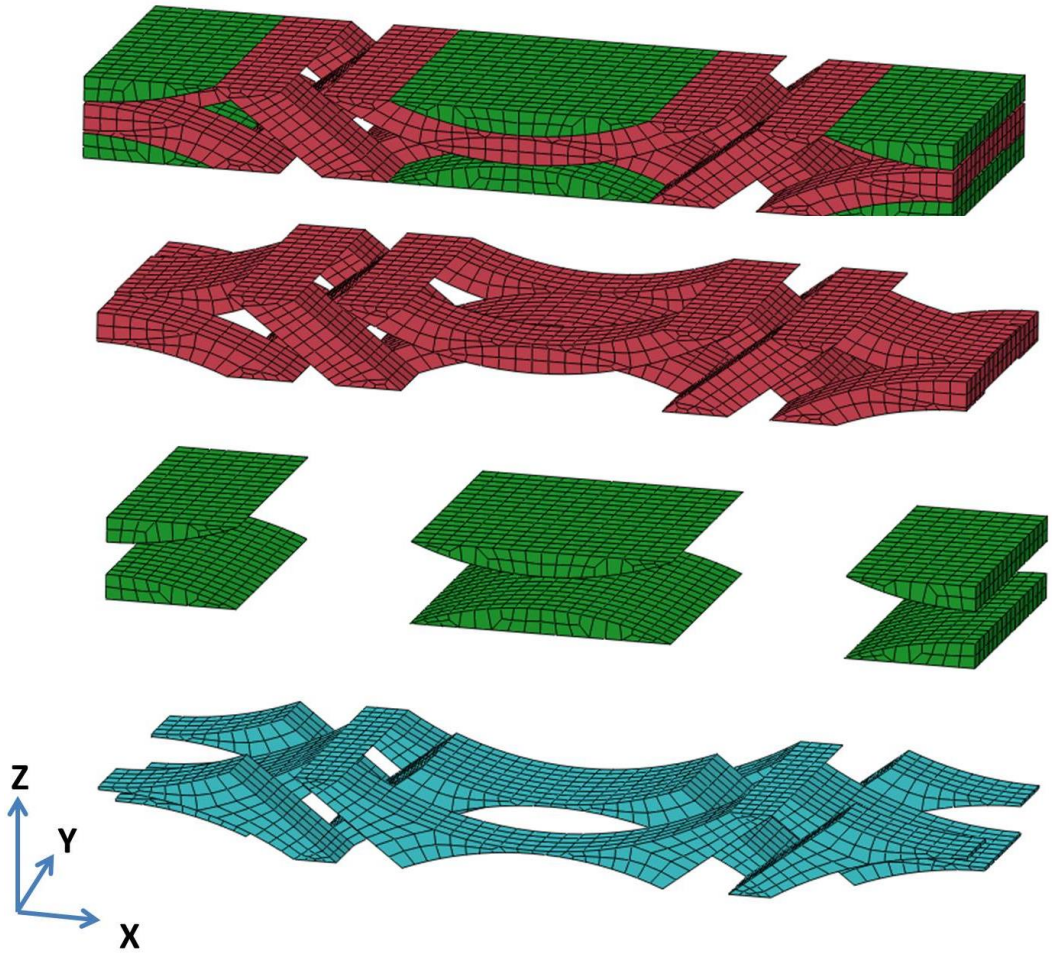

Fig. 6-13 Unit cell model for the 3D woven composites showing mesh of warp tows (red), weft tows (green) and pure matrix material (blue)

Then, based on these geometrical models, using (6-1) and (6-2) below, weft and warp tow volume fractions can be worked out as shown in Table 6-1.

$$V_{t-weft} = \frac{\text{Volume of all weft tows}}{\text{Total volume of 3D woven composites}} \qquad (6\text{-}1)$$

$$V_{t-warp} = \frac{\text{Volume of all warp tows}}{\text{Total volume of 3D woven composites}} \qquad (6\text{-}2)$$

Table 6-1 Tow volume fractions determined from unit cell models

Material type	V_{t-warp} (%)	V_{t-weft} (%)
IM7 CF 3D woven composites	43.8	28.8
GF 3D woven composites	38.2	26.1

Using these calculated tow volume fractions, along with total fibre volume fractions V_f of the 3D woven composites and the weft-to-warp ratios $R_{weft-warp}$ provided by the material manufacturer in Table 4-13 and Table 4-20, the fibre volume fractions within the weft and warp tows can be estimated according to (6-3) and (6-4). These fibre volume fractions are summarised in Table 6-2

$$V_{f-weft} = \frac{V_f R_{weft-warp}}{V_{t-weft}\left(1+R_{weft-warp}\right)} \tag{6-3}$$

$$V_{f-warp} = \frac{V_f}{V_{t-warp}\left(1+R_{weft-warp}\right)} \tag{6-4}$$

Table 6-2 Fibre volume fraction within tows

Material type	V_{f-warp} (%)	V_{f-weft} (%)
IM7 CF 3D woven composites	78.1	74.1
GF 3D woven composites	79.3	75.5

With V_{f-warp} and V_{f-weft} obtained, microscopic level (UD composites) unit cell models are created (Fig. 6-14) such that the unit cell total volume and the

geometrical entity simulating pure fibre are adjusted to correctly represent V_{f-warp} and V_{f-weft} for different tows.

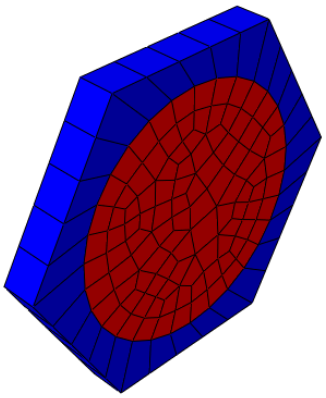

Fig. 6-14 Microscopic level unit cell model for predicting effective tow properties

Then, using material properties in Table 4-5, Table 4-15 and Table 4-21 for pure fibre and cured pure matrix materials, effective properties of undamaged warp and weft tows (Table 6-3 & Table 6-4) are predicted by microscopic level unit cell analyses.

Table 6-3 Tow elastic properties for IM7 CF 3D woven composites

Properties	Values for warp tow	Values for weft tow
E_1 (GPa)	217	207
E_2 $(=E_3)$ (GPa)	12.2	11.3
G_{12} $(=G_{13})$ (GPa)	5.29	4.8
G_{23} (GPa)	4.21	3.91
ν_{12}	0.29	0.3

Table 6-4 Tow elastic properties for GF 3D woven composites

Properties	Values for warp tow	Values for weft tow
E_1 (GPa)	58.9	56.1
$E_2\ (=E_3)$ (GPa)	22.9	19.6
$G_{12}\ (=G_{13})$ (GPa)	8.39	7.13
G_{23} (GPa)	8.62	7.38
ν_{12}	0.24	0.25

With tow elastic properties determined by microscopic level unit cell analysis, these properties along with the pure matrix properties then served as material property inputs for meso-scale unit cell analysis. These analyses are based on unit cell models like the one in Fig. 6-13, where tows are explicitly modelled as UD composites.

After carrying out meso-scale level unit cell analysis, effective elastic properties for the 3D woven composites (Table 6-5 and Table 6-6) are obtained. As can be seen from Table 6-5 and Table 6-6, the predicted values for E_X, E_Y and G_{XY} are close to the experimental result, which validated the applicability of unit cell analyses as a mean for multi-scale material characterisation.

Table 6-5 Effective elastic properties for the IM7 CF 3D woven composite

Properties	Unit cell analysis prediction	Experimental result
E_X (GPa)	43.9	37.8
E_Y (GPa)	62.9	62.7
E_Z (GPa)	8.44	
G_{XY} (GPa)	3.21	3.92
G_{XZ} (GPa)	4.65	
G_{YZ} (GPa)	2.68	
ν_{XY}	0.01	
ν_{XZ}	0.96	
ν_{YZ}	0.43	

Table 6-6 Effective elastic properties for the GF 3D woven composite

Properties	Unit cell analysis prediction	Experimental result
E_X (GPa)	23.7	21.8
E_Y (GPa)	24.8	25.7
E_Z (GPa)	11.6	
G_{XY} (GPa)	5.28	4.03

G_{XZ} (GPa)	5.59	
G_{YZ} (GPa)	4.41	
ν_{XY}	0.12	
ν_{XZ}	0.48	
ν_{YZ}	0.33	

6.2.2 Validation Cases using Unit Cell Models and Intra-tow CDM Model

With the incorporation of the UD composite CDM model, new analysis cases are set up based on the validated unit cell models mentioned above to predict the intra-tow damage inside the 3D woven composites.

In order to conduct the analysis, material property input has to be specified for the tows. According to the UD composite CDM model formulation, both the elastic and the damage-related material properties are required for the tows. For the former, these are already determined by the micro-scale unit cell analysis of tows as reported in the previous section (Table 6-3 & Table 6-4). However, for the latter, which is still unknown, acquiring these properties experimentally by mechanical testing of the individual tows is impractical.

Since the radius of curvature of the tow in the 3D woven composites is orders of magnitude greater than the diameter of the fibres within the tows, the tows can be effectively considered to be straight, therefore regarded as UD composites at microscale. It is anticipated that their mechanical behaviour should be

satisfactorily predicted as a UD lamina at macroscale, provided that the same constituents and the fibre volume fraction are employed. Following this logic, the damage-related properties for intra-tow cracking in the warp and weft tows could be determined from testing on laminates having the same fibre volume fractions. For this research, both the IM7 carbon fibre and the E-glass fibre 3D woven composites tested had the warp tow fibre volume fraction at around 78% and the weft tow fibre volume fraction at around 74% (Table 6-2). However, manufacturing and testing UD laminates with those specific characteristics is not possible due to limited resources available and the time constraints, hence, alternative solution is proposed.

As the best available alternative, damage-related properties previously determined for the IM7 carbon fibre and the E-glass fibre laminates as listed in Table 5-5, Table 5-6 and Table 5-7 are used for modelling the tows. In doing so, the implication is that the difference in fibre volume fractions and the difference in matrix material systems between the laminates and the tows are assumed to have negligible influence on the damage-related properties, such that these determined from the laminate tests can be used for modelling the tows of the same fibre material type.

In addition to this, owing to the lack of experimental data for μ_{III}, a further assumption is made regarding the damage evolution constants: μ_{III} values due to transverse shear loading are assumed to be the same as the values of μ_{II} due to longitudinal shear loading.

With damage-related material properties defined as described above, the complete sets of input properties for the IM7 carbon fibre tow and the E-glass fibre tow are

given in Table 6-7 and Table 6-8. As can be seen, elastic properties for the tows are the same as those shown previously in Table 6-3 and Table 6-4.

Table 6-7 IM7 carbon fibre tow material properties

Symbol	Explanation	Value for warp	Value for weft
E_1	Young's modulus in fibre direction	217 (GPa)	207 (GPa)
$E_2\ (=E_3)$	Young's modulus in transverse direction	12.2 (GPa)	11.3 (GPa)
$G_{12}\ (=G_{13})$	Longitudinal shear modulus	5.29 (GPa)	4.8 (GPa)
G_{23}	Transverse shear modulus	4.21 (GPa)	3.91 (GPa)
ν_{12}	Major Poisson's ratio	0.29	0.3
k	Coupled damage effect factor between transverse tensile damage and longitudinal shear damage as defined in [180]	0.19	0.18
σ_{f-T}	Pure fibre ultimate tensile strength [189]	5655 (MPa)	
σ_{f-C}	Pure fibre ultimate compressive strength [189]	1716 (MPa)	
E_{1f}	Pure fibre longitudinal direction Young's modulus [189]	276 (GPa)	
υ_{12f}	Pure fibre major Poisson's ratio [189]	0.21	
$m_{\sigma f}$	Stress magnification factor for fibre bundles as defined in Puck's criteria [88]	1.1	
$p_{\perp\perp}^{T}$	Slope of the failure envelope relating to transverse tensile and transverse shear action stresses	0.27	

	as defined in Puck's criteria [88]	
$p_{\perp\perp}^{C}$	Slope of the failure envelope relating to transverse compressive and transverse shear action stresses as defined in Puck's criteria [88]	0.28
$p_{\perp\parallel}^{T}$	Slope of the failure envelope relating to transverse tensile and longitudinal shear action stresses as defined in Puck's criteria [88]	0.35
$p_{\perp\parallel}^{C}$	Slope of the failure envelope relating to transverse compressive and longitudinal shear action stresses as defined in Puck's criteria [88]	0.3
$R_{\perp}^{T}$	Transverse tensile stress threshold value for matrix damage initiation	49.2 (MPa)
$R_{\perp}^{C}$	Transverse compressive stress threshold value for matrix damage initiation [196]	286 (MPa)
$R_{\perp\parallel}$	Longitudinal shear stress threshold value for matrix damage initiation	55.9 (MPa)
μ_{I}	Damage evolution constant under mode I type of loading.	0.69 $(MPa)^{-1}$
μ_{II}	Damage evolution constant under mode II type of loading.	6.4 $(MPa)^{-1}$
μ_{III}	Damage evolution constant under mode III type of loading.	6.4 $(MPa)^{-1}$

Table 6-8 E-glass fibre tow material properties

Symbol	Explanation	Value for warp	Value for weft
E_1	Young's modulus in fibre direction	58.9 (GPa)	56.1 (GPa)
$E_2\ (=E_3)$	Young's modulus in transverse direction	22.9 (GPa)	19.6 (GPa)
$G_{12}\ (=G_{13})$	Longitudinal shear modulus	8.39 (GPa)	7.13 (GPa)
G_{23}	Transverse shear modulus	8.62 (GPa)	7.38 (GPa)
ν_{12}	Major Poisson's ratio	0.24	0.25
k	Coupled damage effect factor between transverse tensile damage and longitudinal shear damage as defined in [180]	0.24	0.23
σ_{f-T}	Pure fibre ultimate tensile strength [150]	2150 (MPa)	
σ_{f-C}	Pure fibre ultimate compressive strength [150]	1450 (MPa)	
E_{1f}	Pure fibre longitudinal direction Young's modulus [150]	74 (GPa)	
υ_{12f}	Pure fibre major Poisson's ratio [150]	0.23	
$m_{\sigma f}$	Stress magnification factor for fibre bundles as defined in Puck's criteria [88]	1.3	
$p^T_{\perp\perp}$	Slope of the failure envelope relating to transverse tensile and transverse shear action stresses as defined in Puck's criteria [88]	0.23	

$p_{\perp\perp}^{C}$	Slope of the failure envelope relating to transverse compressive and transverse shear action stresses as defined in Puck's criteria [88]	0.24
$p_{\perp\parallel}^{T}$	Slope of the failure envelope relating to transverse tensile and longitudinal shear action stresses as defined in Puck's criteria [88]	0.3
$p_{\perp\parallel}^{C}$	Slope of the failure envelope relating to transverse compressive and longitudinal shear action stresses as defined in Puck's criteria [88]	0.25
$R_{\perp}^{T}$	Transverse tensile stress threshold value for matrix damage initiation	40 (MPa)
$R_{\perp}^{C}$	Transverse compressive stress threshold value for matrix damage initiation	145 (MPa)
$R_{\perp\parallel}$	Longitudinal shear stress threshold value for matrix damage initiation	35 (MPa)
μ_{I}	Damage evolution constant under mode I type of loading.	$0.98\ (MPa)^{-1}$
μ_{II}	Damage evolution constant under mode II type of loading.	$8.6\ (MPa)^{-1}$
μ_{III}	Damage evolution constant under mode III type of loading.	$8.6\ (MPa)^{-1}$

For modelling the neat matrix material as in the resin pockets of textile composites, since no resin crack was observed in the resin rich areas of the tested 3D woven composite samples, elements in the unit cell models representing neat matrix are assigned with linear elastic isotropic material behaviour where the corresponding input properties are listed in Table 6-9.

Table 6-9 Cured properties of Gurit Prime™ 20LV epoxy material [193]

Symbol	Explanation	Value
E	Young's modulus	3500 (MPa)
ν	Poisson's ratio	0.35

6.2.2.1 IM7 Carbon Fibre Specimens under Warp Direction Uniaxial Tension

The experiment of tensile testing on the IM7 CF 3D woven composite in the warp direction has been reported in Section 4.4.2.2.1. The stress-strain prediction from the unit cell analysis for this case is plotted in Fig. 6-15 along with the experimental result. As can be seen, there is a large discrepancy between the two curves, where the predicted stress-strain curve is linear, while the one obtained in the experiment is highly nonlinear.

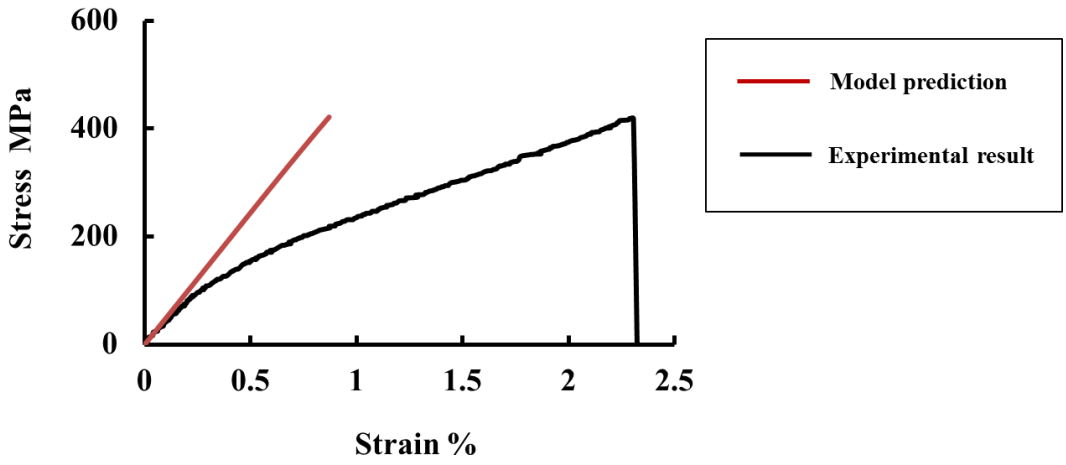

Fig. 6-15 Stress-strain prediction for the IM7 CF 3D woven composite under warp direction tension

Given that the inter-tow cracking damage has not yet been accounted for in the present unit cell analysis, it can be concluded that the intra-tow damage alone has little effect on the stiffness reduction in the 3D woven composite considered, hence the predicted stress-strain response is almost linear. Furthermore, the experimental study in Section 4.4.2.2.1 suggests that the inter-tow cracks be the main contributor for stress-strain nonlinearity in this case. As a result, without the capability to predict the inter-tow damage, it is expected that the model would not be able to reproduce the experimental stress-strain curve.

Nonetheless, modelling the intra-tow damage alone allows one to assess whether the predicted response of the tows is reasonable, without the interference of inter-tow damage, which would serve as an indicator for the validity of the model. Since the tensile loading is applied in the warp direction, fibres in the warp tows should withstand the majority of the applied load. At the same time, the fibre direction of weft tows should be under compression due to the transverse contraction of the 3D woven composite caused by Poisson's effect. From Fig. 6-16, it can be seen that this scenario is indeed captured by the model.

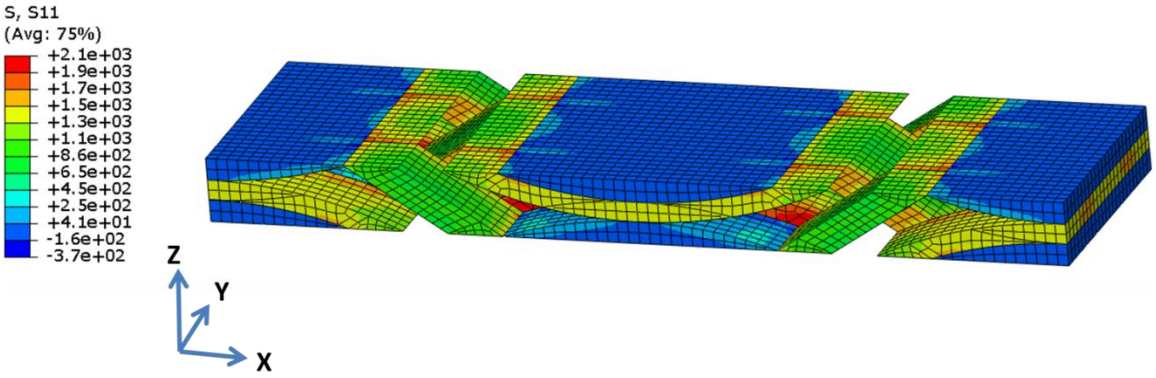

Fig. 6-16 Tow longitudinal stress contour plot for the IM7 CF 3D woven composite under warp direction tension

The damage contour plot shown in Fig. 6-17 indicates that the intra-tow matrix damage is predicted to occur in both the weft and warp tows. Moreover, in both cases, the damage is found to be concentrated in the warp curving regions as marked by the red ellipse in Fig. 6-17, instead of being evenly distributed along the tows. The predicted damage localisation offers an explanation as to why the intra-tow matrix damage was not observed in the middle of the weft tows during the experimental investigation for this test case (Section 4.4.2.2.1).

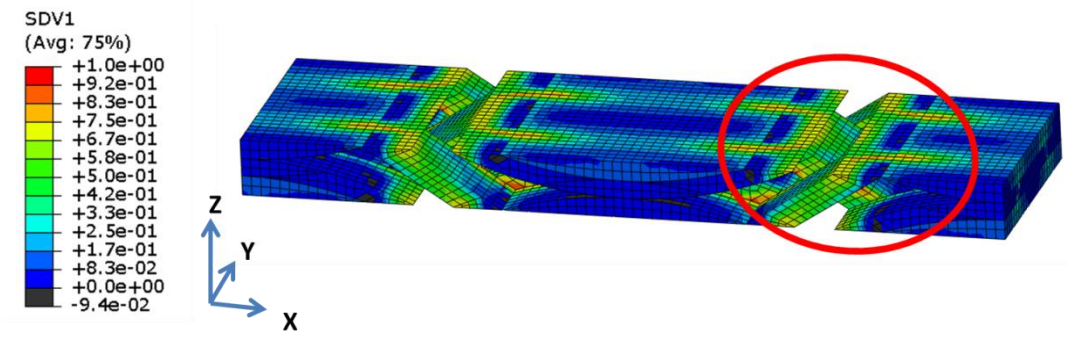

Fig. 6-17 Damage variable contour plot for IM7 CF 3D woven composite under warp direction tension

To understand why the unit cell model has arrived at such a damage prediction, stress distributions within the tows are inspected.

According to the failure theory of Puck [88], which is employed in the current CDM model to define the onset of intra-tow damage, the damage initiation conditions are satisfied on the predicted fracture plane of matrix crack. Therefore, in order to identify the stress components that caused the intra-tow matrix damage, the stresses on this very fracture plane should be examined. For this, the tow elements that sustained high degree of intra-tow damage and positioned closely to the warp curving regions are selected, and stress outputs for those elements are inspected. In the weft tows, the position of such a critical stressed part is marked by a black arrow in Fig. 6-18.

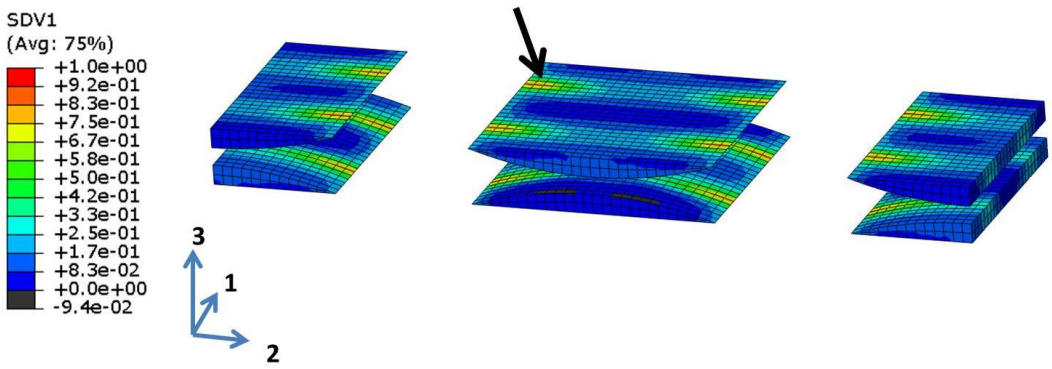

Fig. 6-18 Weft tow damage variable contour plot and the selected element for result inspection

For an element in this part, the stress output on the fracture plane is plotted in Fig. 6-19(a), while the damage prediction is plotted in Fig. 6-19(b). As can be seen, in this case, the transverse tensile, longitudinal shear and transverse shear stresses all contributed to the damage initiation and growth. With reference to the weft tow material principal coordinate system as shown in Fig. 6-18, the fracture plane orientation predicted is at 20.6º anticlockwise from the second material principal axis.

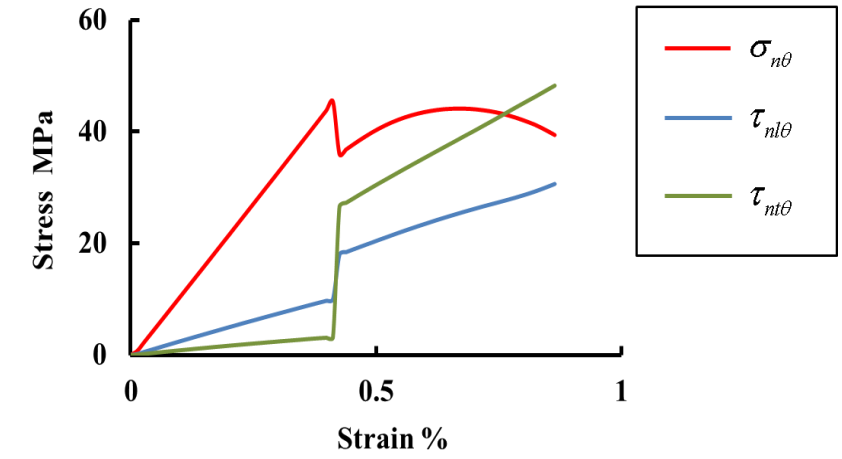

(a)

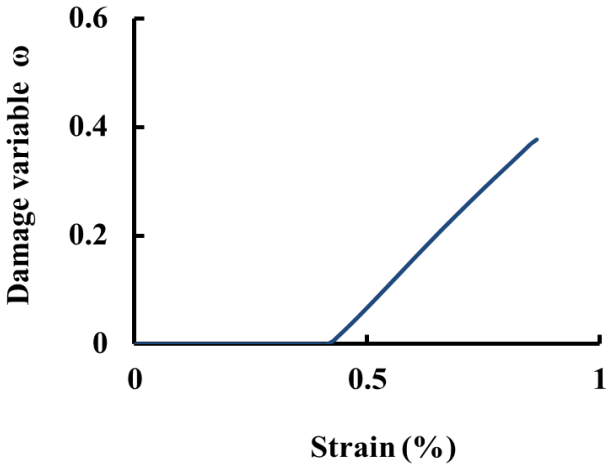

(b)

Fig. 6-19 Damaged weft tow element result: a) Stresses on the fracture plane, b) Damage variable

The stresses causing the damage have been identified to be those in the weft tows. The weft tow stress contour plots of σ_2, σ_3 and τ_{13} are therefore extracted from the analysis and presented in Fig. 6-20.

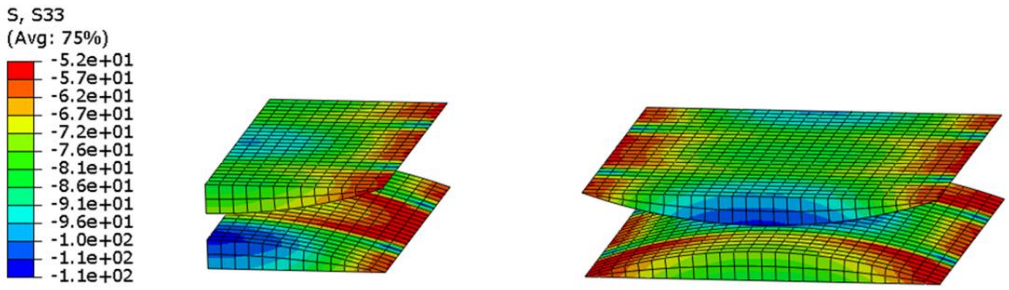

(a)

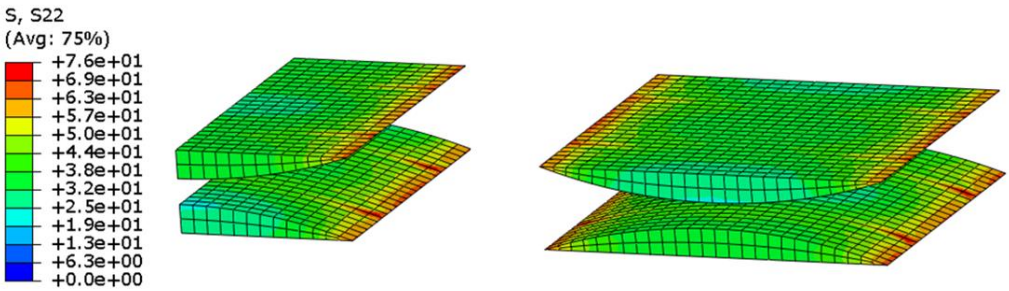

(b)

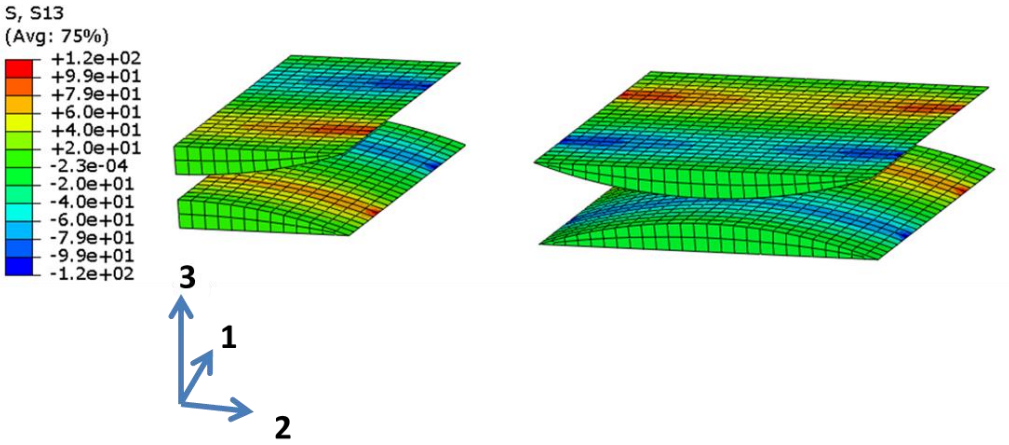

(c)

Fig. 6-20 Weft tow stress contour plot for the IM7 CF 3D woven composite under warp direction tension: a) σ_3 , b) σ_2 , c) τ_{13}

Some observations are made which confirmed that the predicted stress distributions as shown in Fig. 6-20 are reasonable. First of all, σ_3 in the weft tows is predicted to be compressive, as during the loading process, warp tows would

tend to align with the loading direction and therefore compress against the weft tows. This tendency is illustrated by the tow deformation prediction in Fig. 6-21.

Also, the transverse stress σ_2 in the weft tows is predicted to be tensile, which is natural, since the global tensile loading applied to the 3D woven composite is in the warp direction.

For the shear stress τ_{13} in the weft tows as shown in Fig. 6-20(c), high values of this stress are predicted near the intersections of the alternating curved warp tow paths, as can be visualised by assessing Fig. 6-20(c) in conjunction with Fig. 6-21.

This predicted τ_{13} stress distribution is envisaged to be caused by the severe shear deformation in the *Y*-*Z* plane as shown in Fig. 6-21. Moreover, the root cause of such shear deformation in the *Y*-*Z* plane should be attributed to the deformation of warp tows in aligning themselves with the direction of warp direction loading applied, which is also depicted in Fig. 6-21.

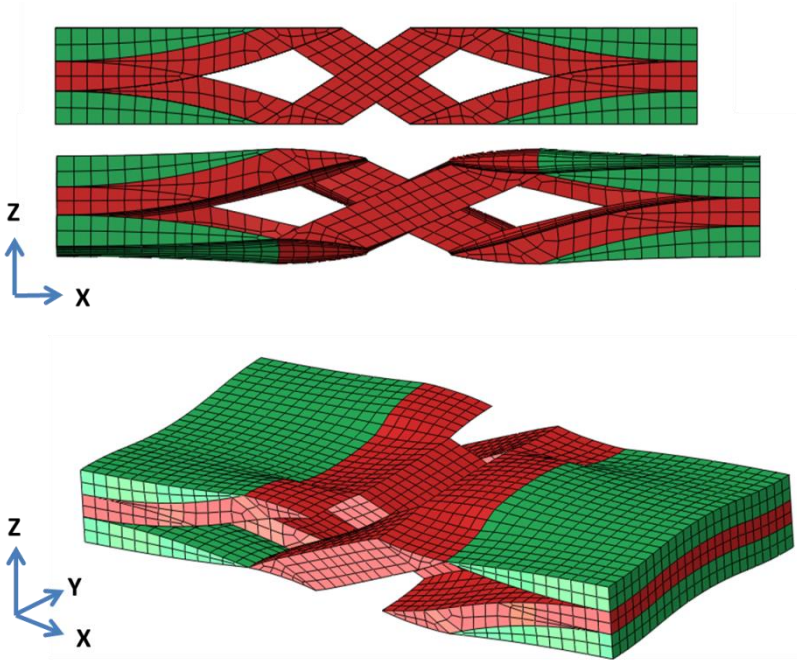

Fig. 6-21 Tow deformation prediction (scaled up) for the IM7 CF 3D woven composite under warp direction tension

Similar element result assessment is also conducted for the warp tow elements. The element output result is extracted from the element indicated by the red arrow in Fig. 6-22.

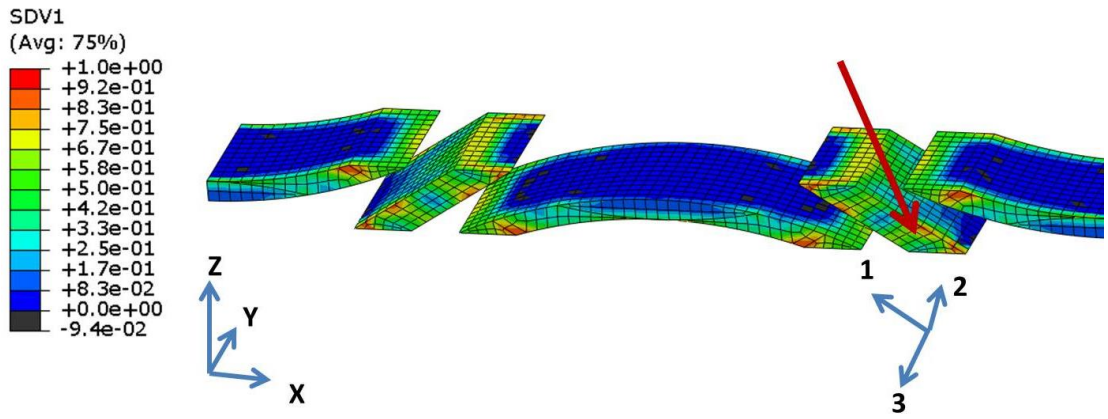

Fig. 6-22 Warp tow damage variable prediction and the selected warp tow element for result inspection

As can be seen from Fig. 6-23(a), in this case, the longitudinal shear and the transverse shear stresses are predicted to be the main stresses on the fracture plane for causing damage initiation and growth. By referring to the warp tow material principal coordinate in Fig. 6-22, the predicted fracture plane orientation in this case is 4.8^{o} anticlockwise from the second material principal axis, which indicates that the fracture plane is almost parallel to the second material principal plane of the warp tow.

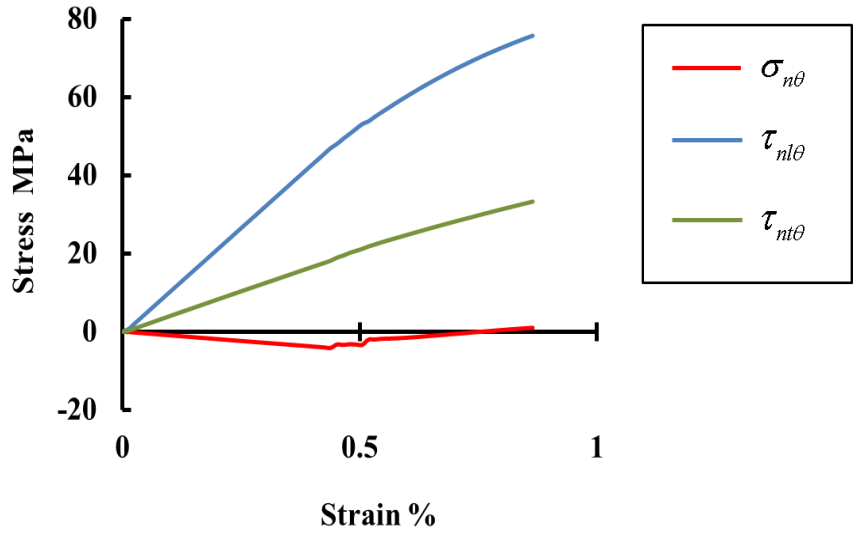

(a)

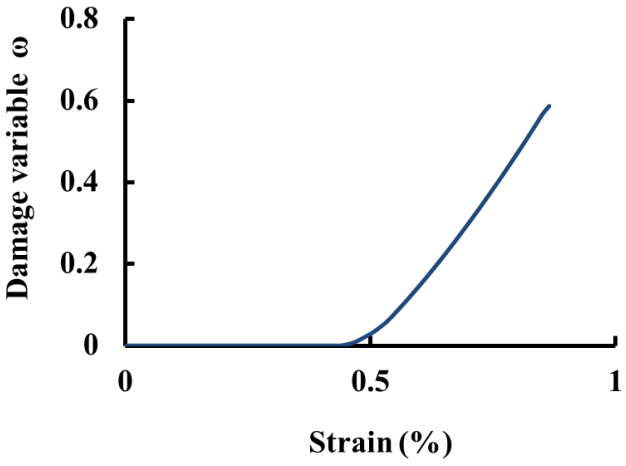

(b)

Fig. 6-23 Damaged warp tow element output result: a) Stresses on the fracture plane, b) Damage variable

Again, the stresses on the fracture plane as shown in Fig. 6-23(a) can be related to the stress distribution within the warp tows as shown in Fig. 6-24.

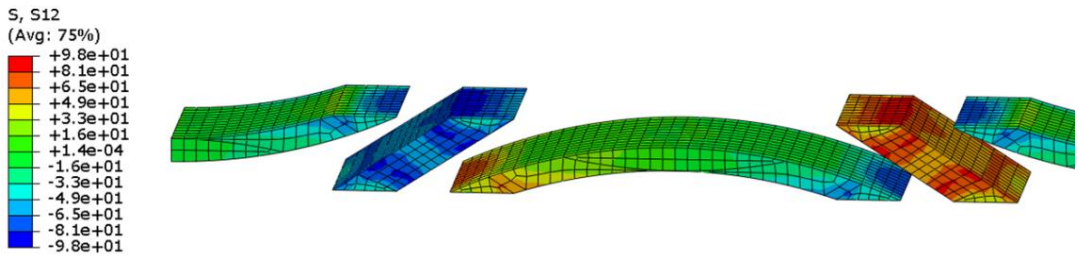

(a)

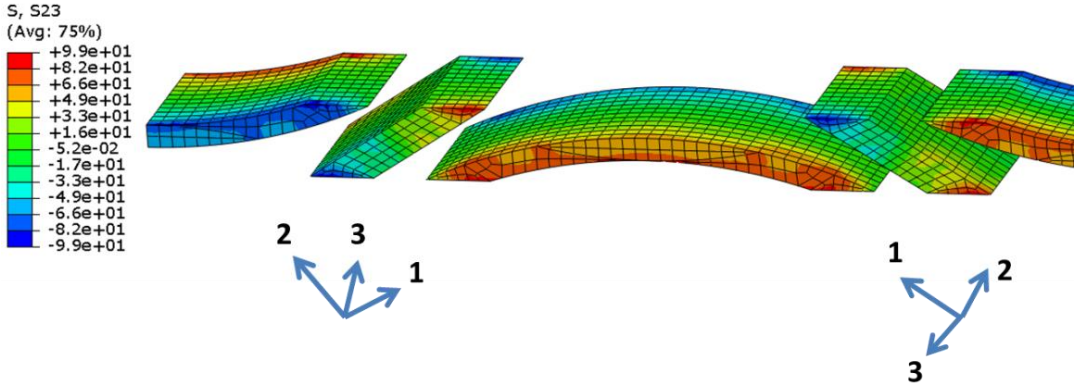

(b)

Fig. 6-24 Warp tow stress contour plot for the IM7 CF 3D woven composite under warp direction tension: a) τ_{12}, b) τ_{23}

As can be seen from the contour plot of τ_{12} in Fig. 6-24(a), τ_{12} reached the highest value in the warp curving regions. This can be explained by the predicted deformation of the warp tows as shown in Fig. 6-21, which confirms that the warp tows in this region underwent a substantial longitudinal shear deformation, γ_{12}. This shear deformation is believed to be induced by the tendency of the warp tows to align themselves with the loading direction.

As shown in the contour plot of the transverse shear stress τ_{23} in Fig. 6-24(b), τ_{23} has reached the highest value along the warp tow edges adjacent to the warp tows of the opposite tow path. Again, consulting with the predicted deformation

for the tows in Fig. 6-21, it can be seen that high values of τ_{23} in this region are due to the severe shear deformation of the tows in the *Y*-*Z* plane, which is already discussed earlier.

Comparing the damage predictions as illustrated above with the actual damage observed in the corresponding test case as described in Section 4.4.2.2.1, some conclusions can be drawn as follows.

First of all, although some intra-tow damage is predicted for the weft tows, it appeared to be localised, which might explain why intra-tow cracks was not found inside the weft tows during the experimental investigation.

Also, severe shear deformation is predicted for the tows in the warp curving regions, which is caused by the tendency of warp tows to align themselves in the direction of the applied warp direction loading. Due to this shear deformation, significant shear-induced intra-tow matrix damage is predicted to occur inside the warp tows in those regions.

However, one may recall that during the experimental investigation of this test case, no intra-tow damage was observed for the warp tows in the warp curving regions. Instead, inter-tow cracks surrounding the warp tows were discovered in those regions. It is therefore envisaged that the predicted shear deformation of warp tows still occurred in the actual specimens during the experiment, but led to the formation of inter-tow cracks rather than the intra-tow matrix cracks predicted, presumably, due to the low interfacial strength between the warp tows and the matrix material.

Nonetheless, the simulation work still successfully identified shear deformation as the most probable cause for the inter-tow cracks surrounding the warp tows in the warp curving regions.

6.2.2.2 IM7 Carbon Fibre Specimens under Weft Direction Uniaxial Tension

The corresponding experiment of this test case is described in Section 4.4.2.2.2. The experimental and the predicted stress-strain curves are plotted in Fig. 6-25. As can be seen, the simulation has accurately reproduced the experimental result. The stress-stress responses appeared to be linear in both cases. However, recall that microscopic inspection of the tested specimens for this test case (Section 4.4.2.2.2) revealed the presence of numerous transverse cracks, which did not have any noticeable effect on the material stiffness. Therefore, the capability of the model in predicting damage cannot be assessed by simply comparing the predicted stress-strain response with the experimental one. If anything, the stress-strain prediction in Fig. 6-25 only proved that the simulation did not over-predict the stiffness degradation due to intra-tow damage.

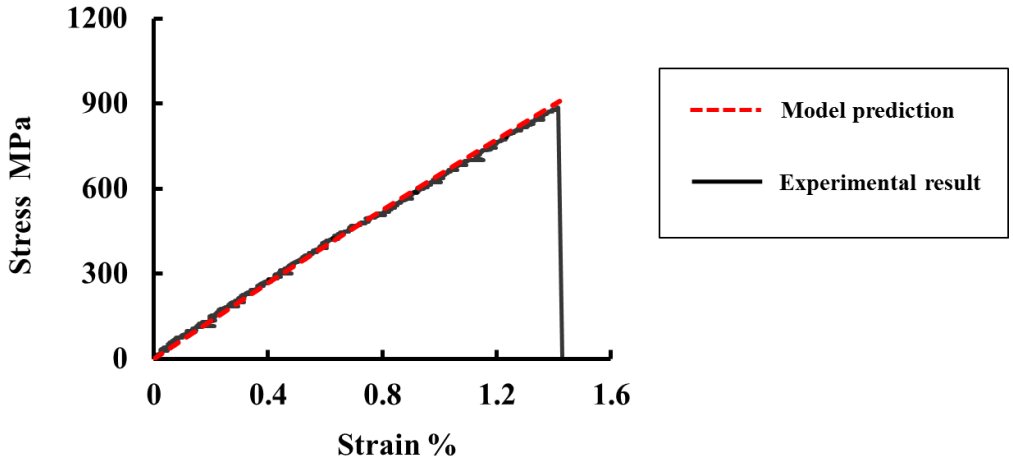

Fig. 6-25 Stress-strain prediction for the IM7 CF 3D woven composite under weft direction tension

Tow longitudinal stress contour plot is shown in Fig. 6-26. As can be seen, the prediction of the stress distribution is quite reasonable in this case, as the weft tows are shown to take majority of the tensile load applied in the weft direction.

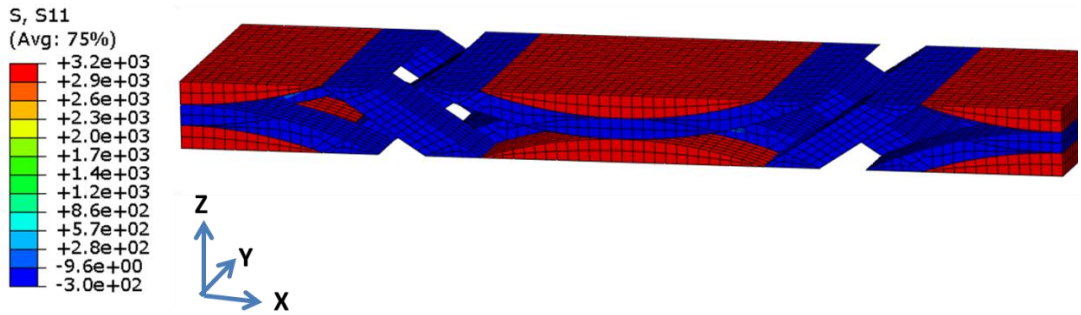

Fig. 6-26 Tow longitudinal stress contour plot for the IM7 CF 3D woven composite under weft direction tension

The predicted deformation due to the applied weft direction load is shown in Fig. 6-27, where the woven fabric is shown to be elongated in the loading direction. Moreover, no apparent distortions of the warp or the weft tows are predicted, indicating that shear deformation of the fabric, if present, should not be significant in this loading case.

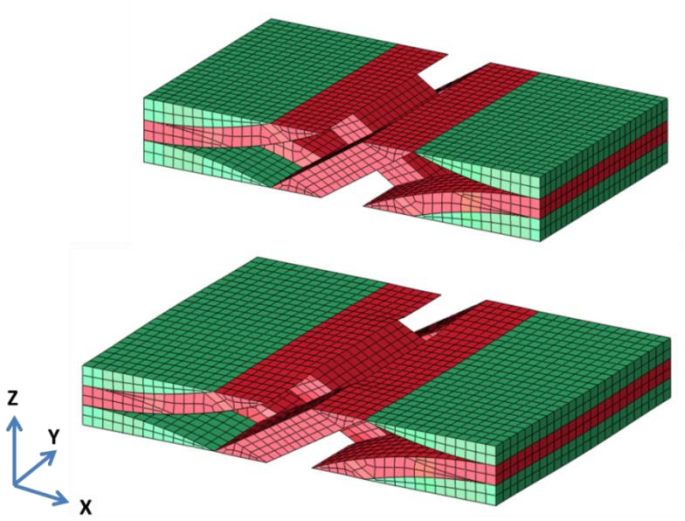

Fig. 6-27 Tow deformation prediction (scaled up) for the IM7 CF 3D woven composite under weft direction tension

The contour plot of damage variable is shown in Fig. 6-28. As can be seen, the predicted damage occurred and evolved only in the warp tows and it is nearly uniformly distributed throughout all the warp tows.

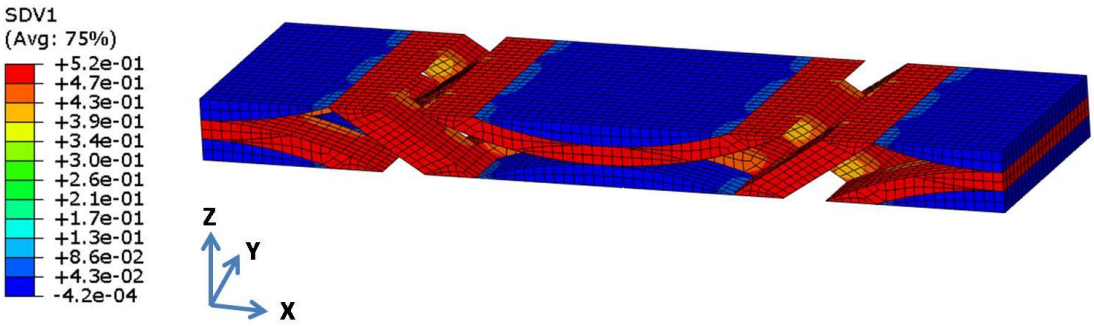

Fig. 6-28 Damage variable contour plot for the IM7 CF 3D woven composite under weft direction tension

To identify the stresses associated with the intra-tow damage initiation and evolution, stresses on the fracture plane are inspected for one of the warp tow elements. The typical stress output is shown in Fig. 6-29(a). As can be seen, on the fracture plane, transverse tensile stress is the only non-zero stress component. Also, the orientation of the fracture plane is found to be 90º, which means the fracture plane is predicted to be perpendicular to the third material principal axis of the warp tows (refer to the warp tow material principal coordinate system in Fig. 6-30).

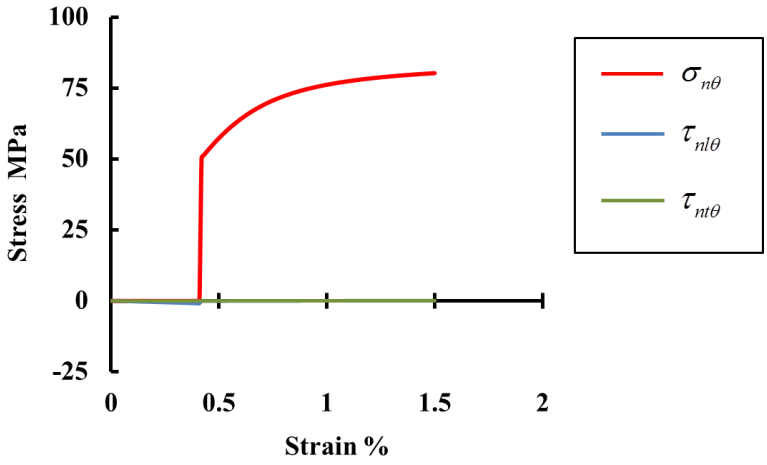

(a)

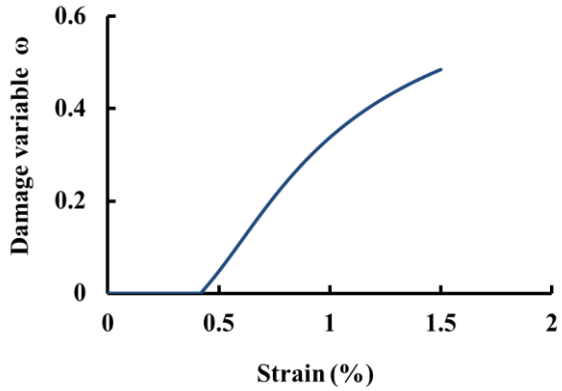

(b)

Fig. 6-29 Damaged warp tow element output result: a) Stresses on the fracture plane, b) Damage variable

The transverse tensile stress on the fracture plane is σ_3 in the warp tows as shown in Fig. 6-30, where a nearly uniform distribution of σ_3 is predicted.

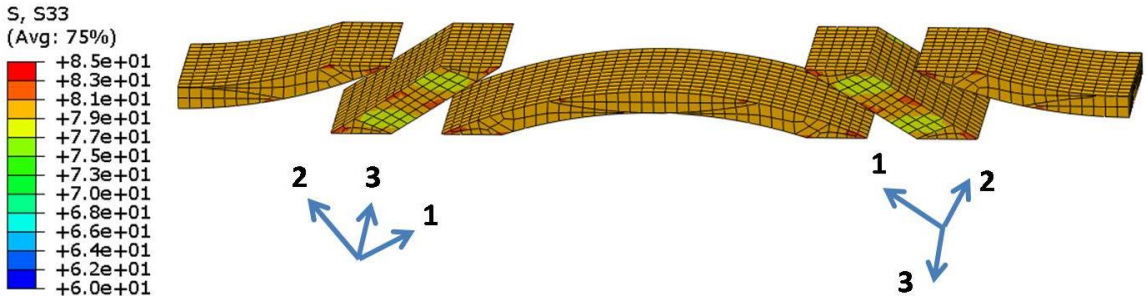

Fig. 6-30 Warp tow σ_3 contour plot for the IM7 CF 3D woven composite under weft direction tension

Based on this, it is obvious that the nearly uniform transverse tensile stress σ_3 in the warp tows is responsible for causing the intra-tow matrix damage. Obviously, this transverse tensile stress resulted from the weft direction tensile loading applied to the 3D woven composite in this test case.

It can be concluded that, for this test case, the prediction of intra-tow damage in the warp tows is in agreement with the actual warp tow transverse cracking damage observed from the experiment (Fig. 4-22). Moreover, the modelling result suggested that this damage results from the transverse tensile stress imposed on the warp tows.

However, from the microscopic examination conducted during the experiment, the transverse cracks were also found to extend beyond warp tows and form through-the-thickness transverse cracks. This type of damage is not captured in the present analysis, since the unit cell model only has the capability of predicting the intra-tow damage.

Nonetheless, a linear stress-strain curve, similar to that obtained from the experiment, is predicted by the model. The explanation for such a linear stress-strain response was already provided in Section 4.4.2.2.2, i.e. the high Young's

modulus value of the straight IM7 carbon fibre weft tows dominated the specimen level stress-strain response such that it is generally not affected by the transverse cracks.

6.2.2.3 E-glass Fibre Specimens under Warp Direction Uniaxial Tension

The stress-strain curve predicted for this case is shown in Fig. 6-31, where it is compared with the experimental data from Section 4.4.3.2.1. As can be seen, the initial linear elastic response of the composite is represented reasonably well by the unit cell analysis. However, the experimental curve became nonlinear at 0.35% strain, while the predicted stress-strain response remained mostly linear until the end of the analysis. This is the same type of discrepancy between the experimental result and the model prediction as was mentioned previously for the case of IM7 CF 3D woven composite in Section 6.2.2.1. Again, the cause for this discrepancy is the lack of inter-tow damage modelling, since the inter-tow cracks are also found to be the major contributor to the stress-strain nonlinearity for this case as mentioned in Section 4.4.3.2.1.

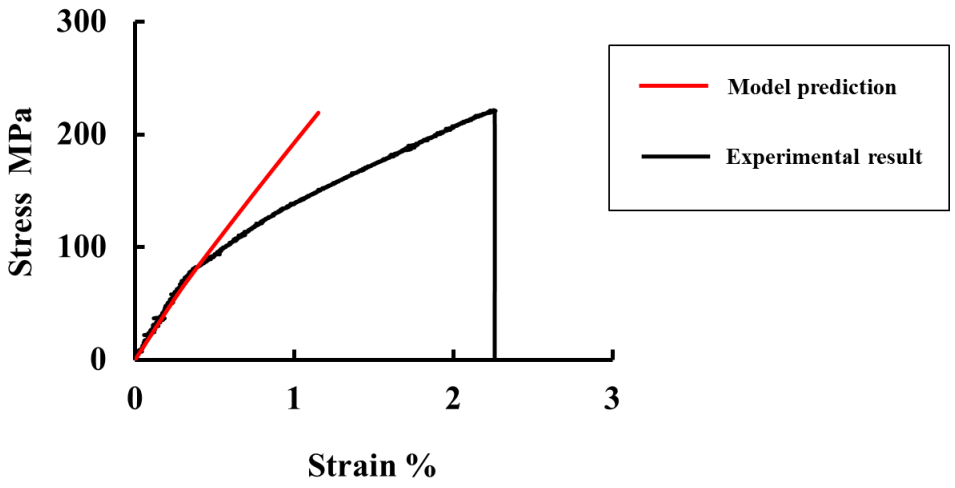

Fig. 6-31 Stress-strain prediction for the GF 3D woven composite under warp direction tension

The contour plot of tow longitudinal stress σ_1 is shown in Fig. 6-32. As can be seen, the warp tows are predicted to withstand the majority of the applied load as expected.

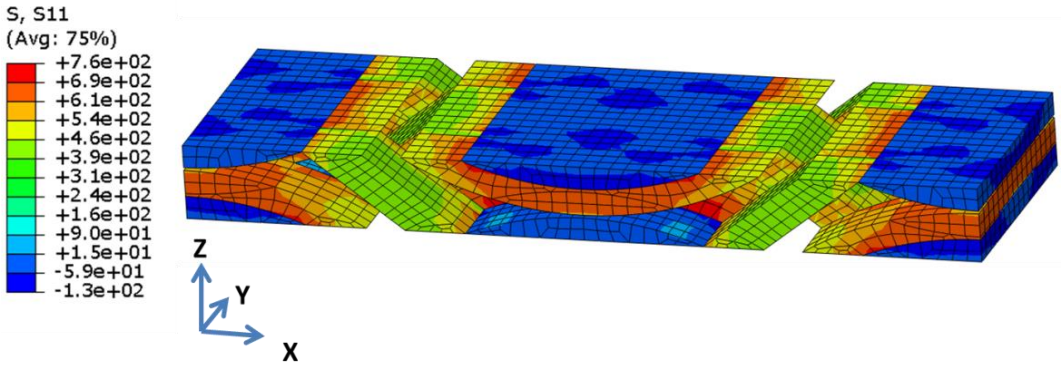

Fig. 6-32 Tow longitudinal stress contour plot for the GF 3D woven composite under warp direction tension

The intra-tow damage prediction for this case is illustrated in Fig. 6-33, where the weft tows are shown to sustain nearly uniformly distributed damage of relatively high magnitude, while damage in the warp tows are predicted to be concentrated at the warp curving regions.

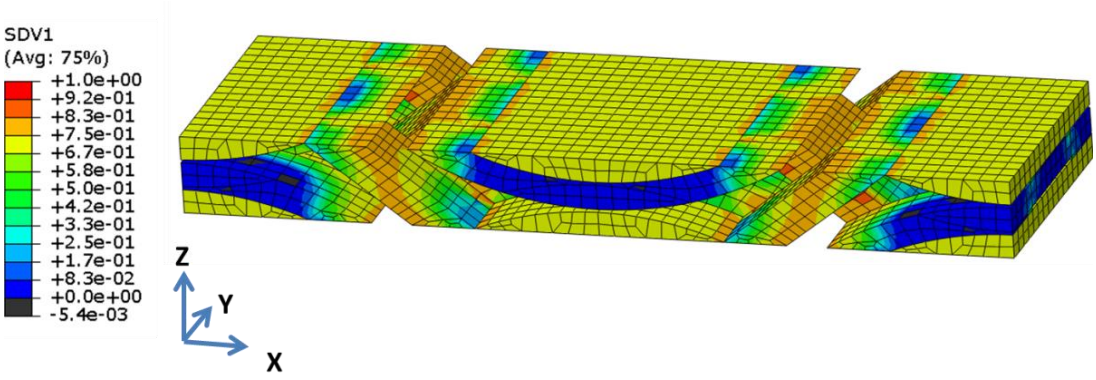

Fig. 6-33 Damage variable contour plot for the GF 3D woven composite under warp direction tension

The prediction of weft tow damage in this case is very different from that obtained previously for the IM7 CF 3D woven composite under the same type of loading (Section 6.2.2.1). In that case, intra-tow damage in the weft tows was predicted to be concentrated only at the warp curving regions without much in the weft tows. This marked difference in weft tow damage prediction between these two cases is illustrated in Fig. 6-34.

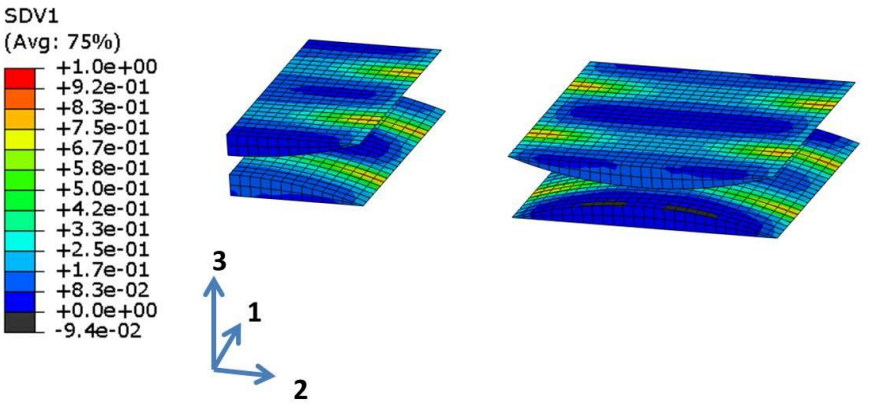

(a)

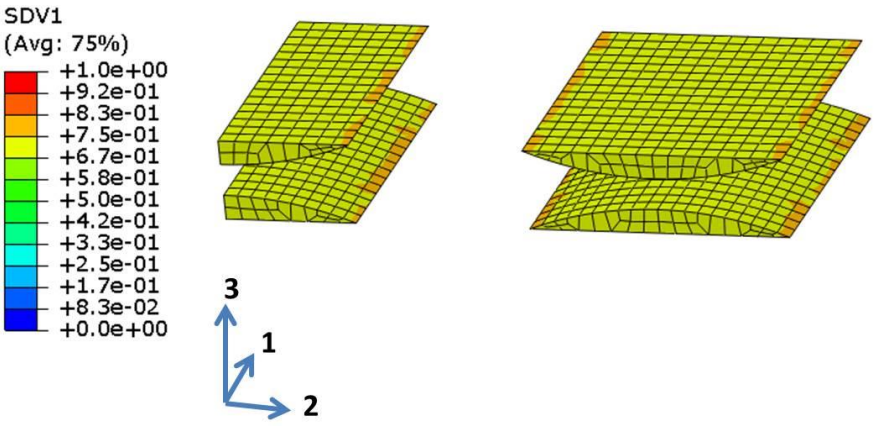

(b)

Fig. 6-34 Damage variable in the weft tows for the case of (a) IM7 CF 3D woven composite, (b) GF 3D woven composite under warp direction tension

To identify the reason for this difference, typical weft tow element result from the present case is extracted and inspected. As illustrated in Fig. 6-35(a), for the weft tows in the present case, the intra-tow damage is predicted to be caused solely by

the transverse tensile stress on the fracture plane. Moreover, the fracture plane is predicted to be parallel to the second material principal plane of the weft tow (i.e. 0º fracture plane orientation). This implies that the warp direction loading applied to the composite has caused the formation of transverse intra-tow cracking in the weft tows.

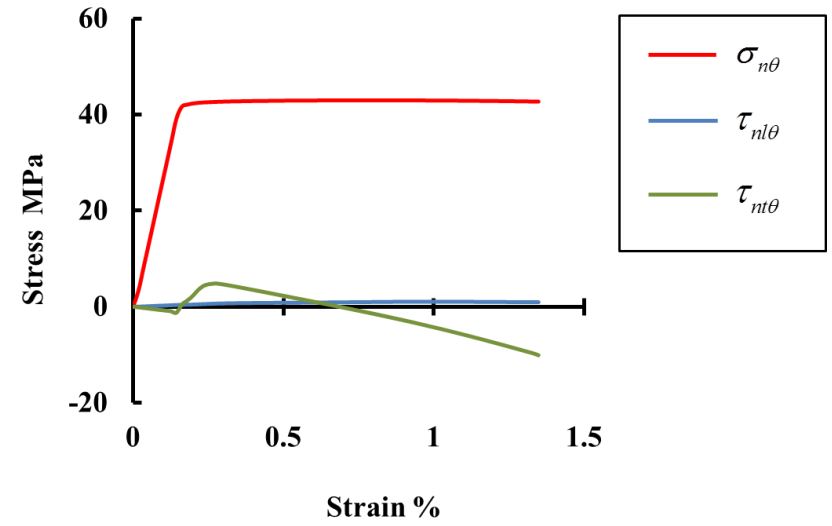

(a)

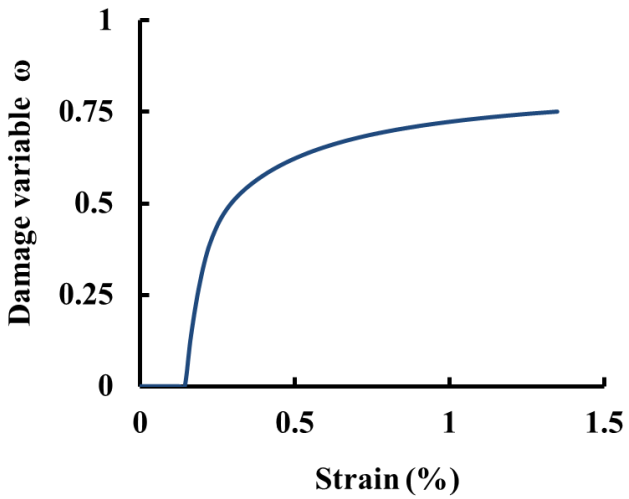

(b)

Fig. 6-35 Damaged weft tow element output result: a) Stresses on the fracture plane, b) Damage variable

Such weft tow element output result is different from that obtained previously for the IM7 CF 3D woven composite case, where transverse shear stress on the fracture plane is also predicted to contribute to damage initiation and evolution (Fig. 6-19(a)). It is envisaged that the lower value of mode I damage initiation stress for the E-glass fibre tows ($R_{\perp}^{T}$ =40 MPa), when compared with that of the IM7 carbon fibre tows ($R_{\perp}^{T}$ =49.2 MPa), has led to this result.

Predicted stress distributions in the weft tows are shown in Fig. 6-36. Comparing these with those obtained previously for the IM7 CF 3D woven composite case (Fig. 6-20), it can be seen that the patterns of predicted stress distributions in these two woven composites are very similar.

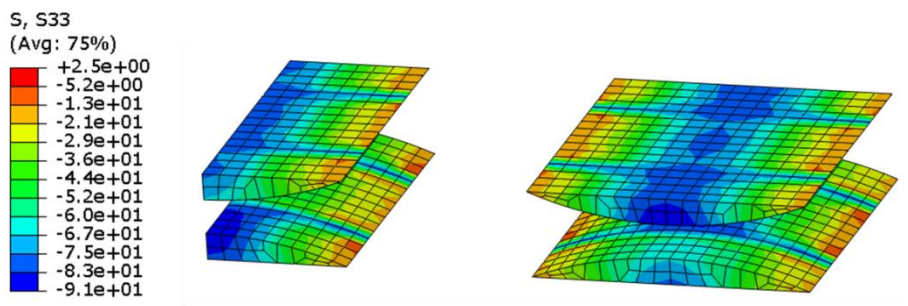

(a)

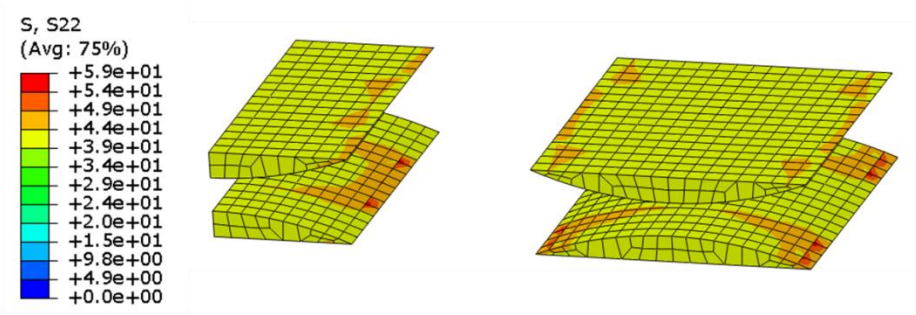

(b)

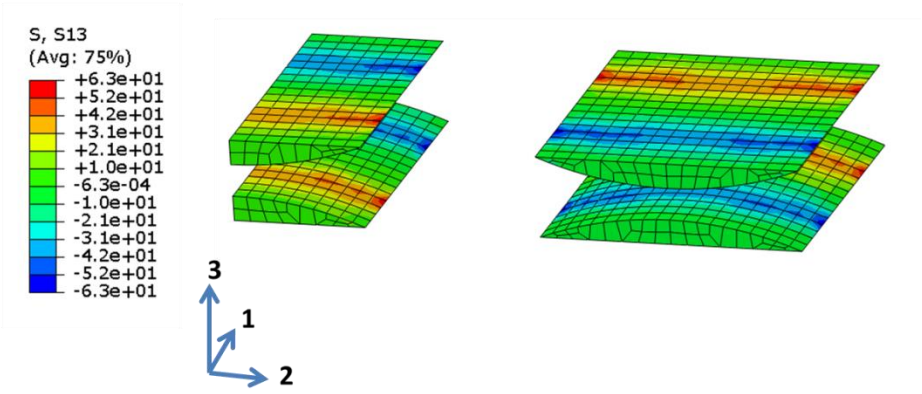

(c)

Fig. 6-36 Weft tow stress contour plot for the GF 3D woven composite under warp direction tension: a) σ_3 , b) σ_2 , c) τ_{13}

Then, by comparing the predicted tow deformation pattern of the current case (Fig. 6-37) with that of the previous IM7 CF 3D woven composite case (Fig. 6-21), the cause for such similarity in stress distributions becomes apparent, as similar tow deformation patterns are predicted for both materials under warp direction tension.

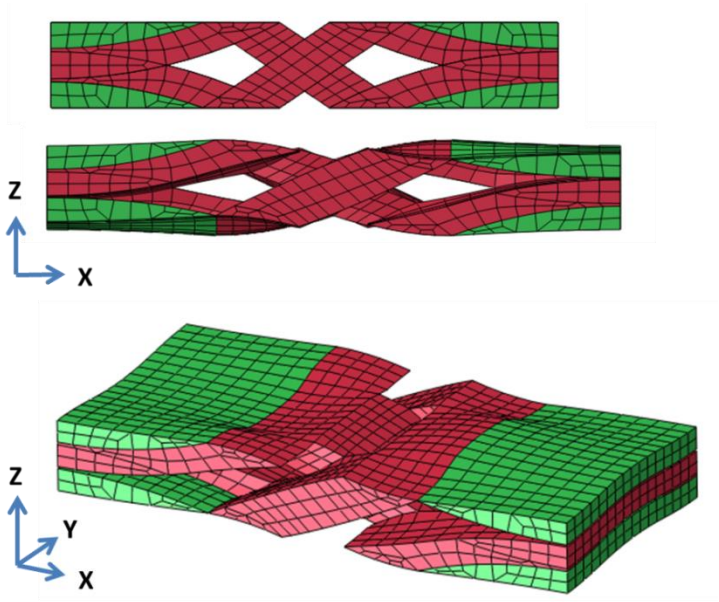

Fig. 6-37 Tow deformation prediction (scaled up) for the GF 3D woven composite under warp direction tension

The prediction of intra-tow damage in the warp tows is shown in Fig. 6-38. For the element marked by the arrow in Fig. 6-38, the stresses on the fracture plane and the damage variable predicted are shown in Fig. 6-39(a) and Fig. 6-39(b), respectively. The predicted stress distributions for the warp tows are shown in Fig. 6-40. Again, due to the similar tow deformation patterns predicted, these results are similar to those predicted previously for the IM7 CF 3D woven composite (Fig. 6-22 - Fig. 6-24).

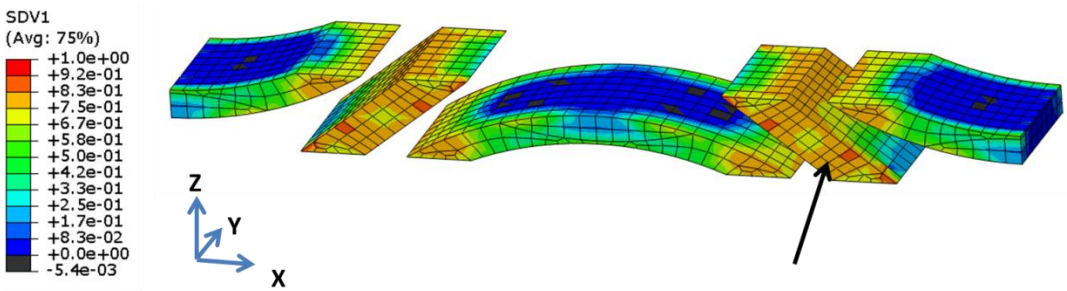

Fig. 6-38 Warp tow damage variable prediction and the selected element

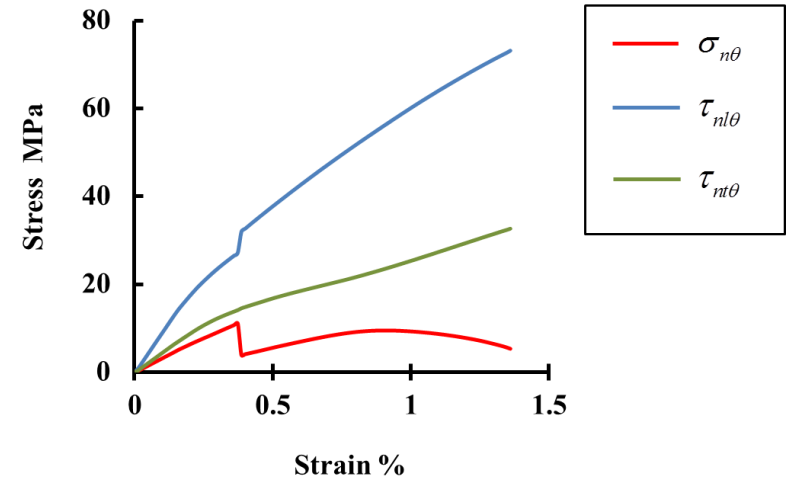

(a)

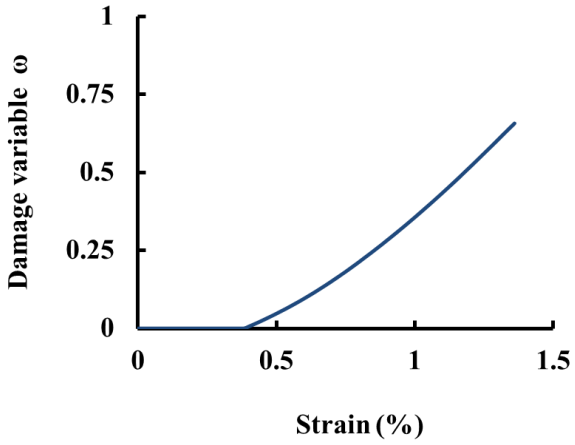

(b)

Fig. 6-39 Damaged warp tow element output result: a) Stresses on the fracture plane, b) Damage variable

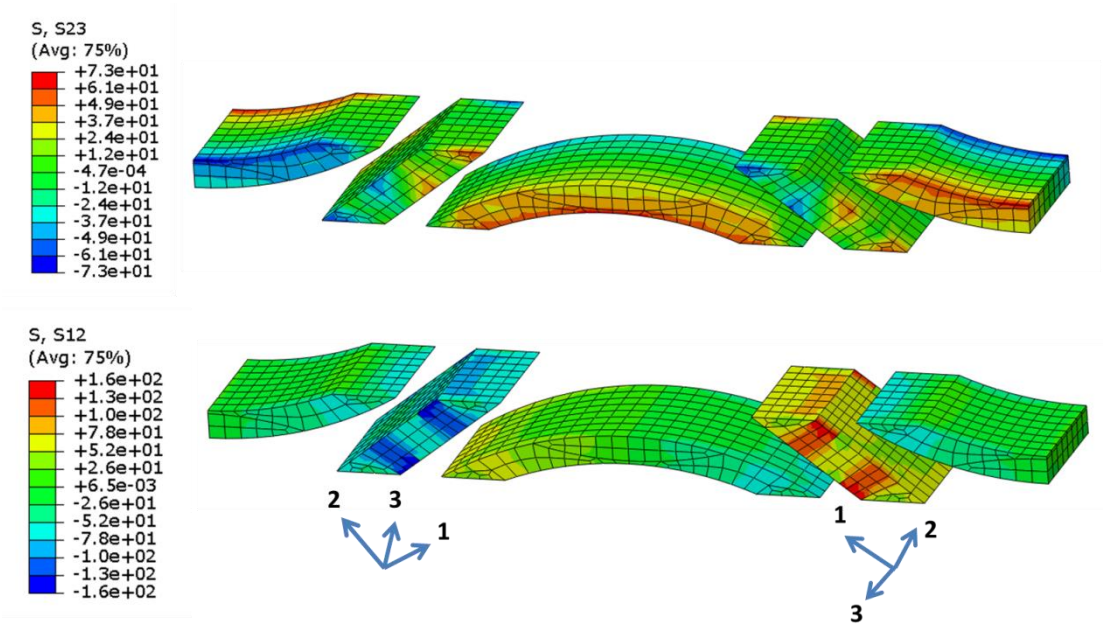

Fig. 6-40 Warp tow stress contour plot for the GF 3D woven composite under warp direction tension

For this test case, it can be concluded that the model has successfully predicted the transverse cracks inside the E-glass fibre weft tows, which is in agreement with the experimental result (Section 4.4.3.2.1). Moreover, the transverse tensile stress in the weft tows is found to be the stress causing these intra-tow transverse cracks.

In addition, the predicted shear deformation pattern of warp tows in this case is similar to that predicted previously for the case of IM7 CF 3D woven composite under warp direction tension. As discussed earlier, this type of shear deformation is believed to be the root cause for the inter-tow cracks in the warp curving regions, which were discovered during the experiment.

6.2.2.4 E-glass Fibre Specimens under Weft Direction Uniaxial Tension

The predicted stress-strain response for this case is plotted in Fig. 6-41 along with the experimental data. As can be seen, a reasonably good agreement has been achieved between the prediction and experimental result. Specifically, the stress-strain nonlinearity due to damage, as was observed experimentally, is captured by the model.

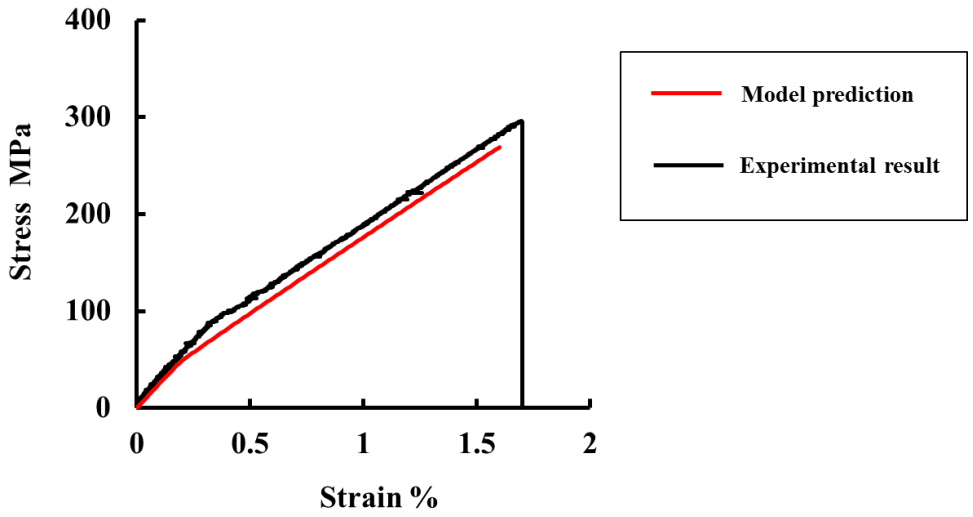

Fig. 6-41 Stress-strain prediction for the GF 3D woven composite under weft direction tension

As shown by the tow longitudinal stress contour plot in Fig. 6-42, weft tows took the majority of the applied load as anticipated.

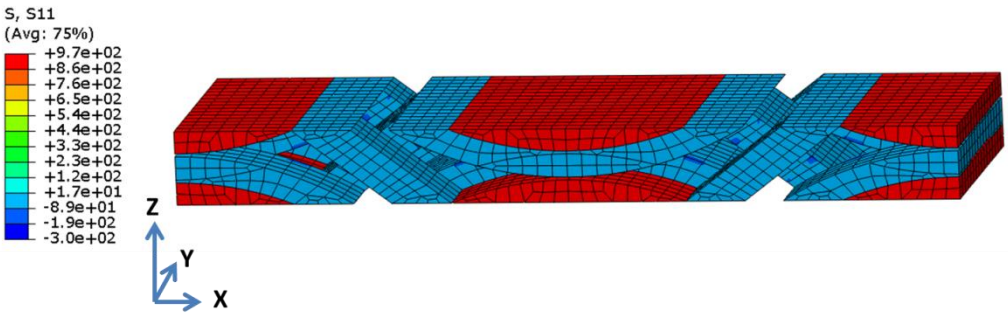

Fig. 6-42 Tow longitudinal stress contour plot for the GF 3D woven composite under weft direction tension

The predicted intra-tow damage distribution, as shown in Fig. 6-43, is almost uniform within the warp tows, and is qualitatively similar to that predicted for the IM7 CF 3D woven composite under the same type of loading (Fig. 6-28). Moreover, the predicted warp tow fracture plane orientation for this case is also the same as in the IM7 CF 3D woven composite case, with the fracture plane parallel to the third material principal plane of the warp tows. However, quantitatively, higher values of intra-tow damage variables are predicted for the E-glass fibre warp tows in this case.

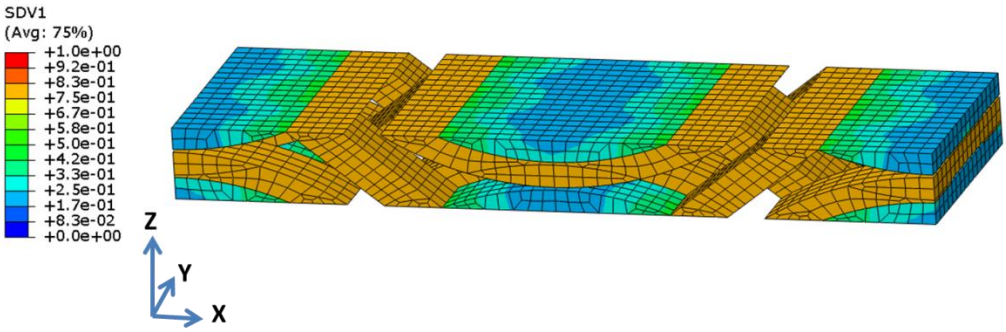

Fig. 6-43 Damage variable contour plot for the GF 3D woven composite under weft direction tension

For the warp tow elements, the stresses on the fracture plane and the damage predicted are shown in Fig. 6-44(a) and Fig. 6-44(b). The predicted stress distribution of σ_3 in the warp tows is illustrated in Fig. 6-45. Comparing these predictions with those obtained previously for the IM7 CF 3D woven composite in Fig. 6-29 and Fig. 6-30, it can be seen that the predicted warp tow damage scenarios in both 3D woven composites are very similar under this loading case.

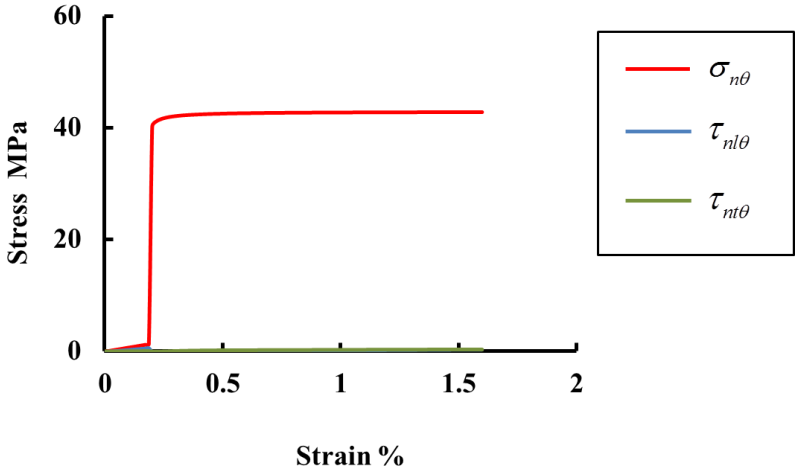

(a)

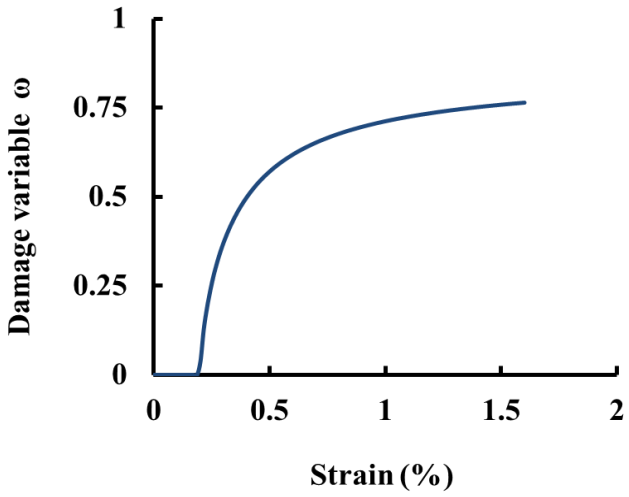

(b)

Fig. 6-44 Damaged warp tow element output result: a) Stresses on the fracture plane, b) Damage variable

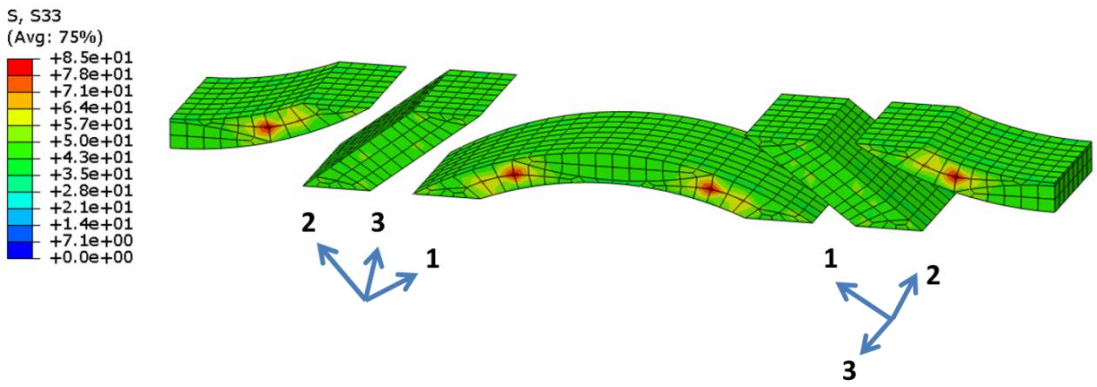

Fig. 6-45 Warp tow σ_3 contour plot for the GF 3D woven composite under weft direction tension

To summarise for this case, the actual through-the-thickness transverse cracks observed in the experiment (Fig. 4-37) are successfully predicted by the model, but only in the form of intra-tow damage within the warp tows, since the unit cell model only incorporated the CDM model for intra-tow damage prediction.

Despite this, the predicted nonlinear stress-strain curve still closely resembled the experimental one. A possible explanation for this could be that, although only intra-tow transverse cracking in the warp tows is modelled by the unit cell analysis, since the warp tows themselves are partially oriented in the thickness direction due to the weave pattern (Fig. 6-45), the predicted damage in the warp tows effectively recreated the through-the-thickness cracks observed in the experiment. As a result, the equivalent smeared damage effect of the through-the-thickness transverse cracks is nonetheless reproduced by the model.

6.2.3 Summary of Model Validation using 3D Woven Composite Test Cases

Based on the unit cell analysis results as shown above, some conclusions can be drawn as follows.

First of all, the CDM model incorporated for intra-tow damage modelling successfully predicted all cases of intra-tow transverse cracking that are observed in the experiments. This is demonstrated for the test cases of 3D woven composites loaded in weft direct tension, where the actual intra-tow cracks found in the warp tows are captured by the model. On the other hand, for the case of 3D woven composites loaded under warp direction tension, not only did the model correctly predict the presence of intra-tow cracks inside the weft tows of the GF 3D woven composite, but also it predicted the phenomenon that the intra-tow cracks inside the weft tows of the IM7 CF 3D woven composite are localised in the warp curving regions, which provided the explanation as to why these intra-tow cracks were not easily observed in the experiment.

In terms of stress-strain behaviour prediction, due to the lack of inter-tow damage modelling, the unit cell models did not reproduce the experimental stress-strain curves for the test cases of warp direction tensile loading. As a result, a separate damage model designed to characterise the damage effect of inter-tow cracks is developed and introduced in the next chapter.

However, in contrast, the unit cell models predicted acceptable stress-strain behaviours for the cases of weft direction tensile loading. In particular, in the case of GF 3D woven composite, the predicted intra-tow damage in the warp tows effectively recreated the through-the-thickness transverse cracks, which led to a reasonable prediction of stress-strain nonlinearity when compared to the experimental result.

For the test cases of tensile loading in the warp direction, as indicated by the predicted shear-induced intra-tow damage, the unit cell models identified warp

tow shear deformation as the main cause for the inter-tow cracks surrounding the warp tows that were observed in the experiments.

7. A Pragmatic Continuum Damage Mechanics Model for Inter-tow Cracks in 3D Woven Composites

7.1 Introduction

As illustrated by the experimental result in Chapter 4, inter-tow cracks between warp tows are identified to be the main cause for stress-strain nonlinearity when the 3D woven composites were loaded in the warp direction. However, this influential damage mode is not incorporated in the UD composite CDM model proposed in Chapter 3 for simulating tow properties, because inter-tow cracks are naturally formed around rather than inside tows. As a result, in addition to the UD composite CDM model, another damage model accounting for inter-tow cracking damage should also be devised so that the damage effects due to both intra-tow and inter-tow cracks can be predicted for 3D woven composites. To meet this need, a pragmatic continuum damage model capturing the main characteristics of inter-tow cracking damage is developed, implemented, verified and validated as shown in this chapter.

However, recall that for the test cases of 3D woven composites under weft direction uniaxial stress (Chapter 4), it was impossible to tell whether the through-thickness transverse cracks were intra-tow cracks or inter-tow cracks. Even for a single transverse crack in there, part of it could be inside tows while part of it could be right on the tow boundary. In light of this and also for the sake of simplicity, the damage model developed here for inter-tow crack modelling is only applicable to the cases of 3D woven composites loaded under warp

direction uniaxial stress where the genuine inter-tow cracks can be clearly identified from experimental result.

Another point to note is that the inter-tow crack damage model proposed here is considered to be pragmatic in the sense that, when developing the model, instead of starting from independent experimental investigation and theoretical characterisation of inter-tow cracks, stiffness reduction in 3D woven composites caused by these cracks is assumed to be directly represented by the difference between the experimental stress-strain curve and the stress-strain curve obtained from the unit cell analysis of 3D woven composites, where the latter only accounts for intra-tow damage. Unit cell analysis of 3D woven composites can be made to predict the effect of intra-tow damage since the UD composite CDM model can be incorporated in the analysis to model tow damage inside 3D woven composites.

This assumption for quantifying inter-tow crack damage effect can be demonstrated graphically using the example shown in Fig. 7-1, where the shaded area is regarded as being due to the contribution from inter-tow cracks. Such an assumption is based on the consideration that, while the stress-strain curves obtained from the unit cell analyses in Chapter 6 only included the effect from intra-tow damage, the real-life experimental stress-strain curves like the ones in Chapter 4 certainly reflected the damage effects from both intra-tow and inter-tow cracks. Therefore, as an approximation, the discrepancy between these curves can be attributed to the damage effect caused by the inter-tow cracks.

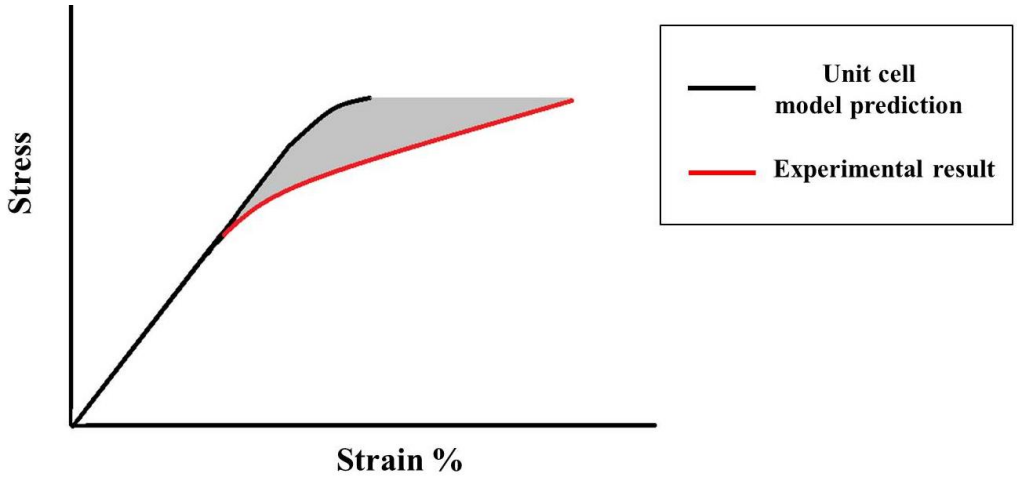

Fig. 7-1 Graphical example showing the assumption for quantifying inter-tow crack damage effect

The procedure for the development and the implementation of this inter-tow damage model is described as follows:

1. A constitutive relationship of the damaged 3D textile composite is established first. It accounts for the damage effect due to both the intra-tow damage and the inter-tow damage, which serves as the damage representation formulation for this inter-tow damage model. Moreover, special unit cell analyses incoprating artificially introduced inter-tow cracks are carried out for characterising the dependence between different inter-tow damage variables. Such a relationship between the inter-tow damage variables is included in the damage representation formulation.
2. Starting from the complementary strain energy function of the damaged 3D textile composite, damage driving force expressions can be derived with regard to inter-tow damage.

3. Then, a damage evolution law based on damage driving force is proposed, where damage evolution constants for inter-tow damage are required to furnish this damage evolution law.
4. The unit cell analysis stress-strain curves presented in Chapter 6 and the original experimental stress-strain curves presented in Chapter 4 are both used to determine the damage evolution constants for inter-tow damage. Since the former accounted for intra-tow damage only while the latter accounted for both intra-tow damage and inter-tow damage, the discrepancy between them is attributed to inter-tow damage effect, which enables inter-tow damage variables to be calculated. This then allows the empirical relationships between the inter-tow damage variables (Ω_D) and the damage driving forces (ρ_D) to be found, where the gradients of the Ω_D - ρ_D plots are the inter-tow damage evolution constants to be obtained.
5. With the damage evolution constants found, the damage evolution law is fully furnished. Then, this inter-tow damage model is available for inter-tow damage prediction on top of the intra-tow damage prediction already provided by the unit cell analysis cases.

Details of the development and the implementation of this inter-tow damage model are described in the sections below.

7.2 Damage Representation

Since inter-tow cracks are positioned outside of tows which are not included in the UD composite constitutive relationship previously adopted for modelling tows, damage representation of inter-tow cracks is defined with respect to the constitutive relationship of the entire 3D woven composites.

For the tested 3D woven composites discussed in Chapter 4, they can be regarded as orthotropic materials. The reason for this is presented in Fig. 7-2 and Fig. 7-3 where the weave patterns of these 3D woven composites demonstrate two planes of symmetry that are perpendicular to each other.

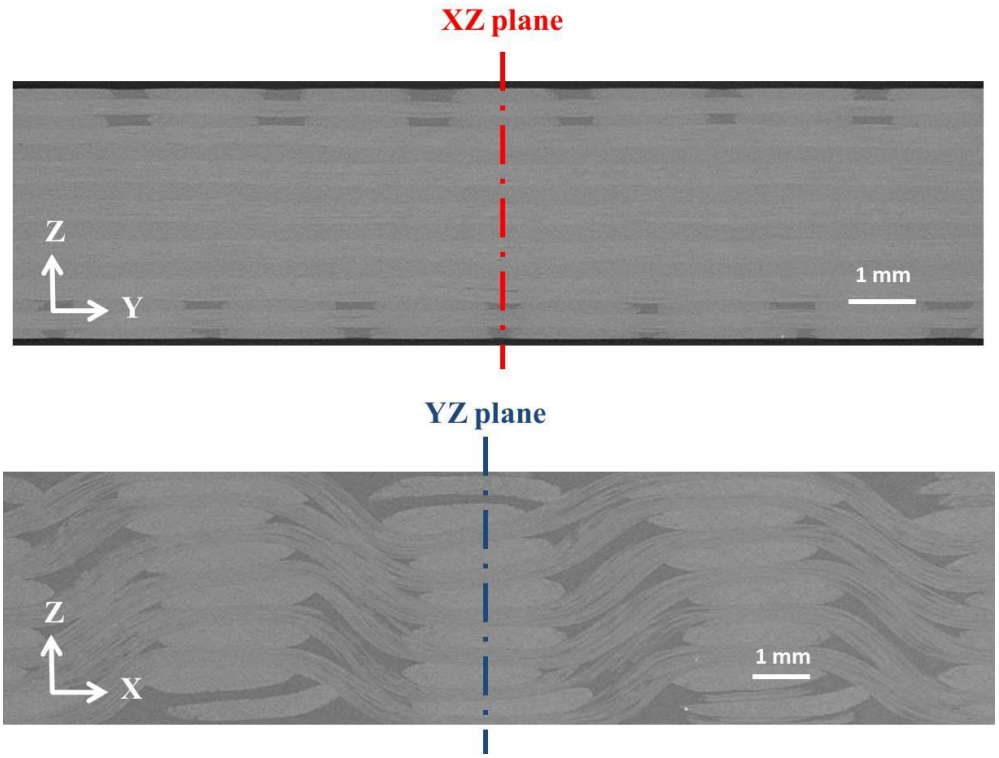

Fig. 7-2 CT scan images of the IM7 3D woven composites showing material symmetry

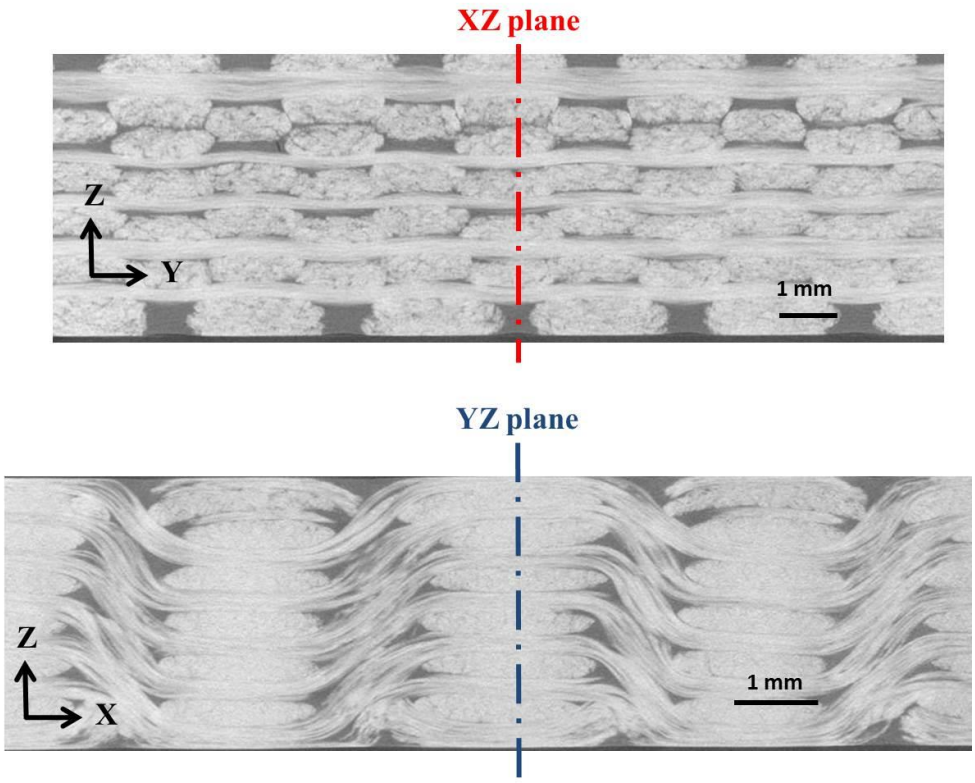

Fig. 7-3 CT scan images of the GF 3D woven composites showing material symmetry

As a result, orthotropic material constitutive relationship is suitable for characterising these 3D woven composites and a compliance matrix representing the constitutive relationship of the damaged 3D woven composites is proposed here as (7-1).

$$[S]=\begin{bmatrix} S_{11} & S_{12} & S_{13} & 0 & 0 & 0 \\ & S_{22} & S_{23} & 0 & 0 & 0 \\ & & S_{33} & 0 & 0 & 0 \\ & & & S_{44} & 0 & 0 \\ & Symm & & & S_{55} & 0 \\ & & & & & S_{66} \end{bmatrix} \tag{7-1}$$

where

$$S_{11}=\frac{1}{E_X^0(1-\Omega_{IX}-\Omega_{DX})}$$

$$S_{12} = -\frac{\nu_{XY}^0}{E_X^0}$$

$$S_{13} = -\frac{\nu_{XZ}^0}{E_X^0}$$

$$S_{22} = \frac{1}{E_Y^0(1-\Omega_{IY}-\Omega_{DY})}$$

$$S_{23} = -\frac{\nu_{YZ}^0}{E_Y^0}$$

$$S_{33} = \frac{1}{E_Z^0(1-\Omega_{IZ}-\Omega_{DZ})}$$

$$S_{44} = \frac{1}{G_{YZ}^0(1-\Omega_{IYZ}-\Omega_{DYZ})}$$

$$S_{55} = \frac{1}{G_{XZ}^0(1-\Omega_{IXZ}-\Omega_{DXZ})}$$

$$S_{66} = \frac{1}{G_{XY}^0(1-\Omega_{IXY}-\Omega_{DXY})}$$

Ω_{Is} and Ω_{Ds} are damage variables associated with intra-tow cracks and inter-tow cracks respectively, where *s=X, Y, Z, XY, XZ* and *YZ* respectively. Note here that Ω_{Is} is defined with respect to the constitutive relationship of 3D woven composites rather than that of tows as in the case of ω.

However, although material orthotropy simplified the constitutive relationship formulation, absolute values of undamaged Young's moduli and Poisson's ratios still need to be determined. Thanks to the quasi-static tests carried out as mentioned in Chapter 4, E_X^0, E_Y^0 and G_{XY}^0 had already been obtained experimentally. For the rest of undamaged material properties, they can all be

determined using unit cell analysis of undamaged 3D woven composites based on constituent material properties of tows and matrix. In addition, experimentally obtained E_X^0 , E_Y^0 and G_{XY}^0 values can also be used to check if the unit cell analysis is able to predict similar values for these properties so that the accuracy of unit cell analysis can be assessed.

Moreover, one may also notice that in (7-1), the damage variables for both intra-tow cracks and inter-tow cracks appeared in all six diagonal components of the compliance matrix associated with the six stresses. The reason behind this is that these cracks can have different orientations at different locations simultaneously within the damaged 3D woven composites. This result in the presence of damage effect for the compliances associated with all six stresses. However, as mentioned before, one should be aware that the values of intra-tow damage variables Ω_{Is} in (7-1) can be predicted by unit cell analysis and the only remaining unknowns will be inter-tow damage variables Ω_{Ds} which are to be determined by the damage model proposed here.

Recall that in Li's damage representation, degradations of some Young's moduli and shear moduli due to cracking damage were found to be not entirely independent (i.e. there is a coupled damage effect) and the relationship between some of them could be characterised using material constants K_{12} and K_{23}. Here, for the case of inter-tow damage induced by warp direction uniaxial tensile stress, one is inspired to ask if similar relationship is also present between different inter-tow damage variables Ω_{Ds} .

In order to investigate this issue further, unit cell analysis is employed with artificially introduced inter-tow cracks. Special unit cell analysis cases are designed with the inter-tow cracks artificially introduced inside the 3D woven composite models. Such a concept of using artificial cracks for damage characterisation is well-accepted as many well-known composite damage analysis theories like the variational analysis method developed by Hashin [116], the shear lag analysis models developed by Smith et al. [113-115] and the finite strip method developed by Li et al. [125] all incorporated definitions of artificial cracks in their theories to facilitate the characterisation of damage effect.

The special unit cell analysis cases have been defined, again, based on the geometrical models previously shown in Fig. 6-13. However, over the boundaries of warp tows, thin layers of pure matrix elements are introduced to represent the resin rich area between tows (Fig. 7-4). As illustrated in Fig. 7-5, these thin layers of elements are of thickness less than a tenth of the warp tow thickness and are treated as interfacial elements for accommodating inter-tow cracks.

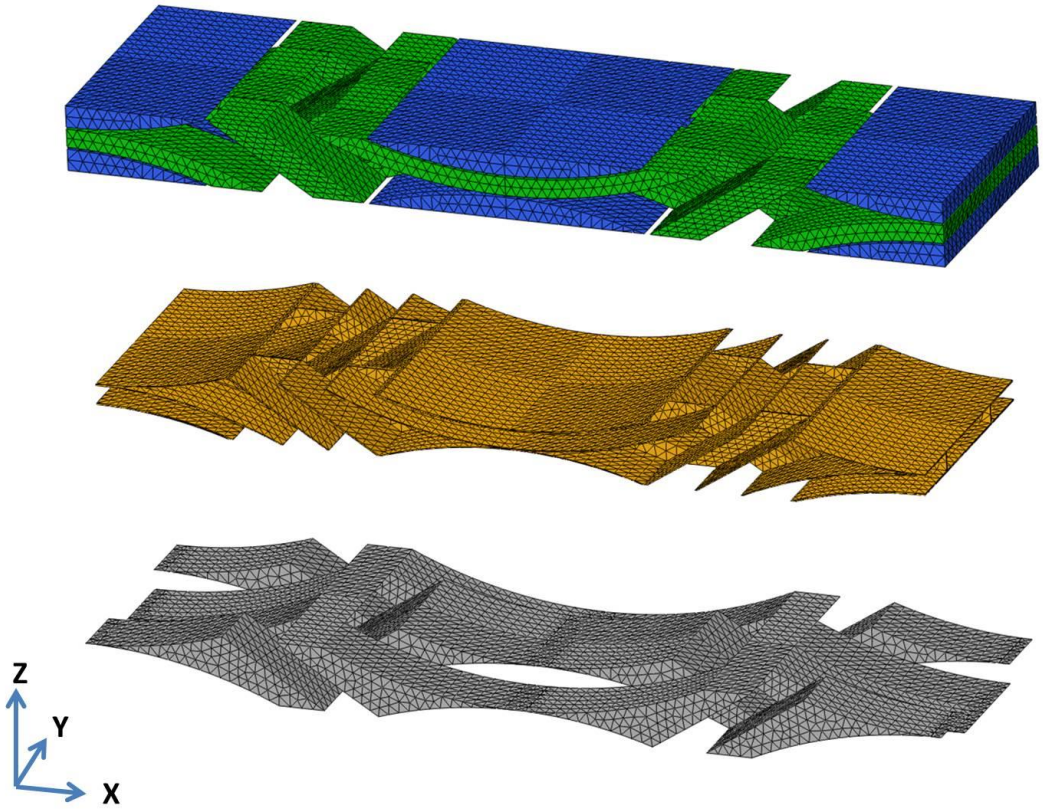

Fig. 7-4 3D woven composites unit cell model with artificially introduced inter-tow cracks showing mesh of warp tows (green), weft tows (blue), interfacial elements (yellow) and pure matrix material (grey)

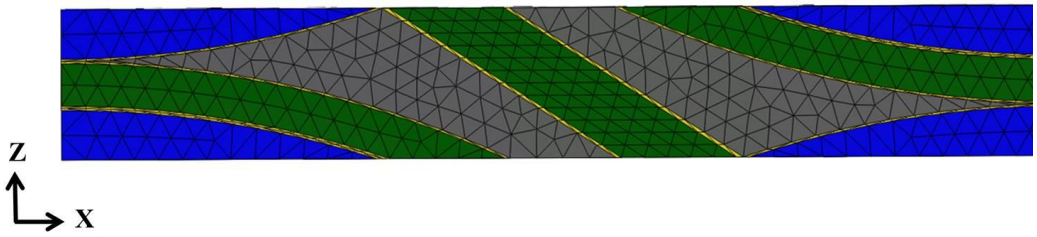

Fig. 7-5 Side view of the unit cell model showing mesh of warp tows (green), weft tows (blue), interfacial elements (yellow) and matrix material (grey)

To simulate inter-tow cracks in a simple but meaningful manner, an imaginary Young's modulus value of trivial magnitude is assigned to some of the interfacial elements so that these elements would effectively lose load-carrying capability and act like cracks. The rest of the interfacial elements still retain the matrix material property originally assigned to them in order to represent interfacial areas

that are still intact. Apart from the interfacial elements, all other elements representing pure matrix and tow materials are still assigned with original virgin material properties so that the only damage effect predicted by this unit cell analysis would be from the introduced inter-tow cracks.

However, in order to rule out possible ill-conditioning in the mesh adopted for the interfacial elements, trial analyses are carried out first, where pure matrix material properties are assigned to all interfacial elements without introducing any damage. Using undamaged tow material properties and matrix material properties as listed previously in Table 4-15, Table 6-3 and Table 6-4, the trial analyses successfully reproduced the effective elastic properties of the IM7 CF 3D woven composites (Table 6-5) and those of the GF 3D woven composites (Table 6-6). This demonstrates that the mesh of thin interfacial elements is acceptable and it did not compromise the performance of unit cell model.

With reference to real inter-tow cracks (Fig. 7-6) observed from the experimental result, a series of unit cell analysis cases with increasing inter-tow crack length (Fig. 7-7) are carried out to reflect the progressive manner of damage development. As can be seen, the artificial cracks are introduced in the models to mimic the real inter-tow cracks as closely as possible.

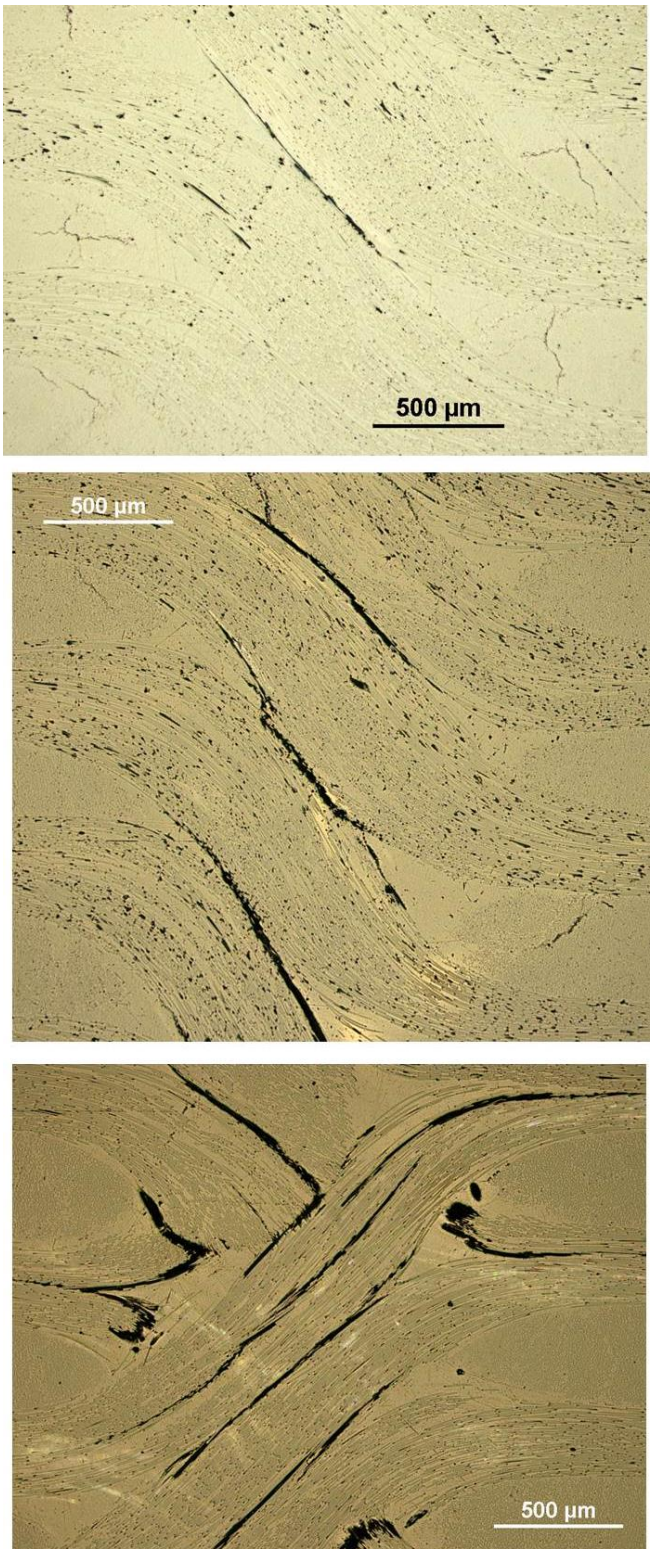

Fig. 7-6 Example of the GF 3D woven composites inter-tow crack damage development under increasing warp direction loading

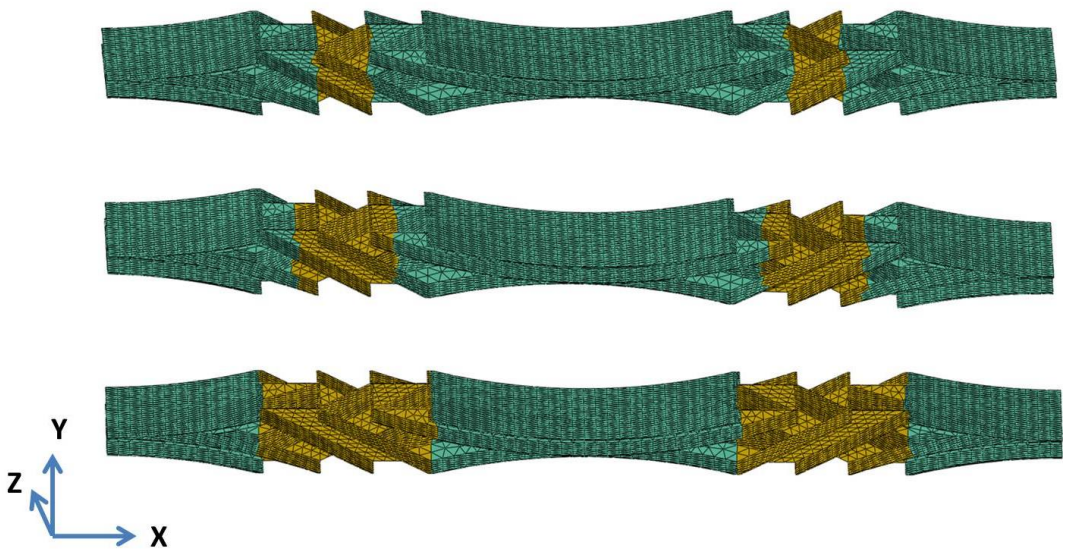

Fig. 7-7 Interfacial element mesh with yellow-coloured elements simulating inter-tow crack development

After carrying out unit cell analysis for all these cases, effective material properties (Table 7-1 & Table 7-2) are obtained for both the IM7 CF and GF 3D woven composites containing introduced inter-tow cracks.

Table 7-1 Effective properties of IM7 CF 3D woven composites with artificially introduced inter-tow cracks

Properties	Predictions from unit cell analysis cases			
	Undamaged case	Crack length = 0.63mm	Crack length = 0.84mm	Crack length = 1.25mm
E_X (GPa)	43.9	42.3	40.1	35.9
Ω_{DX} (%)	0	3.82	8.75	18.4
E_Y (GPa)	62.9	62.6	62	61.3
Ω_{DY} (%)	0	0.62	1.5	2.7
$K_Y = \frac{\Omega_{DY}}{\Omega_{DX}}$	N/A	0.16	0.17	0.15
E_Z (GPa)	8.44	7.92	7.32	6.44

Ω_{DZ} (%)	0	6.17	13.3	23.4
$K_Z = \frac{\Omega_{DZ}}{\Omega_{DX}}$	N/A	1.6	1.5	1.3
G_{XY} (GPa)	3.21	3.03	2.78	2.38
Ω_{DXY} (%)	0	5.43	13.4	26
$K_{XY} = \frac{\Omega_{DXY}}{\Omega_{DX}}$	NA	1.4	1.5	1.4
G_{XZ} (GPa)	4.65	4.63	4.59	4.49
Ω_{DXZ} (%)	0	0.5	1.42	3.44
$K_{XZ} = \frac{\Omega_{DXZ}}{\Omega_{DX}}$	N/A	0.13	0.16	0.19
G_{YZ} (GPa)	2.68	2.54	2.38	2.11
Ω_{DYZ} (%)	0	5.29	11.4	20.4
$K_{YZ} = \frac{\Omega_{DYZ}}{\Omega_{DX}}$	N/A	1.4	1.3	1.1

Table 7-2 Effective properties of GF 3D woven composites with artificially introduced inter-tow cracks

Properties	Predictions from unit cell analysis cases			
	Undamaged case	Crack length = 0.63mm	Crack length = 0.84mm	Crack length = 1.25mm
E_X (GPa)	23.7	23	20.6	16.2
Ω_{DX} (%)	0	3.06	13.1	31.8
E_Y (GPa)	24.8	24.3	23.1	20.2

Ω_{DY} (%)	0	1.74	6.55	18.2
$K_Y = \frac{\Omega_{DY}}{\Omega_{DX}}$	N/A	0.57	0.5	0.57
E_Z (GPa)	11.6	11.3	10.5	8.71
Ω_{DZ} (%)	0	2.31	9.43	24.9
$K_Z = \frac{\Omega_{DZ}}{\Omega_{DX}}$	N/A	0.75	0.72	0.78
G_{XY} (GPa)	5.28	5.07	4.38	2.73
Ω_{DXY} (%)	0	3.82	17	48.4
$K_{XY} = \frac{\Omega_{DXY}}{\Omega_{DX}}$	NA	1.3	1.3	1.52
G_{XZ} (GPa)	5.59	5.47	5.09	4.15
Ω_{DXZ} (%)	0	2.37	8.95	25.9
$K_{XZ} = \frac{\Omega_{DXZ}}{\Omega_{DX}}$	N/A	0.77	0.69	0.81
G_{YZ} (GPa)	4.41	4.31	3.99	3.38
Ω_{DYZ} (%)	0	2.02	9.34	23.4
$K_{YZ} = \frac{\Omega_{DYZ}}{\Omega_{DX}}$	N/A	0.66	0.71	0.73

As can be seen from Table 7-1 and Table 7-2, for cases with longer inter-tow cracks, lower effective Young's moduli values are predicted which demonstrated the effect of damage of these cracks. Also, all Young's moduli and shear moduli are affected by the cracks since the cracks are positioned around the warp tows. There is recognisable dependence between different inter-tow damage variables

Ω_{Ds}, indicating coupled damage effect. This is shown by the ratios of damage variables designated as K_Y, K_Z, K_{YZ}, K_{XZ} and K_{XY} in Table 7-1 and Table 7-2, which are all assessed against Ω_{DX}. Since each of these ratios did not show large variations in value with the increase of inter-tow damage Ω_{DX}, they are therefore regarded as constants with their absolute values approximated by their respective averaged values as summarised in Table 7-3.

Table 7-3 Averaged values for ratios of damage variables

	For IM7 CF 3D woven composites	For GF 3D woven composites
K_Y	0.16	0.55
K_Z	1.5	0.75
K_{XY}	1.4	1.4
K_{XZ}	0.16	0.76
K_{YZ}	1.3	0.7

With the confirmation of coupled damage effect, the constitutive relationship in (7-1) can be modified into (7-2).

$$[S]=\begin{bmatrix} S_{11} & S_{12} & S_{13} & 0 & 0 & 0 \\ & S_{22} & S_{23} & 0 & 0 & 0 \\ & & S_{33} & 0 & 0 & 0 \\ & & & S_{44} & 0 & 0 \\ & Symm & & & S_{55} & 0 \\ & & & & & S_{66} \end{bmatrix} \qquad (7\text{-}2)$$

where

$$S_{11}=\frac{1}{E_X^0(1-\Omega_{IX}-\Omega_{DX})}$$

$$S_{12} = -\frac{\nu_{XY}^0}{E_X^0}$$

$$S_{13} = -\frac{\nu_{XZ}^0}{E_X^0}$$

$$S_{22} = \frac{1}{E_Y^0(1-\Omega_{IY} - K_Y\Omega_{DX})}$$

$$S_{23} = -\frac{\nu_{YZ}^0}{E_Y^0}$$

$$S_{33} = \frac{1}{E_Z^0(1-\Omega_{IZ} - K_Z\Omega_{DX})}$$

$$S_{44} = \frac{1}{G_{YZ}^0(1-\Omega_{IYZ} - K_{YZ}\Omega_{DX})}$$

$$S_{55} = \frac{1}{G_{XZ}^0(1-\Omega_{IXZ} - K_{XZ}\Omega_{DX})}$$

$$S_{66} = \frac{1}{G_{XY}^0(1-\Omega_{IXY} - K_{XY}\Omega_{DX})}$$

Since the intra-tow damage variables Ω_{Is} in (7-2) can all be worked out from unit cell analysis of 3D woven composites where tows are modelled by the UD composite CDM model, (7-2) can therefore be split into two parts as a truncated Taylor series with respect to Ω_{DX} as shown in (7-3), with the effects of inter-tow damage appearing only in $[S_A]$.

$$\begin{aligned}[\varepsilon] &= [S][\sigma] = ([S_I] + [S_A])[\sigma] \\ &= [\varepsilon_I] + [\varepsilon_{D-add}]\end{aligned} \tag{7-3}$$

In (7-3), $[\varepsilon_I]$ represents the strain prediction resulting from the unit cell analysis where only intra-tow damage is present, while $[\varepsilon_{D-add}]$ is the part of the strain in addition to $[\varepsilon_I]$ to account for the effect from inter-tow damage.

In (7-3), $[S_I]$ is expressed as:

$$[S_I] = \begin{bmatrix} S_{I11} & S_{I12} & S_{I13} & 0 & 0 & 0 \\ & S_{I22} & S_{I23} & 0 & 0 & 0 \\ & & S_{I33} & 0 & 0 & 0 \\ & & & S_{I44} & 0 & 0 \\ & Symm & & & S_{I55} & 0 \\ & & & & & S_{I66} \end{bmatrix} \quad (7\text{-}4)$$

where

$$S_{I11} = \frac{1}{E_X^0(1-\Omega_{IX})}$$

$$S_{I12} = -\frac{\nu_{XY}^0}{E_X^0}$$

$$S_{I13} = -\frac{\nu_{XZ}^0}{E_X^0}$$

$$S_{I22} = \frac{1}{E_Y^0(1-\Omega_{IY})}$$

$$S_{I23} = -\frac{\nu_{YZ}^0}{E_Y^0}$$

$$S_{I33} = \frac{1}{E_Z^0(1-\Omega_{IZ})}$$

$$S_{I44} = \frac{1}{G_{YZ}^0(1-\Omega_{IYZ})}$$

$$S_{I55} = \frac{1}{G_{XZ}^0(1-\Omega_{IXZ})}$$

$$S_{I66} = \frac{1}{G_{XY}^0(1-\Omega_{IXY})}$$

while $[S_A]$ is obtained as:

$$[S_A] = [S] - [S_I]$$

$$= \begin{bmatrix} S_{A11} & 0 & 0 & 0 & 0 & 0 \\ & S_{A22} & 0 & 0 & 0 & 0 \\ & & S_{A33} & 0 & 0 & 0 \\ & & & S_{A44} & 0 & 0 \\ & Symm & & & S_{A55} & 0 \\ & & & & & S_{A66} \end{bmatrix} \quad (7\text{-}5)$$

where

$$S_{A11} = \frac{\Omega_{DX}}{E_X^0(1-\Omega_{DX}-2\Omega_{IX})}$$

$$S_{A22} = \frac{K_Y\Omega_{DX}}{E_Y^0(1-K_Y\Omega_{DX}-2\Omega_{IY})}$$

$$S_{A33} = \frac{K_Z\Omega_{DX}}{E_Z^0(1-K_Z\Omega_{DX}-2\Omega_{IZ})}$$

$$S_{A44} = \frac{K_{YZ}\Omega_{DX}}{G_{YZ}^0(1-K_{YZ}\Omega_{DX}-2\Omega_{IYZ})}$$

$$S_{A55} = \frac{K_{XZ}\Omega_{DX}}{G_{XZ}^0(1-K_{XZ}\Omega_{DX}-2\Omega_{IXZ})}$$

$$S_{A66} = \frac{K_{XY}\Omega_{DX}}{G_{XY}^0(1-K_{XY}\Omega_{DX}-2\Omega_{IXY})}$$

7.3 Damage Initiation

As shown previously in Fig. 4-6, according to the assumptions made for the current damage model, inter-tow crack damage is deemed to have initiated only when the unit cell analysis prediction for stress-strain response begins to deviate away from the experimental stress-strain curve. This assumption should be validated against experimental result by showing that the actual inter-tow cracks

indeed first started to appear around this point in reality. If so, then the use of it for defining inter-tow damage initiation is justified.

7.4 Damage Driving Force and Damage Evolution Law

Similar to the earlier derivation process for the damage driving force of the UD composite CDM model in Chapter 3, here, the derivation of damage driving force for inter-tow damage model also starts from energy expression of damaged material, but in the context of damaged 3D woven composites. According to [89], the complementary strain energy density function U_{meso} can be expressed as (7-6).

$$
\begin{aligned}
[U_{meso}] &= \frac{1}{2}[\sigma]^T[\varepsilon] \\
&= \frac{1}{2}\sigma_X\left[\frac{\sigma_X}{E_X^0(1-\Omega_{IX}-\Omega_{DX})} - \frac{\nu_{XY}^0\sigma_Y}{E_X^0} - \frac{\nu_{XZ}^0\sigma_Z}{E_X^0}\right] \\
&\quad + \frac{1}{2}\sigma_Y\left[\frac{\sigma_Y}{E_Y^0(1-\Omega_{IY}-K_Y\Omega_{DX})} - \frac{\nu_{XY}^0\sigma_X}{E_X^0} - \frac{\nu_{YZ}^0\sigma_Z}{E_Y^0}\right] \\
&\quad + \frac{1}{2}\sigma_Z\left[\frac{\sigma_Z}{E_Z^0(1-\Omega_{IZ}-K_Z\Omega_{DX})} - \frac{\nu_{XZ}^0\sigma_X}{E_X^0} - \frac{\nu_{YZ}^0\sigma_Y}{E_Y^0}\right] \\
&\quad + \frac{1}{2}\frac{\tau_{YZ}^2}{G_{YZ}^0(1-\Omega_{IYZ}-K_{YZ}\Omega_{DX})} \\
&\quad + \frac{1}{2}\frac{\tau_{XZ}^2}{G_{XZ}^0(1-\Omega_{IXZ}-K_{XZ}\Omega_{DX})} \\
&\quad + \frac{1}{2}\frac{\tau_{XY}^2}{G_{XY}^0(1-\Omega_{IXY}-K_{XY}\Omega_{DX})}
\end{aligned}
\tag{7-6}
$$

where $[\varepsilon]=[S][\sigma]$.

Then, damage driving force for inter-tow damage (7-7) is derived.

$$\rho_D = \frac{\partial U_{meso}}{\partial \Omega_{DX}} = \rho_{DX} + \rho_{DY} + \rho_{DZ} + \rho_{DYZ} + \rho_{DXZ} + \rho_{DXY} \qquad (7\text{-}7)$$

Where

$$\rho_{DX} = \frac{\sigma_X^2}{2E_X^0(1-\Omega_{IX}-\Omega_{DX})^2}$$

$$\rho_{DY} = \frac{K_Y\sigma_Y^2}{2E_Y^0(1-\Omega_{IY}-K_Y\Omega_{DX})^2}$$

$$\rho_{DZ} = \frac{K_Z\sigma_Z^2}{2E_Z^0(1-\Omega_{IZ}-K_Z\Omega_{DX})^2}$$

$$\rho_{DYZ} = \frac{K_{YZ}\tau_{YZ}^2}{2G_{YZ}^0(1-\Omega_{IYZ}-K_{YZ}\Omega_{DX})^2}$$

$$\rho_{DXZ} = \frac{K_{XZ}\tau_{XZ}^2}{2G_{XZ}^0(1-\Omega_{IXZ}-K_{XZ}\Omega_{DX})^2}$$

$$\rho_{DXY} = \frac{K_{XY}\tau_{XY}^2}{2G_{XY}^0(1-\Omega_{IXY}-K_{XY}\Omega_{DX})^2}$$

As can be seen, similar to the damage driving force ρ derived in Chapter 3 for the UD composite CDM model, damage driving force ρ_D (7-7) for inter-tow crack damage is also a function of undamaged material properties, damage variables and stresses, with the dimension of stresses.

Also, one may notice that all six stresses appeared in the damage driving force expression. The reason for this is similar to that given previously in Section 7.2, namely, the inter-tow cracks caused by warp direction loading may have different crack orientations, with the possibility that any of the six stress components can contribute to the propagation of an arbitrarily orientated crack. As a result, all six stresses should be included in the damage driving force formula.

As shown in (3-17), inter-tow damage Ω_{DX} is defined to be driven by damage driving force components.

$$\Omega_{DX} = fn\left(\rho_{DX}, \rho_{DY}, \rho_{DZ}, \rho_{DYZ}, \rho_{DXZ}, \rho_{DXY}\right) \qquad (7\text{-}8)$$

Imagine a situation where the critical state for inter-tow damage initiation is met with values of damage driving force components reaching ρ_{DX0}, ρ_{DY0}, ρ_{DZ0}, ρ_{DYZ0}, ρ_{DXZ0} and ρ_{DXY0}. Then, expanding (3-17) into a Taylor's series in the neighbourhood of the critical state at a given damage state Ω_{DX0}, with terms higher than first order neglected, the damage evolution law approximated is as shown in (7-9).

$$\begin{aligned}\Omega_{DX} = \Omega_{DX0} &+ \mu_{DX}(\rho_{DX} - \rho_{DX0}) + \mu_{DY}(\rho_{DY} - \rho_{DY0}) \\ &+ \mu_{DZ}(\rho_{DZ} - \rho_{DZ0}) + \mu_{DYZ}(\rho_{DYZ} - \rho_{DYZ0}) \\ &+ \mu_{DXZ}(\rho_{DXZ} - \rho_{DXZ0}) + \mu_{DXY}(\rho_{DXY} - \rho_{XY0}) + \cdots\end{aligned} \qquad (7\text{-}9)$$

or

$$\begin{aligned}\Delta\Omega_{DX} = \mu_{DX}\Delta\rho_{DX} &+ \mu_{DY}\Delta\rho_{DY} + \mu_{DZ}\Delta\rho_{DZ} \\ &+ \mu_{DYZ}\Delta\rho_{DYZ} + \mu_{DXZ}\Delta\rho_{DXZ} + \mu_{DXY}\Delta\rho_{DXY}\end{aligned}$$

where μ_{DX}, μ_{DY}, μ_{DZ}, μ_{DYZ}, μ_{DXZ} and μ_{DXY} are the inter-tow damage evolution constants associated with different stresses. They are regarded as material properties of the specific 3D woven material system concerned.

However, for this research project, the only experimental result available for inter-tow damage process was obtained under warp direction uniaxial stress σ_X as recorded in Chapter 4, which means only μ_{DX} associated with warp direction

stress σ_X can be determined from the experimental result. (7-9) is therefore simplified into (7-10) where only σ_X is considered.

$$\Delta\Omega_{DX} = \mu_{DX}\Delta\rho_{DX} \qquad (7\text{-}10)$$

To determine μ_{DX}, a stress-strain plot like the one in Fig. 7-1 should be referred to so that the values of Ω_{DX} and ρ_{DX} can be extracted to provide reasonable approximation over a practical range of warp direction stress. Then, an empirical relationship between Ω_{DX} and ρ_{DX} can be obtained which is used to estimate the value of μ_{DX} according to (7-11).

$$\mu_{DX} = \frac{d\Omega_{DX}}{d\rho_{DX}} \qquad (7\text{-}11)$$

However, in order to satisfy the second law of thermodynamics, the damage evolution constant μ_{DX} obtained should always ensure that the damage increment $\Delta\Omega_{DX}$ calculated from (7-10) is compliant to the inequality in (7-12).

$$\rho_{DX}\Delta\Omega_{DX} \geq 0 \qquad (7\text{-}12)$$

To implement this incremental inter-tow damage evolution law, the warp direction loading process can be divided into small stress increments of $\Delta\sigma_X$. In addition, simulation result from unit cell analysis is also used so that values of total stress σ_X, total strain ε_{IX} and intra-tow damage variable Ω_{IX} at the start and at the end of every stress increment are evaluated.

Starting from the stress increment just beyond inter-tow damage initiation point, damage driving force increment $\Delta\rho_{DX}$ can be calculated according to (7-13) based on the initial condition that Ω_{DX} is zero.

$$\Delta\rho_{DX(n)} = \frac{\sigma_{X(n+1)}^2}{2E_X^0(1-\Omega_{IX(n+1)}-\Omega_{DX(n)})^2} - \frac{\sigma_{X(n)}^2}{2E_X^0(1-\Omega_{IX(n)}-\Omega_{DX(n-1)})^2} \tag{7-13}$$

where

$$\Omega_{DX(n)} = \Omega_{DX(n-1)} + \Delta\Omega_{DX}$$

$$\Omega_{IX(n+1)} = \Omega_{IX(n)} + \Delta\Omega_{IX}$$

$$\sigma_{X(n+1)} = \sigma_{X(n)} + \Delta\sigma_X$$

After this, substituting the damage driving force increment $\Delta\rho_{DX}$ into (7-10), the damage increment $\Delta\Omega_{DX}$ can be calculated and added to the previous total value of Ω_{DX} for updating the damage status. However, due to the nature of incremental algorithm, the updated damage variable Ω_{DX} will be used in the next increment rather than for the current one as indicated in (7-13).

By substituting this updated damage variable Ω_{DX} into (7-3) and (7-5), the corresponding additional strain term ε_{DX-add} can be worked out, which then modifies the strain value from ε_{IX} to ε_X.

This process is repeated for all stress increments beyond inter-tow damage initiation point. In this way, for a given warp direction stress loading history, the

strain prediction ε_{IX} from unit cell analysis can be modified by the inter-tow damage model. The resulting new stress-strain prediction σ_X - ε_X is expected to approximate the experimental result, having incorporated both intra-tow and inter-tow damage effects in the modelling process.

7.5 Model Implementation and Verification

To verify the formulations and the algorithm derived above for the inter-tow crack damage model, a verification example is designed and implemented. For simplicity, only warp direction stress-strain behaviour is considered in this example.

The warp direction stress-strain behaviour of an imaginary 3D woven composite material is assumed and illustrated in Table 7-4 and Fig. 7-8. As can be seen, the undamaged warp direction Young's modulus value E_X^0 is assumed to be 20 GPa and the initiation point for inter-tow crack damage is set at 100 MPa of σ_X. In addition, the stress-strain response (σ_X - ε_{IX}) accounting only for intra-tow damage is also assumed. As a result, the inter-tow damage model is applied with the presence of intra-tow damage, which is a more general scenario.

Table 7-4 Assumed stress-strain data for the verification case

σ_X (MPa)	ε_{IX} (%)	Ω_{IX} (%)	ε_X (%)
0	0	0	0
20	0.1	0	0.1
40	0.2	0	0.2
60	0.3	0	0.3

80	0.4	0	0.4
100	0.5	0	0.5
117	0.593	1.6	0.6
128	0.676	5.2	0.7
139	0.755	7.9	0.8
150	0.831	9.9	0.9
160	0.903	11.4	1
169	0.972	12.6	1.1
179	1.037	13.6	1.2
188	1.099	14.4	1.3
197	1.158	15	1.4
205	1.214	15.6	1.5
213	1.267	16	1.6
220	1.316	16.3	1.7
227	1.363	16.6	1.8
234	1.406	16.9	1.9
240	1.447	17.1	2

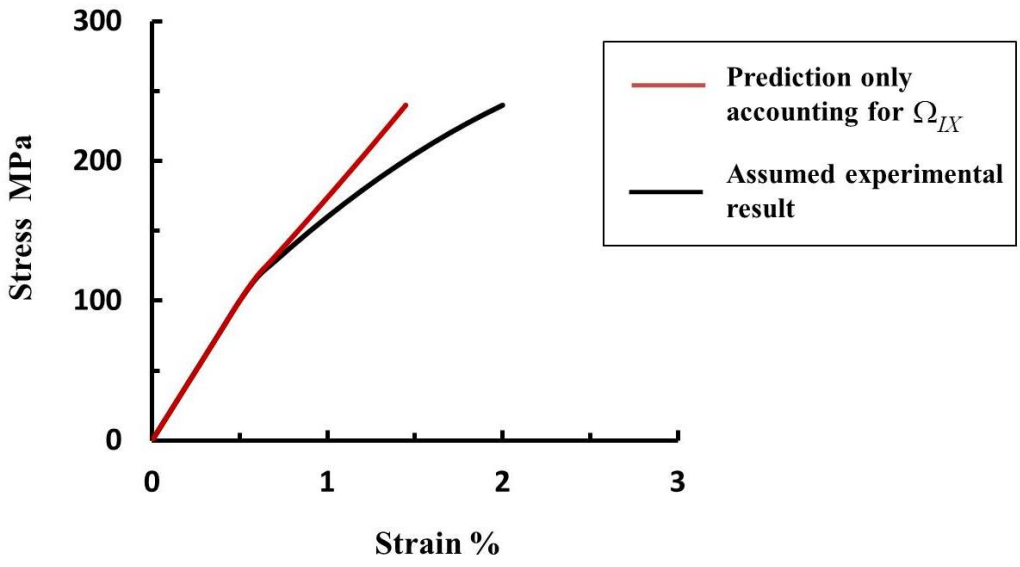

Fig. 7-8 Assumed warp direction stress-strain responses for the verification case

Based on the assumed data in Table 7-4, using (7-14) and (7-15), data points for Ω_{DX} and ρ_{DX} can be obtained as shown in Table 7-5.

$$\Omega_{DX} = 1 - \frac{E_X}{E_X^0} - \Omega_{IX} \qquad (7\text{-}14)$$

$$\rho_{DX} = \frac{\sigma_X^2}{2E_X^0 (1 - \Omega_{IX} - \Omega_{DX})^2} \qquad (7\text{-}15)$$

Table 7-5 Damage data extracted from Fig. 7-8

σ_X (MPa)	Ω_{DX} (%)	ρ_{DX} (MPa)
100	0	0.5
117	1.1	0.72
128	3.2	0.98
139	5.1	1.28
150	6.9	1.62
160	8.6	2
169	10.2	2.42
179	11.7	2.88
188	13.2	3.38
197	14.7	3.92
205	16.1	4.5
213	17.5	5.12
220	18.9	5.78
227	20.3	6.48
234	21.6	7.22
240	22.9	8

Then, using the data in Table 7-5, the empirical relationship between Ω_{DX} and ρ_{DX} can be plotted as in Fig. 7-9. This empirical relationship is fitted into a natural logarithm curve function as shown in (7-16).

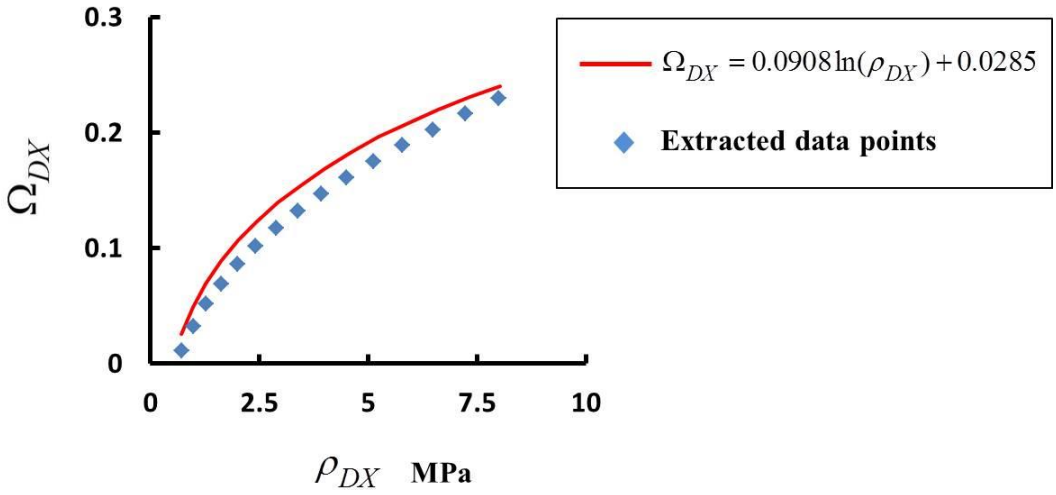

Fig. 7-9 Assumed warp direction stress-strain responses for the verification case

$$\Omega_{DX} = 0.0908\ln(\rho_{DX}) + 0.0285 \qquad (7\text{-}16)$$

With the empirical relationship between Ω_{DX} and ρ_{DX} established, the inter-tow cracking damage evolution constant μ_{DX} can be worked out according to (7-17).

$$\mu_{DX} = \frac{d\Omega_{DX}}{d\rho_{DX}} = \frac{0.0908}{\rho_{DX}} \qquad (7\text{-}17)$$

Now, all assumed material properties necessary for implementing the damage model are defined. The damage model is then used to modify the σ_X - ε_{IX} stress-strain response into the σ_X - ε_X stress-strain response. If the resulting

σ_X - ε_X stress-strain response is similar to the one assumed in Table 7-4, the damage model is verified.

As mentioned, this damage model uses an incremental algorithm based on stress increments of $\Delta\sigma_X$. Correspondingly, the damage driving force increment $\Delta\rho_{DX}$ can be calculated according to (7-18).

$$\Delta\rho_{DX(n)} = \frac{\sigma_{X(n+1)}^2}{2E_X^0(1-\Omega_{IX(n+1)}-\Omega_{DX(n)})^2} - \frac{\sigma_{X(n)}^2}{2E_X^0(1-\Omega_{IX(n)}-\Omega_{DX(n-1)})^2} \tag{7-18}$$

Then, using the damage evolution law in (7-19), damage increment $\Delta\Omega_{DX}$ can be found.

$$\Delta\Omega_{DX} = \mu_{DX}\Delta\rho_{DX} \tag{7-19}$$

After this, the damage increment $\Delta\Omega_{DX}$ calculated from every stress increment is used to update the damage variable as shown in (7-20).

$$\Omega_{DX(n+1)} = \Omega_{DX(n)} + \Delta\Omega_{DX} \tag{7-20}$$

Since in this case only warp direction stress-train behaviour is considered, the constitutive relationship in (7-3) can be simplified to (7-21).

$$\varepsilon_X = \varepsilon_{IX} + \frac{\Omega_{DX}\sigma_X}{E_X^0(1-\Omega_{DX}-2\Omega_{IX})} \qquad (7\text{-}21)$$
$$= \varepsilon_{IX} + \varepsilon_{DX-add}$$

Then, the updated damage variable Ω_{DX} from (7-20) is substituted into (7-21) for updating the strain prediction. Some of the quantities predicted by the damage model are presented in Table 7-6 and they are not far off in value from those in Table 7-5.

Table 7-6 Data produced by the damage model

σ_X (MPa)	Ω_{DX} (%)	ρ_{DX} (MPa)	ε_{DX-add} (%)
100	0	0.5	0
117	2.6	0.7	0.016
128	4.9	0.97	0.037
139	6.9	1.27	0.062
150	8.8	1.62	0.093
160	10.6	2.01	0.128
169	12.3	2.45	0.168
179	13.9	2.93	0.212
188	15.4	3.45	0.261
197	16.9	4.01	0.314
205	18.3	4.61	0.371
213	19.6	5.24	0.431
220	20.8	5.91	0.494
227	22	6.60	0.559
234	23.1	7.32	0.624
240	24	8.04	0.687

The resulting σ_X - ε_X stress-strain response produced by the damage model is illustrated in Fig. 7-10. As can be seen, the prediction is very close to the assumed experimental result which means this inter-tow damage model for modifying σ_X - ε_{IX} stress-strain response is verified.

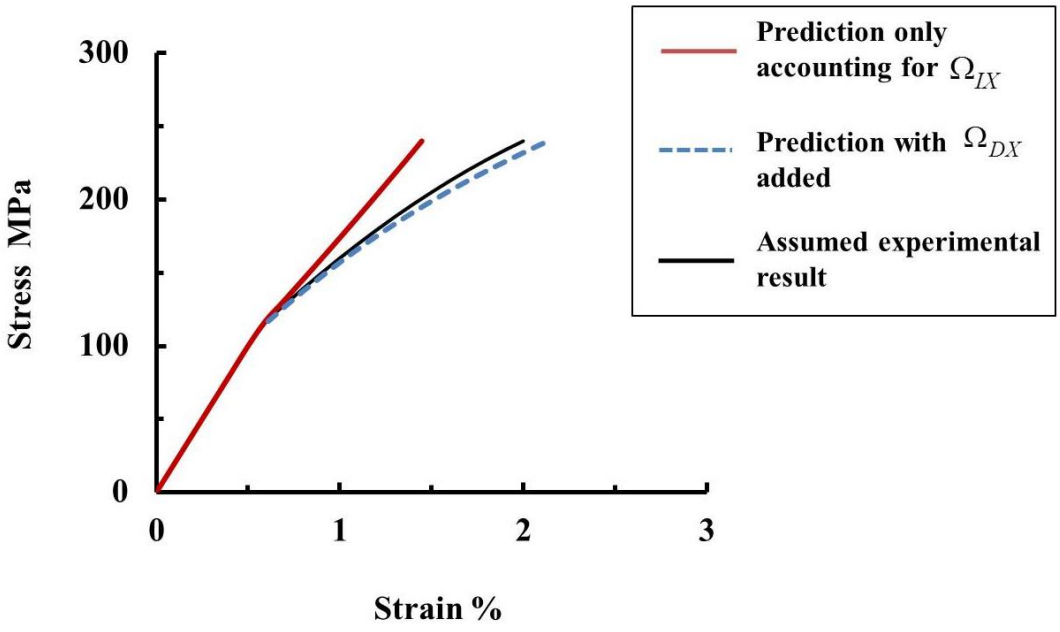

Fig. 7-10 Predicted warp direction stress-strain response for the verification case

7.6 Test Cases for Model Validation

As described in Chapter 6, damage modelling for the 3D woven composites was conducted using unit cell analysis under the condition that damage could initiate and evolve only within the tows. The result from the unit cell analysis suggested that the stress-strain response could not be accurately predicted for the cases where the materials were loaded in the warp direction. The cause for the discrepancy in those cases was the lack of inter-tow damage modelling capability for the unit cell analysis models.

To account for the effect of inter-tow damage, based on the results from aforementioned unit cell analysis where intra-tow damage was already predicted, the pragmatic inter-tow damage model introduced in this chapter is applied for predicting the warp direction stress-strain response of the 3D woven composites.

7.6.1 IM7 Carbon Fibre 3D Woven Composites under Warp Direction Uniaxial Tension

For the case of IM7 CF 3D woven composites under warp direction tension, the discrepancy in stress-strain response between the unit cell model prediction and the experimental result is evident as shown in Fig. 7-11.

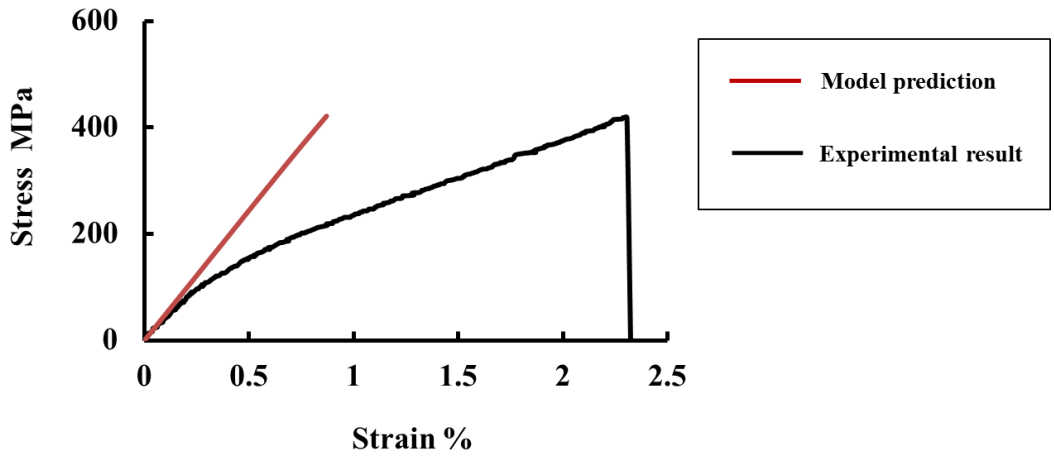

Fig. 7-11 Comparison between the unit cell analysis prediction and the experimental result

Recall that from the experimental result in Section 6.2.2.1, the inter-tow cracks were observed to initiate at 0.25% warp direction strain. This inter-tow damage initiation point is reflected in Fig. 7-11, where the model prediction curve separated from the experimental result curve, which is also at around 0.25% warp direction strain. This confirms that the 0.25% warp direction strain with 80 MPa

warp direction stress can indeed be regarded as the inter-tow damage initiation point.

Moreover, the stress-strain curve predicted by the unit cell analysis was linear, which implies that the predicted intra-tow damage had negligible effect on the 3D woven material stress-strain behaviour. Because of this, the intra-tow damage variable Ω_{IX} can be considered as equal to zero.

Following the procedure introduced in Section 7.5, the stress-strain data in Fig. 7-11 is used to calculate the inter-tow damage variable Ω_{DX} and the damage driving force, ρ_{DX} , which are defined as follows.

$$\Omega_{DX} = 1 - \frac{E_X}{E_X^0} \qquad (7\text{-}22)$$

$$\rho_{DX} = \frac{\sigma_X^2}{2E_X^0(1-\Omega_{DX})^2} \qquad (7\text{-}23)$$

The derivation of (7-22) and (7-23) has already been provided in Section 7.5.

This yields a set of data points for Ω_{DX} and ρ_{DX} , with some of them shown in Table 7-7 for illustration.

Table 7-7 Inter-tow damage data extracted from Fig. 7-11

σ_X (MPa)	Ω_{DX} (%)	ρ_{DX} (MPa)
80	0	0.1
120	27	0.56
170	41	1.7
220	48	3.7

270	56	7.6
320	59	13
370	61	19
420	62	26

The empirical relationship between Ω_{DX} and ρ_{DX} , as specified in Table 7-7, can be visualised by plotting Ω_{DX} against ρ_{DX} . As can be seen in Fig. 7-12, the relationship between them is highly nonlinear and it is found to be best approximated by the natural logarithm curve function as below.

$$\Omega_{DX} = 0.123\ln(\rho_{DX}) + 0.308 \qquad (7\text{-}24)$$

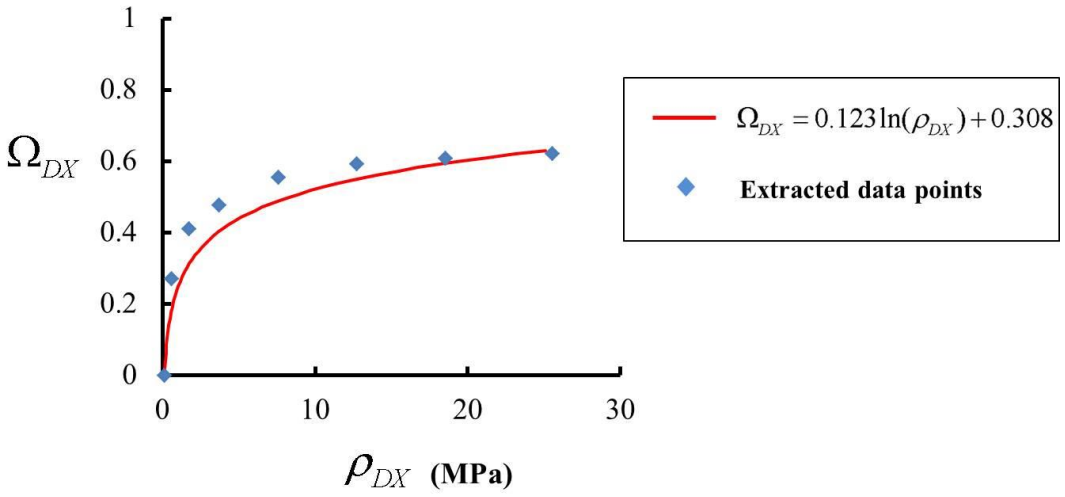

Fig. 7-12 Empirical relationship between Ω_{DX} and ρ_{DX}

With the empirical relationship between Ω_{DX} and ρ_{DX} determined, the inter-tow damage evolution constant can be calculated as

$$\mu_{DX} = \frac{d\Omega_{DX}}{d\rho_{DX}} = \frac{0.123}{\rho_{DX}} \qquad (7\text{-}25)$$

As mentioned previously, the inter-tow damage model uses an incremental algorithm with stress increments of $\Delta\sigma_X$. Correspondingly, the inter-tow damage driving force increment $\Delta\rho_{DX}$ can be calculated according to

$$\Delta\rho_{DX(n)} = \frac{\sigma_{X(n+1)}^2}{2E_X^0(1-\Omega_{DX(n)})^2} - \frac{\sigma_{X(n)}^2}{2E_X^0(1-\Omega_{DX(n-1)})^2} \qquad (7\text{-}26)$$

One should note that the intra-tow damage variable Ω_{IX} is omitted in (7-26) as it equals to zero for this particular case. Then, using the damage evolution law defined in Section 7.4 which is presented here in (7-27), inter-tow damage increment $\Delta\Omega_{DX}$ can be found.

$$\Delta\Omega_{DX} = \mu_{DX}\Delta\rho_{DX} \qquad (7\text{-}27)$$

After this, the damage increment $\Delta\Omega_{DX}$ calculated from every stress increment is used to update the total inter-tow damage variable as shown in (7-28).

$$\Omega_{DX(n+1)} = \Omega_{DX(n)} + \Delta\Omega_{DX} \qquad (7\text{-}28)$$

As in this case only warp direction stress-strain behaviour is concerned, the constitutive relationship can be simplified to (7-29). Then, the updated total inter-tow damage variable Ω_{DX} from (7-28) is substituted into (7-29) for updating the strain prediction.

$$\varepsilon_X = \varepsilon_{IX} + \frac{\Omega_{DX}\sigma_X}{E_X^0(1-\Omega_{DX})} \qquad (7\text{-}29)$$
$$= \varepsilon_{IX} + \varepsilon_{DX-add}$$

With the inter-tow damage model applied as described above, the resulting modified stress-strain curve is plotted in Fig. 7-13 along with the curves from unit cell analysis and the experimental result.

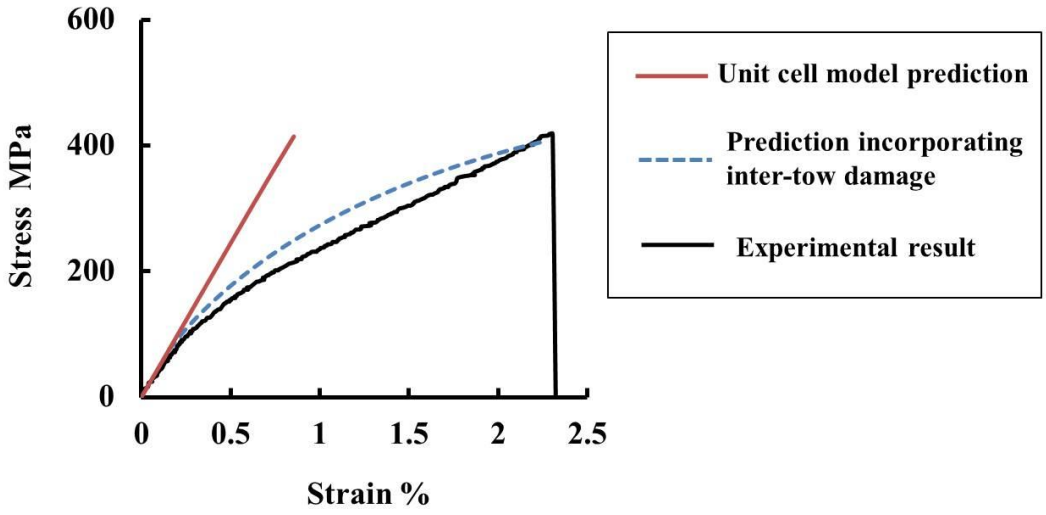

Fig. 7-13 Comparison between predictions for stress-strain response

As can be seen, with the inter-tow damage being accounted for, the modified stress-strain curve appeared to be a much better approximation to the experimental curve.

7.6.2 E-glass Fibre 3D Woven Composites under Warp Direction Uniaxial Tension

Similar to the case of IM7 CF 3D woven composite above, there is also a substantial discrepancy between the predicted and the measured stress-strain

curves for the GF 3D woven composite under warp direction tension. The comparison of the two curves is shown in Fig. 7-14.

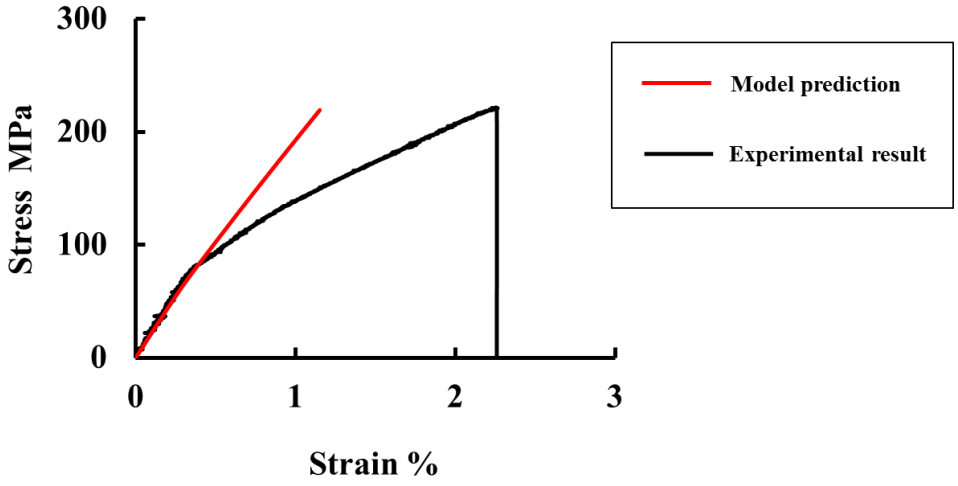

Fig. 7-14 Comparison between the unit cell analysis prediction and the experimental result for stress-strain responses

In this case, as shown in Fig. 7-14, the point of separation between the two curves corresponds to the experimentally determined inter-tow cracking damage initiation point at 0.35% warp direction strain. Consequently, this point is validated as the inter-tow damage initiation point for applying the inter-tow damage model.

In contract to the negligible effect of intra-tow damage on the stress-strain response of IM7 CF 3D woven composite under warp direction tension, the presence of intra-tow damage in the GF 3D woven composite affected the stress-strain response, making it nonlinear. Therefore, the intra-tow damage variable Ω_{IX} cannot be neglected in this case.

Based on the predicted stress values from unit cell analysis in Fig. 7-14, data points for Ω_{DX} and ρ_{DX} are obtained as follows.

$$\Omega_{DX} = 1 - \frac{E_X}{E_X^0} - \Omega_{IX} \qquad (7\text{-}30)$$

$$\rho_{DX} = \frac{\sigma_X^2}{2E_X^O(1-\Omega_{DX}-\Omega_{IX})^2} \qquad (7\text{-}31)$$

Table 7-8 Damage data extracted from Fig. 7-14

σ_X (MPa)	Ω_{IX} (%)	Ω_{DX} (%)	ρ_{DX} (MPa)
85	0	0	0.32
110	6.5	18	0.96
125	8.3	22	1.5
140	8.9	29	2.3
160	11	32	3.5
180	12	37	5.7
200	12	39	7.8
220	12	43	11

The calculated values of Ω_{DX} and ρ_{DX} as summarised in Table 7-5 are plotted in Fig. 7-15.

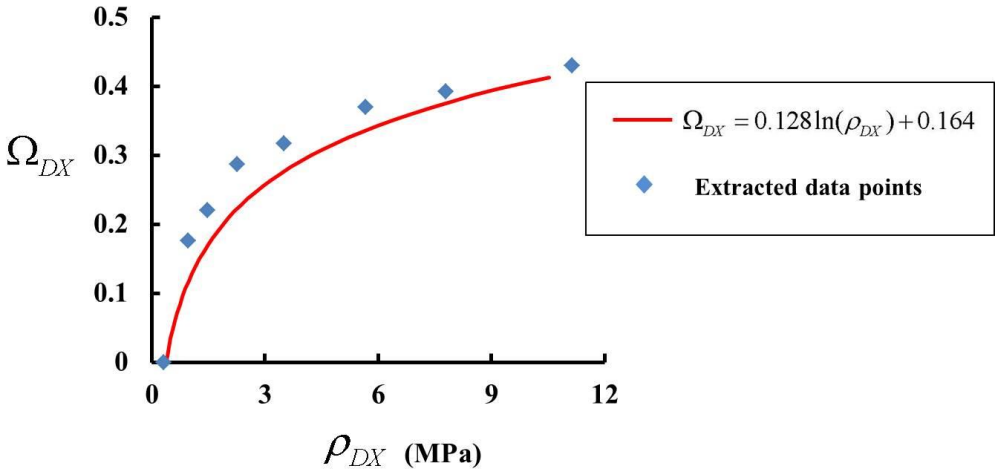

Fig. 7-15 Empirical relationship between Ω_{DX} and ρ_{DX}

As can be seen, the nonlinear relationship in Fig. 7-15 is best approximated by the natural logarithm curve function as below.

$$\Omega_{DX} = 0.128\ln(\rho_{DX}) + 0.164 \qquad (7\text{-}32)$$

With the empirical relationship between Ω_{DX} and ρ_{DX} established, the inter-tow damage model is applied following the same procedure as described in Section 7.6.1. Since the intra-tow damage variable Ω_{IX} needs to be accounted for in this case, the expressions for increment of damage driving force $\Delta\rho_{DX}$ and the strain prediction ε_X are as follows.

$$\Delta\rho_{DX(n)} = \frac{\sigma_{X(n+1)}^2}{2E_X^0(1-\Omega_{DX(n)}-\Omega_{IX(n+1)})^2} - \frac{\sigma_{X(n)}^2}{2E_X^0(1-\Omega_{DX(n-1)}-\Omega_{IX(n)})^2} \qquad (7\text{-}33)$$

$$\varepsilon_X = \varepsilon_{IX} + \frac{\Omega_{DX}\sigma_X}{E_X^0(1-\Omega_{DX}-2\Omega_{IX})} \qquad (7\text{-}34)$$

As can be seen in Fig. 7-16, with the unit cell analysis result modified by the inter-tow damage model, the new stress-strain prediction is much closer to the experimental result.

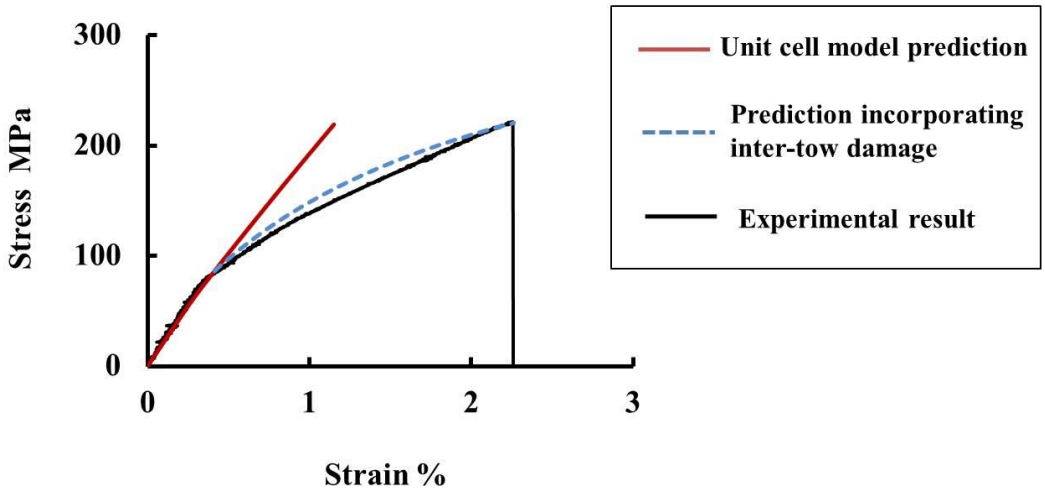

Fig. 7-16 Comparison between predictions for stress-strain response

7.7 Summary

In this chapter, a pragmatic continuum damage model is developed for characterising the damage effect of the inter-tow cracks in 3D woven composites caused by warp direction tensile loading.

In this model, use has been made of the unit cell analysis of 3D woven composites with artificially introduced inter-tow cracks. The coupled damage effect due to the inter-tow cracks is identified and included in the damage representation formulation. An incremental damage evolution law is proposed which works in conjunction with the intra-tow damage predicted by the unit cell analysis cases.

For a given warp direction stress loading history, the strain prediction "ε_{IX}" produced by the unit cell analysis of intra-tow damage is modified by the present inter-tow cracking damage model. The resulting new stress-strain prediction "σ_X - ε_X" is expected to better approximate the experimental result since both intra-tow and inter-tow cracking damage effects are captured during this modelling process.

As demonstrated by the validation cases of IM7 carbon fibre and E-glass fibre reinforced 3D woven composites loaded under warp direction uniaxial tension, in comparison to the stress-strain predictions where only the intra-tow damage was accounted for, the stress-strain predictions modified by the inter-tow cracking damage model indeed showed a much better resemblance to the experimental result.

8. Conclusions and Future work

8.1 Conclusions

8.1.1 Experimental Investigation for Damage in Laminates and 3D Textile Composites

Thanks to the laminate test cases designed and conducted in this project, it is found that the damage initiation and propagation related material constants $R_{\perp}^{T}$, μ_{I}, $R_{\perp\parallel}$ and μ_{II} for a certain type of composites can be determined using the test cases of transverse tensile testing and in-plane shear testing on UD laminates, and tensile testing on cross-ply laminates. As a result, whenever dealing with an unfamiliar composite system, these tests can be employed to determine necessary material properties usable for composite damage modelling.

Apart from the tests on laminates, detailed experimental investigation was carried out regarding damage in two types of layer-to-layer interlock 3D woven composites which are reinforced by IM7 carbon fibre (CF) and E-glass fibre (GF), respectively.

When the 3D woven composites were loaded in the warp direction, both the IM7 CF and the GF 3D woven composites exhibited nonlinear stress-strain responses in the form of almost bilinear relationship, which was shown to be caused by the inter-tow cracks appearing in the warp-curving regions. Moreover, transverse intra-tow cracks were also found inside the weft tows of the GF 3D woven composites, but such damage was not observed in the IM7 CF 3D woven composites due to the higher strengths required to initiate intra-tow cracking damage in the latter material.

On the other hand, when the 3D woven composites were loaded in the weft direction, through-the-thickness transverse cracks bypassing the weft tows were found in both the IM7 CF and the GF 3D woven composites. However, while these cracks gave rise of a source of nonlinearity to the weft direction stress-strain response of the GF 3D woven composite, the appearance of the stress-strain relationship of the IM7 CF 3D woven composite appeared to be rather linear as the high value of the fibre direction Young's modulus of IM7 carbon fibre in the weft tows is believed to have dominated the specimen level stress-strain response.

Furthermore, the experimental data obtained and the damage processes recorded for these layer-to-layer interlock 3D woven composites can serve as a good reference for future interests in this area, since currently only limited studies are available in the literatures regarding damage in this type of 3D woven composites.

8.1.2 A Novel Damage Model for UD Composites

Built on top of a consistent CDM damage representation formulation [149], a novel damage evolution law based on the concept of damage driving force is proposed for modelling the evolution of matrix damage in UD composites. It is to be applied in conjunction with the UD composite failure theory developed by Puck [88] which acts as a damage initiation criterion.

This damage evolution law has the advantage of describing the damage evolution process in terms of the total damage driving force which is naturally partitioned into three components directly associated with the corresponding stress components. This has been achieved through rigorous theoretical derivation, which ensures that the theory proposed is physically-based as there are three

stresses acting on a crack plane to drive damage evolution. Such derivation is consistent with the failure theory by Puck [88] and the damage representation formulation by Li et al [149].

Moreover, thanks to the natural partition of the total damage driving force into three components, different damage evolution constants are allowed for the three loading modes (corresponding to the fracture modes in Fracture Mechanics) when dealing with mixed-mode loading conditions, which avoids the unrealistic assumption in many existing theories ([85,146,147]) that different loading modes make the same contribution to damage evolution.

This damage evolution law is also applicable to unloading and reloading scenarios with the implementation of the unloading and reloading criteria devised based on damage driving force as a part of the present development.

The new UD composite CDM model containing the novel damage evolution law has been implemented as a MATLAB® code for laminate analysis and as an ABAQUS™/Standard UMAT code for finite element unit cell analysis of textile composites. Using the damage-related material constants determined from the experiments conducted for this research and those available in the literatures, the new UD composite CDM model is applied to predict intra-lamina damage in laminates and intra-tow damage in the layer-to-layer interlock 3D woven composites as those cases tested in the experimental part of this research project.

For its application to laminate analysis, it is demonstrated that as long as necessary damage-related material constants are provided, the UD composite CDM model is ready for independent prediction of damage and stress-strain response for laminates of arbitrary stacking sequences under different loading

conditions. The only shortfall exposed for the model is the lack of capability of predicting a severe stress-strain nonlinearity caused by shear. Whenever there was a strong presence of shear, the model prediction deviated away from the experimental data. Nonlinear shear behaviour has been identified as a complicated enough subject in its own right [190] and it has been left aside in the present research in order to focus on the objectives of the present project.

In its application to the 3D woven composites, the UD composite CDM model successfully predicted the intra-tow cracking damage that were observed in the experiments in all cases. The benefits of using this CDM model for intra-tow damage prediction are obvious as not only the stiffness reduction caused by the intra-tow damage can be predicted, but also the crack orientation and the stresses causing the damage can be identified, such that the subsequent deformation can be simulated closely leading to the final failure of the composites.

However, in terms of stress-strain behaviour prediction, due to the lack of inter-tow damage modelling, the unit cell analysis models incorporating the UD composite CDM model alone did not reproduce the experimental stress-strain curves satisfactorily, e.g. for the test cases of warp direction tensile loading. As a result, inter-tow damage modelling is necessary when carrying out damage analysis for layer-to-layer interlock 3D woven composites involving loading in the warp direction.

Without accounting for the inter-tow cracking damage, the unit cell models are capable of predicting acceptable stress-strain behaviours for the test cases of weft direction tensile loading. In particular, in the case of GF 3D woven composite, the predicted intra-tow damage in the warp tows effectively reflected the effects of the through-the-thickness transverse cracks observed in the experiment, which led

to a reasonable prediction of stress-strain nonlinearity when compared to the experimental result.

8.1.3 A New Pragmatic Continuum Damage Model to Capture the Effect of Inter-tow Damage

A new pragmatic continuum damage model is developed to capture the damage effect of inter-tow cracks in 3D woven composites caused by warp direction tensile loading. In this model, the coupled effects due to the intra-tow and inter-tow cracks are incorporated in a new damage representation. An incremental damage evolution law is proposed correspondingly, which works in conjunction with the intra-tow damage predicted by the aforementioned UD composite CDM model.

The composite material characterisation tool UnitCells© [1] has been employed to determine the new damage-related material properties in the new damage representation by artificially introducing inter-tow cracks of constant lengths. Since this inter-tow damage model is also CDM based which offers homogenised effects of damage, there is no need to model the evolution of every inter-tow crack explicitly which can be computationally expensive for engineering applications.

8.1.4 A Novel Damage Modelling Methodology for Textile Composites in Aero-engines

With the successful development of aforementioned UD composite CDM model and pragmatic inter-tow damage model, a novel damage modelling methodology

for textile composites is made possible and implemented in conjunction with the UnitCells© composite characterisation tool [1] and the artificial neural network tool developed in [1]. This methodology is described as follows.

With the UD composite CDM model, intra-tow damage within the tows of the textile composites can be predicted, where the influences due to crack orientation, mixed-mode loading, coupled damage effect and other physically-based considerations are properly accounted for. Then, based on the prediction of intra-tow damage, the pragmatic inter-tow damage model is used to account for the effect of inter-tow damage. Since both damage models are continuum damage mechanics models, explicit modelling of intra-tow and inter-tow cracks is not required for the analysis of damage process. This ensures that these models can be efficiently adopted for engineering applications.

Having established the damage modelling technique, these damage models are then employed in a large number of analysis cases for textile composite corresponding to loading cases of different load combinations, which can be encountered in engineering problems in a form of virtual testing using the composite characterisation tool UnitCells©. The stress and strain predictions from these analysis cases are then fed into the artificial neural network tool as these are essential for the artificial neural network to interpolate the constitutive behaviour of textile composite for general purpose applications [1]. Through the artificial neural network, the constitutive behaviour of textile composite incorporating the effect of damage can be interpolated for any load combination, which is then readily available for engineering applications.

8.2 Future work

The current UD composite CDM model is only capable of characterising matrix cracks in UD composites with a common orientation parallel to the fibre direction. The potential of this CDM model can be extended further by modifying it to characterise matrix cracks of different orientations, thereby making it capable of predicting more general matrix cracking scenarios.

As mentioned previously, the UD composite CDM model also lacks the ability to handle severe non-linear shear behaviour since there is no dedicated formulation in the model to account for this phenomenon. Consequently, this is also an area needing further improvement.

In terms of the inter-tow damage model developed for the layer-to-layer interlock 3D woven composites, one may notice that the inter-tow cracks characterised by the model are symmetric in the sense that they are assumed to appear in every warp curving regions regardless of the direction of the warp tow paths. However, in practice, there can be cases that the inter-tow cracks may only appear in the regions where the warp tow paths are inclined in one particular direction. This scenario is particularly likely when the layer-to-layer interlock 3D woven composites are subjected to the transverse shear loading τ_{XZ}. The appearance of the inter-tow cracks in this case appears to be asymmetric. This has not been incorporated in the present model and will be the subject of future development.

9. Reference

1. Q. Pan, "Multi-scale modelling and material characterisation of textile composites for aerospace applications," University of Nottingham, 2016
2. C. Red, Composites in commercial aircraft engines, 2014-2023, *Composites World*, **June**, (2015)
3. GEnx engine press centre, (General Electric Aviation) http://www.geaviation.com/press/genx.html (Accessed 06, 06 2016)
4. G. Norris, GEnx to have composite fan case, *Flight international*, **December**, (2004)
5. S. Stephenson, Composites enable new advances in engine technology, *High-Performance Composites*, **March**, (2011)
6. Federal aviation regulation part 33, ed., Federal Aviation Administration, 1984
7. Composite Materials Handbook - Volume 3. Polymer matrix composites materials usage, design, and analysis. MIL-HDBK-17-3F, US Department of Defence, 2002
8. M.J. Hinton, P.D. Soden, Predicting failure in composite laminates: the background to the exercise, *Composites Science and Technology*, **58**(7), 1001 - 1010 (1998)
9. P.D. Soden, A.S. Kaddour, M.J. Hinton, Recommendations for designers and researchers resulting from the world-wide failure exercise, *Composites Science and Technology*, **64**(3-4), 589-604 (2004)
10. M.J. Hinton, A.S. Kaddour, P.D. Soden, A comparison of the predictive capabilities of current failure theories for composite laminates, judged against experimental evidence, *Composites Science and Technology*, **62**(12-13), 1725-1797, Pii s0266-3538(02)00125-2, (2002)
11. P.D. Soden, M.J. Hinton, A.S. Kaddour, A comparison of the predictive capabilities of current failure theories for composite laminates, *Composites Science and Technology*, **58**(7), 1225-1254 (1998)
12. A.S. Kaddour, M.J. Hinton, P.A. Smith, S. Li, A comparison between the predictive capability of matrix cracking, damage and failure criteria for fibre reinforced composite laminates: Part A of the third world-wide failure exercise, *Journal of Composite Materials*, **47**(20-21), 2749-U2147 (2013)
13. A.S. Kaddour, M.J. Hinton, Maturity of 3D failure criteria for fibre-reinforced composites: Comparison between theories and experiments: Part B of WWFE-II, *Journal of Composite Materials*, **47**(6-7), 925-966 (2013)
14. M.J. Hinton, A.S. Kaddour, P.D. Soden, A further assessment of the predictive capabilities of current failure theories for composite laminates: comparison with experimental evidence, *Composites Science and Technology*, **64**(3-4), 549-588 (2004)
15. A LEAP toward composites, (SAE international) http://articles.sae.org/7317/ (Accessed March 15 2014)
16. W. Kong, "Macro-scale modelling of the impact response of 3D woven composites for aerospace applications," PhD Thesis, The University of Nottingham, 2016

17. M.C.Y. Niu, Composite airframe structures: practical design information and data, Conmilit Press, 1992
18. R.M. Jones, Mechanics Of Composite Materials, CRC Press, 1998
19. J. Hale, Boeing 787 from the Ground Up, *Boeing aero magazine*, **QTR_04**, (2006)
20. G. Hellard, Composites in Airbus - A Long Story of Innovations and Experiences, Global Investor Forum Workshop, 2008
21. G. Roberts, M. Pereira, D. Revilock, W. Binienda, M. Xie, M. Braley, Ballistic Impact of Braided Composites with a Soft Projectile, *NASA Technical Reports*, **E-14395**, (2002)
22. G. Roberts, R. Goldberg, W. Biniendak, W. Arnold, J. Littell, L. Kohlman, Characterization of Triaxial Braided Composite Material Properties for Impact Simulation, *NASA Technical Reports*, **NASA/TM-2009-215660, E-17002**, (2009)
23. G. Roberts, M. Pereira, M. Braley, W. Arnold, J. Dorer, W. Watson, Design and Testing of Braided Composite Fan Case Materials and Components, *NASA Technical Reports*, **ISABE-2009-1201, E-17015**, (2009)
24. M.K. Bannister, Development and application of advanced textile composites, *Proceedings of the Institution of Mechanical Engineers Part L-Journal of Materials-Design and Applications*, **218**(L3), 253-260 (2004)
25. A.P. Mouritz, M.K. Bannister, P.J. Falzon, K.H. Leong, Review of applications for advanced three-dimensional fibre textile composites, *Composites Part a-Applied Science and Manufacturing*, **30**(12), 1445-1461 (1999)
26. P. Ruffles, The RB211 - The first 25 years, 31st Short brothers commemorative lecture, 1992 (The Queens University of Belfast)
27. J. Brancker, Hyfil or titanium? , *Flight International*, **30-April**, 725-726 (1970)
28. M. Ansar, X. Wang, C. Zhou, Modeling strategies of 3D woven composites: A review, *Composite Structures*, **93**(8), 1947-1963 (2011)
29. CFAN products, http://www.c-fan.com/products.htm (Accessed 15.3 2016)
30. E.W. Stover, I.M. Mark, W. Mueller, Preparation of an Omniweave-reinforced carbon-carbon cylinder as a candidate for evaluation in the Advanced Heat Shield screening program, *AFML-TR-70-283*, (1971)
31. L. Tong, A. Mouritz, M.B. MK, 3D fibre reinforced polymer composites, Elsevier, 2002
32. A.P. Mouritz, B.N. Cox, A mechanistic interpretation of the comparative in-plane mechanical properties of 3D woven, stitched and pinned composites, *Composites Part a-Applied Science and Manufacturing*, **41**(6), 709-728 (2010)
33. J. Bauer, Cost improvement by changing the technology, ed., Proceedings of the 1st Stade Composite Colloquium (Ed. S. Arndt) 2000, p 305–317
34. J. Hinrichsen, Composite materials in the A3XX—from history to future, ed., Proceedings of the 1st Stade Composite Colloquium (Ed. S. Arndt), 2000, p vii–xxxvi
35. A.C. Long, Design and manufacture of textile composites - Introduction, *Design and Manufacture of Textile Composites*, XIII-XVI (2005)

36. R. Wong, Sandwich construction in the Starship, 37th International SAMPE Symposium 1992, pp 186–197
37. LEAP fan casing, http://www.albint.com/businesses/aec/IndustryApplications/SampleApplications/Pages/LEAP-Fan-Casing.aspx (Accessed March 16 2013)
38. A.B. Macander, An X-D braided composite marine propeller, The 10th DOD/NASA/FAA Conference on Fibrous Composites in Structural Design, 1992, pp VII-19–VII-34
39. S. Chou, H.C. Chen, C.C. Wu, BMI RESIN COMPOSITES REINFORCED WITH 3D CARBON-FIBER FABRICS, *Composites Science and Technology*, **43**(2), 117-128 (1992)
40. A.P. Mouritz, C. Baini, I. Herszberg, Mode I interlaminar fracture toughness properties of advanced textile fibreglass composites, *Composites Part a-Applied Science and Manufacturing*, **30**(7), 859-870 (1999)
41. V.A. Guenon, T.W. Chou, J.W. Gillespie, Toughness properties of a three dimensional carbon-epoxy composite, *J Mater Sci Compos*, **24**, 4168–4175 (1989)
42. J.N. Baucom, M.A. Zikry, Low-velocity impact damage progression in woven E-glass composite systems, *Composites Part a-Applied Science and Manufacturing*, **36**(5), 658-664 (2005)
43. Y. Ding, R. Mcllhagger, W. Wenger, Structural characterisation and mechanical properties of 3-D woven composites, ed., European SAMPE, 1993, p 1-9
44. G. Farley, B. Smith, J. Maiden, Compressive response of thick layer composite laminates with through-the-thickness reinforcement, *Journal of Reinforced Plastics and Composites* **11** 787–810 (1992)
45. T. Guess, E. Reedy, Comparison of interlock fabric and laminated fabric Kevlar 49/epoxy composites, *Journal of Composites Technology and Research*, **7**, 136–142 (1985)
46. T. Norman, P. Alsion, J. Baldwin, B. Gracias, D. Seesdorf, Effect of tow alignment on the mechanical performance of 3-D woven textile composites, NASA Conference Publication 3211ed., 1992
47. J. Byun, T. Chou, Elastic properties of 3-D angle-interlock fabric preforms, *Journal of the Textile Institute*, **81**, 538–548 (1990)
48. B. Lee, K.H. Leong, I. Herszberg, Effect of weaving on the tensile properties of carbon fibre tows and woven composites, *Journal of Reinforced Plastics and Composites*, **20**(8), 652-670 (2001)
49. L. Lee, S. Rudov-Clark, A.P. Mouritz, M.K. Bannister, I. Herszberg, Effect of weaving damage on the tensile properties of three-dimensional woven composites, *Composite Structures*, **57**(1-4), 405-413, Pii s0236-8223(02)00108-3, (2002)
50. S. Rudov-Clark, A.P. Mourtiz, L. Lee, M.K. Bannister, Fibre damage in the manufacture of advanced three-dimensional woven composites, *Composites Part a-Applied Science and Manufacturing*, **34**(10), 963-970 (2003)
51. B. Cox, M. Dadkhah, W. Morris, On the tensile properties of 3D woven composites, *Composites*, **27A** 447–458 (1996)

52. P.J. Callus, A.P. Mouritz, M.K. Bannister, K.H. Leong, Tensile properties and failure mechanisms of 3D woven GRP composites, *Composites Part a-Applied Science and Manufacturing*, **30**(11), 1277-1287 (1999)
53. V. Lopresto, V. Melito, C. Leone, G. Caprino, Effect of stitches on the impact behaviour of graphite/epoxy composites, *Composites Science and Technology*, **66**(2), 206-214 (2006)
54. A. Yoshimura, T. Nakao, S. Yashiro, N. Takeda, Improvement on out-of-plane impact resistance of CFRP laminates due to through-the-thickness stitching, *Composites Part a-Applied Science and Manufacturing*, **39**(9), 1370-1379 (2008)
55. F. Larsson, Damage tolerance of a stitched carbon/epoxy laminate, *Composites Part a-Applied Science and Manufacturing*, **28**(11), 923-934 (1997)
56. F. Aymerich, C. Pani, P. Priolo, Damage response of stitched cross-ply laminates under impact loadings, *Engineering Fracture Mechanics*, **74**(4), 500-514 (2007)
57. F. Aymerich, C. Pani, P. Priolo, Effect of stitching on the low-velocity impact response of 0(3)/90(3) (s) graphite/epoxy laminates, *Composites Part a-Applied Science and Manufacturing*, **38**(4), 1174-1182 (2007)
58. G. Caprino, V. Lopresto, D. Santoro, Ballistic impact behaviour of stitched graphite/epoxy laminates, *Composites Science and Technology*, **67**(3-4), 325-335 (2007)
59. M.V. Hosur, U.K. Vaidya, C. Ulven, S. Jeelani, Performance of stitched/unstitched woven carbon/epoxy composites under high velocity impact loading, *Composite Structures*, **64**(3-4), 455-466 (2004)
60. A.P. Mouritz, Ballistic impact and explosive blast resistance of stitched composites, *Composites Part B-Engineering*, **32**(5), 429-437 (2001)
61. K.T. Tan, N. Watanabe, Y. Iwahori, T. Ishikawa, Understanding effectiveness of stitching in suppression of impact damage: An empirical delamination reduction trend for stitched composites, *Composites Part a-Applied Science and Manufacturing*, **43**(6), 823-832 (2012)
62. K.T. Tan, N. Watanabe, Y. Iwahori, Effect of stitch density and stitch thread thickness on low-velocity impact damage of stitched composites, *Composites Part a-Applied Science and Manufacturing*, **41**(12), 1857-1868 (2010)
63. A.P. Mouritz, B.N. Cox, A mechanistic approach to the properties of stitched laminates, *Composites Part a-Applied Science and Manufacturing*, **31**(1), 1-27 (2000)
64. A.P. Mouritz, K.H. Leong, I. Herszberg, A review of the effect of stitching on the in-plane mechanical properties of fibre-reinforced polymer composites, *Composites Part a-Applied Science and Manufacturing*, **28**(12), 979-991 (1997)
65. A.P. Mouritz, Comment on the impact damage tolerance of stitched composites, *Journal of Materials Science Letters*, **22**(7), 519-521 (2003)
66. K.T. Tan, N. Watanabe, M. Sano, Y. Iwahori, H. Hoshi, Interlaminar Fracture Toughness of Vectran-stitched Composites - Experimental and Computational Analysis, *Journal of Composite Materials*, **44**(26), 3203-3229 (2010)

67. R.M. Crane, E.T. Camponeschi, Experimental and analytical characterization of multidimensionally braided graphite/epoxy composites, *Experimental Mechanics*, **26**(3), 259-266 (1986)
68. S.T. Jenq, J. Mo, Ballistic impact response for two-step braided three-dimensional textile composites, *AIAA Journal*, **34**(2), 375-384 (1996)
69. M.P. Flanagan, M.A. Zikry, J.W. Wall, A. El-Shiekh, An experimental investigation of high velocity impact and penetration failure modes in textile composites, *Journal of Composite Materials*, **33**(12), 1080-1103 (1999)
70. B. Sun, Y. Zhang, B. Gu, Low-Velocity Impact Response and Finite Element Analysis of Four-Step 3-D Braided Composites, *Applied Composite Materials*, **20**(4), 397-413 (2013)
71. Y. Zhang, B. Sun, B. Gu, Experimental characterization of transverse impact behaviors of four-step 3-D rectangular braided composites, *Journal of Composite Materials*, **46**(24), 3017-3029 (2012)
72. J.C. Gong, B.V. Sankar, Impact Properties of Three-Dimensional Braided Graphite/Epoxy Composites, *Journal of Composite Materials*, **25**(6), 715-731 (1991)
73. Y. Zhang, P. Wang, C. Guo, Energy absorption behaviors of 3D braided composites under impact loadings with frequency domain analysis, *Polymer Composites*, **37**(5), 1620-1627 (2016)
74. L. Gause, J. Alper, Structural Properties of Braided Graphite/Epoxy Composites, (1987)
75. K.H. Leong, P.J. Falzon, M.K. Bannister, I. Herszberg, An investigation of the mechanical performance of weft-knit Milano-rib glass/epoxy composites, *Composites Science and Technology*, **58**(2), 239-251 (1998)
76. Shen Chou, C.-J. Wu, A Study of the Physical Properties of Epoxy Resin Composites Reinforced with Knitted Glass Fiber Fabrics, *Journal of Reinforced Plastics and Composites*, **11**(11), 1239-1250 (1992)
77. I.M. Daniel, O. Ishai, Engineering Mechanics of Composite Materials, Oxford University Press, 2006
78. J. Echaabi, F. Trochu, R. Gauvin, Review of failure criteria of fibrous composite materials, *Polymer Composites*, **17**(6), 786--798 (1996)
79. R. Hill, A Theory of the Yielding and Plastic Flow of Anisotropic Metals, *Proceedings of the Royal Society of London A: Mathematical, Physical and Engineering Sciences*, **193**(1033), 281-297 (1948)
80. S.W. Tsai, Strength characteristics of composite materials, **NASA CR-224**, (1965)
81. V.D. Azzi, S.W. Tsai, Anisotropic strength of composites, *Experimental Mechanics*, **5**(9), 283-288 (1965)
82. O. Hoffman, The Brittle Strength of Orthotropic Materials, *Journal of Composite Materials*, **1**(2), 200-206 (1967)
83. S.W. Tsai, E.M. Wu, A General Theory of Strength for Anisotropic Materials, *Journal of Composite Materials*, **5**(1), 58-80 (1971)
84. Z. Hashin, FAILURE CRITERIA FOR UNIDIRECTIONAL FIBER COMPOSITES, *Journal of Applied Mechanics-Transactions of the Asme*, **47**(2), 329-334 (1980)
85. A. Puck, H. Schurmann, Failure analysis of FRP laminates by means of physically based phenomenological models, *Composites Science and Technology*, **58**(7), 1045-1067 (1998)

86. M.-h. Yu, Advances in strength theories for materials under complex stress state in the 20th Century, *Applied Mechanics Reviews*, **55**(3), 169-218 (2002)
87. A.S. Kaddour, M. Hinton, P.D. Soden, A comparison of the predictive capabilities of current failure theories for composite laminates: additional contributions, *Composites Science and Technology*, **64**(3-4), 449-476 (2004)
88. M. Knops, Analysis of Failure in Fiber Polymer Laminates: The Theory of Alfred Puck, Springer Berlin Heidelberg, 2008
89. R. Talreja, C.V. Singh, Damage and Failure of Composite Materials, ed., Cambridge University Press, 2012
90. J. Tong, F.J. Guild, S.L. Ogin, P.A. Smith, On matrix crack growth in quasi-isotropic laminates - I. Experimental investigation, *Composites Science and Technology*, **57**(11), 1527-1535 (1997)
91. L.E. Crocker, S.L. Ogin, P.A. Smith, P.S. Hill, Intra-laminar fracture in angle-ply laminates, *Composites Part a-Applied Science and Manufacturing*, **28**(9-10), 839-846 (1997)
92. F.J. Guild, N. Vrellos, B.W. Drinkwater, N. Balhi, S.L. Ogin, P.A. Smith, Intra-laminar cracking in CFRP laminates: observations and modelling, *Journal of Materials Science*, **41**(20), 6599-6609 (2006)
93. K.W. Garrett, J.E. Bailey, Multiple transverse fracture in 90° cross-ply laminates of a glass fibre-reinforced polyester, *Journal of Materials Science*, **12**(1), 157-168 (1977)
94. A. Parvizi, K.W. Garrett, J.E. Bailey, Constrained cracking in glass fibre-reinforced epoxy cross-ply laminates, *Journal of Materials Science*, **13**(1), 195-201 (1978)
95. J.E. Masters, K.L. Reifsnider, An Investigation of Cumulative Damage Development in Quasi-isotropic Graphite/Epoxy Laminates, *Damage in Composite Materials*, **ASTM STP 775**, 40-62 (1982)
96. N.V. Akshantala, R. Talreja, A micromechanics based model for predicting fatigue life of composite laminates, *Materials Science and Engineering a-Structural Materials Properties Microstructure and Processing*, **285**(1-2), 303-313 (2000)
97. J.-M. Berthelot, Transverse cracking and delamination in cross-ply glass-fiber and carbon-fiber reinforced plastic laminates: Static and fatigue loading, *Applied Mechanics Reviews*, **56**(1), 111-147 (2003)
98. P. Johnson, F.K. Chang, Characterization of matrix crack-induced laminate failure - Part I: Experiments, *Journal of Composite Materials*, **35**(22), 2009-2035 (2001)
99. P. Johnson, F.K. Chang, Characterization of matrix crack-induced laminate failure - Part II: Analysis and verifications, *Journal of Composite Materials*, **35**(22), 2037-2074 (2001)
100. A. Parvizi, J.E. Bailey, On multiple transverse cracking in glass fibre epoxy cross-ply laminates, *Journal of Materials Science*, **13**(10), 2131-2136 (1978)
101. K.W. Garrett, J.E. Bailey, The effect of resin failure strain on the tensile properties of glass fibre-reinforced polyester cross-ply laminates, *Journal of Materials Science*, **12**(11), 2189-2194 (1977)
102. J.E. Bailey, P.T. Curtis, A. Parvizi, On the Transverse Cracking and Longitudinal Splitting Behaviour of Glass and Carbon Fibre Reinforced

Epoxy Cross Ply Laminates and the Effect of Poisson and Thermally Generated Strain, *Proceedings of the Royal Society of London A: Mathematical, Physical and Engineering Sciences*, **366**(1727), 599-623 (1979)
103. J.E. Bailey, A. Parvizi, On fibre debonding effects and the mechanism of transverse-ply failure in cross-ply laminates of glass fibre/thermoset composites, *Journal of Materials Science*, **16**(3), 649-659 (1981)
104. F.R. Jones, A.R. Wheatley, J.E. Bailey, The Effect of Thermal Strains on the Microcracking and Stress Corrosion Behaviour of GRP, Composite Structuresed., I.H. Marshall, Ed., Springer Netherlands, 1981, p 415-429
105. J.A. Nairn, S. Hu, Micromechanics of damage: a case study of matrix microcracking, *Damage mechanics of composite materials*, 187-243 (1994)
106. R. Talreja, TRANSVERSE CRACKING AND STIFFNESS REDUCTION IN COMPOSITE LAMINATES, *Journal of Composite Materials*, **19**(4), 355-375 (1985)
107. J.A. Nairn, S. Hu, The formation and effect of outer-ply microcracks in cross-ply laminates: A variational approach, *Engineering Fracture Mechanics*, **41**(2), 203-221 (1992)
108. P.A. Smith, L. Boniface, N.F.C. Glass, A comparison of transverse cracking phenomena in (0/90)(s) and (90/0)(s) CFRP laminates, *Applied Composite Materials*, **5**(1), 11-23 (1998)
109. J. Aveston, G.A. Cooper, A. Kelly, Single and multiple fracture, The properties of fibre composites, 1971 (Surrey, UK), IPC science and technology press, pp 15-26
110. H.L. Cox, The elasticity and strength of paper and other fibrous materials, *British Journal of Applied Physics*, **3**(3), 72 (1952)
111. J. Aveston, A. Kelly, Theory of multiple fracture of fibrous composites, *Journal of Materials Science*, **8**(3), 352-362 (1973)
112. P.W. Manders, T.-W. Chou, F.R. Jones, J.W. Rock, Statistical analysis of multiple fracture in 0°/90°/0° glass fibre/epoxy resin laminates, *Journal of Materials Science*, **18**(10), 2876-2889 (1983)
113. P.A. Smith, S.L. Ogin, On transverse matrix cracking in cross-ply laminates loaded in simple bending, *Composites Part a-Applied Science and Manufacturing*, **30**(8), 1003-1008 (1999)
114. P.A. Smith, S.L. Ogin, Characterization and modelling of matrix cracking in a (0/90)(2s) GFRP laminate loaded in flexure, *Proceedings of the Royal Society a-Mathematical Physical and Engineering Sciences*, **456**(2003), 2755-2770 (2000)
115. K. Ogi, P.A. Smith, Characterisation of transverse cracking in a quasi-isotropic GFRP laminate under flexural loading, *Applied Composite Materials*, **9**(2), 63-79 (2002)
116. Z. Hashin, Analysis of cracked laminates: a variational approach, *Mechanics of Materials*, **4**(2), 121-136 (1985)
117. J. Varna, L. Berglund, Multiple Transverse Cracking and Stiffness Reduction in Cross-Ply Laminates, (1991)
118. J. Varna, L.A. Berglund, Two-dimensional transverse cracking in [0m/90n]s cross-ply laminates, *European Journal of Mechanics A - Solids*, **12**(5), 699-723 (1993)

119. J. Varna, L.A. Berglund, THERMOELASTIC PROPERTIES OF COMPOSITE LAMINATES WITH TRANSVERSE CRACKS, *Journal of Composites Technology & Research*, **16**(1), 77-87 (1994)
120. S. Kuriakose, R. Talreja, Variational solutions to stresses in cracked cross-ply laminates under bending, *International Journal of Solids and Structures*, **41**(9–10), 2331-2347 (2004)
121. S. Li, F. Hafeez, Variation-based cracked laminate analysis revisited and fundamentally extended, *International Journal of Solids and Structures*, **46**(20), 3505-3515 (2009)
122. S. Li, C.V. Singh, R. Talreja, A representative volume element based on translational symmetries for FE analysis of cracked laminates with two arrays of cracks, *International Journal of Solids and Structures*, **46**(7–8), 1793-1804 (2009)
123. K. Srirengan, J.D. Whitcomb, Finite Element Based Degradation Model for Composites with Transverse Matrix Cracks, *Journal of Thermoplastic Composite Materials*, **11**(2), 113-123 (1998)
124. J. Noh, J. Whitcomb, Effect of Various Parameters on the Effective Properties of a Cracked Ply, *Journal of Composite Materials*, **35**(8), 689-712 (2001)
125. S. Li, S.R. Reid, P.D. Soden, A finite strip analysis of cracked laminates, *Mechanics of Materials*, **18**(4), 289-311 (1994)
126. L.M. Kachanov, Rupture Time Under Creep Conditions, *International Journal of Fracture*, **97**(1), 11-18 (1999)
127. J. Lemaitre, J.L. Chaboche, Mécanique des matériaux solides, Dunod, 1988
128. D. Krajcinovic, Continuous Damage Mechanics Revisited: Basic Concepts and Definitions, *Journal of Applied Mechanics*, **52**(4), 829-834 (1985)
129. R. Talreja, A Continuum Mechanics Characterization of Damage in Composite Materials, *Proceedings of the Royal Society of London. Series A, Mathematical and Physical Sciences*, **399**(1817), 195-216 (1985)
130. R. Talreja, DAMAGE MECHANICS OF COMPOSITE-MATERIALS BASED ON THERMODYNAMICS WITH INTERNAL VARIABLES, 1991
131. R. Talreja, Damage and fatigue in composites - A personal account, *Composites Science and Technology*, **68**(13), 2585-2591 (2008)
132. A. Matzenmiller, J. Lubliner, R.L. Taylor, A CONSTITUTIVE MODEL FOR ANISOTROPIC DAMAGE IN FIBER-COMPOSITES, *Mechanics of Materials*, **20**(2), 125-152 (1995)
133. O. Allix, P. Ladeveze, D. Gilletta, R. Ohayon, A DAMAGE PREDICTION METHOD FOR COMPOSITE STRUCTURES, *International Journal for Numerical Methods in Engineering*, **27**(2), 271-283 (1989)
134. P. Ladeveze, E. Ledantec, DAMAGE MODELING OF THE ELEMENTARY PLY FOR LAMINATED COMPOSITES, *Composites Science and Technology*, **43**(3), 257-267 (1992)
135. P. Ladeveze, O. Allix, J.F. Deu, D. Leveque, A mesomodel for localisation and damage computation in laminates, *Computer Methods in Applied Mechanics and Engineering*, **183**(1-2), 105-122 (2000)

136. P. Ladeveze, G. Lubineau, On a damage mesomodel for laminates: micro-meso relationships, possibilities and limits, *Composites Science and Technology*, **61**(15), 2149-2158 (2001)
137. O. Allix, F. Hild, Continuum Damage Mechanics of Materials and Structures, Elsevier Science, 2002
138. S. Murakami, Continuum Damage Mechanics: A Continuum Mechanics Approach to the Analysis of Damage and Fracture, Springer Netherlands, 2012
139. P.A. Zinoviev, S.V. Grigoriev, O.V. Lebedeva, L.P. Tairova, The strength of multilayered composites under a plane-stress state, *Composites Science and Technology*, **58**(7), 1209-1223 (1998)
140. T.A. Bogetti, C.P.R. Hoppel, V.M. Harik, J.F. Newill, B.P. Burns, Predicting the nonlinear response and progressive failure of composite laminates, *Composites Science and Technology*, **64**(3–4), 329-342 (2004)
141. M. Knops, C. Bogle, Gradual failure in fibre/polymer laminates, *Composites Science and Technology*, **66**(5), 616-625 (2006)
142. E. Sitnikova, T. Yu, S. Li, Controversies in some of the commonly used damage models incorporated in commercial FE codes, The 17th European Conference on Composite Materials, 2016 (Munich, Deutschland)
143. F. Daghia, P. Ladeveze, Identification and validation of an enhanced mesomodel for laminated composites within the WWFE-III, *Journal of Composite Materials*, **47**(20-21), 2675-2694 (2013)
144. S.B. Sapozhnikov, S.I. Cheremnykh, The strength of fibre reinforced polymer under a complex loading, *Journal of Composite Materials*, **47**(20-21), 2525-2552 (2013)
145. E.C. Edge, Stress-based grant-sanders method for predicting failure of composite laminates, *Composites Science and Technology*, **58**(7), 1033-+ (1998)
146. L.S.T. CORPORATION, LS-DYNA KEYWORD USER'S MANUAL, Material Models, LS-DYNA R8.0 ed., 2015
147. A. Forghani, N. Zobeiry, A. Poursartip, R. Vaziri, A structural modelling framework for prediction of damage development and failure of composite laminates, *Journal of Composite Materials*, **47**(20-21), 2553-2574 (2013)
148. H.M. Deuschle, B.-H. Kroeplin, Finite element implementation of Puck's failure theory for fibre-reinforced composites under three-dimensional stress, *Journal of Composite Materials*, **46**(19-20), 2485-2513 (2012)
149. S. Li, M. Wang, L. Jeanmeur, F. Yu, Q. Pan, C. Zhou, Determination of damage related material constants associated with matrix cracks in UD composites within the continuum damage mechanics framework, *submitted for publication in Composites Science and Technology*, (2012)
150. P.D. Soden, M.J. Hinton, A.S. Kaddour, Lamina properties, lay-up configurations and loading conditions for a range of fibre-reinforced composite laminates, *Composites Science and Technology*, **58**(7), 1011-1022 (1998)
151. P.D. Soden, M.J. Hinton, A.S. Kaddour, Biaxial test results for strength and deformation of a range of E-glass and carbon fibre reinforced composite laminates: failure exercise benchmark data, *Composites Science and Technology*, **62**(12-13), 1489-1514, Pii s0266-3538(02)00093-3, (2002)

152. A.C. Orifici, I. Herszberg, R.S. Thomson, Review of methodologies for composite material modelling incorporating failure, *Composite Structures*, **86**(1-3), 194-210 (2008)
153. S. Li, S.R. Reid, P.D. Soden, A continuum damage model for transverse matrix cracking in laminated fibre-reinforced composites, *Philosophical Transactions of the Royal Society a-Mathematical Physical and Engineering Sciences*, **356**(1746), 2379-2412 (1998)
154. P. Tan, L.Y. Tong, G.P. Steven, T. Ishikawa, Behavior of 3D orthogonal woven CFRP composites. Part I. Experimental investigation, *Composites Part a-Applied Science and Manufacturing*, **31**(3), 259-271 (2000)
155. W.S. Kuo, T.H. Ko, Compressive damage in 3-axis orthogonal fabric composites, *Composites Part a-Applied Science and Manufacturing*, **31**(10), 1091-1105 (2000)
156. W.-S. Kuo, T.-H. Ko, C.-P. Chen, Effect of weaving processes on compressive behavior of 3D woven composites, *Composites Part a-Applied Science and Manufacturing*, **38**(2), 555-565 (2007)
157. K.H. Leong, B. Lee, I. Herszberg, M.K. Bannister, The effect of binder path on the tensile properties and failure of multilayer woven CFRP composites, *Composites Science and Technology*, **60**(1), 149-156 (2000)
158. S.V. Lomov, D.S. Ivanov, T.C. Truong, I. Verpoest, F. Baudry, K.V. Bosche, H. Xie, Experimental methodology of study of damage initiation and development in textile composites in uniaxial tensile test, *Composites Science and Technology*, **68**(12), 2340-2349 (2008)
159. A.E. Bogdanovich, Multi-scale modeling, stress and failure analyses of 3-D woven composites, *Journal of Materials Science*, **41**(20), 6547-6590 (2006)
160. S.V. Lomov, M. Karahan, A.E. Bogdanovich, I. Verpoest, Monitoring of acoustic emission damage during tensile loading of 3D woven carbon/epoxy composites, *Textile Research Journal*, **84**(13), 1373-1384 (2014)
161. S. John, I. Herszberg, F. Coman, Longitudinal and transverse damage taxonomy in woven composite components, *Composites Part B-Engineering*, **32**(8), 659-668 (2001)
162. B.N. Cox, M.S. Dadkhah, W.L. Morris, J.G. Flintoff, Failure mechanisms of 3D woven composites in tension, compression, and bending, *Acta Metallurgica et Materialia*, **42**(12), 3967-3984 (1994)
163. B.N. Cox, M.S. Dadkhah, THE MACROSCOPIC ELASTICITY OF 3D WOVEN COMPOSITES, *Journal of Composite Materials*, **29**(6), 785-819 (1995)
164. J. Xu, B.N. Cox, M.A. McGlockton, W.C. Carter, A BINARY MODEL OF TEXTILE COMPOSITES .2. THE ELASTIC REGIME, *Acta Metallurgica Et Materialia*, **43**(9), 3511-3524 (1995)
165. K.C. Warren, R.A. Lopez-Anido, J. Goering, Experimental investigation of three-dimensional woven composites, *Composites Part a-Applied Science and Manufacturing*, **73**, 242-259 (2015)
166. D.S. Ivanov, "Damage analysis of textile composites," University of Leuven, 2009
167. A.K. Pickett, M.R.C. Fouinneteau, Material characterisation and calibration of a meso-mechanical damage model for braid reinforced

composites, *Composites Part A: Applied Science and Manufacturing*, **37**(2), 368-377 (2006)
168. M.R.C. Fouinneteau, A.K. Pickett, Shear mechanism modelling of heavy tow braided composites using a meso-mechanical damage model, *Composites Part A: Applied Science and Manufacturing*, **38**(11), 2294-2306 (2007)
169. P. Ladèveze, G. Lubineau, An enhanced mesomodel for laminates based on micromechanics, *Composites Science and Technology*, **62**(4), 533-541 (2002)
170. L. Greve, A.K. Pickett, Modelling damage and failure in carbon/epoxy non-crimp fabric composites including effects of fabric pre-shear, *Composites Part A: Applied Science and Manufacturing*, **37**(11), 1983-2001 (2006)
171. S.V. Lomov, D.S. Ivanov, I. Verpoest, M. Zako, T. Kurashiki, H. Nakai, S. Hirosawa, Meso-FE modelling of textile composites: Road map, data flow and algorithms, *Composites Science and Technology*, **67**(9), 1870-1891 (2007)
172. P.P. Camanho, S.R. Hallett, Numerical Modelling of Failure in Advanced Composite Materials, Elsevier Science & Technology, 2015
173. A. Tabiei, I. Ivanov, Materially and geometrically non-linear woven composite micro-mechanical model with failure for finite element simulations, *International Journal of Non-Linear Mechanics*, **39**(2), 175-188 (2004)
174. V. Carvelli, C. Poggi, A numerical approach for the failure analysis of textile composites, ICCM -14, 2003 (San Diego, USA), pp 1-8
175. A. Miravete, J.M. Bielsa, A. Chiminelli, J. Cuartero, S. Serrano, N. Tolosana, R.G. de Villoria, 3D mesomechanical analysis of three-axial braided composite materials, *Composites Science and Technology*, **66**(15), 2954-2964 (2006)
176. L.G. Zhao, N.A. Warrier, A.C. Long, Finite element modelling of damage propagation in non-crimp fabric reinforced composites, *Compos Sci Techno*, **66**(36-50), (2006)
177. D.S. Ivanov, F. Baudry, B. Van Den Broucke, S.V. Lomov, H. Xie, I. Verpoest, Failure analysis of triaxial braided composite, *Composites Science and Technology*, **69**(9), 1372-1380 (2009)
178. S.D. Green, M.Y. Matveev, A.C. Long, D. Ivanov, S.R. Hallett, Mechanical modelling of 3D woven composites considering realistic unit cell geometry, *Composite Structures*, **118**, 284-293 (2014)
179. W.R. McLendon, J.D. Whitcomb, Random fibre-matrix model for predicting damage in multiscale analysis of textile composites under thermomechanical loads, The 19th International Conference on Composite Materialsed., 2013
180. M.W. S Li, L Jeanmeur, F Yu, Q Pan, C Zhou, Determination of damage related material constants associated with matrix cracks in UD composites within the continuum damage mechanics framework, *submitted for publication in Composites Science and Technology*, (2012)
181. T.L. Anderson, Fracture Mechanics: Fundamentals and Applications, Third Edition, Taylor & Francis, 2005
182. ASTM D3039 / D3039M-14, Standard Test Method for Tensile Properties of Polymer Matrix Composite Materials, ed., ASTM International, 2014

183. ASTM D3518 / D3518M-13, Standard Test Method for In-Plane Shear Response of Polymer Matrix Composite Materials by Tensile Test of a ±45° Laminate, ed., ASTM International, 2013
184. Araldite® standard 2 x 15ml tube product information, ed., Huntsman advanced materials (Switzerland) GmbH, 2011
185. PCI-2 based AE system user's manual, Rev 3 ed., Physical acoustic corporation, 2007
186. A.E. Bogdanovich, M. Karahan, S.V. Lomov, I. Verpoest, Quasi-static tensile behavior and damage of carbon/epoxy composite reinforced with 3D non-crimp orthogonal woven fabric, *Mechanics of Materials*, **62**, 14-31 (2013)
187. C. Angell, 8552/33%/134/IM7(12K) 1200mm test report - batch number W8884, ed., Hexcel composites, 2014
188. HexPly® 8552 Epoxy matrix product data, ed., Hexcel Composites 2013
189. HexTow® IM7 carbon fiber product data, ed., Hexcel composites, 2013
190. S.M. Mohseni Shakib, S. Li, Modified three rail shear fixture (ASTM D 4255/D 4255M) and an experimental study of nonlinear in-plane shear behaviour of FRC, *Composites Science and Technology*, **69**(11–12), 1854-1866 (2009)
191. 2.5D BK-2015-02 (YF) fabric datasheet, ed., Sinoma Science & Technology Co. Ltd, 2015
192. 2.5D BK-2014-02(YF) fabric datasheet, ed., Sinoma Science & Technology Co. Ltd, 2014
193. PRIME™ 20LV epoxy infusion system product data, ed., Gurit AG
194. X. Zhao, "Defects generation in the manufacture of composite materials," University of Nottingham, 2016
195. E-glass fibre information, Sinoma Science & Technology Co. ltd, 2005, [ONLINE] Available at:http://www.sinomatech.com/2009/tezhongxianwei [Accessed 25 April 2016], ed.
196. K. Marlett, Hexcel 8552 IM7 Unidirectional Prepreg Qualification Material Property Data Report, 2011
197. M. Jalalvand, M.R. Wisnom, H. Hosseini-Toudeshky, B. Mohammadi, Experimental and numerical study of oblique transverse cracking in cross-ply laminates under tension, *Composites Part A: Applied Science and Manufacturing*, **67**, 140-148 (2014)
198. S. Li, On the unit cell for micromechanical analysis of fibre-reinforced composites, *Proceedings of the Royal Society of London A: Mathematical, Physical and Engineering Sciences*, **455**(1983), 815-838 (1999)